UPC CTTC

High-order finite volume method for solid dynamics in fluid-structure interaction applications

Centre Tecnològic de Transferència de Calor
Departament de Màquines i Motors Tèrmics
Universitat Politècnica de Catalunya

Pablo Castrillo Green
Doctoral Thesis

High-order finite volume method for solid dynamics in fluid-structure interaction applications

Pablo Castrillo Green

TESI DOCTORAL

presentada al

Departament de Màquines i Motors Tèrmics
E.T.S.E.I.A.T.
Universitat Politècnica de Catalunya

per a l'obtenció del grau de

Doctor per la Universitat Politècnica de Catalunya

Terrassa, XXX 2023

High-order finite volume method for solid dynamics in fluid-structure interaction applications

Pablo Castrillo Green

Directors de la Tesi

Dr. Joaquim Rigola Serrano

Dr. Eugenio Schillaci

Tutor de la Tesi

Dr. Assensi Oliva Llena

Tribunal Qualificador

Dr. XXX
University of XXX

Dr. XXXX
University of XXXX

Dr. XXXXX
University of XXXX

To Chiara and our kids

It ain't what you don't know that gets you into trouble.
It's what you know for sure that just ain't so.

Mark Twain

Acknowledgements

I would like to thank all the people who collaborated and contributed, in one way or another, in the development of this thesis. This work has taken several years, and many people have passed through my life. I hope I remember everyone. Many thanks to:

Prof. Assensi Oliva, head of the *Heat and Mass Transfer Technological Center* (CTTC), for depositing his trust on me as a PhD candidate and for his help during these years.

Joaquim Rigola for his supervision during this thesis and his continued enthusiasm in the development of the finite volume method to solve the solid mechanics problem. Thank you Quim, also for the feedback on the papers presented at conferences and journals; it was very important.

Eugenio Schillaci for his supervision and continuous support, making valuable suggestions and corrections that have been essential to obtain the final version of this thesis. Eugenio, I feel comfortable working with you, and it has been a pleasure to have you as my supervisor. Looking forward to continuing working with you in the future.

Alfredo Canelas, who, despite the distances, was always present when I asked him for help in any matter. Thanks for all the valuable hours you invested, especially at the beginning of the thesis when your guidance was key. Alfredo, because of you, this thesis is possible.

Octavi Pavon, for the help you gave me countless times on various IT issues; sorting them out was fundamental.

The rest of my colleagues from the CTTC for their collaboration and encouragement in the writing of this thesis, especially: Carles Oliet, Nina Morozova, Nicolás Ablanque, Santiago Torras, Daniel Santos, Jesus Ruano, Nicolas Valle, Jordi Muela, Alireza Naseri and Ignacio González.

The Grant FPI-UPC (109 FPI-UPC 2018) from Universitat Politècnica de Catalunya and Banco Santander for the financial support.

Isabel and Volker for their warm welcome and hosting when I arrived to Barcelona. Firstly you were strangers to me and now you are my Catalan parents. I am sure that your help at the beginning of this journey made things easier all along the way. I will always be grateful to you.

My parents, Martha and Juan, for their unconditional support from a distance and during their visits. Also, to my sisters, Caro and Magui, who had to cover my place when necessary, especially with our Grandma Cata.

Thanks to all those other people who, somehow, helped me to carry out this thesis: Paul, Jorge, Martín, Joaquín, Chiara's parents (Lilian and Jorge), Silvia and Nacho.

Chiara for always being there for me. There are no precise words to express

everything you represent to me faithfully. You decided to accompany me on this long journey some time ago, and you are still smiling. In addition to your support, in the middle of this adventure, we started a family, a beautiful one. For that, I am also grateful. Last but not least, I also thank our children, Teo and Ciro, for all the love they have made me know and feel.

Abstract

The present thesis aims at developing a high-order finite volume method for solid dynamics on unstructured three-dimensional meshes. The adoption of high-order interpolation methods has a key importance in the efficient application of numerical methods for the resolution of real engineering problems where stress concentration occurs, and it helps to avoid the appearance of the well-known shear locking effect. Avoiding such a detrimental effect would be possible without adopting high-order schemes, but with more costly and complex numerical simulations, i.e., by drastically increasing the number of mesh elements and/or with the need of remeshing until a suitable mesh is found.

This thesis has been developed within the *Heat and Mass Transfer Technological Center* (CTTC) research group, with a strong tradition of resolving fluid flow and fluid-structure interaction problems and where structural analysis through numerical methods is a developing field of research. Likewise, until this thesis, there was no development of the finite volume method with high-order interpolation on unstructured meshes, which placed the method far behind the finite element method in the resolution of structural problems. Using finite volume mehod strategies for resolving governing equations in both solid and fluid would lead to highly efficient couplings in fluid-structure interaction problems. Hence, this thesis is the first attempt to develop this kind of methodology, not only within the research group but in the general field of study of computational solid mechanics.

This work is developed into five chapters. The first is an introduction presenting a review of the bibliography, the motivations for developing this thesis, and the main objectives to be achieved. The following three chapters reveal, through different examples, the validation and verification of the proposed mathematical formulation. It is worth noting that much of the content included in these three chapters has already been presented or published in international journals and conferences. However, some changes have been introduced with respect to the original documents. For instance, many validations and verification examples were created specifically for this thesis. The last chapter summarizes the main contributions and proposes ideas to expand this thesis in the future. At last, five appendices are included to help the reader to understand some specific parts of the work without disturbing the normal reading of the thesis.

In detail, this work starts in Chapter 1 by introducing the reader to the historical development of the finite volume method to solve solid problems. Likewise, an example is shown where the shear locking phenomenon appears, explaining how this phenomenon can also affect the solution of bending-dominant real problems, such as a compressor reed valve.

Next, in Chapter 2, the mathematical formulation is displayed with all the theoret-

ical concepts needed to reproduce the method, from basic concepts of solid mechanics to the introduction of the two adopted interpolation methods: moving least squares and local regression estimators. In addition, the used spatial and temporal discretization are presented, as well as the resolution process, through the Newton-Raphson method, and the nonlinear problems associated with geometric or material nonlinearities.

Following the above, the verification and validation of the presented method are carried out in Chapter 3. An exhaustive analysis of all the parameters involved in formulating both two-dimensional and three-dimensional problems is performed. Likewise, in all the examples, the results are compared with analytical solutions and with solutions obtained by other methods, such as the finite element method or the finite volume method with linear interpolation. Several examples are disclosed, including: static and dynamic problems, linear and nonlinear forces (impact force), materials with linear elastic or hyperelastic behavior, and two or three-dimensional problems with regular and complex geometries.

Subsequently, Chapter 4 presents the analysis of an industrial example carried out in collaboration with the Voestalpine company. The objective of this collaboration was to characterize the behavior of the reed valve of a compressor in its cyclic operation. The company developed a custom-built impact fatigue test rig, from which displacement measurements were obtained and used to validate the method. The experiment measures the displacement of the valve as the compressed air opens and closes it by repeatedly hitting the seat, which leads to valve failure due to fatigue stresses. Therefore, this example involves several physics, such as the solid, the fluid, the interaction between them, and the impact between the valve and its seat. For this reason, it is an ambitious and essential example for the industry since it allows understanding, at least in part, the behavior of a valve before collapsing. Given its relevance, in this case, this example has been analyzed with the TermoFluids software, the finite element method, and the formulation presented in this thesis. Throughout the chapter, comparisons are made between the methods, obtaining very accurate results and explaining the main differences.

Finally, the conclusions are summarized and exposed in Chapter 5.

Contents

1

Introduction

1.1 Background and motivation

Since its most original formulations, the Finite Volume Method (FVM) is usually associated with fluid and heat transfer problems [1–3]. Unlike other numerical methods, such as the Finite Element Method (FEM) [4–6] and the Finite Difference Method [7, 8], which were first devised to solve problems in solid mechanics, the FVM began to be used in this field only since the work of Demirdžić et al. [9]. After the first cell-centered two-dimensional development of the FVM in [9] using linear displacement interpolation for linear elasticity, its use has been extended to other areas such as: material nonlinearity (Elastoplasticity [10], and Viscoelasticity [11]); large strains [12]; Fluid-Structure Interaction (FSI) [13–16] among others [17]. In Cardiff et al. [17], an exhaustive review of the development of the FVM method in solid mechanics is carried out for different approaches. The cell-centered method has been widely spread; however, some works use the vertex-centered method [18, 19]. Moreover, it is common to see the use of FEM and FVM in solving the same problem, e.g., in [19–22] the results obtained with both methods are compared, concluding that there is still no consensus on which is better to solve a specific type of problem (solid or fluid equation). The FVM has always excelled in Computational Fluid Dynamics (CFD) by solving equations that come from conservative laws. Furthermore, the FVM has a more straightforward mathematical formulation than the FEM, making it better to introduce and understand. Another remarkable advantage of the FVM is that fluxes only need to be evaluated on the faces of the elements, which is also valid for nonlinear problems, making the method simpler and cheaper from a computational point of view. On the other hand, the FEM has always stood out for its ability to increase, in a straightforward way, the order of interpolation of the main variable of the problem, which is an advantage in stress concentration problems or when the shear locking effect appears. On the contrary, for the FVM, the functions that

approximate the solution cannot be easily made of higher order, especially when the mesh is unstructured.

From the review carried out by Cardiff and Demirdžić [17], it can be deduced that there is a lack of development in the high-order interpolation of the displacement field, something that is very usual in FEM [6, 23]. The work that stands out in [17] on high order is the cell-centered developed by Demirdžić [24], which is developed for structured meshes in two dimensions and linear elasticity. A high-order interpolation is helpful, especially for problems dominated by bending. In those problems, an effect called *shear locking* appears. The shear locking occurs in bending-dominant problems due to the inability of the element edges to bend, which causes the appearance of an artificial shear deformation, making the element stiffer. This problem happens when using the FEM or the FVM with linear interpolation [24]. Refining the mesh makes it possible to obtain a sufficiently accurate solution to these problems. However, the computational cost is usually unacceptable, and the best way to address the problem is to increase the interpolation order. An example of shear locking is presented in Figure 1.1. In the left image, there is a slender clamped beam, with its geometric and mechanical parameters, for which an approximation of the displacement of the free end can be obtained [25]. The image on the right shows the results obtained when using FreeFEM[1] [26] for two types of interpolations: linear and quadratic. It is possible to see how, for linear interpolation, a larger number of elements is needed to obtain an acceptable relative error. In this case, with 141121 tetrahedrons, the relative error is 3.31 %, while 42 tetrahedrons are necessary to obtain the same error in a quadratic interpolation. Moreover, with 17971 tetrahedrons the relative errors are 11.35 % and 0.18 % using linear and quadratic interpolation, respectively.

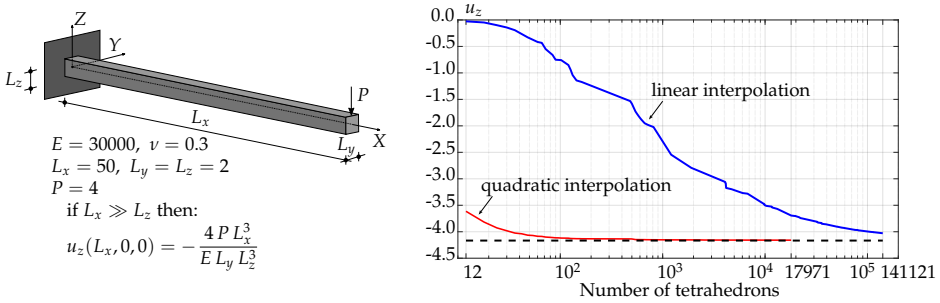

Figure 1.1: Geometric and mechanical parameters of the slender clamped beam (left) and results obtained using FreeFEM with two types of interpolation (right).

A common real example where the effect of shear locking appears is in compressor reed valves. Due to its small thickness, the solution of the simulation may be affected

[1] Free software that uses FEM.

by this phenomenon and could require a high computational effort if linear interpolation is used. The correct simulation of a compressor valve is of great industrial interest since it would allow predicting the failure of the piece, usually caused by fatigue. Fatigue is one of the main failures of machine parts in service and civil engineering structures such as bridges or buildings [27, 28]. Generally, fatigue failures are associated with stress concentrations produced by cyclic or repeatedly applied loads, which are usually wide below the loads that would result in the yielding of the material. It is a phenomenon mostly understood as an alteration in material properties. After a certain number of cycles, the material loses strength which can be interpreted as a change in the elastic, plastic, and damage behavior [29]. Usually, it starts with a crack that propagates and ends with an unpredictable collapse. A widespread and straightforward example of fatigue failure is when a metal wire is bent; at the beginning, there is no damage, but after a repetitive upward and downward bend, the wire fails. Generally, the failure of the valve is produced by the impact stresses that are generated due to the repeated impact of the valve against the seat after a large number of cycles [30–33]. Experimentally it is possible to observe that this impact produces a failure in the tip of the valve; see the left image of Figure 1.2.

As a final result of this thesis, a numerical procedure for assessing and quantifying the presence of painful stresses in the valve tip area is presented. The right image in Figure 1.2 shows the result of the von Mises stress at four points on the tip of the valve during a complete simulation of a work cycle, see Chapter 4 for more details.

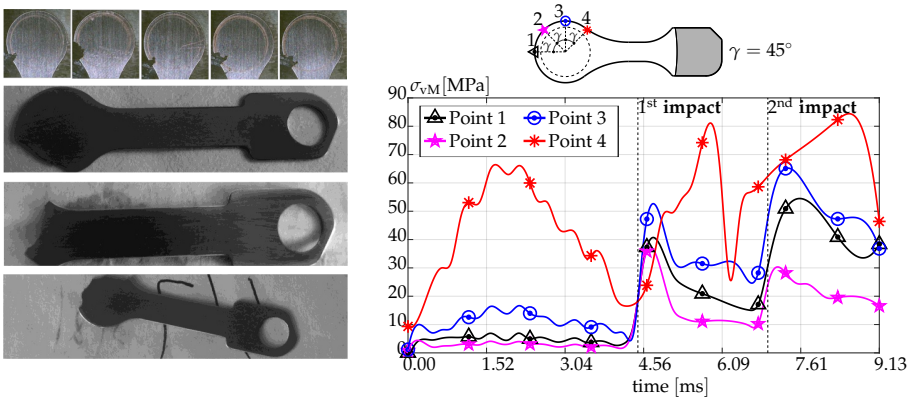

Figure 1.2: Valve failure in experiments [30, 34] (left) and von Mises stress at critical points obtained with the simulation presented in Chapter 4 (right).

In order to perform a numerical analysis of the phenomenon described above, it is necessary to take into account different physics: (1) the fluid, (2) the solid, (3) the interaction between fluid and structure, and (4) the simulation of the impact. The numerical analysis implies difficulties in mathematical formulation, complex

algorithms, and high computational costs. Generally, the finite element method is used to solve these types of problems [30, 35–37]. The previously mentioned works use commercial software, e.g., ADINA, and usually show the boundary conditions without delving into the method used. Adopting FVM strategies for resolving governing equations in both solid and fluid would lead to highly efficient couplings in fluid-structure interaction problems. In this sense, the procedures used to solve the solid and fluid problems must be compatible in some aspects, such as the mesh structure, the method to discretize the equations spatially, and the exchange of information in the fluid-structure interface [38]. Therefore, to avoid the shear locking effect when using FVM, it is necessary to use high-order interpolation to reduce the computational effort. However, the only work where a high-order interpolation scheme for the displacement field is used is the work of Demirdžić [24]. In that paper, structured two-dimensional Cartesian meshes were used following the idea proposed in [39]. Therefore, various aspects of the high-order interpolation schemes in solving these problems are still under intensive investigation [17]. One of these aspects is the use of unstructured meshes, which are of great importance for the adequate description of complex geometries and adaptive mesh refinement techniques, which are necessary in stress concentration cases.

The key feature of the current thesis consists of the formulation and validation of a high-order interpolation method for hyperelastic materials using FVM on unstructured meshes. Two techniques are used to approximate the displacement and its derivatives: the original Moving Least Squares (MLS) [40,41] and the Local Regression Estimators (LRE) [42, 43]. These methodologies allow working with unstructured meshes and arbitrary order of interpolation. Until now, none of these methods had been used to solve linear elasticity problems with finite volumes; moreover, the LRE, to the best of the author's knowledge, has never been used in continuum mechanics. The LRE is a numerical method that comes from the discipline of statistics, and the main difference with the MLS lies in how the derivatives of the main variable are approximated. In the proposed method, the coefficients of the high-order interpolation are treated implicitly in a direct solution strategy which differs from what is described in [24]. The presented method has been validated and verified with two and three-dimensional problems, considering static and dynamic cases for hyperelastic materials. In addition, the method has been used to solve the case of a real reed valve, including the simulation of the impact on the valve, thus obtaining the pressures and stresses of the impact, see Chapter 4.

1.2 Objectives

The main objective of this thesis is the development of a new formulation of the finite volume method that allows using a high-order interpolation of the displacement field

for unstructured meshes. With this, it would be possible to solve problems where the shear locking effect affects the solution while reducing the number of volumes necessary for an accurate solution. This formulation must be validated with analytical examples and compared with the solution provided by other methods such as FEM or traditional FVM [44].

The specific objectives of this thesis are:

1. Development of a high-order formulation for solid mechanics problems using the cell-centered finite volume method, see Chapter 2.
2. Verification and validation of the developed method, obtaining an adequate set of parameters for two-dimensional problems, see Section 3.1.
3. Verification and validation of the developed method, obtaining an adequate set of parameters for three-dimensional problems, see Section 3.2.
4. Simulation of a compressor reed valve considering the interaction between fluid and structure and the impact of the valve on the seat. Adopting the high-order method presented to obtain the displacement, velocity, and stress tensor of a reed valve, see Chapter 4.

1.3 Outline of the thesis

The next chapter (Chapter 2) presents the mathematical formulation and development of the high-order interpolation method. A brief introduction to solid mechanics is made [45], introducing classical strain and stress tensors. Likewise, the models of hyperelastic materials and the temporal discretization of finite volume are presented. Finally, the construction of the matrices that define the system of equations is illustrated in a pseudo-code.

The validation and verification of the method in two and three dimensions are presented in Chapter 3. The numerical results obtained with the high-order method are compared with analytical or approximate solutions under specific hypotheses. Moreover, this chapter compares the numerical results with those obtained using the FEM and a classical formulation of FVM [44]. The outcome of the exhaustive analysis presented in this chapter is a set of parameters suitable for both two-dimensional and three-dimensional problems.

In Chapter 4, the previously verified method is used to obtain the fields of displacements and stresses in the case of a compressor valve. This chapter briefly presents the different methodologies to simulate the interaction between fluid and structure and the impact of the valve on the seat. Then, the high-order formulation presented

in this thesis is used to obtain the displacement, velocity, and stress tensor of the valve. Furthermore, the distribution of contact pressures in the valve is illustrated. An increase in stresses due to the impact force is identified in the areas where the valves usually break, producing failure in the compressor operation.

Finally, in Chapter 5, the main conclusions of the thesis are presented, and research lines for future work are proposed.

References

[1] P. W. McDonald. The Computation of Transonic Flow Through Two-Dimensional Gas Turbine Cascades. In *ASME 1971 International Gas Turbine Conference and Products Show*, pages 71–89. American Society of Mechanical Engineers, mar 1971.

[2] R. Maccormack and A. Paullay. Computational efficiency achieved by time splitting of finite difference operators. In *10th Aerospace Sciences Meeting*, pages 72–154, Reston, Virigina, jan 1972. American Institute of Aeronautics and Astronautics.

[3] Suhas V. Patankar. *Numerical Heat Transfer and Fluid Flow*. CRC Press, 1st editio edition, oct 2018.

[4] R Courant. Variational methods for the solution of problems of equilibrium and vibrations. *Bulletin of the American Mathematical Society*, 49(1):1–23, 1943.

[5] T.J.R. Hughes. *The Finite Element Method: Linear Static and Dynamic Finite Element Analysis*. Dover Publications, nov 2003.

[6] Olek Zienkiewicz, Robert Taylor, and J. Z. Zhu. *The Finite Element Method: its Basis and Fundamentals*. Elsevier, 7th edition, 2013.

[7] Randall J. LeVeque. *Finite difference methods for ordinary and partial differential equations : steady-state and time-dependent problems*. Society for Industrial and Applied Mathematics, 2007.

[8] H. (Hyman) Levy and F. Lessman. *Finite difference equations*. Dover Publications, 1992.

[9] I. Demirdžić and M. Perić. Space conservation law in finite volume calculations of fluid flow. *International Journal for Numerical Methods in Fluids*, 8(9):1037–1050, sep 1988.

[10] I. Demirdžić and D. Martinović. Finite volume method for thermo-elasto-plastic stress analysis. *Computer Methods in Applied Mechanics and Engineering*, 109(3-4):331–349, nov 1993.

[11] I. Demirdžić, E. Džaferović, and A. Ivanković. FINITE-VOLUME APPROACH TO THERMOVISCOELASTICITY. *http://dx.doi.org/10.1080/10407790590901675*, 47(3):213–237, mar 2007.

[12] P. Cardiff, A. Karač, and A. Ivanković. A large strain finite volume method for orthotropic bodies with general material orientations. *Computer Methods in Applied Mechanics and Engineering*, 268:318–335, jan 2014.

[13] I. Demirdžić and S. Muzaferija. Numerical method for coupled fluid flow, heat transfer and stress analysis using unstructured moving meshes with cells of arbitrary topology. *Computer Methods in Applied Mechanics and Engineering*, 125(1-4):235–255, sep 1995.

[14] Ignacio González Acedo, Alireza Naseri, Jorge Chiva Segura, Joaquim Rigola Serrano, and Carlos David Pérez Segarra. An enhanced finite volume based solver for thermoelastic materials in fluid-structure coupled problems. In *ECCM6/ECFD 7 - 6th European Conference on Computational Mechanics / 7th European Computational Fluid Dynamics Conference*, pages 1361–1372, 2018.

[15] Ignacio González Acedo. *Development of a finite volume method for elastic materials and fluid-solid coupled applications*. PhD thesis, Universitat Politècnica de Catalunya, 2019.

[16] Alireza Naseri. *Developing numerical methods for fully-coupled nonlinear fluid-structure interaction problems*. PhD thesis, Universitat Politècnica de Catalunya, 2019.

[17] P. Cardiff and I. Demirdžić. Thirty Years of the Finite Volume Method for Solid Mechanics. *Archives of Computational Methods in Engineering*, 28:3721–3780, 2021.

[18] Y. D. Fryer, C. Bailey, M. Cross, and C. H. Lai. A control volume procedure for solving the elastic stress-strain equations on an unstructured mesh. *Applied Mathematical Modelling*, 15(11-12):639–645, nov 1991.

[19] C. Bailey and M. Cross. A finite volume procedure to solve elastic solid mechanics problems in three dimensions on an unstructured mesh. *International Journal for Numerical Methods in Engineering*, 38(10):1757–1776, may 1995.

[20] V. Selmin. The node-centred finite volume approach: Bridge between finite differences and finite elements. *Computer Methods in Applied Mechanics and Engineering*, 102(1):107–138, jan 1993.

[21] N. A. Fallah, C. Bailey, M. Cross, and G. A. Taylor. Comparison of finite element and finite volume methods application in geometrically nonlinear stress analysis. *Applied Mathematical Modelling*, 24(7):439–455, jun 2000.

[22] F. D. Molina-Aiz, H. Fatnassi, T. Boulard, J. C. Roy, and D. L. Valera. Comparison of finite element and finite volume methods for simulation of natural ventilation in greenhouses. *Computers and Electronics in Agriculture*, 72(2):69–86, jul 2010.

[23] P. Solin, K. Segeth, and I. Dolezel. *Higher-Order Finite Element Methods (Studies in Advanced Mathematics)*. Chapman and Hall/CRC, 2003.

[24] I. Demirdžić. A fourth-order finite volume method for structural analysis. *Applied Mathematical Modelling*, 40(4):3104–3114, feb 2016.

[25] Martin H. Sadd. *Elasticity: Theory, Applications, and Numerics*. Elsevier, 2009.

[26] F. Hecht. New development in freefem++. *J. of Numerical Math.*, 20(3-4):251–265, 2012.

[27] Sergio Oller, Omar Salomón, and Eugenio Oñate. A continuum mechanics model for mechanical fatigue analysis. *Computational Materials Science*, 32(2):175–195, feb 2005.

[28] Weiwei Lin and Teruhiko Yoda. Repair, Strengthening, and Replacement. In *Bridge Engineering*, pages 245–271. Butterworth-Heinemann, jan 2017.

[29] L. G. Barbu, S. Oller, X. Martinez, and A. Barbat. High cycle fatigue simulation: A new stepwise load-advancing strategy. *Engineering Structures*, 97:118–129, aug 2015.

[30] Xiaoling Yu, Qin Tan, Yumei Ren, Xiaofei Jia, and Liwen Jin. Numerical Study of the Reed Valve Impact in the Rotary Compressor by FSI Model. *Energy Procedia*, 105:4890–4897, 2017.

[31] Tofique Waqas Muhammad, Löf Alexander, Millward Chris, and Nawaz Azhar. Investigation of the influence of valve reed-impact seat plate interaction on their impact fatigue properties. In *International Compressor Engineering Conference, Purdue University*, pages 1–11, 2018.

[32] Seong-Woo Woo and Dennis L. O'Neal. Improving the Reliability of a Domestic Refrigerator Compressor Subjected to Repetitive Loading. *Engineering*, 8(3):99–115, mar 2016.

[33] Mathias Hareland, Anders Hoel, Stefan Jonsson, David Liang, and Guocai Chai. Selection of Flapper Valve Steel for High Efficient Compressor. In *International Compressor Engineering Conference*, jan 2014.

[34] Muhammad Tofique, Alexander Löf, Eugenio Schillaci, Pablo Castrillo, and Joaquim Rigola. Experimental and Numerical Analysis Of Reed Valve Movement In An Impact Fatigue Test System and Reciprocating Compressors. In *International Compressor Engineering Conference*, may 2021.

[35] Xiaoling Yu, Yumei Ren, Qin Tan, Zhao Lu, Xiaofei Jia, and Xiaolin Wang. Study on the torsional movement of a reed valve in a rotary compressor. *Advances in Mechanical Engineering*, 10(6):1–10, 2018.

[36] Yongseok Lee and Seungkil Son. Study on the Fatigue Strength of a Suction Flapper Valve used in a High Efficient Reciprocating Compressor 2 . DESIGN PARAMETERS OF SUCTION VALVEG. *International Compressor Engineering Conference*, pages 1–6, 2008.

[37] Jo. Nilsson, L. Nilsson, and M. Oldenburg. Impact stresses in flapper valves - a finite element analysis. *International Compressor Engineering Conference*, 1980.

[38] A. K. Slone, K. Pericleous, C. Bailey, and M. Cross. Dynamic fluid-structure interaction using finite volume unstructured mesh procedures. *Computers & Structures*, 80(5-6):371–390, mar 2002.

[39] Željko Lilek and Milovan Perić. A fourth-order finite volume method with colocated variable arrangement. *Computers & Fluids*, 24(3):239–252, mar 1995.

[40] P Lancaster and K Salkauskas. Surfaces generated by moving least squares methods. *Math. of Computation*, 37(155):141–158, jul 1981.

[41] T. Belytschko, Y.Y. Lu, L. Gu, and M. Tabbara. Element-free galerkin methods for static and dynamic fracture. *International Journal of Solids and Structures*, 32(17-18):2547–2570, sep 1995.

[42] Charles J. Stone. Consistent Nonparametric Regression. *The Ann. of Stat.*, 5(4):5(4):595–620, jul 1977.

[43] C. Loader. *Local Regression and Likelihood*. Statistics and Computing. Springer-Verlag, New York, 1999.

[44] P. Cardiff, Ž. Tuković, H. Jasak, and A. Ivanković. A block-coupled Finite Volume methodology for linear elasticity and unstructured meshes. *Computers & Structures*, 175:100–122, oct 2016.

[45] Morton E. Gurtin, Eliot. Fried, and Lallit. Anand. *The Mechanics and Thermodynamics of Continua*. Cambridge University Press, 2010.

2

High-order finite volume method for solid dynamics

Part of what is presented in this chapter was published, for small deformations and two dimensions, in:

[1] Pablo Castrillo, Alfredo Canelas, Eugenio Schillaci, Joaquim Rigola, and Asensio Oliva. High-order finite volume method for linear elasticity on unstructured meshes. *Computers & Structures*, 268:106829, aug 2022.
https://doi.org/10.1016/j.compstruc.2022.106829

Section 2.1 of this chapter expose the equations that govern the problem. In this thesis, the differential equations of the solid are solved using the finite volume method with a cell-centered formulation, which is detailed in Section 2.2. Section 2.3 presents the formulation that allows using a high-order interpolation of the displacement field [1]. Section 2.4 shows a synthesis of the algorithm. Finally, Section 2.5 introduces temporal discretization and summarizes the generalized method for structured dynamics applications developed in [2].

2.1 Governing equations

This section describes the equations associated with continuum mechanics used in this thesis.

2.1.1 Motion and deformation

In continuum mechanics, it is usual to define *material* and *spatial* points. A material point (or *particle*) $\boldsymbol{X}$ belongs to the *reference configuration* $\mathcal{B}_0$. The choice of the reference

configuration is arbitrary [3], although it is usually defined as that of the initial time or as the undeformed configuration of the solid. The movement of $\mathcal{B}_0$ is defined with a smooth function χ that assigns to each material point $\boldsymbol{X}$ and time t a point

$$\boldsymbol{x} = \chi(\boldsymbol{X}, t)\,, \tag{2.1}$$

where $\boldsymbol{x}$ is the spatial point occupied by $\boldsymbol{X}$ at time t. $\chi(\boldsymbol{X}, t)$ is called *deformation* or *deformation function*, which must meet some properties that are not detailed in this thesis; for more references, see Gurtin et al. [3]. The displacement field is defined as:

$$\mathbf{u}(\boldsymbol{X}, t) = \boldsymbol{x} - \boldsymbol{X} = \chi(\boldsymbol{X}, t) - \boldsymbol{X}\,. \tag{2.2}$$

The region occupied by the body at instant t is $\mathcal{B}_t = \chi(\mathcal{B}_0, t)$, called the *deformed body* or *deformed configuration*. Being ∇_0 the material gradient (finds the derivatives with respect to the material coordinates), it is possible to define the tensor field

$$\mathbf{F} = \nabla_0 \chi\,, \tag{2.3}$$

which is the *deformation gradient* that must fulfill that:

$$J = \det(\mathbf{F}) > 0\,. \tag{2.4}$$

Therefore

$$\mathbf{F} = \nabla_0 \chi = \nabla_0(\boldsymbol{x}) = \mathbf{I} + \nabla_0 \mathbf{u}\,, \tag{2.5}$$

where $\mathbf{I}$ is the identity tensor. If the deformation is homogeneous[1]:

$$\chi(\boldsymbol{X}) = \chi(\boldsymbol{Y}) + \mathbf{F}\ (\boldsymbol{X} - \boldsymbol{Y})\ , \tag{2.6}$$

for all material points $\boldsymbol{X}$ and $\boldsymbol{Y}$. The previous equation means that $\mathbf{F}$ maps material vectors to spatial vectors. In the general case, assuming that χ is continuous, differentiable and invertible, then:

$$\chi(\boldsymbol{X} + \mathbf{h}) = \chi(\boldsymbol{X}) + \nabla_0 \chi(\boldsymbol{X})\, \mathbf{h} + \mathbf{o}(\boldsymbol{X}, \mathbf{h})\,, \quad \text{with } \lim_{\mathbf{h}\to 0} \frac{\mathbf{o}(\boldsymbol{X}, \mathbf{h})}{\|\mathbf{h}\|}\,, \tag{2.7}$$

therefore a tiny volume around the material point $\boldsymbol{X}$ deforms about the same as with a uniform deformation tensor $\mathbf{F}$, see Eq. (2.6). With the above, it is possible to show relationships between the magnitudes of the reference configuration and the current configuration. The relation within differentials volumes is:

$$\mathrm{d}V = J\, \mathrm{d}V_0\,, \tag{2.8}$$

[1] The instantaneous deformation gradient $\mathbf{F}$ is independent of $\boldsymbol{X}$.

where $\mathrm{d}V$ is the differential volume in the deformed configuration while $\mathrm{d}V_0$ is the differential volume in the reference configuration. Once again, relationships between the differential area vector $\mathbf{n}\,\mathrm{d}A$ in $\mathcal{B}_t$ and the differential area vector $\mathbf{n}_0\,\mathrm{d}A_0$ in $\mathcal{B}_0$ may be identified:

$$\mathbf{n}\,\mathrm{d}A = J\,\mathbf{F}^{-\mathrm{T}}\mathbf{n}_0\,\mathrm{d}A_0\,, \tag{2.9}$$

where $\mathbf{n}$ and $\mathbf{n}_0$ are the unit normal vectors in $\mathcal{B}_t$ and $\mathcal{B}_0$, respectively.

The tensor $\mathbf{F}$ includes information about rigid body rotation, which does not produce any stress in the body. For that reason it is usual to write tensor $\mathbf{F}$ in polar decomposition $\mathbf{F} = \mathbf{R}\,\mathbf{U}$ where $\mathbf{U} = \sqrt{\mathbf{F}^{\mathrm{T}}\,\mathbf{F}}$ is a positive-definite symmetric tensor and $\mathbf{R}$ is a rotation. The tensor $\mathbf{U}$ is often problematic to apply because of the square root; therefore, it is usual to introduce the right Cauchy-Green tensor:

$$\mathbf{C} = \mathbf{U}^2 = \mathbf{F}^{\mathrm{T}}\,\mathbf{F}\,, \tag{2.10}$$

which is also symmetric and positive-definite. Another functional tensor for applications is the Green-Lagrange tensor:

$$\mathbf{E} = \frac{1}{2}\left(\mathbf{C} - \mathbf{I}\right) = \frac{1}{2}\left(\mathbf{F}^{\mathrm{T}}\,\mathbf{F} - \mathbf{I}\right)\,. \tag{2.11}$$

If the hypothesis of small deformations is assumed, $\|\nabla_0\mathbf{u}\| \ll 1$,

$$\mathbf{E} = \frac{1}{2}\left[\nabla_0\mathbf{u} + \left(\nabla_0\,\mathbf{u}\right)^{\mathrm{T}} + \left(\nabla_0\,\mathbf{u}\right)^{\mathrm{T}}\nabla_0\mathbf{u}\right] \approx \frac{1}{2}\left[\nabla_0\mathbf{u} + \left(\nabla_0\,\mathbf{u}\right)^{\mathrm{T}}\right] = \mathbf{D}\,, \tag{2.12}$$

where $\mathbf{D}$ is the infinitesimal strain tensor.

2.1.2 Balance laws

The fundamental balance equations that govern the continuum mechanics are expressed in this section.

Mass balance The total mass of any region $\mathcal{P}_t = \chi(\mathcal{P}_0, t) \subset \mathcal{B}_t$ at time t has to be equal to the total mass of region $\mathcal{P}_0 \subset \mathcal{B}_0$:

$$\int_{\mathcal{P}_t} \rho(\boldsymbol{x}, t)\,\mathrm{d}V = \int_{\mathcal{P}_0} \rho_0(\boldsymbol{X})\,\mathrm{d}V_0\,, \tag{2.13}$$

where $\rho > 0$ is the mass density in the deformed body $\mathcal{B}_t$ and $\rho_0 > 0$ is the mass density in the reference body $\mathcal{B}_0$. Using Eq. (2.8) and since $\mathcal{P}_0$ is arbitrary,

$$\int_{\mathcal{P}_0} J\,\rho - \rho_0\,\mathrm{d}V_0 = 0 \Rightarrow \rho_0 = J\,\rho\,. \tag{2.14}$$

Linear momentum balance The balance of linear momentum is expressed as:

$$\frac{\mathrm{d}}{\mathrm{d}t}\int_{\mathcal{P}_t}\rho\,\dot{\mathbf{u}}\,\mathrm{d}V=\int_{\partial\mathcal{P}_t}\mathbf{t}(\mathbf{n})\,\mathrm{d}A+\int_{\mathcal{P}_t}\mathbf{b}\,\mathrm{d}V\,, \tag{2.15}$$

where $\dot{\mathbf{u}} = \partial\mathbf{u}/\partial t$ is the velocity, $\mathbf{b}$ is a body force, and $\mathbf{t}$ is the surface traction assuming the Cauchy's hypothesis which implies that the traction depends on the outward-pointing normal $\mathbf{n}$ of the closed surface $\partial\mathcal{P}_t$.

From Cauchy's theorem $\mathbf{t}(\mathbf{n},\boldsymbol{x},t)=\boldsymbol{\sigma}(\boldsymbol{x},t)\,\mathbf{n}(\boldsymbol{x},t)$ where $\boldsymbol{\sigma}$ is a spatial tensor field called Cauchy tensor [3], therefore Eq. (2.15) is rewritten as:

$$\frac{\mathrm{d}}{\mathrm{d}t}\int_{\mathcal{P}_t}\rho\,\dot{\mathbf{u}}\,\mathrm{d}V=\int_{\partial\mathcal{P}_t}\boldsymbol{\sigma}\,\mathbf{n}\,\mathrm{d}A+\int_{\mathcal{P}_t}\mathbf{b}\,\mathrm{d}V\,, \tag{2.16}$$

where using Reynold's transport theorem:

$$\int_{\mathcal{P}_t}\rho\,\frac{\partial\dot{\mathbf{u}}}{\partial t}\,\mathrm{d}V=\int_{\partial\mathcal{P}_t}\boldsymbol{\sigma}\,\mathbf{n}\,\mathrm{d}A+\int_{\mathcal{P}_t}\mathbf{b}\,\mathrm{d}V\,. \tag{2.17}$$

Using the divergence theorem, it is possible to rewrite Eq. (2.17) as:

$$\int_{\mathcal{P}_t}\nabla\cdot\boldsymbol{\sigma}+\mathbf{b}-\rho\,\frac{\partial\dot{\mathbf{u}}}{\partial t}\,\mathrm{d}V=\mathbf{0}\,, \tag{2.18}$$

where $\nabla\cdot$ is the spatial divergence (finds the derivatives with respect to the spatial coordinates), and since this must hold for all spatial region $\mathcal{P}_t$:

$$\nabla\cdot\boldsymbol{\sigma}+\mathbf{b}=\rho\,\frac{\partial\dot{\mathbf{u}}}{\partial t}\,, \tag{2.19}$$

which is called the *local form of the linear momentum balance*.

Angular momentum balance Using the expressions mentioned above, the angular momentum balance is:

$$\int_{\mathcal{P}_t}\mathbf{r}_\mathrm{p}\times\rho\,\frac{\partial\dot{\mathbf{u}}}{\partial t}\,\mathrm{d}V=\int_{\partial\mathcal{P}_t}\mathbf{r}_\mathrm{p}\times\boldsymbol{\sigma}\,\mathbf{n}\,\mathrm{d}A+\int_{\mathcal{P}_t}\mathbf{r}_\mathrm{p}\times\mathbf{b}\,\mathrm{d}V\,, \tag{2.20}$$

where $\mathbf{r}_\mathrm{p}$ is the position vector $\mathbf{r}_\mathrm{p}=\boldsymbol{x}-\boldsymbol{o}$ being $\boldsymbol{o}$ a spatial point. An important consequence of the angular momentum balance is that the Cauchy tensor is symmetric:

$$\boldsymbol{\sigma}=\boldsymbol{\sigma}^\mathrm{T}\,, \tag{2.21}$$

this result is found deriving the *local form of the momentum balance* which is similar to the derivation of the Eq. (2.19), see [3].

Energy balance The energy balance has the form:

$$\frac{\mathrm{d}}{\mathrm{d}t}\left[\mathcal{E}(\mathcal{P}_t,t)+\mathcal{K}(\mathcal{P}_t,t)\right]=\mathcal{P}_{\text{ext}}(\mathcal{P}_t,t)+\mathcal{Q}(\mathcal{P}_t,t)\,, \tag{2.22}$$

where the rate of the addition of specific internal-energy $\mathcal{E}$ and kinetic energy $\mathcal{K}$ is equal to the addition of external mechanical power $\mathcal{P}_{\text{ext}}$ and heat flow $\mathcal{Q}$. The above expressions are defined as:

$$\mathcal{E}(\mathcal{P}_t,t) = \int_{\mathcal{P}_t}\rho\, e\,\mathrm{d}V\,, \tag{2.23}$$

$$\mathcal{K}(\mathcal{P}_t,t) = \frac{1}{2}\int_{\mathcal{P}_t}\rho\,\dot{\mathbf{u}}\cdot\dot{\mathbf{u}}\,\mathrm{d}V\,, \tag{2.24}$$

$$\mathcal{P}_{\text{ext}}(\mathcal{P}_t,t) = \int_{\mathcal{P}_t}\boldsymbol{\sigma}:\nabla\dot{\mathbf{u}}\,\mathrm{d}V+\frac{\mathrm{d}}{\mathrm{d}t}\left[\mathcal{K}(\mathcal{P}_t,t)\right]\,, \tag{2.25}$$

$$\mathcal{Q}(\mathcal{P}_t,t) = -\int_{\partial\mathcal{P}_t}\mathbf{q}\cdot\mathbf{n}\,\mathrm{d}A+\int_{\mathcal{P}_t}q\,\mathrm{d}V\,, \tag{2.26}$$

where e is the total specific energy, $\mathbf{q}$ is the heat flux, q is a scalar heat supply (e.g., radiation), and ∇ is the spatial gradient (finds the derivatives with respect to the spatial coordinates), therefore:

$$\frac{\mathrm{d}}{\mathrm{d}t}\left[\int_{\mathcal{P}_t}\rho\, e\,\mathrm{d}V\right]=-\int_{\partial\mathcal{P}_t}\mathbf{q}\cdot\mathbf{n}\,\mathrm{d}A+\int_{\mathcal{P}_t}q\,\mathrm{d}V+\int_{\mathcal{P}_t}\boldsymbol{\sigma}:\nabla\dot{\mathbf{u}}\,\mathrm{d}V\,. \tag{2.27}$$

Thermoelastic materials are not considered in this thesis, so the energy equation is not used.

2.1.3 Constitutive relationship

In this thesis, only hyperelastic-isotropic materials neglecting thermal effects are considered. From the *strain energy* ψ, it is possible to obtain the stress tensors related to the strain tensors defined in Section 2.1.1. The three most commonly used stress tensors are: (1) the Cauchy tensor $\boldsymbol{\sigma}$, (2) the second Piola stress tensor $\mathbf{S}$, and (3) the Piola stress tensor $\mathbf{P}$. The second Piola stress tensor $\mathbf{S}$ is obtained from the strain energy as:

$$\mathbf{S}=2\,\frac{\partial\,\psi(\mathbf{C})}{\partial\,\mathbf{C}}\,, \tag{2.28}$$

where $\mathbf{C}$ is the right Cauchy-Green tensor defined in Eq. (2.10), the other tensors are related to $\mathbf{S}$ as:

$$\boldsymbol{\sigma}=\frac{1}{J}\,\mathbf{F}\,\mathbf{S}\,\mathbf{F}^{\mathrm{T}}\ \text{and}\ \mathbf{P}=\mathbf{F}\,\mathbf{S}\,. \tag{2.29}$$

Saint-Venant-Kirchhoff material model For large displacement but small strains, the Saint-Venant-Kirchhoff material model is the most frequently used [3,4]. The free energy function that defines this model is:

$$\psi(\mathbf{E}) = \frac{1}{2}\lambda\,\mathrm{tr}(\mathbf{E})^2 + \mu\,\mathrm{tr}(\mathbf{E}^2)\,, \tag{2.30}$$

where $\mathbf{E}$ is the Green-Lagrange tensor defined in Eq. (2.11), λ and μ are the Lamé parameters. Using that $\mathbf{E} = (\mathbf{C} - \mathbf{I})/2$ it is possible to obtain that:

$$\mathbf{S} = \lambda\,\mathrm{tr}(\mathbf{E})\,\mathbf{I} + 2\,\mu\,\mathbf{E}\,. \tag{2.31}$$

Simo-Miehe material model This model is more suitable for materials that suffer large deformations [4,5]. The free energy function that defines this model is:

$$\psi(\mathbf{C}, J) = \frac{\mu}{2}\left(J^{-2/3}\,\mathrm{tr}(\mathbf{C}) - 3\right) + \frac{\kappa}{4}\left(J^2 - 1 - 2\,\ln(J)\right)\,, \tag{2.32}$$

where $\mathbf{C}$ and J are defined in Eqs. (2.10) and (2.4), respectively, and $\kappa = \lambda + 2\,\mu/3$ is the material bulk. From Eq. (2.28), it is possible to obtain that:

$$\mathbf{S} = \mu\,J^{-2/3}\left(\mathbf{I} - \frac{1}{3}\mathrm{tr}(\mathbf{C})\,\mathbf{C}^{-1}\right) + \frac{\kappa}{2}\left(J^2 - 1\right)\,\mathbf{C}^{-1}\,. \tag{2.33}$$

Small deformations hypothesis model If the hypothesis of small deformations is considered $\|\nabla_0\,\mathbf{u}\| \ll 1$, then both of the materials models defined above are rewritten as:

$$\mathbf{S} = \lambda\,\mathrm{tr}(\mathbf{D})\,\mathbf{I} + 2\,\mu\,\mathbf{D}\,, \tag{2.34}$$

where $\mathbf{D}$ is the infenitesimal strain tensor defined in Eq. (2.12). In addition, it is fulfilled for the stress tensors that $\boldsymbol{\sigma} = \mathbf{S} = \mathbf{P}$.

2.1.4 Mathematical model

As it was mentioned above, the thermal effect is neglected in this thesis; therefore, the equations that need to be solved are:

$$\begin{aligned} \int_{\mathcal{P}_t} \rho\,\frac{\partial \dot{\mathbf{u}}}{\partial t}\,\mathrm{d}V &= \int_{\partial\mathcal{P}_t} \boldsymbol{\sigma}\,\mathbf{n}\,\mathrm{d}A + \int_{\mathcal{P}_t} \mathbf{b}\,\mathrm{d}V\,, \\ \rho &= \rho_0/J\,, \\ \boldsymbol{\sigma} &= \boldsymbol{\sigma}^{\mathrm{T}}\,, \end{aligned} \tag{2.35}$$

where $\boldsymbol{\sigma}$ is related to the displacement field $\mathbf{u}$ trough the constitutive relationship defined in Section 2.1.3, $\mathbf{n}$ is the outward-pointing normal, $\mathbf{b}$ is the body force and $\dot{\mathbf{u}} = \partial\mathbf{u}/\partial t$.

Small deformations hypothesis

Assuming the small deformation hypothesis Eq. (2.35) is reduced to

$$\begin{aligned} \int_{\mathcal{P}_0} \rho_0 \, \ddot{\mathbf{u}} \, \mathrm{d}V_0 = \int_{\partial\mathcal{P}_0} \boldsymbol{\sigma} \, \mathbf{n}_0 \, \mathrm{d}A_0 + \int_{\mathcal{P}_0} \mathbf{b}_0 \, \mathrm{d}V_0 \,, \\ \boldsymbol{\sigma} = \lambda \, \mathrm{tr}(\mathbf{D}) \, \mathbf{I} + 2 \, \mu \, \mathbf{D} \,, \\ \mathbf{D} = \left[\nabla_0 \, \mathbf{u} + (\nabla_0 \, \mathbf{u})^{\mathrm{T}} \right] / 2 \,, \end{aligned} \tag{2.36}$$

where $\ddot{\mathbf{u}} = \partial^2 \mathbf{u} / \partial t^2$ is the acceleration. In this case, the local form of the linear momentum balance is:

$$\nabla_0 \cdot \boldsymbol{\sigma} + \mathbf{b}_0 = \rho_0 \, \frac{\partial \dot{\mathbf{u}}}{\partial t} \,, \tag{2.37}$$

where $\nabla_0 \cdot$ is the material divergence (finds the derivatives with respect to the material coordinates).

Large deformations

For solids, it is generally more convenient to use a material description, therefore replacing in Eq. (2.35) that $\boldsymbol{\sigma} = J^{-1} \, \mathbf{P} \, \mathbf{F}^{\mathrm{T}}$ and the relations between magnitudes in $\mathcal{P}_t$ and $\mathcal{P}_0$ defined in Eqs. (2.8) and (2.9):

$$\begin{aligned} \int_{\mathcal{P}_0} \rho_0 \, \ddot{\mathbf{u}} \, \mathrm{d}V_0 = \int_{\partial\mathcal{P}_0} \mathbf{P} \, \mathbf{n}_0 \, \mathrm{d}A_0 + \int_{\mathcal{P}_0} \mathbf{b}_0 \, \mathrm{d}V_0 \,, \\ \rho = \rho_0 / J \,, \\ \mathbf{P} \, \mathbf{F}^{\mathrm{T}} = \mathbf{F} \, \mathbf{P}^{\mathrm{T}} \,. \end{aligned} \tag{2.38}$$

In this case, the local form of the linear momentum balance is:

$$\nabla_0 \cdot \mathbf{P} + \mathbf{b}_0 = \rho_0 \, \frac{\partial \dot{\mathbf{u}}}{\partial t} \,. \tag{2.39}$$

Eq. (2.38) is nonlinear since $\mathbf{P}$ is, for large deformation, nonlinear with respect to $\mathbf{u}$. For that reason, to solve Eq. (2.38) for large deformation, the implementation of a Newton-Raphson scheme is needed [6]. Being $\mathbf{u} = \chi(\boldsymbol{X}, t) - \boldsymbol{X}$ the solution of Eq. (2.38) then it is necessary to find χ as:

$$\mathbf{r}(\chi) = \int_{\partial\mathcal{P}_0} \mathbf{P} \, \mathbf{n}_0 \, \mathrm{d}A_0 + \int_{\mathcal{P}_0} \mathbf{b}_0 \, \mathrm{d}V_0 - \int_{\mathcal{P}_0} \rho_0 \, \ddot{\mathbf{u}} \, \mathrm{d}V_0 = \mathbf{0} \,, \tag{2.40}$$

where $\mathbf{r}$ is the residual. Therefore, assuming that $\mathbf{b}_0$ does not depend on χ and applying the Netwon-Raphson method to the previous equation, see Appendix A, it

is obtained that the solution is $\mathbf{u}(\chi_{k+1}, t) = \mathbf{u}(\chi_k, t) + \delta\,\mathbf{u}$ such as:

$$\begin{aligned} \mathbf{r}(\chi_{k+1}) &= \mathbf{r}(\chi_k) + \int_{\partial\mathcal{P}_0} \mathbf{f}_\mathbf{S}(\chi_k, \delta\mathbf{u})\,\mathrm{d}A_0 + \int_{\partial\mathcal{P}_0} \mathbf{f}_\mathbf{C}(\chi_k, \delta\mathbf{u})\,\mathrm{d}A_0 \\ &\quad - \int_{\mathcal{P}_0} \rho_0\,\delta\ddot{\mathbf{u}}\,\mathrm{d}V_0\,, \\ &= \mathbf{0}\,, \end{aligned} \tag{2.41}$$

where k represents the iteration of the Netwon-Raphson method and

$$\mathbf{f}_\mathbf{S}(\chi_k, \delta\mathbf{u}) = [\nabla_0\,\delta\mathbf{u}]\;\mathbf{S}(\chi_k)\,\mathbf{n}_0\,, \tag{2.42}$$

$$\mathbf{f}_\mathbf{C}(\chi_k, \delta\mathbf{u}) = \mathbf{F}(\chi_k)\,\mathbb{C}(\chi_k) : \left[\frac{(\nabla_0\,\delta\mathbf{u})^\mathrm{T}\;\mathbf{F}(\chi_k) + \mathbf{F}^\mathrm{T}(\chi_k)\;(\nabla_0\,\delta\mathbf{u})}{2}\right]\mathbf{n}_0\,, \tag{2.43}$$

being $\mathbb{C}$ a fourth order tensor called *elastic moduli* [4,7], see Appendix C.

2.2 Finite volume discretization

This section illustrates the discretization using the finite volume method of the equations presented in Section 2.1.4. Firstly, the discretization of Eq. (2.36) in the case of small deformations is presented in a general sense in Section 2.2.1. Then in Section 2.2.2 the discretization of Eq. (2.40) and Eq. (2.41) for large deformations is shown.

2.2.1 Small deformations hypothesis

The body $\mathcal{P}_0$ is discretized in N_v finite volumes (internal volumes and boundary faces) where Eq. (2.36) has to be satisfied for each finite volume. In Figure 2.1, the discretization for two-dimensional problems is shown, and in Figure 2.2, a finite volume for three-dimensional is presented. In what follows, the focus is placed on three-dimensional problems; for two-dimensional problems, see [1]. V_v is the volume of the internal finite volume Ω_v, A_f is the area of the face Σ_f, and $\mathbf{n}_{0,f}$ is the outward normal of that face. $\boldsymbol{X}_n$ is the centroid of the volume, $\boldsymbol{X}_f$ is the centroid of the face (for boundary faces $\boldsymbol{X}_n = \boldsymbol{X}_f$) and $\boldsymbol{X}_{f,g}$ is the g-th quadrature point on the face Σ_f. In this thesis, the centroids of the volumes and faces are called *nodes* or *cells* of the discretization. The total of finite volumes, N_v, can be segregated as $N_\mathrm{v} = N_\mathrm{ic} + N_\mathrm{bc}$ where N_ic and N_bc are the number of internal cells and boundary cells, respectively.

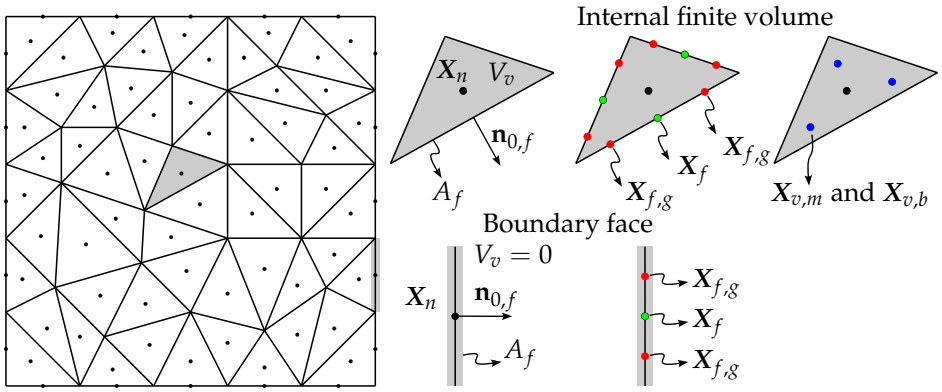

Figure 2.1: Discretization using the finite volume scheme for two-dimensional problems.

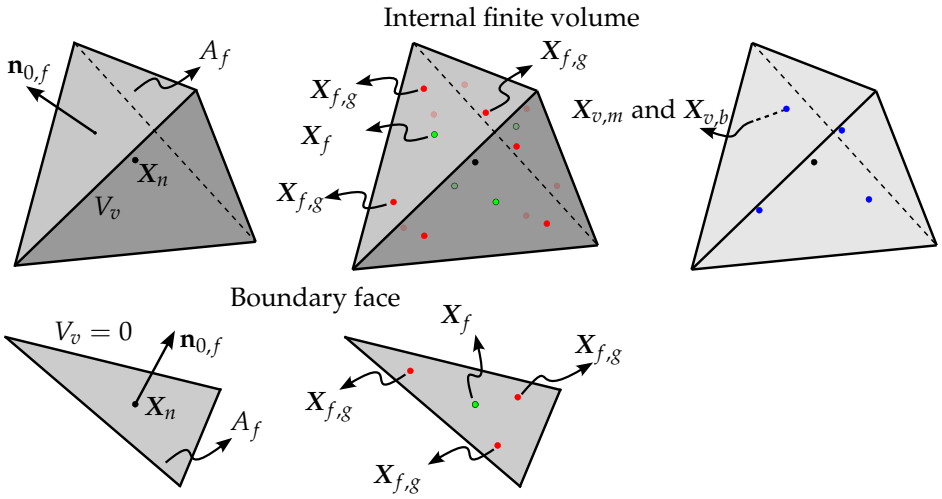

Figure 2.2: Discretization using the finite volume scheme for three-dimensional problems.

Using numerical quadrature, Eq. (2.36), for volume Ω_v, is approximated as:

$$\sum_{f=1}^{f=N_f} \left[\sum_{g=1}^{g=N_g} \alpha_g \, \boldsymbol{\sigma}(\boldsymbol{X}_{f,g}) \right] \mathbf{n}_f + \sum_{b=1}^{b=N_b} \beta_b \, \mathbf{b}_0 \left(\boldsymbol{X}_{v,b}\right) - \sum_{m=1}^{m=N_m} \gamma_m \, \rho_0(\boldsymbol{X}_{v,m}) \, \ddot{\mathbf{u}}(\boldsymbol{X}_{v,m}) = \mathbf{0}\,, \quad (2.44)$$

where N_{f} is the number of faces of the discretized finite volume Ω_v, N_{g} is the number of quadrature points used to approximate the integral on the face Σ_f, α_g are the quadrature weights, N_{m} and β_m are the number of quadrature points and weights to approximate the integral of the inertial term, respectively, and, N_{b} and β_b are the number of quadrature points and weights to approximate the integral of the body force, respectively, see Figures 2.1 and 2.2. $\boldsymbol{X}_{v,m}$ and $\boldsymbol{X}_{v,b}$ are the coordinates in the volume Ω_v of the m-th and b-th quadrature points used to integrate the inertial term and the body force, respectively. Numerical quadrature weights for different geometries are illustrated in Appendix B. Replacing Eq. (2.34) and Eq. (2.12) into Eq. (2.44):

$$\sum_{f=1}^{f=N_{\mathrm{f}}} \left[\sum_{g=1}^{g=N_{\mathrm{g}}} \alpha_g \left(\lambda \operatorname{tr}\left(\nabla_0 \mathbf{u}(\boldsymbol{X}_{f,g}) \right) \mathbf{I} + \mu \nabla_0 \mathbf{u}(\boldsymbol{X}_{f,g}) + \mu \left(\nabla_0 \mathbf{u}(\boldsymbol{X}_{f,g}) \right)^{\mathrm{T}} \right) \right] \mathbf{n}_{0,f} + \sum_{b=1}^{b=N_{\mathrm{b}}} \beta_b \, \mathbf{b}_0 \left(\boldsymbol{X}_{v,b} \right) - \sum_{m=1}^{m=N_{\mathrm{m}}} \gamma_m \, \rho_0(\boldsymbol{X}_{v,m}) \, \ddot{\mathbf{u}}(\boldsymbol{X}_{v,m}) = \mathbf{0} \,. \quad (2.45)$$

2.2.2 Large deformations

In the general case of large deformations, it is necessary to discretize Eq. (2.40) and (2.41). Therefore $\mathbf{r}(\chi_k)$ is approximated using numerical quadrature and the notation presented in Section 2.2.1 as:

$$\mathbf{r}_{\mathrm{d}}(\chi_k) = \sum_{f=1}^{f=N_{\mathrm{f}}} \left[\sum_{g=1}^{g=N_{\mathrm{g}}} \alpha_g \, \mathbf{P}(\mathbf{u}_k(\boldsymbol{X}_{f,g})) \right] \mathbf{n}_{0,f} + \sum_{b=1}^{b=N_{\mathrm{b}}} \beta_b \, \mathbf{b}_0 \left(\boldsymbol{X}_{v,b} \right) - \sum_{m=1}^{m=N_{\mathrm{m}}} \gamma_m \, \rho_0(\boldsymbol{X}_{v,m}) \, \ddot{\mathbf{u}}_k(\boldsymbol{X}_{v,m}) \,, \quad (2.46)$$

where $\mathbf{P}$ depends of the material constitutive relationship, see Section (2.1.3), as:

$$\mathbf{P}(\mathbf{u}_k(\boldsymbol{X}_{f,g})) = \mathbf{F}(\mathbf{u}_k(\boldsymbol{X}_{f,g}))\mathbf{S}(\mathbf{u}_k(\boldsymbol{X}_{f,g})) = \left[\mathbf{I} - \nabla_0 \mathbf{u}_k(\boldsymbol{X}_{f,g}) \right] \mathbf{S}(\mathbf{u}_k(\boldsymbol{X}_{f,g})) \,, \quad (2.47)$$

being $\mathbf{u}_k \left(\boldsymbol{X}_{f,g} \right)$ the displacement at iteration k evaluated at point $\boldsymbol{X}_{f,g}$. In Eq. (2.46) $\ddot{\mathbf{u}}_k(\boldsymbol{X}_{v,m})$ is the acceleration at iteration k evaluated at point $\boldsymbol{X}_{v,m}$ and it is assumed

that $\mathbf{b}_0$ do not depend on χ_k. Eq. (2.41) it is discretized as:

$$\mathbf{r}_\mathrm{d}(\chi_{k+1}) = \mathbf{r}_\mathrm{d}(\chi_k) + \sum_{f=1}^{f=N_\mathrm{f}} \left[\sum_{g=1}^{g=N_\mathrm{g}} \alpha_g \, \mathbf{f}_\mathbf{S}(\chi_k, \delta\mathbf{u}) + \alpha_g \, \mathbf{f}_\mathbf{C}(\chi_k, \delta\mathbf{u}) \right] - \sum_{m=1}^{m=N_\mathrm{m}} \gamma_m \, \rho_0(\boldsymbol{X}_{v,m}) \, \delta\ddot{\mathbf{u}}(\boldsymbol{X}_{v,m}) = \mathbf{0}\,, \quad (2.48)$$

where $\mathbf{f}_\mathbf{S}$ and $\mathbf{f}_\mathbf{C}$ are defined in Eq. (2.42) and Eq. (2.43), respectively.

To finish the spatial discretization it is necessary to write the displacement field $\mathbf{u}$ and its derivatives with respect to X, Y, and Z as a function of the nodes/cells displacements. The following section shows the high-order method developed in this thesis to carry out the aforementioned and thus complete the spatial discretization.

2.3 High-order interpolation methods

This section describes the interpolation for $\mathbf{u}\left(\tilde{\boldsymbol{X}}\right)$ and its derivatives. Two methods are used for the interpolation: Moving Least Squares and Local Regression Estimators. If $\tilde{\boldsymbol{X}}$ is the field point, then the interpolations using either of the methods are:

$$\mathbf{u}(\tilde{\boldsymbol{X}}) = \sum_{n=1}^{n=N_\mathrm{n}} c_n(\tilde{\boldsymbol{X}}) \, \mathbf{u}_n, \quad (2.49)$$

$$\frac{\partial \mathbf{u}}{\partial X}(\tilde{\boldsymbol{X}}) = \sum_{n=1}^{n=N_\mathrm{n}} c_{X,n}(\tilde{\boldsymbol{X}}) \, \mathbf{u}_n, \quad (2.50)$$

$$\frac{\partial \mathbf{u}}{\partial Y}(\tilde{\boldsymbol{X}}) = \sum_{n=1}^{n=N_\mathrm{n}} c_{Y,n}(\tilde{\boldsymbol{X}}) \, \mathbf{u}_n \quad (2.51)$$

$$\frac{\partial \mathbf{u}}{\partial Z}(\tilde{\boldsymbol{X}}) = \sum_{n=1}^{n=N_\mathrm{n}} c_{Z,n}(\tilde{\boldsymbol{X}}) \, \mathbf{u}_n\,, \quad (2.52)$$

where $\mathbf{u}_n = \left(u_{x,n} \; u_{y,n} \; u_{z,n}\right)^\mathrm{T}$ is the displacement at the node $\boldsymbol{X}_n$ of certain surrounding stencil (see Section 2.3.3), $\mathbf{c}^\mathrm{T} = \left(c_1 \; c_2 \; \cdots \; c_{N_\mathrm{n}}\right)$ is the vector of coefficients of the interpolation of $\mathbf{u}$ and $\mathbf{c}_X^\mathrm{T} = \left(c_{X,1} \; c_{X,2} \; \cdots \; c_{X,N_\mathrm{n}}\right)$ is the vector of coefficients of the interpolation of the derivative of $\mathbf{u}$ with respect to X. The differences between MLS and LRE recall in the coefficients for the interpolation of the derivatives, while the obtained coefficients are equal for the interpolation of the function. The previous

sentence is illustrated in the following sections. In what follows, it is explained how to obtain the coefficients c_n, $c_{X,n}$, $c_{Y,n}$ and $c_{Z,n}$ for the MLS and LRE methods.

2.3.1 Moving least squares

The MLS is one of the most used methods for building continuous functions that interpolate a discrete set of point samples [8,9]. For the set $\{(\boldsymbol{X}_n, u_n) : n = 1, \ldots, N_\mathrm{n}\}$ of point samples, the MLS method defines the continuous scalar function $u(\tilde{\boldsymbol{X}})$[2] at the field point $\tilde{\boldsymbol{X}}$ as the value $\tilde{u}(\tilde{\boldsymbol{X}})$ that takes an auxiliary function $\tilde{u}$ which is found by using weighted least squares. More precisely, $\tilde{u}$ is the function

$$\tilde{u}(\boldsymbol{X}) = \mathbf{p}^\mathrm{T}(\boldsymbol{X} - \tilde{\boldsymbol{X}})\,\mathbf{a}(\tilde{\boldsymbol{X}})\,, \tag{2.53}$$

where $\mathbf{p}^\mathrm{T} = \left(p_1, p_2, \ldots, p_{N_\mathrm{p}}\right)$ is a vector of *basis functions* (for example, polynomials), and $\mathbf{a}^\mathrm{T}(\tilde{\boldsymbol{X}}) = \left(a_1(\tilde{\boldsymbol{X}}), a_2(\tilde{\boldsymbol{X}}), \ldots, a_{N_\mathrm{p}}(\tilde{\boldsymbol{X}})\right)$ is the vector of parameters which minimizes the following weighted sum of squares:

$$\begin{aligned}\mathcal{R} &= \frac{1}{2}\sum_{n=1}^{n=N_\mathrm{n}} w(\boldsymbol{X}_n - \tilde{\boldsymbol{X}})\;\left[\tilde{u}(\boldsymbol{X}_n) - u_n\right]^2 \\ &= \frac{1}{2}\sum_{n=1}^{n=N_\mathrm{n}} w(\boldsymbol{X}_n - \tilde{\boldsymbol{X}})\;\left[\mathbf{p}^\mathrm{T}(\boldsymbol{X}_n - \tilde{\boldsymbol{X}})\,\mathbf{a}(\tilde{\boldsymbol{X}}) - u_n\right]^2 .\end{aligned} \tag{2.54}$$

In the previous equation, w is a certain weight function described in Section 2.3.4. Note that the continuous interpolation function u coincides with the auxiliary function $\tilde{u}$ only at the point $\tilde{\boldsymbol{X}}$, since at any other point, say $\hat{\boldsymbol{X}}$, the MLS method defines $u(\hat{\boldsymbol{X}}) = \hat{u}(\hat{\boldsymbol{X}})$, where $\hat{u}$ is the auxiliary function corresponding to $\hat{\boldsymbol{X}}$, which is generally different from $\tilde{u}$ since it is found by minimizing a different weighted sum of squares ($\tilde{\boldsymbol{X}}$ is replaced by $\hat{\boldsymbol{X}}$ in Eq. (2.54)).

In order to find the minimum of the weighted sum, the gradient of $\mathcal{R}$ with respect to $\mathbf{a}$ is set to be zero. This gives the following set of *normal equations*:

$$\frac{\partial \mathcal{R}}{\partial a_k} = \sum_{n=1}^{n=N_\mathrm{n}} w(\boldsymbol{X}_n - \tilde{\boldsymbol{X}})\,p_k(\boldsymbol{X}_n - \tilde{\boldsymbol{X}})\left[\mathbf{p}^\mathrm{T}(\boldsymbol{X}_n - \tilde{\boldsymbol{X}})\,\mathbf{a}(\tilde{\boldsymbol{X}}) - u_n\right] = 0\,, \tag{2.55}$$

for all $k = 1, 2, .., N_\mathrm{p}$. The normal equations conform a square system of linear equations that can be solved for $\mathbf{a}(\tilde{\boldsymbol{X}})$. By rearranging the terms, this system can be written as:

$$\mathbf{M}_\mathrm{I}(\tilde{\boldsymbol{X}})\,\mathbf{a}(\tilde{\boldsymbol{X}}) = \mathbf{P}_\mathrm{I}(\tilde{\boldsymbol{X}})\,\mathbf{W}(\tilde{\boldsymbol{X}})\,\mathbf{u}_\mathrm{I}\,, \tag{2.56}$$

[2] $u(\boldsymbol{X})$ is a general function but it is convenient associate it with a displacement component: u_x, u_y or u_z; and the set $\{(\boldsymbol{X}_n, u_n) : n = 1, \ldots, N_\mathrm{n}\}$ of point samples to the sets $(\boldsymbol{X}_n, u_{x,n})$, $(\boldsymbol{X}_n, u_{y,n})$ or $(\boldsymbol{X}_n, u_{z,n})$.

where $\mathbf{M}_{\mathrm{I}}(\tilde{\boldsymbol{X}}) = \mathbf{P}_{\mathrm{I}}(\tilde{\boldsymbol{X}})\,\mathbf{W}(\tilde{\boldsymbol{X}})\,\mathbf{P}_{\mathrm{I}}^{\mathrm{T}}(\tilde{\boldsymbol{X}})$ is the $N_{\mathrm{p}} \times N_{\mathrm{p}}$ *moment matrix* of the system, $\mathbf{P}_{\mathrm{I}}(\tilde{\boldsymbol{X}})$ is the $N_{\mathrm{p}} \times N_{\mathrm{n}}$ matrix whose n-th column is $\mathbf{p}(\boldsymbol{X}_n - \tilde{\boldsymbol{X}})$, $\mathbf{W}$ is the $N_{\mathrm{n}} \times N_{\mathrm{n}}$ matrix $\mathrm{diag}\left(w(\boldsymbol{X}_n - \tilde{\boldsymbol{X}})\right)$, and $\mathbf{u}_{\mathrm{I}}^{\mathrm{T}} = [u_1, u_2, \ldots, u_{N_{\mathrm{n}}}]$. By assuming that $\mathbf{M}_{\mathrm{I}}(\tilde{\boldsymbol{X}})$ is invertible, then the solution of Eq. (2.56) is $\mathbf{a}(\tilde{\boldsymbol{X}}) = \mathbf{M}_{\mathrm{I}}(\tilde{\boldsymbol{X}})^{-1}\,\mathbf{P}_{\mathrm{I}}(\tilde{\boldsymbol{X}})\,\mathbf{W}(\tilde{\boldsymbol{X}})\,\mathbf{u}_{\mathrm{I}}$ [3]. Defining

$$\mathbf{A}(\tilde{\boldsymbol{X}}) = \mathbf{M}_{\mathrm{I}}(\tilde{\boldsymbol{X}})^{-1}\,\mathbf{P}_{\mathrm{I}}(\tilde{\boldsymbol{X}})\,\mathbf{W}(\tilde{\boldsymbol{X}}) \text{ and } \mathbf{N}^{\mathrm{T}}(\tilde{\boldsymbol{X}}) = \mathbf{p}^{\mathrm{T}}(\mathbf{0})\,\mathbf{A}(\tilde{\boldsymbol{X}})\,, \tag{2.57}$$

then it is obtained that:

$$u(\tilde{\boldsymbol{X}}) = \tilde{u}(\tilde{\boldsymbol{X}}) = \mathbf{p}^{\mathrm{T}}(\mathbf{0})\,\mathbf{a}(\tilde{\boldsymbol{X}}) = \mathbf{p}^{\mathrm{T}}(\mathbf{0})\,\mathbf{A}(\tilde{\boldsymbol{X}})\,\mathbf{u}_{\mathrm{I}} = \mathbf{N}^{\mathrm{T}}(\tilde{\boldsymbol{X}})\,\mathbf{u}_{\mathrm{I}}\,. \tag{2.58}$$

Hence, $\mathbf{N}$ is a $N_{\mathrm{n}} \times 1$ matrix function whose entries can be seen as the shape functions of the MLS method. Together with the shape functions, there is interest in their partial derivatives. To obtain the partial derivatives of $\mathbf{N}$, the partial derivatives of $\mathbf{A}$ must be obtained through differentiation of the equation $\mathbf{M}_{\mathrm{I}}(\tilde{\boldsymbol{X}})\,\mathbf{A}(\tilde{\boldsymbol{X}}) = \mathbf{P}_{\mathrm{I}}(\tilde{\boldsymbol{X}})\,\mathbf{W}(\tilde{\boldsymbol{X}})$. For instance, the derivatives with respect to the coordinate X satisfy:

$$\frac{\partial \mathbf{M}_{\mathrm{I}}}{\partial X}(\tilde{\boldsymbol{X}})\,\mathbf{A}(\tilde{\boldsymbol{X}}) + \mathbf{M}_{\mathrm{I}}(\tilde{\boldsymbol{X}})\,\frac{\partial \mathbf{A}}{\partial X}(\tilde{\boldsymbol{X}}) = \frac{\partial \mathbf{P}_{\mathrm{I}}}{\partial X}(\tilde{\boldsymbol{X}})\,\mathbf{W}(\tilde{\boldsymbol{X}}) + \mathbf{P}_{\mathrm{I}}(\tilde{\boldsymbol{X}})\,\frac{\partial \mathbf{W}}{\partial X}(\tilde{\boldsymbol{X}})\,. \tag{2.59}$$

Then the following equations are obtained:

$$\frac{\partial \mathbf{A}}{\partial X}(\tilde{\boldsymbol{X}}) = \mathbf{M}_{\mathrm{I}}(\tilde{\boldsymbol{X}})^{-1}\left[\frac{\partial \mathbf{P}_{\mathrm{I}}}{\partial X}(\tilde{\boldsymbol{X}})\,\mathbf{W}(\tilde{\boldsymbol{X}}) + \mathbf{P}_{\mathrm{I}}(\tilde{\boldsymbol{X}})\,\frac{\partial \mathbf{W}}{\partial X}(\tilde{\boldsymbol{X}}) - \frac{\partial \mathbf{M}_{\mathrm{I}}}{\partial X}(\tilde{\boldsymbol{X}})\,\mathbf{A}(\tilde{\boldsymbol{X}})\right]\,, \tag{2.60}$$

and

$$\frac{\partial \mathbf{N}^{\mathrm{T}}}{\partial X}(\tilde{\boldsymbol{X}}) = \mathbf{p}^{\mathrm{T}}(\mathbf{0})\,\frac{\partial \mathbf{A}}{\partial X}(\tilde{\boldsymbol{X}})\,. \tag{2.61}$$

Partial derivatives of higher order could be obtained by successive differentiation of the equation $\mathbf{M}_{\mathrm{I}}(\tilde{\boldsymbol{X}})\,\mathbf{A}(\tilde{\boldsymbol{X}}) = \mathbf{P}_{\mathrm{I}}(\tilde{\boldsymbol{X}})\,\mathbf{W}(\tilde{\boldsymbol{X}})$, which leads to more complex formulas involving $\mathbf{M}_{\mathrm{I}}(\tilde{\boldsymbol{X}})^{-1}$ and high order derivatives of the matrix functions $\mathbf{M}_{\mathrm{I}}$, $\mathbf{P}_{\mathrm{I}}$, and $\mathbf{W}$.

The moment matrix $\mathbf{M}_{\mathrm{I}}(\tilde{\boldsymbol{X}})$ of the normal equations is known to be ill-conditioned. Details of how to accurately compute $\mathbf{N}$ and its first partial derivatives are given in Section 2.3.5.

2.3.2 Local regression estimators

The LRE method can estimate the first and higher-order derivatives of the MLS interpolation function. In fact, it is used to estimate a complete truncated Taylor

[3] Sub-index I is used to indicated that it is associated to an interpolation.

expansion of the interpolation function. The Taylor series of u at the field point $\tilde{\boldsymbol{X}}$ is:

$$u(\tilde{\boldsymbol{X}}) + \frac{\partial u}{\partial X}(\tilde{\boldsymbol{X}})(X-\tilde{X}) + \frac{\partial u}{\partial Y}(\tilde{\boldsymbol{X}})(Y-\tilde{Y}) + \frac{\partial u}{\partial Z}(\tilde{\boldsymbol{X}})(Z-\tilde{Z}) + \frac{1}{2}\frac{\partial^2 u}{\partial X^2}(\tilde{\boldsymbol{X}})(X-\tilde{X})^2 + \frac{\partial^2 u}{\partial X \partial Y}(\tilde{\boldsymbol{X}})(X-\tilde{X})(Y-\tilde{Y}) + \dots \quad (2.62)$$

Let $\bar{u}$ be a truncated Taylor expansion of u of N_p terms. Then, $\bar{u}$ can be represented in compact form as

$$\bar{u}(\boldsymbol{X}) = \mathbf{q}^\mathrm{T}(\boldsymbol{X}-\tilde{\boldsymbol{X}})\,\bar{\mathbf{a}}(\tilde{\boldsymbol{X}})\,, \quad (2.63)$$

where $\mathbf{q}^\mathrm{T} = \left(q_1, q_2, \dots, q_{N_\mathrm{q}}\right)$ is a vector of polynomial basis functions, and $\bar{\mathbf{a}}^\mathrm{T}(\tilde{\boldsymbol{X}})$ is a vector of parameters whose entries are the partial derivatives of u, i.e.:

$$\mathbf{q}^\mathrm{T}(\boldsymbol{X}-\tilde{\boldsymbol{X}}) = \left(1, (X-\tilde{X}), (Y-\tilde{Y}), (Z-\tilde{Z}), \dots\right)$$
$$\text{and } \bar{\mathbf{a}}^\mathrm{T}(\tilde{\boldsymbol{X}}) = \left(u(\tilde{\boldsymbol{X}}), \frac{\partial u}{\partial X}(\tilde{\boldsymbol{X}}), \frac{\partial u}{\partial Y}(\tilde{\boldsymbol{X}}), \frac{\partial u}{\partial Z}(\tilde{\boldsymbol{X}}), \dots\right). \quad (2.64)$$

Instead of computing the exact vector of parameters (the exact derivatives of u), the LRE looks for an approximate vector $\bar{\mathbf{a}}(\tilde{\boldsymbol{X}})$ by minimizing the following weighted sum of squares:

$$\mathcal{R} = \frac{1}{2}\sum_{n=1}^{n=N_\mathrm{n}} w(\boldsymbol{X}_n - \tilde{\boldsymbol{X}})\,\left[\bar{u}(\boldsymbol{X}_n) - u_n\right]^2$$
$$= \frac{1}{2}\sum_{n=1}^{n=N_\mathrm{n}} w(\boldsymbol{X}_n - \tilde{\boldsymbol{X}})\,\left[\mathbf{q}^\mathrm{T}(\boldsymbol{X}_n - \tilde{\boldsymbol{X}})\,\bar{\mathbf{a}}(\tilde{\boldsymbol{X}}) - u_n\right]^2. \quad (2.65)$$

Following the same steps as in the MLS, the vector $\bar{\mathbf{a}}(\tilde{\boldsymbol{X}})$ is found by solving the following linear system of equations, which is analogous to Eq. (2.56):

$$\bar{\mathbf{M}}_\mathrm{I}(\tilde{\boldsymbol{X}})\,\bar{\mathbf{a}}(\tilde{\boldsymbol{X}}) = \mathbf{Q}_\mathrm{I}(\tilde{\boldsymbol{X}})\,\mathbf{W}(\tilde{\boldsymbol{X}})\,\mathbf{u}_\mathrm{I}\,. \quad (2.66)$$

In the previous equation $\bar{\mathbf{M}}_\mathrm{I}(\tilde{\boldsymbol{X}}) = \mathbf{Q}_\mathrm{I}(\tilde{\boldsymbol{X}})\,\mathbf{W}(\tilde{\boldsymbol{X}})\,\mathbf{Q}_\mathrm{I}^\mathrm{T}(\tilde{\boldsymbol{X}})$, $\mathbf{Q}_\mathrm{I}(\tilde{\boldsymbol{X}})$ is the $N_\mathrm{q} \times N_\mathrm{n}$ matrix whose n-th column is $\mathbf{q}(\boldsymbol{X}_n - \tilde{\boldsymbol{X}})$. Defining $\bar{\mathbf{A}}(\tilde{\boldsymbol{X}}) = \bar{\mathbf{M}}_\mathrm{I}(\tilde{\boldsymbol{X}})^{-1}\mathbf{Q}_\mathrm{I}(\tilde{\boldsymbol{X}})\,\mathbf{W}(\tilde{\boldsymbol{X}})$ the solution of the system is:

$$\bar{\mathbf{a}}(\tilde{\boldsymbol{X}}) = \bar{\mathbf{A}}(\tilde{\boldsymbol{X}})\,\mathbf{u}_\mathrm{I}\,, \quad (2.67)$$

when $\bar{\mathbf{M}}_\mathrm{I}(\tilde{\boldsymbol{X}})$ is invertible.

Note the strong analogy in the representations Eq. (2.53) and Eq. (2.63), in the weighted sums Eq. (2.54) and Eq. (2.65), and in the linear systems Eq. (2.56) and Eq. (2.66). In fact, the estimate $\bar{u}(\tilde{\boldsymbol{X}}) = \mathbf{q}(\mathbf{0})^{\mathrm{T}}\bar{\mathbf{a}}(\tilde{\boldsymbol{X}})$ for the zeroth order derivative of u can be seen as an MLS interpolation function generated by a polynomial basis. In the case that $\mathbf{p} = \mathbf{q}$, i.e. the MLS uses the same Taylor basis functions, then $\bar{u}(\tilde{\boldsymbol{X}}) = \tilde{u}(\tilde{\boldsymbol{X}})$. In other words, if $\mathbf{p} = \mathbf{q}$, then the zeroth order derivative of u estimated by the LRE is exact. However, the LRE estimation of the higher order derivatives of u is generally not exact, even if $\mathbf{p} = \mathbf{q}$.

As well as the moment matrix of the MLS, the matrix $\bar{\mathbf{M}}_{\mathrm{I}}(\tilde{\boldsymbol{X}})$ of the LRE is ill-conditioned. Details of how to accurately compute $\bar{\mathbf{a}}(\tilde{\boldsymbol{X}})$ are given in Section 2.3.5.

2.3.3 Stencil

The interpolation considers a set of nodes conforming a surrounding *stencil*. There are many ways to define the stencil [10, 11]. This thesis proposes to set a number N_{n} and consider the N_{n}-nearest nodes to the point $\boldsymbol{X}$. With these N_{n}-nearest nodes, the maximum distance $r_{\mathrm{s}} = \max \|\boldsymbol{X} - \boldsymbol{X}_n\|$ is calculated, and all nodes at that distance from the point $\boldsymbol{X}$ are included in the stencil. Note that the stencil of $\boldsymbol{X}$ could contain more than N_{n} nodes (this is more common in structured meshes). There is a minimum number of nodes N_{n} corresponding to the dimension of the polynomial basis [10], which, for two dimensions, is given by $N_{\mathrm{n,min}} = (i+1)(i+2)/2$ where i indicates the order of the interpolation, and in three dimensions is $N_{\mathrm{n,min}} = (i+1)(i+2)(i+3)/6$.

To calculate the integrals it is necessary to obtain the coefficients for each Gaussian point of each surface, and consequently, obtain a stencil of N_{n} points for each Gaussian point, being computationally expensive. For that reason, two ways of obtaining the stencil for each Gauss point of a surface are proposed:

$\mathrm{s_{eq}}$: Obtain the stencil of the centroid of the face $\boldsymbol{X}_f$ and use that stencil for all the Gauss points $\boldsymbol{X}_{f,g}$ of that surface, see left image of Figure 2.3.

$\mathrm{s_{df}}$: Obtain a different stencil for each Gauss point, see right image of Figure 2.3.

Figure 2.3 shows the two types of stencils proposed in this thesis for $N_{\mathrm{n}} = 16$. The image on the left shows the stencil $\mathrm{s_{eq}}$ with the N_{n} nodes closest to $\boldsymbol{X}_f$, which is used to obtain the interpolation coefficients of all the Gauss points. It is interesting to see how, in that example, it ends up being 17 points because $\|\boldsymbol{X}_f - \boldsymbol{X}_{16}\| = \|\boldsymbol{X}_f - \boldsymbol{X}_{17}\|$. The right image presents the stencil $\mathrm{s_{df}}$ for a Gaussian point of the face f, which is 16 points. In this second image, the cells belonging to the stencil and the ones that do not, squares and asterisks, respectively, have been identified.

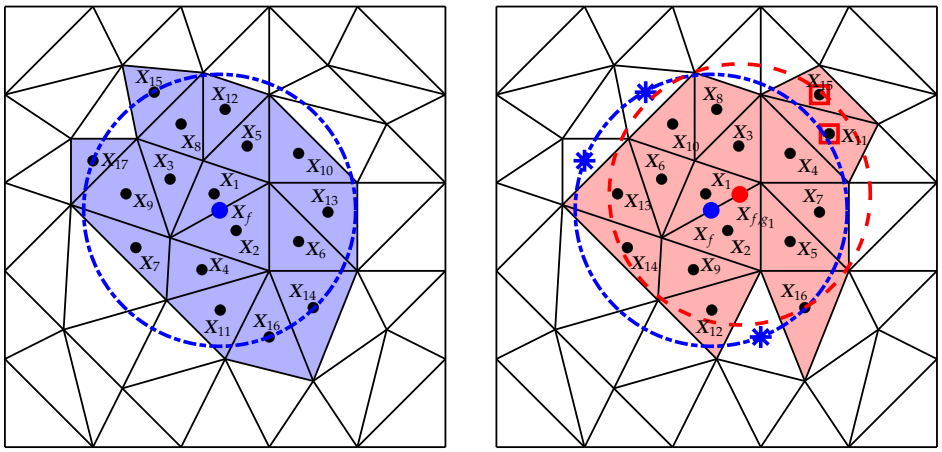

Figure 2.3: Stencil s_{eq} (left) and stencil s_{df} (right).

2.3.4 Weight function

Several different weight functions are available in the literature [11, 12]; in this thesis, the following radially symmetric exponential function is used:

$$w(\boldsymbol{X}, \boldsymbol{X}_n, k) = \frac{e^{-\left(\frac{d}{d_m}\right)^2 k^2} - e^{-k^2}}{1 - e^{-k^2}}, \tag{2.68}$$

where $d = \|\boldsymbol{X} - \boldsymbol{X}_n\|$, $d_m = 2\,r_s$ and k is a shape parameter, being $r_s = \max \|\boldsymbol{X} - \boldsymbol{X}_n\|$ the maximum distance, $\boldsymbol{X}_n$ is a node of the stencil of face Σ_f and $\boldsymbol{X}$ is the cell whose stencil is sought.

2.3.5 Accurate solution of the MLS and LRE linear systems

The MLS linear systems Eq. (2.57) and Eq. (2.60), as well as the LRE systems Eq. (2.67) are defined by a usually ill-conditioned moment matrix $\mathbf{M}_I$. There can be several sources of ill-conditioning, which are described below:

a) *Inadequate basis*: the basis functions conforming the vector $\mathbf{p}$ should ideally be linearly independent in order not to affect the rank of the rows of $\mathbf{P}_I$. The Taylor basis fulfills this requirement, but the conditioning can be affected by the different order of magnitude of the components of the Taylor basis. To alleviate

this difficulty, the basis should be scaled, e.g., by redefining it as:

$$\hat{\mathbf{p}}^{\mathrm{T}}(\boldsymbol{X}-\tilde{\boldsymbol{X}}) = \left[1, \frac{(X-\tilde{X})}{h}, \frac{(Y-\tilde{Y})}{h}, \frac{(Z-\tilde{Z})}{h}, \frac{(X-\tilde{X})^2}{h^2}, \frac{(X-\tilde{X})(Y-\tilde{Y})}{h^2}, \cdots\right], \quad (2.69)$$

where $h = 2\,r_{\mathrm{s}}$ is a scaling coefficient, and r_s is defined in Section 2.3.3.

b) *Inadequate stencil*: the rank of $\mathbf{P}_{\mathrm{I}}$ can be deficient if there is a small number of points in the stencil or if they are in a bad geometric configuration, e.g., if they are all aligned. Then, an appropriate rule has to be used to define the stencil, e.g., the given in Section 2.3.3, which should provide an adequate stencil in a good quality mesh.

c) *Inadequate weight function*: if the support of the weight function is too small or has a bad aspect ratio, then it can lead to the same difficulties mentioned in item b). Then, the parameters of the weight function must be chosen considering the definition of the stencil, e.g., as described in Section 2.3.4.

d) *Inadequate solution algorithm*: It is well known that the linear systems of weighted least squares problems can require specialized algorithms to obtain accurate solutions since the moment matrix itself can be a source of ill-conditioning. The QR decomposition is one of the most popular approaches to accurately solve these linear systems, as explained below.

The typical form of the normal equations in weighted least squares problems is given by Eq. (2.70), where $\mathbf{P}_{\mathrm{I}}$ is an $N_{\mathrm{p}} \times N_{\mathrm{n}}$ matrix with $N_{\mathrm{n}} \geq N_{\mathrm{p}}$, $\mathbf{W}$ is an $N_{\mathrm{n}} \times N_{\mathrm{n}}$ diagonal positive definite matrix, $\mathbf{X}$ is the $N_{\mathrm{p}} \times N_{\mathrm{k}}$ unknown matrix, and $\mathbf{B}$ is an $N_{\mathrm{p}} \times N_{\mathrm{k}}$ matrix. For instance, in the MLS linear system Eq. (2.57), $N_{\mathrm{k}} = N_{\mathrm{n}}$, $\mathbf{X}$ represents $\mathbf{A}(\tilde{\mathbf{x}})$ and $\mathbf{B}$ is the identity matrix.

$$\mathbf{P}_{\mathrm{I}}\mathbf{W}\mathbf{P}_{\mathrm{I}}^{\mathrm{T}}\mathbf{X} = \mathbf{P}_{\mathrm{I}}\mathbf{W}\mathbf{B}\,. \quad (2.70)$$

The previous system can be rewritten as $\mathbf{P}_{\mathrm{I}}\mathbf{W}(\mathbf{P}_{\mathrm{I}}^{\mathrm{T}}\mathbf{X} - \mathbf{B}) = \mathbf{0}$, hence $\mathbf{X}$ is such that the column space of $(\mathbf{P}_{\mathrm{I}}^{\mathrm{T}}\mathbf{X} - \mathbf{B})$ is normal to the column space of $\mathbf{P}_{\mathrm{I}}^{\mathrm{T}}$ for the scalar product of $\mathbb{R}^{N_{\mathrm{n}}}$ given by $\mathbf{W}$. By defining $\hat{\mathbf{P}}_{\mathrm{I}} = \mathbf{P}_{\mathrm{I}}\mathbf{W}^{1/2}$ and $\hat{\mathbf{B}} = \mathbf{W}^{1/2}\mathbf{B}$ the following equation is obtained:

$$\hat{\mathbf{P}}_{\mathrm{I}}\hat{\mathbf{P}}_{\mathrm{I}}{}^{\mathrm{T}}\mathbf{X} = \hat{\mathbf{P}}_{\mathrm{I}}\hat{\mathbf{B}}\,, \quad (2.71)$$

so $\mathbf{X}$ is such that $(\hat{\mathbf{P}}_{\mathrm{I}}{}^{\mathrm{T}}\mathbf{X} - \hat{\mathbf{B}})$ is normal to $\hat{\mathbf{P}}_{\mathrm{I}}{}^{\mathrm{T}}$ for the Euclidean scalar product of $\mathbb{R}^{N_{\mathrm{n}}}$. Let $\hat{\mathbf{P}}_{\mathrm{I}}{}^{\mathrm{T}} = \mathbf{Q}\mathbf{R}$, where the orthogonal $N_{\mathrm{n}} \times N_{\mathrm{n}}$ matrix $\mathbf{Q}$ and the upper triangular

$N_\mathrm{n} \times N_\mathrm{p}$ matrix $\mathbf{R}$ correspond to the QR decomposition of $\hat{\mathbf{P}}_\mathrm{I}{}^\mathrm{T}$. Then, it is easy to show that $\mathbf{X}$ is the solution to the following system:

$$\bar{\mathbf{R}}\mathbf{X} = \bar{\mathbf{Q}}^\mathrm{T}\hat{\mathbf{B}}\,, \tag{2.72}$$

where $\bar{\mathbf{R}}$ is the square upper triangular matrix corresponding to the first N_p rows of $\mathbf{R}$ and $\bar{\mathbf{Q}}$ is the rectangular matrix corresponding to the first N_p columns of $\mathbf{Q}$. Hence, the solution of Eq. (2.72) can be promptly obtained once the QR factorization of $\hat{\mathbf{P}}_\mathrm{I}{}^\mathrm{T}$ is computed. In addition, since $\mathbf{M}_\mathrm{I} = \mathbf{P}_\mathrm{I}\mathbf{W}\mathbf{P}_\mathrm{I}^\mathrm{T} = \bar{\mathbf{R}}^\mathrm{T}\bar{\mathbf{R}}$, then the condition number of $\bar{\mathbf{R}}$ is the square root of that of the moment matrix $\mathbf{M}_\mathrm{I}$. Then, the solution of the linear system Eq. (2.72) avoids dealing with the usually highly ill-conditioned system Eq. (2.70). However, the QR approach is more expensive since the QR decomposition involves a number of operations of the order of $N_\mathrm{n} \times N_\mathrm{p}^2$ instead of a number of operations of the order N_p^3 that would require, e.g., the Cholesky decomposition for solving Eq. (2.70).

The QR approach can be used to obtain $\bar{\mathbf{A}}(\tilde{\boldsymbol{X}})$ from Eq. (2.67) of the LRE scheme. In the case of the MLS, it can be used to obtain $\mathbf{A}(\tilde{\boldsymbol{X}})$ and then the MLS matrix $\mathbf{N}(\tilde{\boldsymbol{X}})$ of Eq. (2.57). If $\mathbf{p}$ is defined by the Taylor basis involving all the polynomial functions up to certain order, the QR algorithm can be used to solve Eq. (2.60) as well. To show that, let $\mathbf{P}_\mathrm{I}$, $\mathbf{W}$, $\mathbf{A}$, $\mathbf{P}_{\mathrm{I},x}$, $\mathbf{W}_x$ and $\mathbf{A}_x$ be short notations respectively for $\mathbf{P}_\mathrm{I}(\tilde{\boldsymbol{X}})$, $\mathbf{W}(\tilde{\boldsymbol{X}})$, $\mathbf{A}(\tilde{\boldsymbol{X}})$, $\partial\mathbf{P}_\mathrm{I}/\partial X(\tilde{\boldsymbol{X}})$, $\partial\mathbf{W}/\partial X(\tilde{\boldsymbol{X}})$ and $\partial\mathbf{A}/\partial X(\tilde{\boldsymbol{X}})$. Then Eq. (2.60) can be written as

$$\mathbf{P}_\mathrm{I}\mathbf{W}\mathbf{P}_\mathrm{I}^\mathrm{T}\mathbf{A}_x = \mathbf{P}_{\mathrm{I},x}\mathbf{W}(\mathbf{I} - \mathbf{P}_\mathrm{I}^\mathrm{T}\mathbf{A}) + \mathbf{P}_\mathrm{I}\mathbf{W}_x(\mathbf{I} - \mathbf{P}_\mathrm{I}^\mathrm{T}\mathbf{A}) - \mathbf{P}_\mathrm{I}\mathbf{W}\mathbf{P}_{\mathrm{I},x}^\mathrm{T}\mathbf{A}\,. \tag{2.73}$$

Note that $\mathbf{A}$ is the solution $\mathbf{X}$ of Eq. (2.70) for $\mathbf{B} = \mathbf{I}$, so that $\mathbf{P}_\mathrm{I}\mathbf{W}(\mathbf{P}_\mathrm{I}^\mathrm{T}\mathbf{A} - \mathbf{I}) = \mathbf{0}$. This means that $\mathbf{P}_\mathrm{I}^\mathrm{T}\mathbf{A} - \mathbf{I}$ is normal to $\mathbf{P}_\mathrm{I}^\mathrm{T}$ for the scalar product given by $\mathbf{W}$. Since $\mathbf{P}_{\mathrm{I},x}$ is generated by the derivatives of the Taylor basis functions, then the column space of $\mathbf{P}_{\mathrm{I},x}$ is a subspace of the column space of $\mathbf{P}_\mathrm{I}$, hence $\mathbf{P}_{\mathrm{I},x}^\mathrm{T}$ is normal to $\mathbf{P}_\mathrm{I}^\mathrm{T}\mathbf{A} - \mathbf{I}$, and then $\mathbf{P}_{\mathrm{I},x}\mathbf{W}(\mathbf{P}_\mathrm{I}^\mathrm{T}\mathbf{A} - \mathbf{I}) = \mathbf{0}$. The previous equation can then be written as:

$$\mathbf{P}_\mathrm{I}\mathbf{W}\mathbf{P}_\mathrm{I}^\mathrm{T}\mathbf{A}_x = \mathbf{P}_\mathrm{I}\mathbf{W}\left[\mathbf{W}^{-1}\mathbf{W}_x(\mathbf{I} - \mathbf{P}_\mathrm{I}^\mathrm{T}\mathbf{A}) - \mathbf{P}_{\mathrm{I},x}^\mathrm{T}\mathbf{A}\right]\,, \tag{2.74}$$

which is of the form Eq. (2.70) for $\mathbf{B} = \mathbf{W}^{-1}\mathbf{W}_x(\mathbf{I} - \mathbf{P}_\mathrm{I}^\mathrm{T}\mathbf{A}) - \mathbf{P}_{\mathrm{I},x}^\mathrm{T}\mathbf{A}$. Note that $\mathbf{B}$ can be easily obtained since $\mathbf{W}$ is diagonal. Therefore, the previous system can accurately be solved for $\mathbf{A}_x$ using the QR approach [13].

2.4 Solution algorithm

In Sections 2.4.1 and 2.4.2, the equations for the interior and the boundary faces cells, respectively, are presented. Then in Section 2.4.3 the global systems of equations are

illustrated, and in Section 2.4.4, a summarized algorithm to obtain the stiffness matrix of the system is presented.

2.4.1 Equations for interior volumes

Equations for small deformation

Replacing Eqs. (C.8), (C.9), and (C.10) into Eq. (2.45) it is possible to obtain the equations for an interior cell v as:

$$\sum_{f=1}^{f=N_\mathrm{f}} \sum_{g=1}^{g=N_\mathrm{g}} \alpha_g \sum_{n=1}^{n=N_\mathrm{n}} \left(\lambda\, \mathbf{n}_{0,f}\, \mathbf{c}_{\mathbf{x},n}^\mathrm{T} + \mu\, \mathbf{c}_{\mathbf{x},n}^\mathrm{T}\, \mathbf{n}_{0,f}\, \mathbf{I} + \mu\, \mathbf{c}_{\mathbf{x},n}\, \mathbf{n}_{0,f}^\mathrm{T} \right) \mathbf{u}_n + \sum_{b=1}^{b=N_\mathrm{b}} \beta_b\, \mathbf{b}_0\left(\boldsymbol{X}_{v,b}\right) - \sum_{m=1}^{m=N_\mathrm{m}} \gamma_m\, \rho_0(\boldsymbol{X}_{v,m}) \sum_{n=1}^{n=N_\mathrm{n}} c_n\, \mathbf{I}\, \ddot{\mathbf{u}}_n = \mathbf{0}\,. \quad (2.75)$$

where $\mathbf{c}_{\mathbf{x},n}^\mathrm{T}(\boldsymbol{X}_{f,g}) = (c_{X,n}(\boldsymbol{X}_{f,g}),\, c_{Y,n}(\boldsymbol{X}_{f,g}),\, c_{Z,n}(\boldsymbol{X}_{f,g}))$ and $c_n(\boldsymbol{X}_{v,m})$ are interpolation coefficients, $\mathbf{n}_{0,f}^\mathrm{T} = (N_{x,f},\, N_{y,f},\, N_{z,f})$ is the material outward pointing normal of face Σ_f and $\mathbf{u}_n^\mathrm{T} = (u_{x,n},\, u_{y,n},\, u_{z,n})$ is the unknown displacement of node n. Eq. (2.75) can be rearranged as

$$\sum_{f=1}^{f=N_\mathrm{f}} \sum_{g=1}^{g=N_\mathrm{g}} \alpha_g \sum_{n=1}^{n=N_\mathrm{n}} \mathbf{L}_n^\mathrm{SD}(\boldsymbol{X}_{f,g})\, \mathbf{u}_n + \sum_{b=1}^{b=N_\mathrm{b}} \beta_b\, \mathbf{b}_0\left(\boldsymbol{X}_{v,b}\right) - \sum_{m=1}^{m=N_\mathrm{m}} \gamma_m\, \rho_0(\boldsymbol{X}_{v,m}) \sum_{n=1}^{n=N_\mathrm{n}} c_n\, \mathbf{I}\, \ddot{\mathbf{u}}_n = \mathbf{0}\,. \quad (2.76)$$

where

$$\mathbf{L}_n^\mathrm{SD} = \lambda \left[\mathbf{n}_{0,f}\, \mathbf{c}_{\mathbf{x},n}^\mathrm{T}\right] + \mu \left[\mathbf{c}_{\mathbf{x},n}^\mathrm{T}\, \mathbf{n}_{0,f}\, \mathbf{I}\right] + \mu \left[\mathbf{c}_{\mathbf{x},n}\, \mathbf{n}_{0,f}^\mathrm{T}\right], \quad (2.77)$$

and the superscript SD is because it is associated with *small deformations*. The expression associated with $\ddot{\mathbf{u}}_n$ is discussed with an example in Chapter 3.

Equations for large deformation

For an interior volume v, it is possible to obtain the discretized versions of Eqs. (2.40) and (2.41):

$$\mathbf{r}_{\mathrm{d},v,k} = \sum_{f=1}^{f=N_\mathrm{f}} \left[\sum_{g=1}^{g=N_\mathrm{g}} \alpha_g \, \mathbf{P}(\mathbf{u}_k(\boldsymbol{X}_{f,g})) \right] \mathbf{n}_{0,f} + \sum_{b=1}^{b=N_\mathrm{b}} \beta_b \, \mathbf{b}_0 \left(\boldsymbol{X}_{v,b} \right) - \sum_{m=1}^{m=N_\mathrm{m}} \gamma_m \, \rho_0(\boldsymbol{X}_{v,m}) \sum_{n=1}^{n=N_\mathrm{n}} c_n \, \mathbf{I} \, \ddot{\mathbf{u}}_{n,k} \,, \quad (2.78)$$

and

$$\mathbf{r}_{\mathrm{d},v,k+1} = \mathbf{r}_{\mathrm{d},v,k} + \sum_{f=1}^{f=N_\mathrm{f}} \sum_{g=1}^{g=N_\mathrm{g}} \alpha_g \sum_{n=1}^{n=N_\mathrm{n}} \left(\mathbf{c}_{\mathbf{x},n}^\mathrm{T} \, \mathbf{f}_{\mathbf{S},f,k} \, \mathbf{I} + \mathbf{C}_\mathbf{x} \, c_{X,n} \, \mathbf{u}_n + \mathbf{C}_\mathbf{y} \, c_{Y,n} \, \mathbf{u}_n + \mathbf{C}_\mathbf{z} \, c_{Z,n} \right) \delta \mathbf{u}_n - \sum_{m=1}^{m=N_\mathrm{m}} \gamma_m \, \rho_0(\boldsymbol{X}_{v,m}) \sum_{n=1}^{n=N_\mathrm{n}} c_n \, \mathbf{I} \, \delta \ddot{\mathbf{u}}_n = \mathbf{0} \,, \quad (2.79)$$

where $\mathbf{f}_{\mathbf{S},f,k}$, $\mathbf{C}_\mathbf{x}$, $\mathbf{C}_\mathbf{y}$ and $\mathbf{C}_\mathbf{z}$ are defined in Eq. (C.11), (C.19), (C.20) and (C.21), respectively, and depends on $\boldsymbol{X}_{f,g}$, $\mathbf{n}_{0,f}$ and the displacement field $\mathbf{u}(\boldsymbol{X}_{f,g})$ at iteration k. For what follows, it is convenient to define:

$$\mathbf{L}_n^\mathrm{LD}(\boldsymbol{X}_{f,g}) = \mathbf{c}_{\mathbf{x},n}^\mathrm{T} \, \mathbf{f}_{\mathbf{S},f,k} \, \mathbf{I} + \mathbf{C}_\mathbf{x} \, c_{X,n} \, \mathbf{u}_n + \mathbf{C}_\mathbf{y} \, c_{Y,n} \, \mathbf{u}_n + \mathbf{C}_\mathbf{z} \, c_{Z,n} \,, \quad (2.80)$$

where the superscript LD is because it is associated with *large deformations*

2.4.2 Equations for boundary faces

In boundary faces, one of the cells of the stencil is the face itself. In what follows, Σ_f is the boundary face. In this section $\mathbf{L}_n$ represents either $\mathbf{L}_n^\mathrm{SD}$ or $\mathbf{L}_n^\mathrm{LD}$, and $\mathbf{u}_n$ represents either $\mathbf{u}_n$ or $\delta\mathbf{u}_n$.

Neumann condition The equation for a boundary face where a Neumann condition is applied is

$$\sum_{g=1}^{g=N_\mathrm{g}} \alpha_g \sum_{n=1}^{n=N_\mathrm{n}} \mathbf{L}_n \, \mathbf{u}_n = \int_{\Sigma_f} \mathbf{f}_\mathrm{a} \, \mathrm{d}A \,, \quad (2.81)$$

where Σ_f is the face and $\mathbf{f}_\mathrm{a}$ is the applied tension. In this thesis, the integral of the last expression is obtained using numerical quadrature.

Dirichlet condition The Dirichlet condition is included as

$$\sum_{n=1}^{n=N_{\mathrm{n}}} c_n \, \mathbf{I} \, \mathbf{u}_n = \bar{\mathbf{u}} \text{ at } \boldsymbol{X}_f \,, \tag{2.82}$$

where $\bar{\mathbf{u}}$ is the known displacement.

Symmetry condition This is a condition where the normal component of the displacement is zero and the shear component of the traction vector is zero.

The traction condition is

$$\left(\mathbf{I} - \mathbf{n}_{0,f}\mathbf{n}_{0,f}^{\mathrm{T}}\right) \sum_{g=1}^{g=N_{\mathrm{g}}} \alpha_g \sum_{n=1}^{n=N_{\mathrm{n}}} \mathbf{L}_n \, \mathbf{u}_n = \mathbf{0} \,, \tag{2.83}$$

and the displacement condition is

$$\mathbf{n}_{0,f}\mathbf{n}_{0,f}^{\mathrm{T}} \sum_{n=1}^{n=N_n} c_n \, \mathbf{I} \, \mathbf{u}_n = \mathbf{0} \,. \tag{2.84}$$

As described by Cardiff et al. [14], Eq. (2.83) and Eq. (2.84) are linearly independent and must be added in order to enforce the original mixed boundary condition.

2.4.3 Global system

This section defines the global system of equations that is obtained by allocating the equations presented in the previous section.

Small deformations hypothesis

In order to use the temporal discretization presented in Modak et al. [2], it is convenient to define the global stiffness matrix $\mathbf{K}$, the global mass matrix $\mathbf{M}$ and the generalized external vector $\mathbf{f}_{\mathrm{ext}}$. With those definitions Eq. (2.76) can be rewritten as:

$$\mathbf{M} \, \ddot{\mathbf{u}}_{\mathrm{N}} + \mathbf{K} \, \mathbf{u}_{\mathrm{N}} = \mathbf{f}_{\mathrm{ext}} \,, \tag{2.85}$$

where

$$\mathbf{K}\,\mathbf{u}_{\mathrm{N}} = \mathcal{A}\Big|_{v=1}^{v=N_{\mathrm{v}}} \left\{ \sum_{f=1}^{f=N_{\mathrm{f}}} \sum_{g=1}^{g=N_{\mathrm{g}}} \alpha_g \sum_{n=1}^{n=N_{\mathrm{n}}} \mathbf{L}_n^{\mathrm{SD}}(\boldsymbol{X}_{f,g})\,\mathbf{u}_n \right\}, \tag{2.86}$$

$$\mathbf{M}\,\ddot{\mathbf{u}}_{\mathrm{N}} = \mathcal{A}\Big|_{v=1}^{v=N_{\mathrm{v}}} \left\{ -\sum_{m=1}^{m=N_{\mathrm{m}}} \gamma_m\,\rho_0(\boldsymbol{X}_{v,m}) \sum_{n=1}^{n=N_{\mathrm{n}}} c_n\,\mathbf{I}\,\ddot{\mathbf{u}}_n \right\}, \tag{2.87}$$

$$\mathbf{f}_{\mathrm{ext}} = \mathbf{f}_{\mathrm{bc}} + \mathbf{f}_{\mathbf{b}_0} \quad \text{with} \quad \mathbf{f}_{\mathbf{b}_0} = \mathcal{A}\Big|_{v=1}^{v=N_{\mathrm{v}}} \left\{ -\sum_{b=1}^{b=N_{\mathrm{b}}} \beta_b\,\mathbf{b}_0\,(\boldsymbol{X}_{v,b}) \right\}, \tag{2.88}$$

where $\mathbf{f}_{\mathrm{bc}}$ is the external vector that includes the boundary conditions defined in Section 2.4.2, $\mathcal{A}\,\{\}$ is a function that allocate the $3 \times 3\,N_{\mathrm{v}}$ equations obtained from the Eq. (2.76), $\mathbf{K}$ and $\mathbf{M}$ are matrices of size $3\,N_{\mathrm{v}} \times 3\,N_{\mathrm{v}}$, $\mathbf{f}_{\mathrm{ext}}$ is a vector of size $3\,N_{\mathrm{v}} \times 1$, $\mathbf{u}_{\mathrm{N}}$ is a vector of size $3\,N_{\mathrm{v}} \times 1$ which contains the displacements of the nodes and $\ddot{\mathbf{u}}_{\mathrm{N}}$ is a vector of size $3\,N_{\mathrm{v}} \times 1$ which contains the nodes accelerations. Assuming Cartesian coordinates, the displacement field is:

$$\mathbf{u}(\boldsymbol{X}) = u_x(\boldsymbol{X})\,\mathbf{e}_x + u_y(\boldsymbol{X})\,\mathbf{e}_y + u_z(\boldsymbol{X})\,\mathbf{e}_z \quad \forall\ \boldsymbol{X} \in \mathcal{P}_0\,, \tag{2.89}$$

therefore

$$\mathbf{u}_{\mathrm{N}} = \left(u_{x,1}\ u_{y,1}\ u_{z,1} \ldots u_{x,N_{\mathrm{v}}}\ u_{y,N_{\mathrm{v}}}\ u_{z,N_{\mathrm{v}}}\right)^{\mathrm{T}}. \tag{2.90}$$

The mass matrix $\mathbf{M}$ can be obtained using the method presented in Eq. (2.87) or by the more usual mass matrix form called *lumped mass matrix*:

$$\mathbf{M}\,\ddot{\mathbf{u}}_{\mathrm{N}} = \mathcal{A}\Big|_{v=1}^{v=N_{\mathrm{v}}} \left\{ -\rho_0\,V_v\,\ddot{\mathbf{u}}(\boldsymbol{X}_v) \right\}, \tag{2.91}$$

where V_v is the volume of the finite volume v and it is assumed that $\ddot{\mathbf{u}}$ and ρ_0 are uniform in v. As it was explained above, the matrix $\mathbf{M}$ has size $3\,N_{\mathrm{v}} \times 3\,N_{\mathrm{v}}$. It is simple to see that obtaining the matrix defined in Eq. (2.91) requires less computational effort. Besides, since it is a diagonal matrix, its use would allow using simpler strategies to solve linear systems.

Large deformations

In the case of large deformations, the following is obtained by rewriting Eq. (2.78):

$$\mathbf{r}_{\mathrm{d},k} = \mathbf{f}_{\mathbf{P}} - \mathbf{f}_{\mathbf{b}_0} + \mathbf{M}\,\ddot{\mathbf{u}}_{\mathrm{N},k}\,, \tag{2.92}$$

being

$$\mathbf{f_P} = \mathcal{A}\Big|_{v=1}^{v=N_v} \left\{ \sum_{f=1}^{f=N_f} \left[\sum_{g=1}^{g=N_g} \alpha_g \, \mathbf{P}(\mathbf{u}_k(\boldsymbol{X}_{f,g})) \right] \mathbf{n}_{0,f} \right\} , \tag{2.93}$$

where $\mathbf{P}$ depends on the material constitutive relationship and the displacement at iteration k. Eq. (2.79) it is rewriting as:

$$\mathbf{r}_{\mathrm{d},k+1} = \mathbf{r}_{\mathrm{d},k} + \mathbf{K}_{\mathrm{tan}} \, \delta\mathbf{u}_{\mathrm{N},k} + \mathbf{M} \, \delta\ddot{\mathbf{u}}_{\mathrm{N},k} = \mathbf{0} \, , \tag{2.94}$$

being

$$\mathbf{K}_{\mathrm{tan}} \, \delta\mathbf{u}_{\mathrm{N},k} = \mathcal{A}\Big|_{v=1}^{v=N_v} \left\{ \sum_{f=1}^{f=N_f} \sum_{g=1}^{g=N_g} \alpha_g \sum_{n=1}^{n=N_n} \mathbf{L}_n^{\mathrm{LD}}(\boldsymbol{X}_{f,g}) \, \delta\mathbf{u}_n \right\} . \tag{2.95}$$

Substituting Eq. (2.92) into Eq. (2.94) it is obtained that:

$$\mathbf{K}_{\mathrm{tan}} \, \delta\mathbf{u}_{\mathrm{N},k} + \mathbf{M} \, \delta\ddot{\mathbf{u}}_{\mathrm{N},k} = \mathbf{f}_{\mathrm{ext}} - \mathbf{f}_{\mathrm{int}} \, , \tag{2.96}$$

being

$$\mathbf{f}_{\mathrm{ext}} = \mathbf{f}_{\mathrm{bc}} + \mathbf{f}_{\mathbf{b}_0} \quad \text{and} \quad \mathbf{f}_{\mathrm{int}} = \mathbf{f_P} + \mathbf{M} \, \ddot{\mathbf{u}}_{\mathrm{N},k} \, . \tag{2.97}$$

2.4.4 Algorithm to obtain stiffness matrix K

In what follows, it is illustrated how to obtain the stiffness matrix $\mathbf{K}$ for small deformations, for mass $\mathbf{M}$ and tangential matrix $\mathbf{K}_{\mathrm{tan}}$ is analogous.

input: E, ν, *mesh*, N_{n}, k, $\mathbf{p}$ and N_{g}.
Obtain the total number of faces N_{f}, interior cells N_{ic} and boundary cells N_{bc} from the *mesh*.
for $f = 1 \rightarrow N_{\mathrm{f}}$ **do**

- Compute the N_{g} Gaussian points $\boldsymbol{X}_{f,g}$ for the face Σ_f.
- Obtain, for each Gaussian point, the stencil $\mathrm{s_{eq}}$ or $\mathrm{s_{df}}$ using the N_{n}-nearest nodes as illustrated in Section 2.3.3.
- Compute the interpolation coefficients at each Gaussian point using the previous stencil:

$$\begin{aligned}
\mathbf{c}_X^{\mathrm{T}}(\boldsymbol{X}_{f,g}) &= \Big(c_{X,1}(\boldsymbol{X}_{f,g}), \cdots, c_{X,N_{\mathrm{n}}}(\boldsymbol{X}_{f,g}) \Big) \, , \\
\mathbf{c}_Y^{\mathrm{T}}(\boldsymbol{X}_{f,g}) &= \Big(c_{Y,1}(\boldsymbol{X}_{f,g}), \cdots, c_{Y,N_{\mathrm{n}}}(\boldsymbol{X}_{f,g}) \Big) \, , \\
\mathbf{c}_Z^{\mathrm{T}}(\boldsymbol{X}_{f,g}) &= \Big(c_{Z,1}(\boldsymbol{X}_{f,g}), \cdots, c_{Z,N_{\mathrm{n}}}(\boldsymbol{X}_{f,g}) \Big) \, ,
\end{aligned}$$

defined in Eq. (2.49), using either MLS by Eq. (2.60) (first row of $\partial\mathbf{A}/\partial X$, $\partial\mathbf{A}/\partial Y$ and $\partial\mathbf{A}/\partial Z$, respectively) or LRE by Eq. (2.67) (second, third and fourth row of $\bar{\mathbf{A}}$, respectively).

- Obtain:

$$\mathbf{c}^{\mathrm{T}}_{\mathbf{x},n}(\boldsymbol{X}_{f,g}) = \Big(c_{X,n}(\boldsymbol{X}_{f,g}),\, c_{Y,n}(\boldsymbol{X}_{f,g}),\, c_{Z,n}(\boldsymbol{X}_{f,g})\Big)\,,$$

defined in Eq. (2.75) for each node of the stencil.

end

for $ic = 1 \rightarrow N_{\mathrm{ic}}$ **do**

- Obtain the entries of the system matrix $\mathbf{K}$ from Eqs. (2.76) and (2.77).

end

for $bc = 1 \rightarrow N_{\mathrm{bc}}$ **do**

- Obtain the entries of the system matrix $\mathbf{K}$ and the independent vector $\mathbf{F}$, from Eqs. (2.81) to (2.84).

end

2.5 Temporal discretization

In this thesis, the formulation presented in [2] is used for the temporal discretization, as it is summarized in what follows. In [2] a formulation called *generalized algorithm* is developed which includes nine parameters and is capable of representing other standard and more common formulations for solid dynamics such as Newmark [15], HHT-α [16], Generalized-α and SS32 [17,18] among others.

The first three parameters ($\beta_{\mathrm{M},0}$, $\beta_{\mathrm{M},1}$ and $\beta_{\mathrm{M},2}$) appear after applying a truncation of Taylor series expansions of $\mathbf{u}$, $\dot{\mathbf{u}}$, and $\ddot{\mathbf{u}}$. The next three parameters ($\theta_{\mathrm{M},1}$, $\theta_{\mathrm{M},2}$ and $\theta_{\mathrm{M},3}$) emerge after applying a weighted-average form of the equilibrium equation as in [17]:

$$\mathbf{M}\,\ddot{\mathbf{u}} + \mathbf{C}_{\mathrm{d}}\,\dot{\mathbf{u}} + \mathbf{K}\,\mathbf{u} = \mathbf{f}\,, \tag{2.98}$$

where $\mathbf{C}_{\mathrm{d}}$ is the damping term that is neglected in this thesis. The final three parameters ($\gamma_{\mathrm{M},0}$, $\gamma_{\mathrm{M},1}$ and $\gamma_{\mathrm{M},2}$) show after applying another truncation to the Taylor series of the weighted-average form.

The basic equations for the generalized method developed in [2] are:

$$\mathbf{M}\,\ddot{\mathbf{u}}^{n+\theta} + \mathbf{C}_{\mathrm{d}}\,\dot{\mathbf{u}}^{n+\theta} + \mathbf{K}\,\mathbf{u}^{n+\theta} = \mathbf{f}^{n+\theta}\,, \tag{2.99}$$

where n represent previous instant t_n and being $t_{n+1} = t_n + \Delta t$ the actual instant:

$$\mathbf{u}^{n+\theta} = \mathbf{u}^n + \theta_{\mathrm{M},1}\,\Delta t\,\dot{\mathbf{u}}^n + \frac{\theta_{\mathrm{M},2}\,\Delta t^2}{2}\,\ddot{\mathbf{u}}^n + \frac{\theta_{\mathrm{M},3}\,\gamma_{\mathrm{M},0}\,\Delta t^2}{6}\,\Delta\,\ddot{\mathbf{u}}\,, \tag{2.100}$$

$$\dot{\mathbf{u}}^{n+\theta} = \dot{\mathbf{u}}^n + \theta_{\mathrm{M},1}\,\Delta t\,\ddot{\mathbf{u}}^n + \frac{\theta_{\mathrm{M},2}\,\gamma_{\mathrm{M},1}\,\Delta t}{2}\,\Delta\,\ddot{\mathbf{u}}\,, \tag{2.101}$$

$$\ddot{\mathbf{u}}^{n+\theta} = \ddot{\mathbf{u}}^n + \theta_{\mathrm{M},1}\,\gamma_{\mathrm{M},2}\,\Delta\,\ddot{\mathbf{u}}\,, \tag{2.102}$$

where $\Delta\,\ddot{\mathbf{u}} = \ddot{\mathbf{u}}^{n+1} - \ddot{\mathbf{u}}^{n}$ is the acceleration increment obtained after solving Eq. (2.99) and then the updated magnitudes at time t_{n+1} are:

$$\mathbf{u}^{n+1} = \mathbf{u}^{n} + \Delta t\,\dot{\mathbf{u}}^{n} + \frac{\Delta t^2}{2}\,\ddot{\mathbf{u}}^{n} + \frac{\beta_{\mathrm{M},0}\,\Delta t^2}{6}\,\Delta\,\ddot{\mathbf{u}}\,, \tag{2.103}$$

$$\dot{\mathbf{u}}^{n+1} = \dot{\mathbf{u}}^{n} + \Delta t\,\ddot{\mathbf{u}}^{n} + \frac{\beta_{\mathrm{M},1}\,\Delta t}{2}\,\Delta\,\ddot{\mathbf{u}}\,, \tag{2.104}$$

$$\ddot{\mathbf{u}}^{n+1} = \ddot{\mathbf{u}}^{n} + \beta_{\mathrm{M},2}\,\Delta\,\ddot{\mathbf{u}}\,. \tag{2.105}$$

Note that in the general case $\mathbf{K} = \mathbf{K}_{\mathrm{tan}}$.

In addition to the generalized algorithm presented above, it is decided to use Euler's method, where:

$$\ddot{\mathbf{u}}^{n+1} = \frac{\dot{\mathbf{u}}^{n+1} - \dot{\mathbf{u}}^{n}}{\Delta t} = \frac{\mathbf{u}^{n+1} - \mathbf{u}^{n}}{\Delta t^2} - \frac{\dot{\mathbf{u}}^{n}}{\Delta t}\,, \tag{2.106}$$

which cannot be written with the method presented in [2].

Nonlinear contact/impact force In the case of a nonlinearity, for example, if there is an external force due to contact/impact, it is necessary to solve Eq. (2.99) with an iterative process. In that case, as it is mentioned in Section 2.1.4, a Newton-Raphson method is needed [13, 19]. Firstly $\Delta\,\tilde{\ddot{\mathbf{u}}}_s$ is estimated[4] and Eqs. (2.100), (2.101) and (2.102) are evaluated. Then it is obtained that:

$$\mathbf{r}(\Delta\,\tilde{\ddot{\mathbf{u}}}_s) = \mathbf{f}^{n+\theta} - \left[\mathbf{M}\,\ddot{\mathbf{u}}_s^{n+\theta} + \mathbf{C}_{\mathrm{d}}\,\mathbf{u}_s^{n+\theta} + \mathbf{K}\,\mathbf{u}_s^{n+\theta}\right]\,, \tag{2.107}$$

where s indicate the s-th iteration of Newton-Raphson. Then the increment of acceleration is

$$\delta\Delta\,\ddot{\mathbf{u}} = \mathbf{K}_{\mathrm{d}}^{-1}\,\mathbf{r}(\Delta\,\tilde{\ddot{\mathbf{u}}}_s)\,, \tag{2.108}$$

where

$$\mathbf{K}_{\mathrm{d}} = \gamma_{\mathrm{M},2}\,\theta_{\mathrm{M},1}\,\mathbf{M} + \frac{\gamma_{\mathrm{M},1}\,\theta_{\mathrm{M},2}\,\Delta t}{2}\,\mathbf{C}_{\mathrm{d}} + \frac{\gamma_{\mathrm{M},0}\,\theta_{\mathrm{M},3}\,\Delta t^2}{6}\,\mathbf{K} + \mathbf{K}_{\mathrm{c}}, \tag{2.109}$$

being $\mathbf{K}_{\mathrm{c}} = -\partial\,\mathbf{F}_{\mathrm{c}}/\partial\,\delta\Delta\,\ddot{\mathbf{u}}$ a matrix related to the contact force. In order to solve the dynamic contact problem, it is not necessary to include that matrix. However, it helps to reduce the computational effort (reducing the total number of iterations N_{s} to solve the Newton-Raphson method).

[4] Generaly $\Delta\,\tilde{\ddot{\mathbf{u}}}_0 = \Delta\,\ddot{\mathbf{u}}^{n}$ where $\Delta\,\ddot{\mathbf{u}}^{n}$ is the acceleration increment obtained in the previous time t_n, if $n = 0$ then $\Delta\,\tilde{\ddot{\mathbf{u}}}_0 = \mathbf{0}$.

Finally, the expressions are updated as follows:

$$\Delta\,\tilde{\tilde{\mathbf{u}}} = \Delta\,\tilde{\tilde{\mathbf{u}}} + \delta\Delta\,\ddot{\mathbf{u}}\,, \tag{2.110}$$

$$\mathbf{u}^{n+\theta} = \mathbf{u}^{n} + \theta_{\mathrm{M},1}\,\Delta t\,\dot{\mathbf{u}}^{n} + \frac{\theta_{\mathrm{M},2}\,\Delta t^2}{2}\,\ddot{\mathbf{u}}^{n} + \frac{\gamma_{\mathrm{M},0}\,\theta_{\mathrm{M},3}\,\Delta t^2}{6}\,\Delta\,\tilde{\tilde{\mathbf{u}}}\,, \tag{2.111}$$

$$\dot{\mathbf{u}}^{n+\theta} = \dot{\mathbf{u}}^{n} + \theta_{\mathrm{M},1}\,\Delta t\,\ddot{\mathbf{u}}^{n} + \frac{\gamma_{\mathrm{M},1}\,\theta_{\mathrm{M},2}\,\Delta t^2}{2}\,\Delta\,\tilde{\tilde{\mathbf{u}}}\,, \tag{2.112}$$

$$\ddot{\mathbf{u}}^{n+\theta} = \ddot{\mathbf{u}}^{n} + \gamma_{\mathrm{M},2}\,\theta_{\mathrm{M},1}\,\Delta\,\tilde{\tilde{\mathbf{u}}}\,, \tag{2.113}$$

and Eq. (2.109) is solved again until convergence is reached, e.g., when $\|\mathbf{r}(\Delta\,\tilde{\tilde{\mathbf{u}}}_s)\|$ or/and $\|\delta\Delta\,\ddot{\mathbf{u}}\|$ are sufficiently small.

References

[1] Pablo Castrillo, Alfredo Canelas, Eugenio Schillaci, Joaquim Rigola, and Asensio Oliva. High-order finite volume method for linear elasticity on unstructured meshes. *Computers & Structures*, 268:106829, 2022.

[2] Sukomal Modak and Elisa D. Sotelino. The generalized method for structural dynamics applications. *Advances in Engineering Software*, 33(7-10):565–575, jul 2002.

[3] Morton E. Gurtin, Eliot. Fried, and Lallit. Anand. *The Mechanics and Thermodynamics of Continua*. Cambridge University Press, 2010.

[4] Yuri Bazilevs, Kenji Takizawa, and Tayfun E. Tezduyar. *Computational Fluid-Structure Interaction: Methods and Applications*. John Wiley and Sons, dec 2012.

[5] J. C. Simo and T. J. R. Hughes. *Computational Inelasticity*, volume 7 of *Interdisciplinary Applied Mathematics*. Springer-Verlag, New York, 1998.

[6] O. C. Zienkiewicz and R. L. Taylor. *Finite Element Method: Volume 2 - Solid Machanics*. Butterworth-Heinemann, 5 edition, sep 2000.

[7] David C. Kellermann, Mario M. Attard, and Daniel J. O'Shea. Fourth-order tensor algebraic operations and matrix representation in continuum mechanics. *Archive of Applied Mechanics*, 91(12):4631–4668, dec 2021.

[8] Wing-Kam Liu, Shaofan Li, and Ted Belytschko. Moving least-square reproducing kernel methods (I) Methodology and convergence. *Computer Methods in Applied Mechanics and Engineering*, 143(1-2):113–154, apr 1997.

[9] Shaofan Li and Wing Kam Liu. Moving least-square reproducing kernel method Part II: Fourier analysis. *Computer Methods in Applied Mechanics and Engineering*, 139(1-4):159–193, dec 1996.

[10] Sofiane Khelladi, Xesús Nogueira, Farid Bakir, and Ignasi Colominas. Toward a higher order unsteady finite volume solver based on reproducing kernel methods. *Computer Methods in Applied Mechanics and Engineering*, 200(29-32):2348–2362, jul 2011.

[11] Luis Ramírez, Xesús Nogueira, Sofiane Khelladi, Jean-Camille Chassaing, and Ignasi Colominas. A new higher-order finite volume method based on Moving Least Squares for the resolution of the incompressible Navier-Stokes equations on unstructured grids. *Computer Methods in Applied Mechanics and Engineering*, 278:883–901, aug 2014.

[12] Luis Cueto-Felgueroso, Ignasi Colominas, Xesús Nogueira, Fermín Navarrina, and Manuel Casteleiro. Finite volume solvers and Moving Least-Squares approximations for the compressible Navier-Stokes equations on unstructured grids. *Computer Methods in Applied Mechanics and Engineering*, 196(45-48):4712–4736, sep 2007.

[13] Alfio Quarteroni, Riccardo Sacco, and Fausto Saleri. *Numerical Mathematics*, volume 37 of *Texts in Applied Mathematics*. Springer New York, New York, NY, 2007.

[14] P. Cardiff, Ž. Tuković, H. Jasak, and A. Ivanković. A block-coupled Finite Volume methodology for linear elasticity and unstructured meshes. *Computers & Structures*, 175:100–122, oct 2016.

[15] Nathan M. Newmark. A Method of Computation for Structural Dynamics. *Journal of the Engineering Mechanics Division*, 85(3):67–94, jul 1959.

[16] Hans M. Hilber, Thomas J.R. Hughes, and Robert L. Taylor. Improved numerical dissipation for time integration algorithms in structural dynamics. *Earthquake Engineering & Structural Dynamics*, 5(3):283–292, jul 1977.

[17] O. C. Zienkiewicz, W. L. Wood, N. W. Hine, and R. L. Taylor. A unified set of single step algorithms. Part 1: General formulation and applications. *International Journal for Numerical Methods in Engineering*, 20(8):1529–1552, aug 1984.

[18] W. L. Wood. A unified set of single step algorithms. Part 2: Theory. *International Journal for Numerical Methods in Engineering*, 20(12):2303–2309, dec 1984.

[19] Ted Belytschko, Wing Kam Liu, Brian Moran, and Khalil Elkhodary. *Nonlinear Finite Elements for Continua and Structures, 2nd Edition | Wiley*. Wiley, 2014.

3

Verification and validation of the proposed method

In this chapter, two-dimensional (2D) and three-dimensional (3D) problems with analytical solutions are solved and analyzed in Section 3.1.1 and 3.2.1, respectively. Those examples are used to obtain an adequate set of parameters for the high-order method in each case (2D and 3D).

The Lamé parameters mentioned in Section 2.1.3 are expressed in terms of the more common Young modulus E and the Poisson ratio ν: $\mu = 0.5\,E/(1+\nu)$ and $\lambda = E\nu/\left[(1+\nu)(1-2\nu)\right]$ which are the expressions for three-dimensional problems and plane strain. In the case of plane stress the parameters are $\bar{\mu} = \mu$ and $\bar{\lambda} = \lambda\left[1-\lambda/\left(2\mu+\lambda\right)\right]$.

In what follows, p_i represents the interpolation order, e.g., interpolation p_1 is linear, which implies that the vector of basis functions is:

$$\begin{aligned} \text{for 3D} \quad &\rightarrow \quad \hat{\mathbf{p}}^{\mathrm{T}} = \left(1, (X-\tilde{X})/h, (Y-\tilde{Y})/h, (Z-\tilde{Z})/h\right), \\ \text{for 2D} \quad &\rightarrow \quad \hat{\mathbf{p}}^{\mathrm{T}} = \left(1, (X-\tilde{X})/h, (Y-\tilde{Y})/h\right), \end{aligned} \tag{3.1}$$

as defined in Eq. (2.69). The software FreeFEM [1] with linear (p_1) or quadratic (p_2) interpolation (FF p_1 and FF p_2 in figures and tables) and the 2nd-order method developed by Cardiff et al. [2] are used to compare with the proposed method. In order to obtain the value at a certain point, using the 2nd-order method, the LRE and MLS interpolation methods are used. It is important to note that the size of the system of equations is the same for the same mesh using any of the FVM interpolations (2nd-order by Cardiff or the high-order presented in this work). However, for the high-order method when using p_{i-1}, the system is sparser than using p_i (assuming that the number of points used for the stencil with p_i is greater than the number of

points for p_{i-1}). Structured meshes with squares and hexahedrons are created using GMSH [3], while those of triangles or tetrahedrons are created with FreeFEM [1].

3.1 Two-dimensional examples

In the case of two-dimensional examples, the hypothesis of small deformations and static problems are considered for all the examples.

3.1.1 Two-dimensional analytical example

A known displacement field $\mathbf{u}$ is imposed on the boundary of the domain, and the corresponding body force $\mathbf{b}_0$ is imposed in the interior. The domain is a square of size $L = 1$, i.e. $\Omega = \{(X, Y) : X,\, Y \in [0, 1]\}$. The displacement field imposed on the boundary is $\mathbf{u} = u_x\, \mathbf{e}_x + u_y\, \mathbf{e}_y + u_z\, \mathbf{e}_z$, where

$$\begin{aligned} u_x(X, Y) &= e^{X^2} \sin(Y)\,, \\ u_y(X, Y) &= \ln(3 + Y)\, \cos(X) + \sin(Y), \\ u_z(X, Y) &= 0\,. \end{aligned} \tag{3.2}$$

This example assumes plane strain, and the material properties are $E = 1$ and $\nu = 0.3$. The body force $\mathbf{b}_0 = b_{0,x}\, \mathbf{e}_x + b_{0,y}\, \mathbf{e}_y + b_{0,z}\, \mathbf{e}_z$ is obtained from Eq. (2.37) using $\partial \dot{\mathbf{u}}/\partial t = \mathbf{0}$ and integrated with numerical quadrature as in Eq. (2.76) using 48 and 64 Gaussian points for each finite triangle and square, respectively, see Appendix B.

In this example, an exhaustive study varying all the parameters of the proposed formulation is carried out:

1. Type of stencil, as defined in Section 2.3.3: $\mathrm{s_{eq}}$ or $\mathrm{s_{df}}$.
2. Type of interpolation method: LRE or MLS.
3. Interpolation order: p_1, p_2, p_3 and p_4.
4. Shape parameter k, defined in Section 2.3.4: $k = \{1, 2, 3, 4, 5, 6, 7, 8, 9, 10\}$.
5. Number of Gauss points N_g to obtain the coefficients of the system, defined in Section 2.4: $N_\mathrm{g} = \{1, 2, 4, 7\}$.
6. Number of points for the stencil of the interpolation method $N_\mathrm{n} = N_{\mathrm{n,min}} + N_+$, where N_+ takes values of the set $\{0, 1, 2, 3, \ldots 60\}$.

Additionally, all the parameters mentioned above are tested in 18 meshes, including different types of meshes, such as: (1) structured quadrilateral mesh (SQM), see the left image of Figure 3.1; (2) structured triangular mesh (STM), see the center image of Figure 3.1; and (3) unstructured triangular mesh (UTM), see the right image of Figure 3.1. Table E.1 shows more information about the meshes used in this example; for the parametric analysis, the first 18 meshes were considered. With this, it is possible to compare the accuracy of the method related to the disposition of the cells.

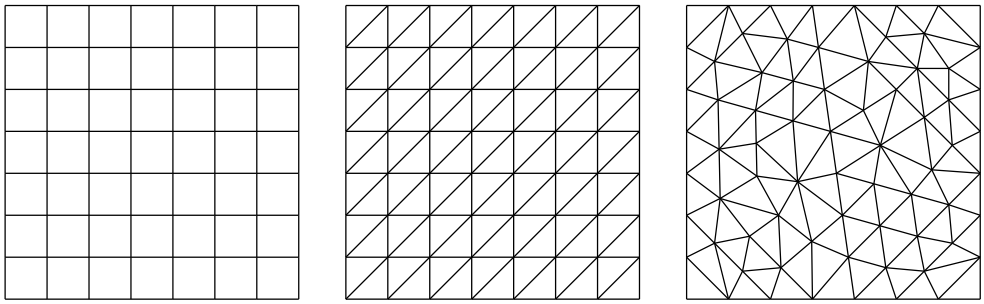

Figure 3.1: Structured quadrilateral mesh (SQM, left), structured triangular mesh (STM, center), and unstructured triangular mesh (UTM, right).

Consequently, more than 2.1 million cases[1] were studied hindering the possibility of showing the complete analysis here. In Appendix D additional results can be found.

The relative errors in the displacement field $\mathrm{RE}_{\mathbf{u}}$ and in the stress field RE_{σ} are computed in order to understand the influence of the parameters of the method on the results

$$\mathrm{RE}_{\mathbf{u}} = \sqrt{\frac{\int_{\Omega} \|\mathbf{u} - \mathbf{u}_{\mathrm{num}}\|^2 \mathrm{d}V}{\int_{\Omega} \|\mathbf{u}\|^2 \mathrm{d}V}}\, 100\% \text{ and } \mathrm{RE}_{\sigma} = \sqrt{\frac{\int_{\Omega} \|\sigma - \sigma_{\mathrm{num}}\|^2 \mathrm{d}V}{\int_{\Omega} \|\sigma\|^2 \mathrm{d}V}}\, 100\%\,, \quad (3.3)$$

and the absolute errors in the displacement field $\mathrm{AE}_{\mathbf{u}}$ and in the stress field AE_{σ} are considered in order to test the convergence order of the method

$$\mathrm{AE}_{\mathbf{u}} = \sqrt{\frac{\int_{\Omega} \|\mathbf{u} - \mathbf{u}_{\mathrm{num}}\|^2 \mathrm{d}V}{\int_{\Omega} \mathrm{d}V}} \text{ and } \mathrm{AE}_{\sigma} = \sqrt{\frac{\int_{\Omega} \|\sigma - \sigma_{\mathrm{num}}\|^2 \mathrm{d}V}{\int_{\Omega} \mathrm{d}V}}\,. \quad (3.4)$$

The integrals defined in Eqs. (3.3) and (3.4) are calculated using 7 and 9 Gaussian points for each finite triangle and square, respectively, see Appendix B.

[1] #Cases $= 2 \times 2 \times 4 \times 10 \times 4 \times 61 \times 18 \times 3 = 2108160$.

Number of Gauss points

In order to define the adequate number of Gauss points, the relative error for the displacement and stress fields using p_3 and stencil s_{eq} are presented in Figure 3.2 and 3.3, respectively. For those figures, unstructured mesh #18 is used; see Appendix E. Likewise, different shape parameters k and number of stencil points N_n have been used.

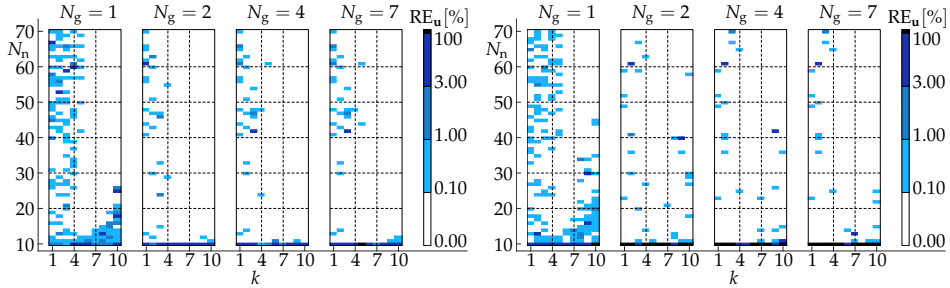

Figure 3.2: $RE_{\mathbf{u}}$ using UTM#18 with LRE (left) and MLS (right).

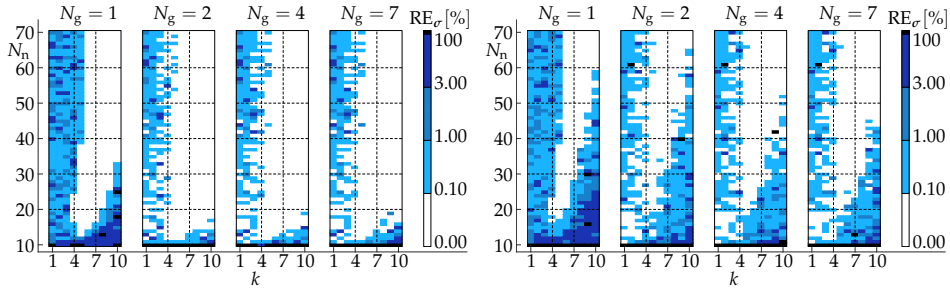

Figure 3.3: RE_σ using UTM#18 with LRE (left) and MLS (right).

It can be seen that with $N_g = 2$, the displacement field is approximated accurately using either LRE or MLS. However, for the stress field using MLS, it is seen that when increasing the Gauss points, the accuracy improves. For this reason and to present results similar to [4], it is decided to use $N_g = 7$ in what follows.

Selection of the stencil

In order to compare the results of using different types of stencils, $\mathrm{RE}_{\mathbf{u},\mathrm{s}}$ and $\mathrm{RE}_{\sigma,\mathrm{s}}$ are defined:

$$\mathrm{RE}_{\mathbf{u},\mathrm{s}} = \sqrt{\frac{\int_\Omega \|\mathbf{u}_{\mathrm{num},\mathrm{s}_{\mathrm{df}}} - \mathbf{u}_{\mathrm{num},\mathrm{s}_{\mathrm{eq}}}\|^2 \mathrm{d}V}{\int_\Omega \|\mathbf{u}_{\mathrm{num},\mathrm{s}_{\mathrm{eq}}}\|^2 \mathrm{d}V}}\, 100\%$$

$$\text{and } \mathrm{RE}_{\sigma,\mathrm{s}} = \sqrt{\frac{\int_\Omega \|\boldsymbol{\sigma}_{\mathrm{num},\mathrm{s}_{\mathrm{df}}} - \boldsymbol{\sigma}_{\mathrm{num},\mathrm{s}_{\mathrm{eq}}}\|^2 \mathrm{d}V}{\int_\Omega \|\boldsymbol{\sigma}_{\mathrm{num},\mathrm{s}_{\mathrm{eq}}}\|^2 \mathrm{d}V}}\, 100\%\,, \quad (3.5)$$

where $\mathbf{u}_{\mathrm{num},\mathrm{s}_i}$ and $\boldsymbol{\sigma}_{\mathrm{num},\mathrm{s}_i}$ are the numerical solution using the type of stencil s_i, see Section 2.3.3. The integrals defined in Eq. (3.5) are computed using 7 and 9 Gaussian points for each finite triangle and square, respectively; see Appendix B.

The $\mathrm{RE}_{\mathbf{u},\mathrm{s}}$ and $\mathrm{RE}_{\sigma,\mathrm{s}}$ using p_2 and p_3 for the mesh #18 for SQM, STM and UTM is shown in Figures 3.4, 3.5 and 3.6, respectively. As it was mentioned before, in all the cases, $N_\mathrm{g} = 7$. Beyond that, it is possible to conclude that if $N_\mathrm{g} = 1$, the error is always null since the stencils s_{eq} and s_{df} are equal because the Gauss point coincides with the centroid of the face. Likewise, it should be noted that there are differences for small values of N_n; due to problems of poor conditioning of the linear systems, as mentioned in Section 2.3.5.

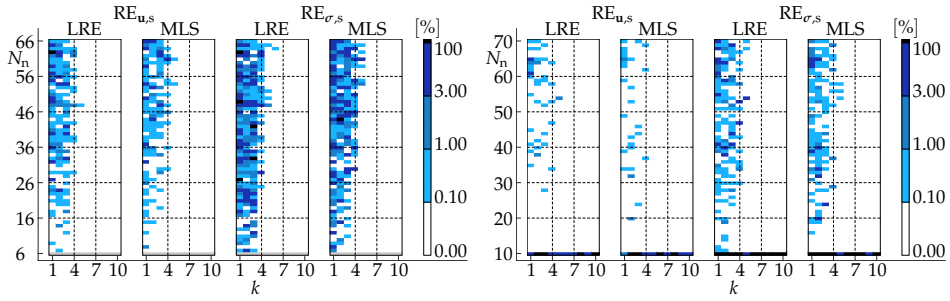

Figure 3.4: RE_s using SQM#18 with LRE and MLS for p_2 (left) and p_3 (right).

In all cases, there is a lower difference in using s_{eq} or s_{df} for p_3 than for p_2, as well as less difference when using LRE than MLS. The latter is more noticeable for the case of unstructured meshes, which makes the LRE a more efficient method since using s_{eq} is less expensive from a computational point of view, see Figure 3.6. It is also possible to see that the less structured the mesh, the greater the difference between using s_{eq} or s_{df}; however, in all cases, there is a region of the parameters for which the difference between s_{eq} and s_{df} is negligible. In these figures, when low values of

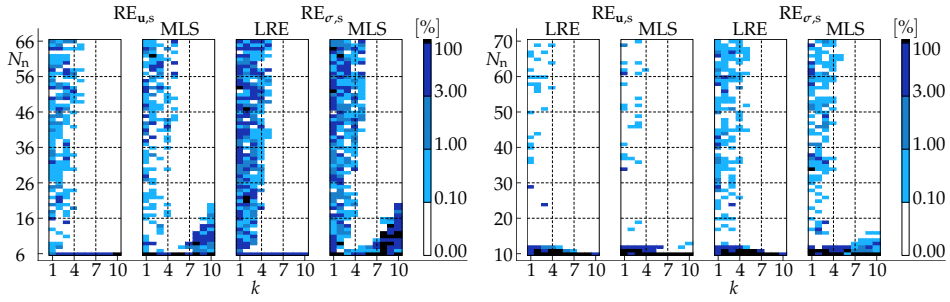

Figure 3.5: RE$_s$ using STM#18 with LRE and MLS for p_2 (left) and p_3 (right).

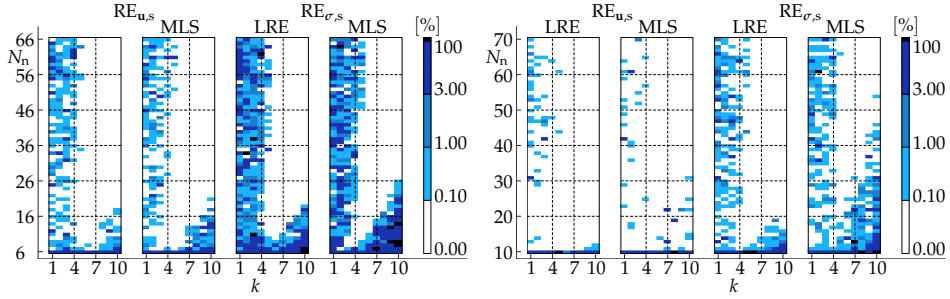

Figure 3.6: RE$_s$ using UTM#18 with LRE and MLS for p_2 (left) and p_3 (right).

N_n are used, the gray color indicates a NaN solution due to the bad conditioning of the moment matrices used to obtain the LRE or MLS interpolations.

It is interesting to see that for small values of k, there are differences in using s_{eq} or s_{df}, later it is shown that for those values of k, the solution is not accurate. From what was mentioned above and completing the analysis with what is presented in Appendix D, it can be concluded that in the case of two dimensions, it is the same to use s_{eq} as s_{df}.

Therefore, in what follows, results are presented only using s_{eq} due to the lower computational cost; however, they have also been analyzed using s_{df}, obtaining the same conclusions.

Set of parameters and comparison between LRE and MLS

In what follows, the results obtained using mesh #18 are analyzed for different types of meshes; see Table E.1. Likewise, $N_g = 7$ is used for all cases, and the stencil type is s_{eq}.

Using SQM: Figures 3.7 and 3.8 show the value of the relative errors of the displacement and stress field using either LRE or MLS. The figures correspond to the RE for the different interpolations: p_1, p_2, p_3 and p_4; using in all the cases the mesh #18 and different values of the parameters N_n and k. These figures show the most accurate results for $5 \leq k \leq 10$. Likewise, it is observed how the relative error is greater for the stress field than for the displacement field, something that, as mentioned, was expected. Moreover, as was foreseeable, the RE is smaller with p_{i+1} than with p_i.

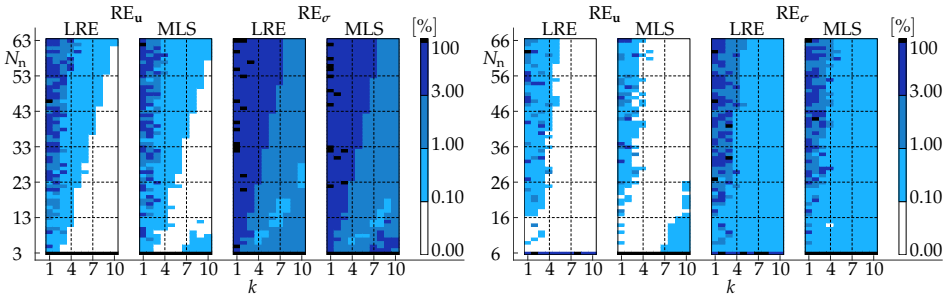

Figure 3.7: RE using SQM#18 with LRE and MLS for p_1 (left) and p_2 (right).

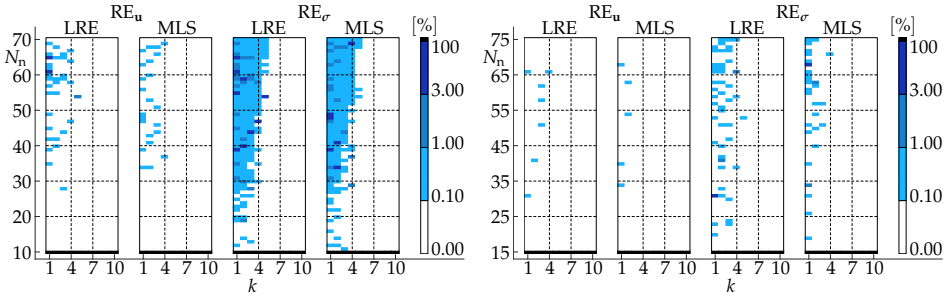

Figure 3.8: RE using SQM#18 with LRE and MLS for p_3 (left) and p_4 (right).

Using STM: As for SQM, Figures 3.9 and 3.10 show the relative error of the displacement and stress fields. It is possible to observe that the results obtained with STM have a lower RE than using SQM; however, it is important to highlight that the number of triangles using STM (648) doubles the number of squares using SQM (324), see Table E.1. As previously mentioned before, the gray color means that, due to the bad conditioning of the linear systems of the high-order method, the solution is NaN.

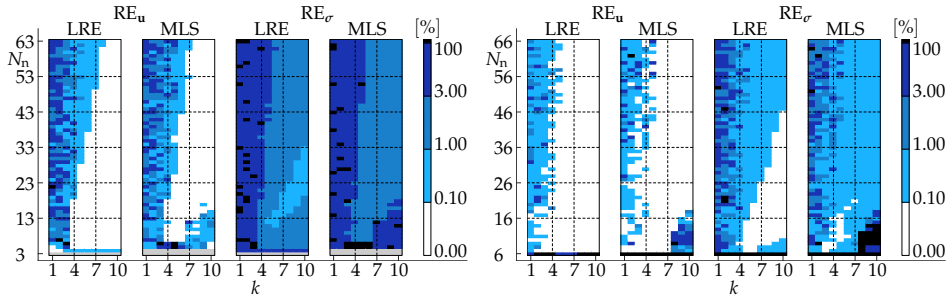

Figure 3.9: RE using STM#18 with LRE and MLS for p_1 (left) and p_2 (right).

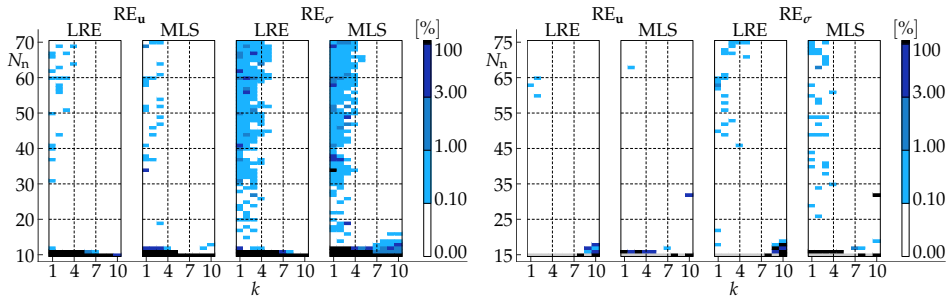

Figure 3.10: RE using STM#18 with LRE and MLS for p_3 (left) and p_4 (right).

Using UTM: As exposed for SQM and STM, Figures 3.11 and 3.12 show the relative errors in displacements and stresses when using UTM. Again, the figures reveal the RE for different interpolation orders varying the rest of parameters that define the formulation, reaching similar conclusions. However, in this case, the differences between using LRE or MLS are even more noticeable, obtaining better results with the first one, see the left image of Figure 3.12.

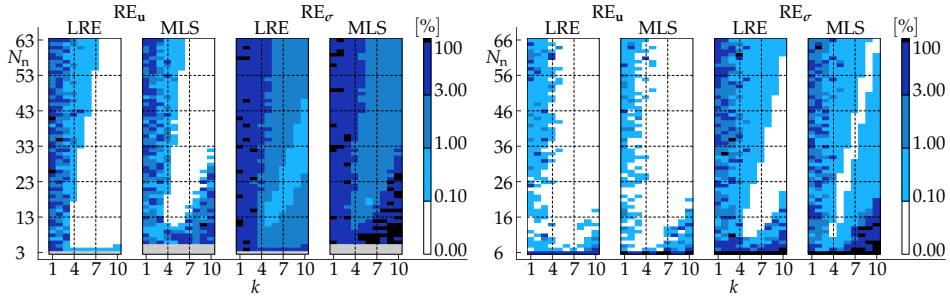

Figure 3.11: RE using UTM#18 with LRE and MLS for p_1 (left) and p_2 (right).

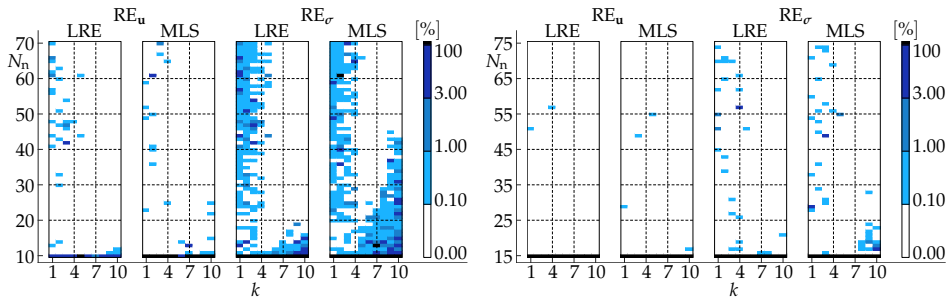

Figure 3.12: RE using UTM#18 with LRE and MLS for p_3 (left) and p_4 (right).

Order of convergence

Another indicator used to define the set of parameters is the order of convergence (OC). The theoretical order of convergence (TOC) of the displacement field is $i+1$ when the interpolation p_i is used, while for the stress field is i. As previously mentioned and illustrated in [4], stencil s_{eq}, $k = 6$ and $N_g = 7$ perform properly. To define the number of stencil points N_n, OC results are shown for different values and interpolations in Appendix D for SQM, STM, and UTM at Tables D.1, D.2 and D.3, respectively. It has been decided to use the same value of N_n for each type of mesh, which may vary depending on the interpolation method, see Table 3.1.

Table 3.1: Order of convergence for the displacement and stress fields using LRE or MLS. $N_g = 7$ and $k = 6$ are used.

Mesh	p_i	N_n		**Disp. field (u)**			**Stress field (σ)**		
		LRE	MLS	TOC	LRE	MLS	TOC	LRE	MLS
SQM	p_1	13	13	2	1.71	1.78	1	1.26	1.21
	p_2	16	16	3	1.86	1.58	2	1.84	1.67
	p_3	20	33	4	3.61	3.58	3	3.06	3.29
	p_4	25	25	5	3.29	3.70	4	2.93	3.00
STM	p_1	13	13	2	2.03	2.10	1	1.11	1.05
	p_2	16	16	3	2.04	2.11	2	1.97	1.88
	p_3	20	33	4	3.93	3.99	3	3.25	3.05
	p_4	25	25	5	3.81	4.14	4	3.93	4.02
UTM	p_1	13	13	2	2.08	1.64	1	1.21	0.84
	p_2	16	16	3	2.03	2.00	2	2.09	1.95
	p_3	20	33	4	4.02	3.94	3	3.19	3.27
	p_4	25	25	5	4.11	4.50	4	4.06	4.03

The values of N_n in Table 3.1 are chosen based on the UTM since this type of

mesh is the most useful and it was the one presented in [4], and the OC values were obtained using all the meshes of Table E.1. A better combination of parameters for SQM and STM are shown in Tables D.1 and D.2, respectively.

As explained in [4] and can be seen in Table 3.1, when using p_2 and p_4, the TOC for the displacement field is not usually obtained. However, for the stress field, the TOC is reached. Figures 3.13 and 3.14 show the orders of convergence for the displacement and stress fields using p_1, p_2, p_3 and p_4 by varying the parameters of the problem. In the case of p_2, it is observed that obtaining the TOC in the displacement field is possible with MLS but not with LRE. Anyway, the set of parameters needed to do it using MLS is not a straightforward definition. It is appreciated that, in general, when using the LRE, the convergence zone has more uniform colors, while for the MLS, this is not the case. A clear example is observed when using p_3; see the left image of Figure 3.14. On the other hand, the OC for the stress field using different parameters of the problem is achieved either using LRE or MLS. Furthermore, it can be appreciated that for the stresses, there is a great variety of parameters that satisfy the TOC when using LRE. It is worth highlighting from Figures 3.13 and 3.14 that obtaining the adequate parameters is more challenging when using MLS [4].

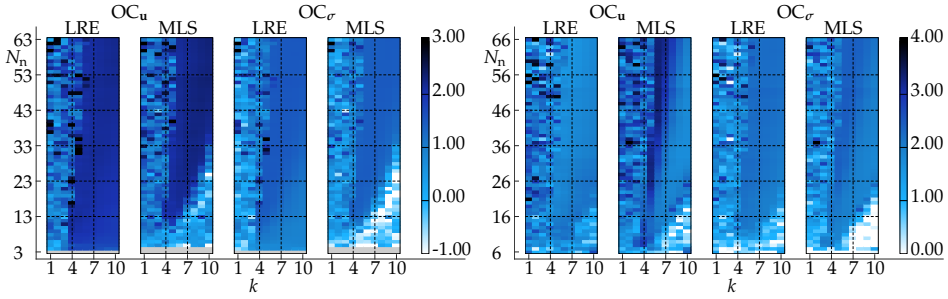

Figure 3.13: OC using UTM with LRE and MLS for p_1 (left) and p_2 (right).

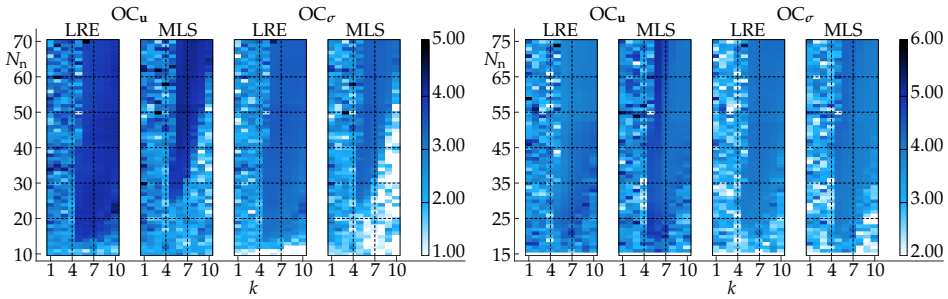

Figure 3.14: OC using UTM with LRE and MLS for p_3 (left) and p_4 (right).

Figures 3.15 and 3.16 show the convergence of the absolute error of the displace-

ment field and the stress field using LRE and MLS, respectively. For these graphs, the parameters of Table 3.1 and the unstructured meshes defined in Table E.1 are used. Meshes #1, #2, #3 and #4 are excluded from these graphs because the number of cells is less than the number of points needed for p_4. It can be concluded that with the LRE, the results are more precise, particularly for p_1, where, when using MLS, it is possible to find parameters that improve the convergence. In Table 3.1 it is observed that for the stress field, for which a precise determination is critical in evaluating the structural stability, the expected TOC is achieved in all the cases when LRE and p_3 are used. On the other hand, for the displacement field, the TOC is achieved using p_1 and p_3 but not using p_2 and p_4, but the error using p_{i+1} is smaller than using p_i, see Figures 3.15 and 3.16.

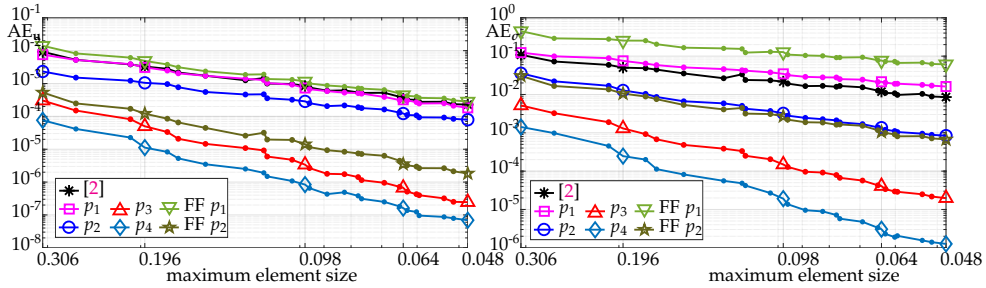

Figure 3.15: Convergence of $\mathrm{AE}_{\mathbf{u}}$ (left) and AE_{σ} (right) using LRE with the parameters of Table 3.1 for UTM.

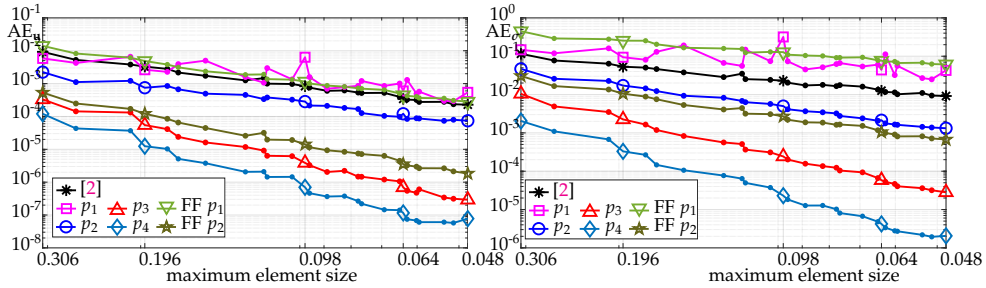

Figure 3.16: Convergence of $\mathrm{AE}_{\mathbf{u}}$ (left) and AE_{σ} (right) using MLS with the parameters of Table 3.1 for UTM.

Section D.1 shows the evolution of the displacement and stress field through the first 18 unstructured meshes when using LRE for different interpolations. In the following two-dimensional examples, only unstructured meshes are used with the parameters defined in Table 3.1, using $N_{\mathrm{g}} = 7$ and stencil s_{eq}.

3.1.2 Clamped beam with uniformly varying loading

In [4,5], it is possible to find examples of a cantilever beam where the shear locking effect appears, comparing in [4] the results with those obtained in [6] concluding that the method presented in this thesis is accurate and can deal with the shear locking effect.

This section shows a cantilever beam clamped at the left end and subject to a uniformly varying loading $\mathbf{f} = -p(L_x - X)/L_x\,\mathbf{e}_y$ at the top boundary as shown in Figure 3.17. In [7], it is possible to find an analytical approximation of the solution, where the stress σ_x is:

$$\sigma_x(X,Y) = \frac{p\,(L_x - X)\,Y}{30\,L_x\,I}\left[5\,(L_x - X)^2 - 10\,Y^2 + \frac{3}{2}\,L_y^2\right], \tag{3.6}$$

In this case, for the simulation, $L_x = 50$, $L_y = 2$, $p = 0.1$, the inertia $I = L_y^3/12$, $E = 30000$, $\nu = 0.3$ and plane stress is considered.

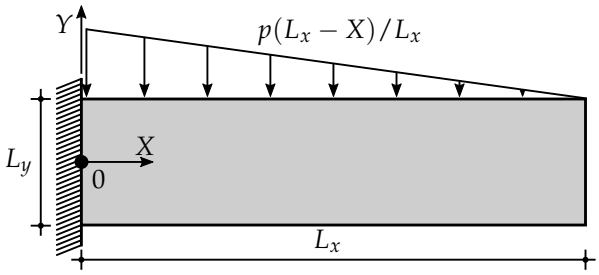

Figure 3.17: Geometry for the clamped beam with uniformly varying loading.

The approximated analytical solution of $\sigma_x(L_x/2,\, L_y/4)$ is compared with the presented formulation and other methods in Table 3.2, where #m indicates the number of the mesh for which information is available in Table E.2.

In Table 3.2, it is possible to observe that with low order interpolation (using p_1 or the method developed in [2]), it is not possible to obtain an accurate solution. Nevertheless, a better approximation of the solution is achieved with high-order interpolation (p_2, p_3, and p_4). It is worth noting that, generally, with LRE, the solution is even better than the one obtained with MLS. In the case of the 2nd-order method, [2], it is possible to see the differences between using MLS or LRE to interpolate the derivatives.

Table 3.2: Solution of $\sigma_x(L_x/2, L_y/4)$ using LRE and MLS where the analytical solution is $\sigma_x(L_x/2, L_y/4) = 3.91$.

#m	LRE					MLS					FreeFEM	
	[2]	p_1	p_2	p_3	p_4	[2]	p_1	p_2	p_3	p_4	p_1	p_2
1	2.03	4.89	3.90	3.91	3.91	2.39	2.34	3.70	3.91	3.91	2.08	3.98
2	3.58	5.58	3.83	3.91	3.91	3.36	58.02	3.78	3.91	3.91	4.89	3.94
3	3.62	3.74	3.89	3.91	3.91	3.67	4.33	3.85	3.91	3.91	3.40	3.91
4	3.72	2.85	3.89	3.91	3.91	3.66	3.05	3.90	3.91	3.91	4.38	3.91
5	3.73	4.31	3.91	3.91	3.91	3.74	3.57	3.90	3.91	3.91	3.73	3.92
6	3.73	4.20	3.91	3.91	3.91	3.77	3.89	3.90	3.91	3.91	3.80	3.92
7	3.95	3.88	3.91	3.91	3.91	3.96	3.98	3.91	3.91	3.91	3.85	3.91
8	3.60	3.72	3.91	3.91	3.91	3.66	4.39	3.91	3.91	3.91	4.21	3.91
9	3.73	3.96	3.91	3.91	3.91	3.76	3.77	3.91	3.91	3.91	3.35	3.91
10	3.81	4.23	3.91	3.91	3.91	3.83	3.29	3.91	3.91	3.91	4.24	3.91
11	3.81	3.91	3.91	3.91	3.91	3.80	3.75	3.91	3.91	3.91	4.00	3.91

3.1.3 Stressed infinite plane with an elliptical hole

In [4, 5] more examples of two-dimensional problems are presented, showing that the method can deal with problems including stress concentrations and complex geometries, where unstructured meshes are mandatory.

As in [5], this section presents an infinite plane containing a stress-free elliptical hole loaded with a uniform stress at infinity, as shown in the left image of Figure 3.18.

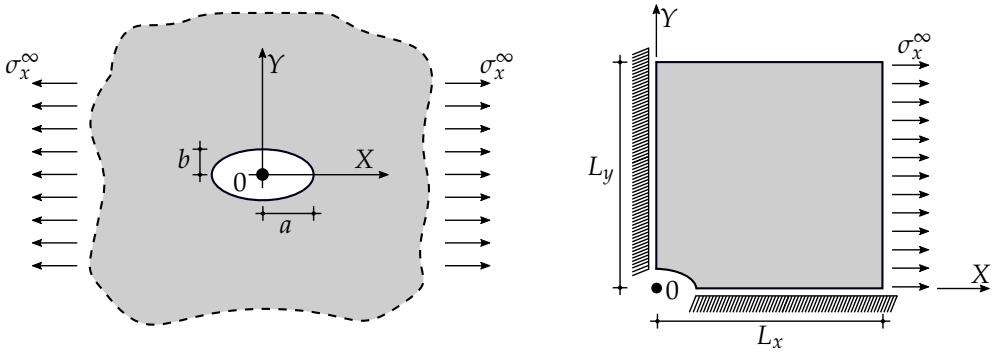

Figure 3.18: Geometry and model for the stressed infinite plane with an elliptical hole problem.

This problem is modeled as shown in the right image of Figure 3.18: left and bottom boundaries have symmetry conditions, while on the rest of the surfaces Neumann conditions are imposed. In this case, plane stress is considered, and $E = 1$, $\nu = 0.3$, $a = 1$, $L_x = L_y = 300$ and $\sigma_x^\infty = 1$ are used. Unlike in [5], in this thesis, the parameter b varies in order to show its impact on the stress concentration factor, and for that reason, L_x and L_y are ten times larger than those values in [5][2].

The analytical stress concentration factor is defined in [7]:

$$F_{\sigma_\infty} = \frac{\sigma_x(0,b)}{\sigma_x^\infty} = 1 + 2\,\frac{b}{a}\,, \tag{3.7}$$

where $\sigma_x(0,b) = \sigma_x^\infty(1 + 2b/a)$. In Figure 3.19, one of the meshes used to solve the problem is presented; it is possible to see that an unstructured mesh is needed for this example.

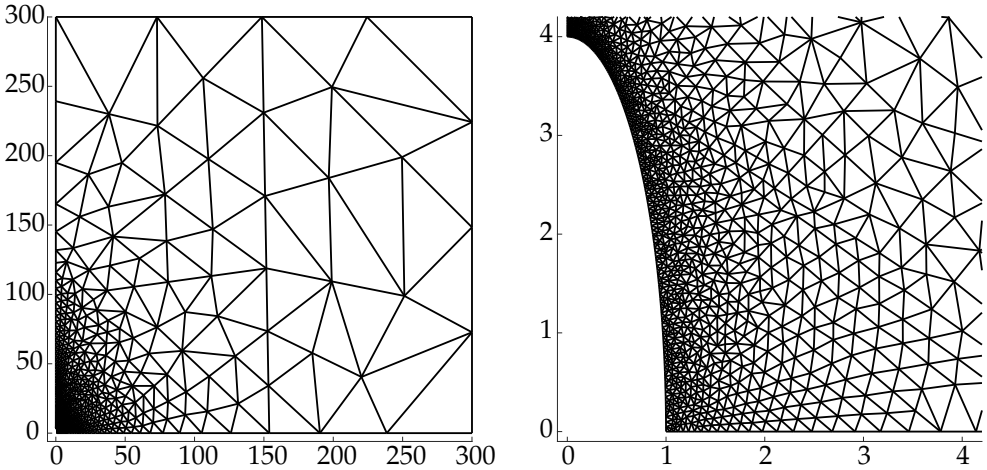

Figure 3.19: Mesh to solve the infinite plane with an elliptical hole problem with $b = 4$ (left) and zoom of the mesh near the elliptical hole (right).

In Table 3.3, the solution of F_{σ_∞} using LRE and MLS is presented and compared with the analytical expression defined in Eq. (3.7), concluding that both methods work properly. In Table E.3, more information about the meshes can be found.

[2]The analytical expression is obtained assuming an infinite plane, therefore $L_x = L_y \gg b$.

Table 3.3: Solution of F_{σ_∞} for different values of b.

F_{σ_∞}	LRE					MLS				
	[2]	p_1	p_2	p_3	p_4	[2]	p_1	p_2	p_3	p_4
1.5	1.50	1.49	1.50	1.50	1.50	1.50	1.49	1.50	1.50	1.50
2.0	2.01	1.98	2.00	2.00	2.00	2.01	2.02	2.00	2.00	2.00
2.5	2.52	2.46	2.50	2.51	2.50	2.52	2.53	2.50	2.50	2.50
3.0	3.04	2.94	3.00	3.00	3.00	3.05	2.99	3.00	3.00	3.00
3.5	3.48	3.40	3.50	3.50	3.50	3.49	3.44	3.50	3.51	3.50
4.0	3.95	3.88	4.00	4.01	4.01	3.98	3.89	4.00	4.01	4.01
4.5	4.45	4.35	4.49	4.50	4.49	4.47	4.09	4.49	4.50	4.50
5.0	4.92	4.80	4.98	4.98	4.98	4.96	4.79	4.98	5.00	4.99
5.5	5.41	5.27	5.48	5.54	5.54	5.42	5.25	5.47	5.52	5.54
6.0	5.92	5.72	5.97	6.02	6.05	5.94	5.66	5.94	6.01	6.04
6.5	6.41	6.16	6.46	6.51	6.51	6.37	6.04	6.45	6.50	6.51
7.0	6.92	6.67	6.98	7.03	7.10	6.89	6.42	6.95	7.02	7.09
7.5	7.39	7.11	7.47	7.52	7.56	7.41	7.01	7.44	7.52	7.56
8.0	7.74	7.57	7.96	8.00	7.99	7.84	7.57	7.92	8.00	7.99
8.5	8.31	8.02	8.43	8.45	8.34	8.37	7.93	8.41	8.44	8.39
9.0	8.72	8.48	8.92	8.98	8.93	8.81	8.30	8.92	8.97	8.93
9.5	9.28	8.92	9.44	9.52	9.50	9.31	8.85	9.41	9.51	9.50
10.0	9.56	9.33	9.90	9.90	9.80	9.74	9.26	9.88	9.90	9.82
10.5	10.09	9.77	10.41	10.45	10.41	10.23	9.68	10.38	10.46	10.44
11.0	10.81	10.31	11.05	11.18	11.22	10.92	10.31	10.97	11.14	11.20

3.2 Three-dimensional examples

For three-dimensional cases, it is decided to analyze only the LRE method since, as seen in the two-dimensional analysis, the MLS method does not work as well as the first one and has a higher computational cost [4]. However, in some of the examples, the results obtained with the MLS are shown using the same parameters as with the LRE in order to illustrate how the LRE continues to have better results in the case of three dimensions. Likewise, it is decided, not to use the interpolation p_4 due to its high computational effort, knowing, from Section 3.1, that results with p_2 and p_3 are accurate enough.

In this section, static and dynamic problems, as well as hyperelastic problems, are analyzed.

3.2.1 Three-dimensional analytical example

In this example, a known displacement field $\mathbf{u}$ is imposed on the boundary of the domain, and the corresponding body force $\mathbf{b}_0$ is imposed in the interior. The domain is a cube of size $L = 1$, i.e. $\Omega = \{(X, Y, Z) : X,\ Y,\ Z \in [0, 1]\}$. The displacement field imposed on the boundary is $\mathbf{u} = u_x\,\mathbf{e}_x + u_y\,\mathbf{e}_y + u_z\,\mathbf{e}_z$, where

$$\begin{aligned} u_x(X, Y) &= \ln(X + 3)\,Y\,(Z + 1) + e^Z\,, \\ u_y(X, Y) &= \sin(Y\,Z) + 3\,Y, \\ u_z(X, Y) &= e^{X\,Z}\,Y - 4\,\cos(Z)\,. \end{aligned} \tag{3.8}$$

The body force $\mathbf{b}_0 = b_{0,x}\,\mathbf{e}_x + b_{0,y}\,\mathbf{e}_y + b_{0,z}\,\mathbf{e}_z$ is obtained from Eq. (2.37) using $\partial\dot{\mathbf{u}}/\partial t = \mathbf{0}$ and integrated using numerical quadrature as in Eq. (2.76) with 56 and 64 Gaussian points for each finite tetrahedron and hexahedron, respectively, see Appendix B. In this example, the material properties are $E = 1$ and $\nu = 0.3$. Four different types of meshes are used to compare the accuracy of the method related to the disposition of the cells: (1) structured hexahedral mesh (SHM), see the top-left image of Figure 3.20; (2) structured tetrahedral mesh (STM), see the top-right image of Figure 3.20; (3) unstructured-plane tetrahedral mesh (UpTM), see the bottom-left image of Figure 3.20; and (4) unstructured tetrahedral mesh (UTM), see the bottom-right image of Figure 3.20. UpTM meshes are useful in cases where the need to use unstructured meshes is in a plane, e.g., a compressor reed valve. Table E.4 shows more information about the meshes used in this example. In this case, all meshes are used for the parametric analysis.

When analyzing the number of Gauss points needed to integrate over the surfaces, it is necessary to distinguish between hexahedrons and tetrahedrons. For the case of hexahedrons $N_{\text{g}} = \{1, 9, 25, 49\}$ and for the case of tetrahedrons $N_{\text{g}} = \{1, 7, 19, 37\}$. Consequently, more than one million cases were studied[3], so it is challenging to show the complete analysis and for that reason, some additional results can be found in the Appendix D.

As in the two-dimensional analytical example, see Section 3.1, the relative errors in the displacement field $\text{RE}_{\mathbf{u}}$ and in the stress field RE_{σ} are computed using Eq. (3.3), in order to observe the influence of the parameters of the method on the results, and the absolute errors in the displacement field $\text{AE}_{\mathbf{u}}$ and in the stress field AE_{σ}, using Eq. (3.4), are considered in order to test the convergence order of the method. The integrals defined in Eqs. (3.3) and (3.4) are computed using 56 and 64 Gaussian points for each finite tetrahedron and hexahedrons, respectively, see Appendix B.

[3] #Cases $= 2 \times 1 \times 3 \times 10 \times 4 \times 61 \times 18 \times 4 = 1054080$.

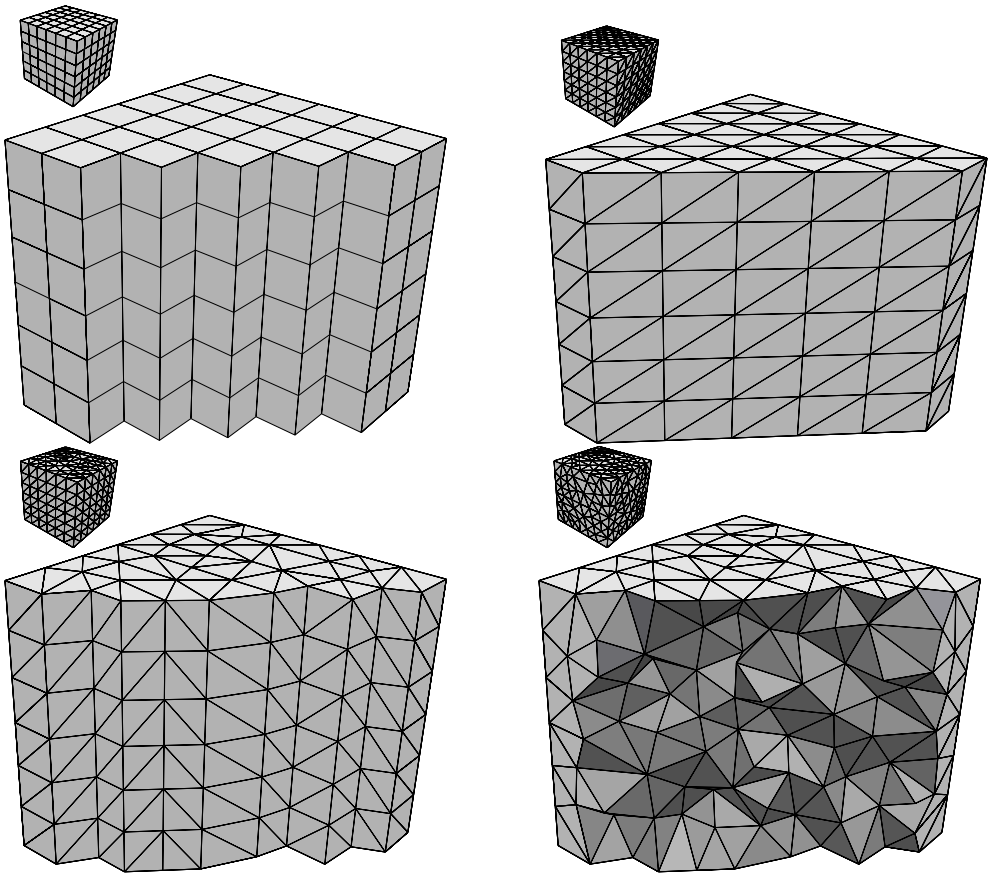

Figure 3.20: Structured hexahedral mesh (SHM, top-left), structured tetrahedral mesh (STM, top-right), unstructured-plane tetrahedral mesh (UpTM, bottom-left) and unstructured tetrahedral mesh (UTM, bottom-right).

Number of Gauss points

Figures 3.21 and 3.22 show the relative errors of the field of displacements and stresses for the mesh #7 with UpTM and UTM, respectively. It is possible to conclude that at least $N_g = 7$ is needed. In the analysis of this example, $N_g = 37$ is used for tetrahedrons and $N_g = 49$ for the SHM to reduce errors introduced by this approximation. However, in other examples, the number of Gaussian points may vary in order to reduce the computational effort.

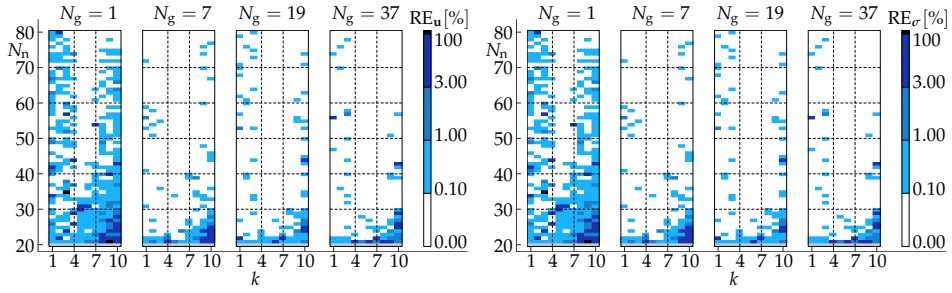

Figure 3.21: $RE_{\mathbf{u}}$ (left) and RE_{σ} (right) using UpTM#7, p_3 and s_{df}.

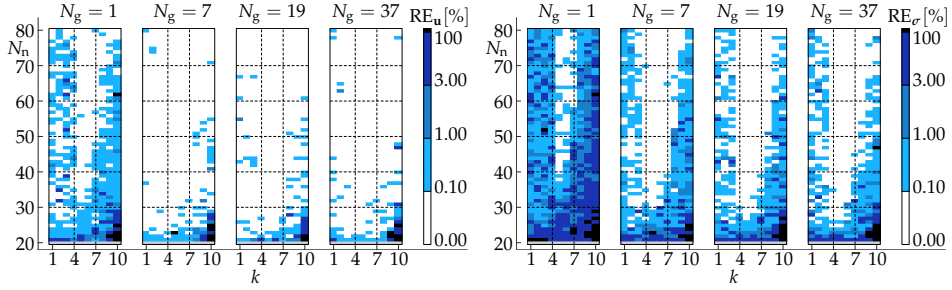

Figure 3.22: $RE_{\mathbf{u}}$ (left) and RE_{σ} (right) using UTM#7, p_3 and s_{df}.

Selection of the stencil

As in the two-dimensional case, see Section 3.1, the $RE_{\mathbf{u},s}$ and $RE_{\sigma,s}$, defined in Eq. (3.5), are obtained. The integrals defined in Eq. (3.5) are computed using 56 and 64 Gaussian points for each finite tetrahedron and hexahedron, respectively; see Appendix B. Figures 3.23, 3.24, 3.25 and 3.26 show the results of the RE_s using LRE and different parameters that define the problem for mesh #7, see Table E.4, of SQM, STM, UpTM and UTM, respectively.

It is possible to observe that the more unstructured the mesh, the worse the comparison between stencils. This indicates that for structured meshes, especially with hexahedrons, using s_{eq} or s_{df} is practically indifferent, but for unstructured meshes it is not clear. Likewise, it is notorious that when increasing the interpolation order, the error between the stencils is also higher. Surprisingly, using p_2 is even worse than using p_3. However, this fact can be related to what has already been seen in the case of two dimensions, where it was observed that using p_2 is not advisable because it is not possible to obtain the order of convergence suitable for the displacement field in most cases.

Due to the aforementioned, and to use the same type of stencil for each type of mesh, it is decided to use the stencil s_{df} in the analysis presented in this section.

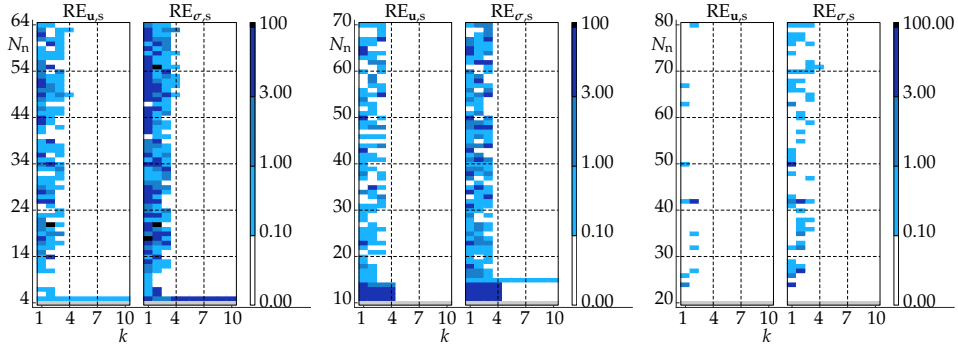

Figure 3.23: RE$_s$ using SHM#7 and LRE with p_1 (left), p_2 (center) and p_3 (right).

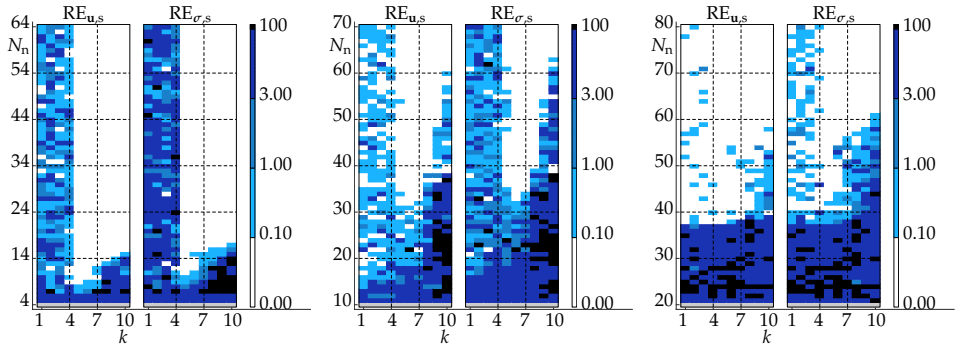

Figure 3.24: RE$_s$ using STM#7 and LRE with p_1 (left), p_2 (center) and p_3 (right).

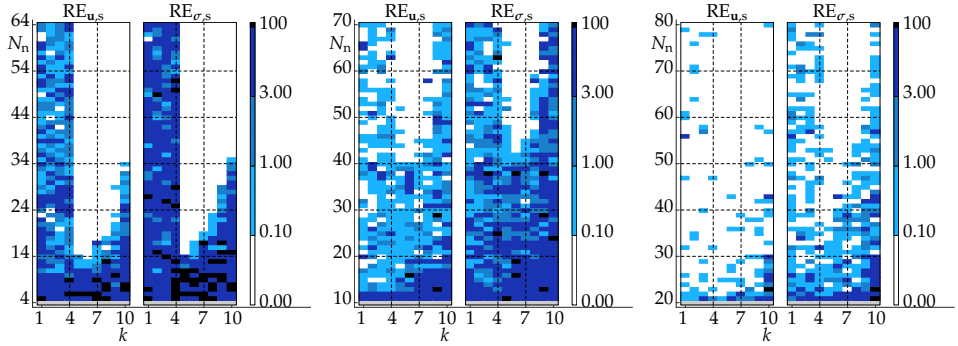

Figure 3.25: RE$_s$ using UpTM#7 and LRE with p_1 (left), p_2 (center) and p_3 (right).

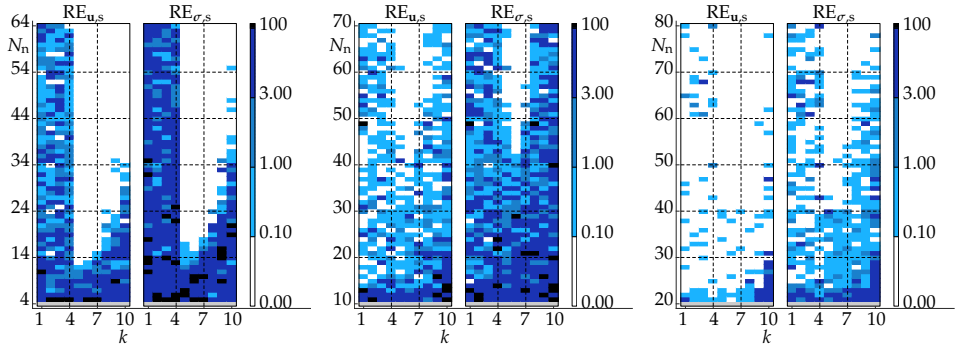

Figure 3.26: RE$_s$ using UTM#7 and LRE with p_1 (left), p_2 (center) and p_3 (right).

Set of parameters

In what follows, the results obtained using mesh #7 are analyzed for the different types of meshes; see Table E.1. Likewise, for all cases, $N_g = 37$ when using triangular meshes and $N_g = 49$ for hexahedral ones.

Using SHM: Figure 3.27 shows the value of the relative errors of the displacement and stress field using LRE, for different interpolations using the hexahedral mesh #7, see Table E.4.

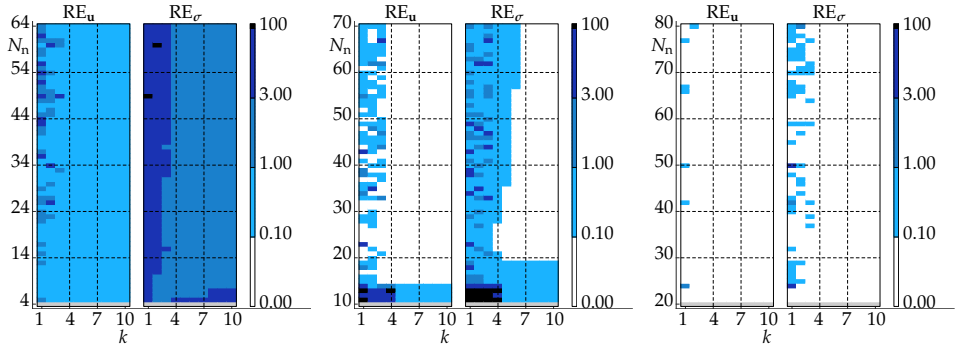

Figure 3.27: RE using SHM#7 and LRE with p_1 (left), p_2 (center) and p_3 (right).

The images correspond to the RE for the different interpolations: p_1, p_2, and p_3; for different values of the parameters N_n and k. These images show the most accurate results for $4 \leq k \leq 10$. Likewise, it is observed that the relative error is greater for the stress field than for the displacement field, which is consistent with

the two-dimensional case. Moreover, as it was expected, the RE is smaller with p_{i+1} than with p_i. As commented in previous examples, the gray color indicates a bad conditioned system and, therefore, a NaN solution.

Using STM: For structured triangular meshes, similar conclusions to those obtained with SHM are achieved; see Figure 3.28. Nevertheless, in this case, it is possible to appreciate that for p_3, it is necessary to impose a more significant number of stencil points N_n, and the gap for the shape form is reduced to $5 \leq k \leq 10$.

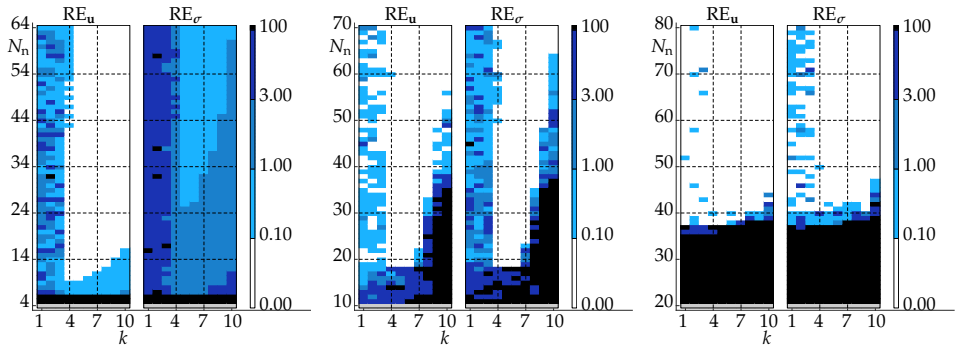

Figure 3.28: RE using STM#7 and LRE with p_1 (left), p_2 (center) and p_3 (right).

Using UpTM: When using an unstructured-plane tetrahedral mesh, the solution shows an accurate performance; see Figure 3.29. Also, in this case, the obtained solution is better than that obtained with STM, where the system is usually poorly conditioned due to the distribution of the cells.

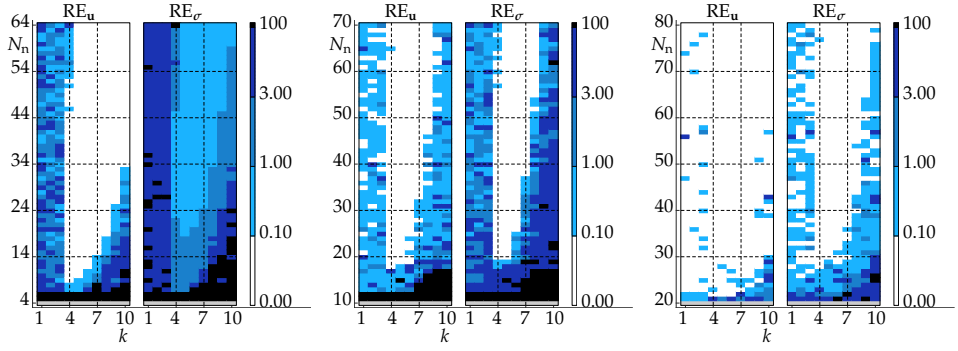

Figure 3.29: RE using UpTM#7 and LRE with p_1 (left), p_2 (center) and p_3 (right).

Using UTM: For unstructured meshes, the results are similar to those obtained when using UpTM; see Figure 3.30.

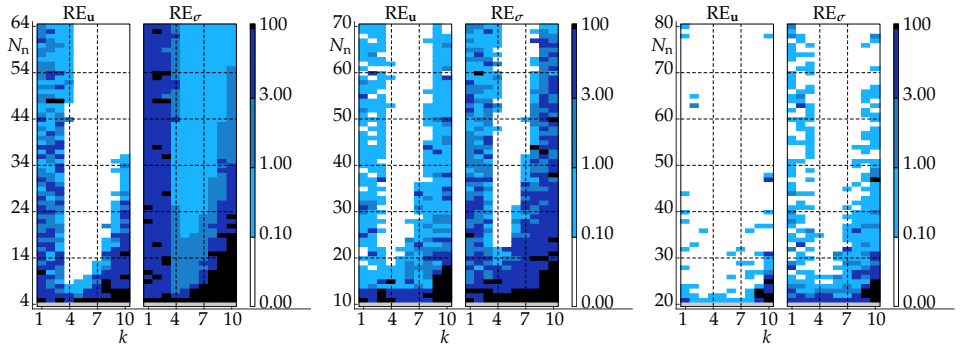

Figure 3.30: RE using UTM#7 and LRE with p_1 (left), p_2 (center) and p_3 (right).

A conclusion for the above is that $k = 6$, as in two-dimensional cases, is a good choice for the shape parameter in all cases. In order to define the number of points in the stencil, the order of convergence is studied.

Order of convergence

As in the two-dimensional analytical example, the order of convergence is analyzed to define the parameters. As it was mentioned, $k = 6$ is used in all the cases. In Tables D.4, D.5, D.6 and D.7 the solution for various values of N_n and $N_g = 37$ (tetrahedral meshes) or $N_g = 49$ (hexahedral meshes) are presented for all the types of meshes. Table 3.4 summarizes the chosen parameters in each case. In order to simplify the analysis, it is decided to add 40 points to the minimum ($N_{n,min}$) required for each interpolation, see Section 2.3.3. As it is possible to observe in Table 3.4, the solution using MLS is also included, being, in general, less accurate than the LRE solution when unstructured meshes are used. In addition, results using the two types of stencils are displayed, concluding that there is no significant difference between one and the other when using LRE. However, in Figures 3.31 and 3.32, the convergence of AE is shown using UTM and the values presented in Table 3.4 for LRE and MLS, respectively, being clear that, for LRE, when using s_{eq} the convergence is not as straightforward as when using s_{df}[4]. On the other hand, when using MLS even negative OC are obtained; see Table 3.4. In Section D.2, analogous graphs to those presented in Figure 3.31 for the cases of SHM, STM, and UpTM are presented. It can be seen that in the cases of structured meshes (SHM and STM), the differences between using s_{eq} or s_{df} are

[4]Mesh #1 is excluded from these graphs because the number of cells is less than the number of points needed.

negligible. On the contrary, when using UpTM appreciable differences are observed, especially when using p_3, where, as with UTM, the convergence when using s_{eq} is not clear, presenting inconsistencies. Therefore, it is recommended that for unstructured meshes, which is the purpose of this thesis, the s_{df} stencil is used in three-dimensional problems.

Table 3.4: Order of convergence for the displacement and stress fields using LRE or MLS and number of stencil points N_n for each method using either s_{eq} or s_{df}. $k = 6$ and $N_g = 37$ (tetrahedral meshes) or $N_g = 49$ (quadrilateral meshes) are used.

Mesh	p_i - N_n	**Disp. field (u)** TOC	LRE s_{df}	LRE s_{eq}	MLS s_{df}	MLS s_{eq}	**Stress field (σ)** TOC	LRE s_{df}	LRE s_{eq}	MLS s_{df}	MLS s_{eq}
SHM	p_1 - 44	2	1.55	1.55	1.75	1.78	1	1.71	1.70	1.58	1.59
	p_2 - 50	3	2.72	2.68	2.13	2.19	2	1.94	1.95	1.91	1.92
	p_3 - 60	4	4.07	4.05	4.01	4.03	3	3.32	3.32	3.14	3.15
STM	p_1 - 44	2	2.09	2.09	2.15	2.05	1	1.42	1.47	1.26	1.29
	p_2 - 50	3	3.14	3.06	3.31	3.27	2	2.28	2.28	2.09	2.09
	p_3 - 60	4	4.52	4.44	4.06	0.31	3	3.53	3.52	2.57	-0.94
UpTM	p_1 - 44	2	2.17	2.15	2.18	2.11	1	1.62	1.66	1.30	1.34
	p_2 - 50	3	3.06	3.18	2.95	2.92	2	2.38	2.46	2.25	2.25
	p_3 - 60	4	4.64	5.87	2.57	2.21	3	3.69	4.90	1.55	1.41
UTM	p_1 - 44	2	2.16	2.21	0.58	-0.50	1	1.53	1.60	-0.32	-1.51
	p_2 - 50	3	3.34	2.45	3.51	3.42	2	2.49	1.72	2.34	2.26
	p_3 - 60	4	4.54	3.96	0.13	0.95	3	3.60	3.20	-1.09	-0.16

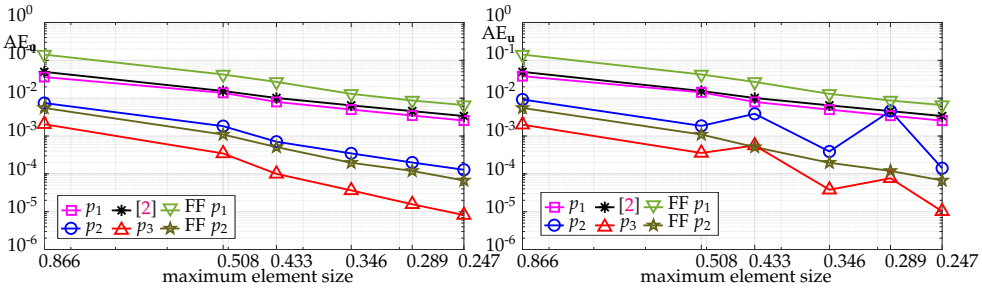

Figure 3.31: Convergence of $AE_{\mathbf{u}}$ using LRE and s_{df} (left) or s_{eq} (right) with the parameters of Table 3.4 for UTM.

In Figure 3.32, it is possible to see that when using MLS with p_2 the results are correct. However, the bad behavior for p_1 and p_3 discourages using MLS. At this point, it is necessary to emphasize, again, that the MLS is computationally more expensive

than the LRE. In conclusion, using the LRE with the s_{df} stencil is recommended, especially in unstructured meshes, despite being more expensive than s_{eq}.

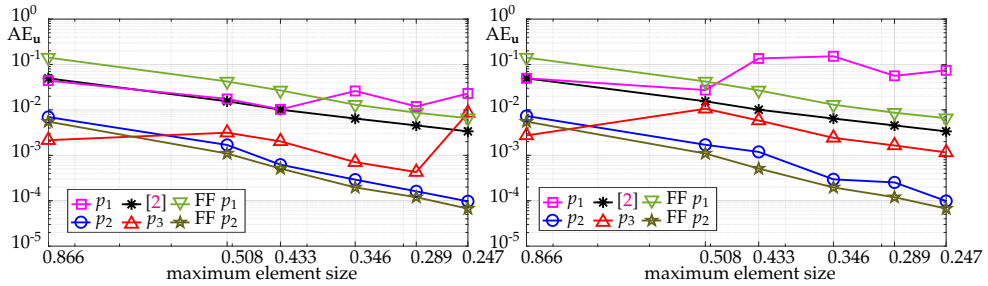

Figure 3.32: Convergence of $AE_\mathbf{u}$ using MLS and s_{df} (left) or s_{eq} (right) with the parameters of Table 3.4 for UTM.

In the previous section, it was concluded that unaccurate OC were obtained when using p_2 in two dimensions. However, this is is not observed in Table 3.4, using LRE for s_{df}. Figure 3.33 shows the OC for the displacement and stress fields using UTM#7 for different values of k, N_n and interpolations p_1, p_2 and p_3. In these images, it is possible to observe that the TOC is reached when using p_2, although the set of parameters which allow this is smaller than for p_1 and p_3. Therefore, it is recommended to use p_3, as in two dimensions, for high-order interpolation.

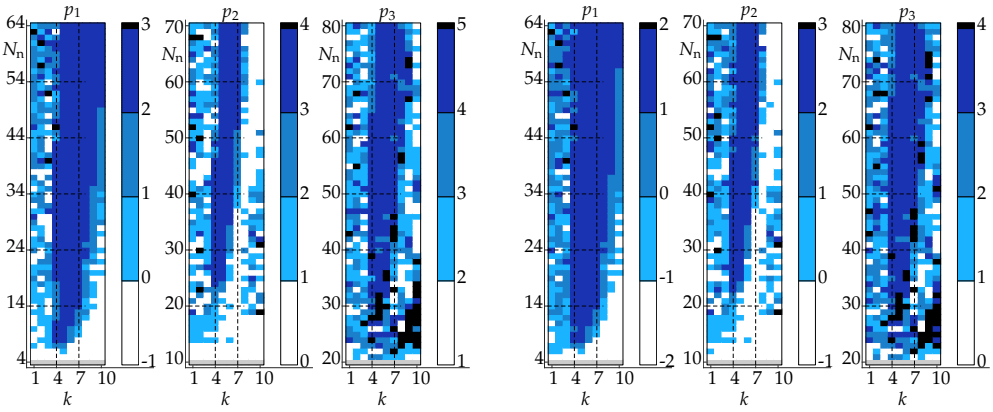

Figure 3.33: $OC_\mathbf{u}$ (left) and OC_σ (right) using UTM with LRE.

Section D.2 shows the evolution of the displacement and stress field through the seven unstructured meshes when using LRE for different interpolations. In the following examples, only unstructured meshes (UTM) are used with the parameters defined in Table 3.4.

3.2.2 Cantilever beam with a uniformly distributed load

In [5], it is possible to find an example of a cantilever beam subjected to a vertical force at the free end, where the shear locking effect appears, using a structured hexahedral mesh.

This section considers a three-dimensional cantilever beam subjected to a uniformly distributed load, as shown in Figure 3.34. For this example $E = 30000$, $\nu = 0.3$, $L_x = 50$, $L_y = L_z = 2$ and $q = 0.05$.

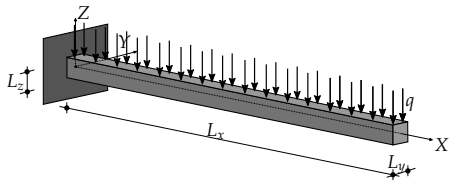

Figure 3.34: Geometry of the beam subject to a uniformly distributed load.

An approximate analytical solution from [7] is used to compare the numerical results. The displacement u_z at the free end and the stress σ_x at $(L_x/2, 0, L_z/4)$, when $L_x \gg L_z$, are:

$$u_z(L_x, 0, 0) = -\frac{3}{2}\frac{q\,L_x^4}{E\,L_z^3}, \quad \sigma_x(L_x/2, 0, L_z/4) = \frac{q}{80}\left(7 + 30\,\frac{L_x^2}{L_z^2}\right). \tag{3.9}$$

Clips of three of the seven meshes used in this problem are shown in Figure 3.35.

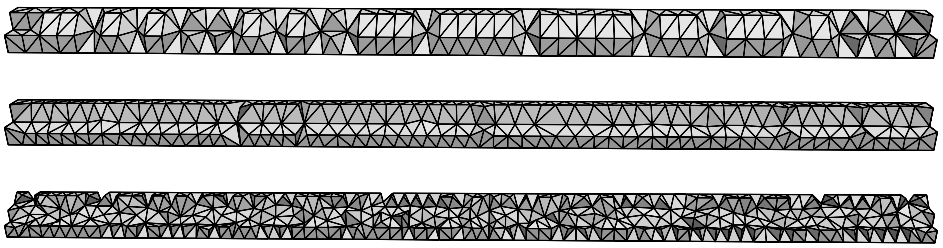

Figure 3.35: Mesh #1 (top), #4 (middle) and #7 (bottom).

Tables 3.5 and 3.6 show the results of the displacement and stress defined in Eq. (3.9), respectively. From Table 3.5, it can be deduced, as mentioned in the previous section, that when using the LRE for unstructured meshes, in three-dimensional cases, it is more convenient to use the stencil s_{df}. For example, when using the mesh #6 and

the stencil s_{eq} the relative error is triggered much higher than that obtained when using s_{df}[5]. When analyzing the results using the MLS, it is observed that, in general, the results are not accurate enough, even when using p_2, which was where the best behavior of the MLS had been seen. Again, it is observed that when using s_{eq}, the results are also worse than using s_{df}. It is then concluded that using LRE is more convenient than MLS, not only from a computational effort point of view but also when obtaining the numerical solution.

Table 3.5: Solution of $u_z(L_x, 0, 0)$ where the approximated analytical value is $u_z(L_x, 0, 0) = -1.953$.

s_i	#m	LRE				MLS				FF	
		[2]	p_1	p_2	p_3	[2]	p_1	p_2	p_3	p_1	p_2
s_{df}	1	-1.045	-2.393	-1.914	-1.956	-1.045	-1.863	-1.881	-1.963	-1.124	-1.945
	2	-2.500	-2.026	-1.906	-1.948	-2.500	-2.262	-1.856	-2.714	-1.153	-1.946
	3	-1.418	-2.028	-1.931	-1.953	-1.418	0.874	-1.928	-1.913	-1.280	-1.946
	4	-1.840	-2.126	-1.936	-1.951	-1.840	-3.365	-1.970	-2.989	-1.252	-1.945
	5	-2.178	-2.082	-1.940	-1.953	-2.178	-2.523	-1.996	-1.934	-1.267	-1.946
	6	-2.441	-2.040	-1.959	-1.956	-2.441	-1.696	-2.012	-1.444	-1.252	-1.946
	7	-1.570	-2.025	-1.943	-1.955	-1.570	-1.679	-1.931	-2.037	-1.427	-1.948
s_{eq}	1	-1.045	-2.378	-1.871	-1.955	-1.045	-1.617	-1.909	-2.957	-1.124	-1.945
	2	-2.500	-1.888	-1.929	-1.955	-2.500	-4.009	-1.884	-1.696	-1.153	-1.946
	3	-1.418	-2.001	-1.925	-1.944	-1.418	0.205	-1.946	-1.820	-1.280	-1.946
	4	-1.840	-2.166	-1.977	-1.954	-1.840	-0.344	-1.967	-0.052	-1.252	-1.945
	5	-2.178	-2.078	-1.936	-1.951	-2.178	146.65	-1.976	-1.943	-1.267	-1.946
	6	-2.441	-2.045	-2.066	-1.871	-2.441	0.675	-1.989	-2.740	-1.252	-1.946
	7	-1.570	-2.026	-1.938	-1.955	-1.570	-0.934	-1.931	-2.731	-1.427	-1.948

When comparing the results of the LRE using p_1 with the other linear interpolation methods ([2] and FF p_1), it is observed that it is not possible to obtain adequate results, which was expected due to the effect of shear locking. However, for LRE and p_1, although the result is not correct, the behavior seems adequate, thus obtaining a sufficiently approximate solution with p_1. When comparing with FreeFEM p_2, it is observed that the error of FF with mesh #7 is similar to that of using LRE with p_2. However, for the same mesh using p_3, the result of the presented method is more accurate.

Table 3.6 shows the stress results defined in Eq. (3.9), reaching the same conclusions as for the displacement: the convenience of using LRE and the stencil s_{df}. Here, it is possible to see the difference between the LRE and MLS when interpolating derivatives by looking at the values obtained using [2].

[5]For example with p_3 the error when s_{df} is 0.15% while using s_{eq} it is 4.20%.

Table 3.6: Solution of $\sigma_x(L_x/2, 0, L_z/4)$ where the approximated analytical value is $\sigma_x(L_x/2, 0, L_z/4) = 11.72$.

s_i	#m	LRE				MLS				FF	
		[2]	p_1	p_2	p_3	[2]	p_1	p_2	p_3	p_1	p_2
s_{df}	1	5.17	11.73	11.40	11.67	6.17	12.02	11.22	11.71	-1.03	11.45
	2	19.02	12.30	11.38	11.70	16.02	15.29	10.96	11.68	0.02	11.91
	3	7.89	15.50	11.67	11.72	4.63	66.39	11.65	12.34	0.88	11.85
	4	6.12	14.61	11.66	11.71	10.24	8.90	11.89	66.02	5.37	11.62
	5	22.32	17.25	11.69	11.72	22.79	23.08	12.05	12.80	10.27	11.72
	6	5.12	15.11	11.65	11.71	-10.04	5.90	12.03	9.95	4.94	11.73
	7	11.22	11.20	11.70	11.73	10.86	2.40	11.65	11.68	9.92	11.71
s_{eq}	1	5.17	11.09	11.50	11.67	6.17	-0.54	11.37	-20.37	-1.03	11.45
	2	19.02	11.65	11.38	11.70	16.02	13.65	11.07	9.61	0.02	11.91
	3	7.89	15.58	11.83	11.73	4.63	-18.87	11.65	11.11	0.88	11.85
	4	6.12	14.85	11.97	11.72	10.24	13.39	11.75	-22.02	5.37	11.62
	5	22.32	17.25	11.40	11.71	22.79	-931.8	11.96	11.79	10.27	11.72
	6	5.12	15.12	11.57	11.72	-10.04	196.1	11.85	19.04	4.94	11.73
	7	11.22	11.03	11.67	11.73	10.86	16.35	11.66	18.12	9.92	11.71

In the following examples, from what was said above, only unstructured meshes (UTM) are used with the parameters defined in Table 3.4 using LRE and stencil s_{df}.

3.2.3 Vibration of a cantilever beam

In this example, a cantilever beam subjected to a time-varying vertical force at the free end is studied; see Figure 3.36. The mechanical and geometric parameters used in [8] and [9] are used. For this example the mechanical parameters are $E = 10\,\text{MPa}$, $\nu = 0.3$ and $\rho = 2600\,\text{kg/m}^3$, while the geometrical parameters are $L_x = 20\,\text{m}$, $L_y = L_z = 2\,\text{m}$ and $F_{\max} = 500\,\text{N}$.

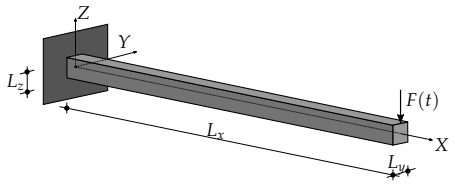

Figure 3.36: Geometry of the beam subject to a time-varying vertical force.

The time-varying vertical force is imposed linearly from zero to 500 N during the

first 7 seconds, and then it is released:

$$F(t) = \begin{cases} F_{\max} \dfrac{t}{t_1} & \text{if} \quad t \leq t_1\,, \text{ where } t_1 = 7\,\mathrm{s}\,, \\ 0 & \text{if} \quad t > t_1\,. \end{cases} \tag{3.10}$$

The first analysis performed in this example is to obtain the lowest natural frequency and compare it with analytical approaches and other methods. The first natural frequency is fundamental in the dynamic analysis due to the consequences it may have in the case of imposing stresses that enter into resonance with it. Furthermore, in this case, due to the type of load imposed, the response of the structure is mainly related to the first vibration mode associated with the lowest natural frequency. To obtain the natural frequencies ω, the free structural problem is solved, obtaining the equation that relates natural frequencies with the vibration modes $\boldsymbol{\phi}$:

$$\left(\mathbf{M} + \omega^2\,\mathbf{K}\right)\,\boldsymbol{\phi} = \mathbf{0}\,. \tag{3.11}$$

Then the frequencies and periods are $f_\omega = \omega/(2\,\pi)$ and $T = 1/f_\omega$, respectively. From the Euler-Bernoulli beam theory, it is possible to obtain an approximation for the frequencies, where the first frequency is:

$$f_{\omega_1,\mathrm{EB}} = \frac{\beta^2}{2\,\pi}\sqrt{\frac{E\,I}{\rho\,A}}\,, \tag{3.12}$$

where $\beta\,L_x = 1.8751041$ m, $I = L_y\,L_z^3/12$ is the inertia and $A = L_y\,L_z$ is the area of the transverse section. Table 3.7 shows the relative errors in the first natural frequency, ω_1, for different meshes when comparing the frequency obtained using the lumped mass matrix, Eq. (2.91), with that obtained using the high-order method, Eq. (2.87), with p_3 for three values of $N_\mathrm{m} = \{1,\,10,\,35\}$.

Table 3.7: Relative error [%] obtaining ω_1 when using different methods to calculate the mass matrix.

$\#m$	N_m		
	1	10	35
1	4.08×10^{-6}	1.40×10^{-3}	1.40×10^{-3}
3	1.01×10^{-5}	3.33×10^{-4}	3.31×10^{-4}
7	3.61×10^{-6}	1.52×10^{-3}	1.52×10^{-3}
11	6.69×10^{-7}	7.56×10^{-4}	7.56×10^{-4}
15	5.41×10^{-7}	7.18×10^{-4}	7.18×10^{-4}

This comparison was also made for the following four natural frequencies, obtaining results similar to those in Table 3.7. Likewise, it was verified that these minimal

differences are also observed when using p_1 or p_2. It is concluded then that there is no difference in using the lumped mass matrix or the high-order mass matrix. For this reason, due to its lower computational cost, it is decided to use the expression of Eq. (2.91) for the mass matrix. The value obtained for the first frequency f_{ω_1} using p_1, p_2 and p_3 with the mass matrix of Eq. (2.91) is compared to other methods in Table 3.8. It is observed that with the method presented, a very accurate approximation is obtained for both p_2 and p_3. It is interesting to see how when using p_1, the result of the method presented here is much better than when using another method with linear interpolation.

Table 3.8: Values of $100\, f_{\omega_1}$ for different methods where the analytical value is $f_{\omega_1,\text{EB}} = 5.009 \times 10^{-2}$ Hz.

#m	[2]	LRE			FF	
		p_1	p_2	p_3	p_1	p_2
1	5.271	4.672	5.059	4.982	6.518	5.008
2	4.887	4.862	5.035	4.984	6.385	5.007
3	5.151	4.658	5.007	4.973	6.462	5.005
4	5.370	4.738	5.014	4.982	6.384	5.007
5	5.360	4.734	5.007	4.981	6.387	5.004
6	5.305	4.783	4.984	4.982	6.364	5.005
7	5.031	4.830	4.987	4.979	6.282	5.002
8	5.212	4.810	4.907	4.983	6.224	5.002
9	5.245	4.769	4.991	4.995	6.340	5.006
10	5.354	4.851	4.989	4.978	5.754	4.999
11	5.254	4.877	4.992	4.977	5.736	4.998
12	5.347	4.823	4.990	4.975	5.706	4.998
13	5.264	4.896	4.982	4.973	5.643	4.998
14	5.254	4.893	4.984	4.975	5.613	4.998
15	5.196	4.915	4.979	4.974	5.636	4.998
16	5.219	4.896	4.979	4.975	5.630	4.998
17	5.180	4.932	4.984	4.982	5.471	4.996

Next, the evolution in time of the displacement of the free end of the beam is analyzed for different temporal discretizations. The temporal discretization methods can be written from the generalized algorithm presented in Section 2.5, see Table 3.9 that indicates the parameters used.

Table 3.9: Parameters of the generalized algorithm [10] for different methods.

Method	$\theta_{M,1}$	$\theta_{M,2}$	$\theta_{M,3}$	$\gamma_{M,0}$	$\gamma_{M,1}$	$\gamma_{M,2}$	$\beta_{M,0}$	$\beta_{M,1}$	$\beta_{M,2}$
Trapezoidal	1.000	1.000	1.000	1.500	1.000	1.000	1.500	2.000	1.000
HHT-α [11]	0.510	0.510	0.510	3.33015	1.980	1/0.51	3.33015	1.980	1.000
Modak [10]	0.541	1.092	1.000	0.904	0.569	1.102	0.017	1.111	1.000

The displacement of the free end is obtained using p_3, $N_n = 60$, $N_g = 7$, LRE and a stencil s_{df}, see Figure 3.37. The results of [9] are used as references. An unstructured mesh of 3753 tetrahedral elements was used, while in [9], a mesh of $80 \times 8 \times 8 = 5140$ tri-linear hexahedral elements was selected. It is clearly observed how the methods converge when the step decreases, although in the trapezoidal case for $\Delta_t = 0.1\,s$ a finer mesh is needed. Euler's method shows that a very small step is required, making it unacceptable.

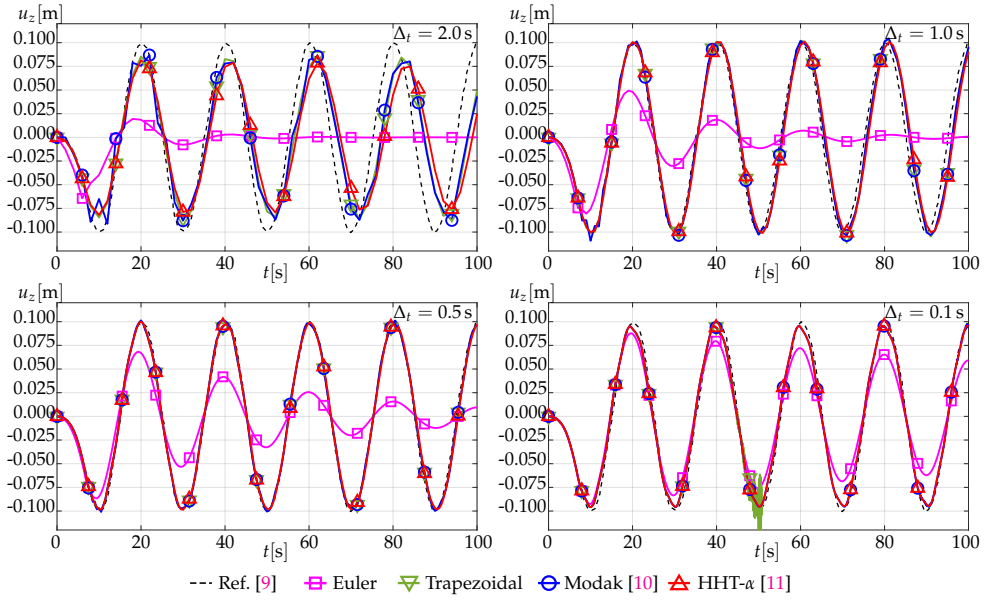

Figure 3.37: Displacement $u_z(L_x, L_y/2, L_z/2, t)$ of the free end for different increments of time Δ_t and temporal discretization methods using p_3.

3.2.4 Analytic hyperelastic case

This example and the one presented in the next section show that the method is suitable for hyperelastic problems. Both examples are solved for the two hyperelastic

models presented in Section 2.1.3. Likewise, these results are compared with those where small deformations hypothesis is assumed.

In this example, a known displacement field $\mathbf{u}$ is imposed on the boundary of the domain, and the corresponding body force $\mathbf{b}_0$ is imposed in the interior. The domain is a cube of size $L = 1$, i.e. $\Omega = \{(X, Y, Z) : X, Y, Z \in [0, 1]\}$. The displacement field imposed on the boundary is $\mathbf{u} = u_x\,\mathbf{e}_x + u_y\,\mathbf{e}_y + u_z\,\mathbf{e}_z$, where

$$\begin{aligned} u_x(X, Y, Z) &= \alpha\,\ln(1 + X)\,, \\ u_y(X, Y, Z) &= 0, \\ u_z(X, Y, Z) &= 0\,. \end{aligned} \tag{3.13}$$

with $\alpha \in [-0.5, 0.5]$.

The material properties are $E = 1$ and $\nu = 0.3$. The same UTM meshes used in the first three-dimensional example were chosen for the numerical resolution, which can be found in Table E.4. The body force $\mathbf{b}_0 = b_{0,x}\,\mathbf{e}_x + b_{0,y}\,\mathbf{e}_y + b_{0,z}\,\mathbf{e}_z$ is obtained from Eq. (2.39) using $\partial\dot{\mathbf{u}}/\partial t = \mathbf{0}$ and integrated using numerical quadrature as in Eqs. (2.78) and (2.79) using 56 Gaussian points for each finite tetrahedron, see Appendix B. The components of the body force $\mathbf{b}$ are zero except for $b_{0,x} = -\partial P_{xx}/\partial X$ where P_{xx} is the first component of the Piola stress tensor $\mathbf{P}$. Therefore, the different body forces are:

$$b_{0,x,\mathrm{SD}} = \frac{\alpha}{(1+X)^2}\,(\lambda + 2\,\mu)\,, \tag{3.14}$$

$$b_{0,x,\mathrm{SVK}} = \frac{\alpha}{(1+X)^2}\left(\frac{3\,r^2 - 1}{2}\right)(\lambda + 2\,\mu)\,, \tag{3.15}$$

$$b_{0,x,\mathrm{SM}} = \frac{\alpha}{(1+X)^2}\left[\left(\frac{r^2+1}{2\,r^2}\right)\lambda + \left(\frac{2\,r^2+10}{9\,r^{8/3}} + \frac{r^2+1}{3\,r^2}\right)\mu\right], \tag{3.16}$$

where $r = 1 + \alpha/(X+1)$ and the subscripts refer to Small Deformations (SD), Saint Venant-Kirchhoff (SVK), and Simo-Miehe (SM). It is possible to see that when applying the hypothesis of small deformations, $\alpha \to 0$, in Eqs. (3.15) and (3.16), it is obtained, in both cases, Eq. (3.14)[6].

[6]The Taylor linear approximation, when $\alpha \to 0$, of a function of the form $f(\alpha) = \alpha\,g(\alpha)$ is $f(\alpha) \approx \alpha\,g(0)$:

$$\left.\begin{aligned} f_1(\alpha) &= \alpha\left(\frac{3\,r^2-1}{2}\right), \\ f_2(\alpha) &= \alpha\left(\frac{r^2+1}{2\,r^2}\right), \\ f_3(\alpha) &= \alpha\left(\frac{2\,r^2+10}{9\,r^{8/3}} + \frac{r^2+1}{3\,r^2}\right). \end{aligned}\right\} \Rightarrow \text{Taylor aproximation} \Rightarrow \left\{\begin{aligned} f_1(\alpha) &\approx \alpha\,, \\ f_2(\alpha) &\approx \alpha\,, \\ f_2(\alpha) &\approx 2\,\alpha\,. \end{aligned}\right.$$

The convergence of the method using SVK or SM, when $\alpha = -0.3$, can be seen in Figures 3.38 and 3.39, respectively. Mesh #1 is excluded from these graphs because the number of cells is less than the number of points needed for the interpolation. A correct convergence is observed for the SM model. However, in the SVK model, the convergence is unclear, especially when refining the meshes. The latter is because the SVK model is known to be unstable in the strong compression regime [12, 13], which happens for $\alpha = -0.3$. When using the SM, the expected orders of convergence are obtained for both the stresses and the displacement, except for the displacement field and p_2, as seen in previous sections.

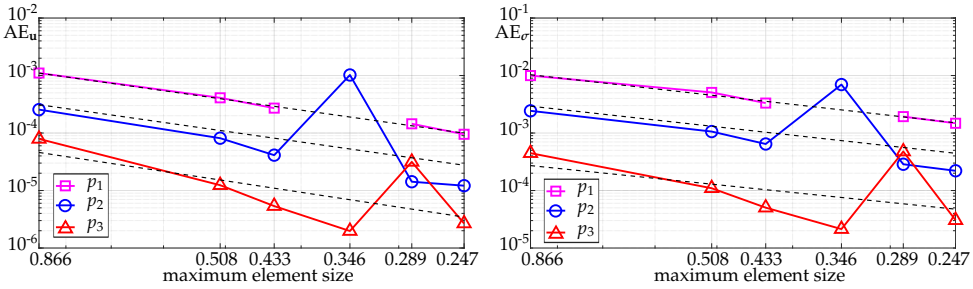

Figure 3.38: Convergence using the SVK model of the displacement field $\mathbf{u}$ (left) and the stress field σ (right) when $\alpha = -0.3$.

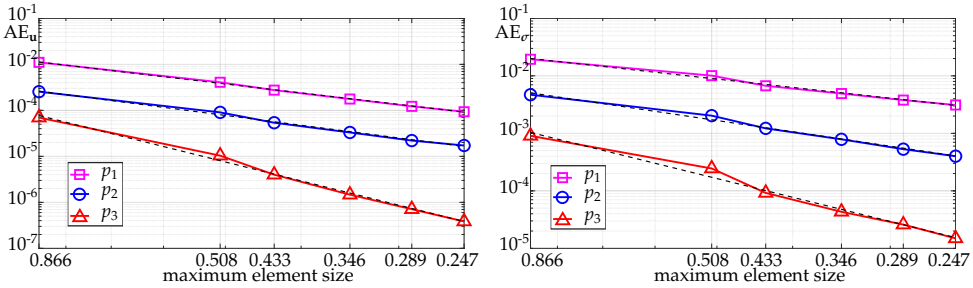

Figure 3.39: Convergence using the SM model of the displacement field $\mathbf{u}$ (left) and the stress field σ (right) when $\alpha = -0.3$.

Figure 3.40 shows the numerical solution compared to the analytic of the displacement u_x and the stress σ_{xx} at the point $\boldsymbol{X} = (0.5, 0.5, 0.5)$ for different values of α

using mesh #5 and p_3. The Cauchy stress tensors for each model are:

$$\boldsymbol{\sigma}_{\mathrm{SD}} = \frac{\alpha}{X+1}\left[\begin{pmatrix} 1 & 0 & 0 \\ 0 & 1 & 0 \\ 0 & 0 & 1 \end{pmatrix}\lambda + \begin{pmatrix} 1 & 0 & 0 \\ 0 & 0 & 0 \\ 0 & 0 & 0 \end{pmatrix} 2\mu\right], \tag{3.17}$$

$$\boldsymbol{\sigma}_{\mathrm{SVK}} = \frac{\alpha}{X+1}\left[\left(\frac{1+r}{2r}\right)\begin{pmatrix} r^2 & 0 & 0 \\ 0 & 1 & 0 \\ 0 & 0 & 1 \end{pmatrix}\lambda + (1+r)\begin{pmatrix} r & 0 & 0 \\ 0 & 0 & 0 \\ 0 & 0 & 0 \end{pmatrix}\mu\right], \tag{3.18}$$

$$\begin{aligned}\boldsymbol{\sigma}_{\mathrm{SM}} = {} & \frac{\alpha}{X+1}\left(\frac{1+r}{2r}\right)\begin{pmatrix} 1 & 0 & 0 \\ 0 & 1 & 0 \\ 0 & 0 & 1 \end{pmatrix}\lambda \\ & + \frac{\alpha}{X+1}\left(\frac{1+r}{3r}\right)\left[\left(\frac{1}{r^{2/3}}\right)\begin{pmatrix} 2 & 0 & 0 \\ 0 & -1 & 0 \\ 0 & 0 & -1 \end{pmatrix} + \begin{pmatrix} 1 & 0 & 0 \\ 0 & 0 & 0 \\ 0 & 0 & 0 \end{pmatrix}\right]\mu,\end{aligned} \tag{3.19}$$

where, again, it is possible to observe that linearizing the SVK and SM expressions for $\alpha \to 0$ gives the SD one. It is worth noting that for $\alpha = \{-0.5, -0.4\}$, no solution is obtained when using SVK model, due, again, to its instability for strong compressions.

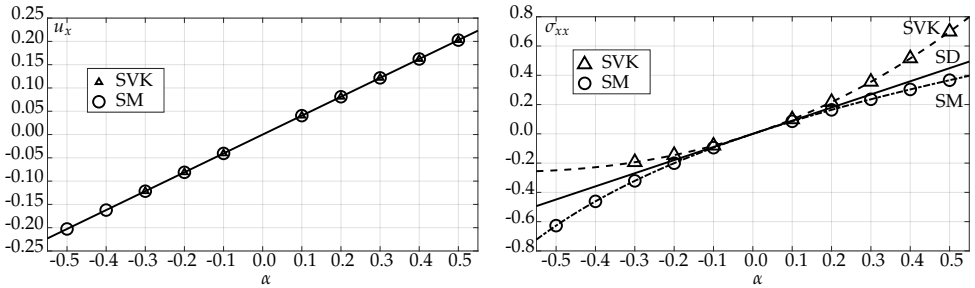

Figure 3.40: Comparison between analytical and numerical solutions of u_x (left) and σ_{xx} (right) at the point $\boldsymbol{X} = (0.5, 0.5, 0.5)$ using mesh # 5 and interpolation p_3.

3.2.5 Large deformation of a clamped beam

In this example, the large displacement and moderate rotation of a three-dimensional cantilever beam, clamped at the left end and subjected to a vertical force at the right end, are obtained. The numerical results for this case are compared with those obtained in [14] and [15]. The mechanical and geometrical properties are the same as those used in [14] where: the Young modulus is $E = 15293\,\mathrm{kPa}$ and the Poisson ratio

is $\nu = 0.3$; the structure is a prismatic body with a square diamond cross-section with side $a = 0.2\,\mathrm{m}$ and length $\ell = 2\,\mathrm{m}$, see Figure 3.41.

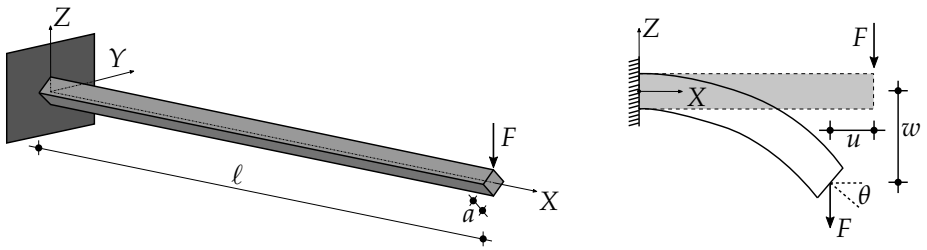

Figure 3.41: Geometry of the clamped beam which suffers large deformations.

The load at the free end is

$$\mathbf{F} = \frac{\mathcal{F}\, E\, I}{\ell^2}\,(0,\, 0,\, -1)\,, \tag{3.20}$$

where $\mathcal{F}$ is a dimensionless parameter that characterized the load $\mathbf{F}$. The obtained computed solution is compared with the numerical results from [8, 14, 15] for a range of values of $\mathcal{F}$ that goes from 0.2 to 10.

Both Gonzalez et al. [8], and Tukovic et al. [14] use the finite volume method with linear interpolation and compare their numerical results with those obtained by Mattiasson [15]. In Mattiasson's work, the numerical evaluation of the elliptic integrals that define the problem is performed, ignoring the axial and shear strains. This last point is important since the results presented in [8] and [14], as well as the high-order method presented here, are obtained with numerical simulations that do take these deformations into account, especially the shear deformation, which, as it has already been mentioned, is important because of the shear locking effect.

In [14] the results are obtained for $\mathcal{F} = \{0.2, 0.4, 0.8, 1.6\}$ in two structured meshes using the the SVK model. The comparison between the results obtained in [15] and those obtained with the finer mesh in [8] and [14] as well as those using p_3 are presented in Table 3.10. This table shows the results for different meshes, # Elem indicates the number of elements (hexahedrons or tetrahedrons). Although the closest result to [15] is the one obtained with [8], for example, for $\mathcal{F} = 1.6$ the relative error is 0.25 %, the number of elements employed (40960 hexahedrons) is more than ten times higher than those of the finest mesh using the high-order method (3803 tetrahedrons) for which a relative error of 0.73 % is obtained. In the case of using the SM model, the error for $\mathcal{F} = 1.6$ when comparing with [15] is 0.63 %, see results in Table 3.11.

Table 3.10: Displacement w/ℓ for different loads $\mathcal{F}$ and meshes using the SVK model.

$\mathcal{F}$	# Elem.	10000	40960	448	889	1674	2318	3803
	[15]	[14]	[8]	High order method using p_3				
0.2	0.06636	0.06545	0.06625	0.06772	0.06705	0.06688	0.06682	0.06664
0.4	0.13098	0.12905	0.13080	0.13363	0.13234	0.13201	0.13189	0.13156
0.8	0.24945	0.24545	0.24940	0.25438	0.25213	0.25157	0.25136	0.25077
1.6	0.42941	0.42535	0.43050	0.43732	0.43434	0.43365	0.43335	0.43256

Table 3.11: Displacement w/ℓ for different loads $\mathcal{F}$ and meshes using the SM model.

$\mathcal{F}$	# Elem.	448	889	1674	2318	3803
	[15]	High order method using p_3				
0.2	0.06636	0.06772	0.06705	0.06688	0.06682	0.06664
0.4	0.13098	0.13361	0.13232	0.13200	0.13188	0.13154
0.8	0.24945	0.25424	0.25202	0.25149	0.25126	0.25066
1.6	0.42941	0.43680	0.43390	0.43329	0.43293	0.43212

The next test is to raise the factor $\mathcal{F}$ to 10, which is the maximum value used in [15]. The results of using the finest mesh (3803 tetrahedrons) with p_3 and the SVK model are shown in the left image of Figure 3.42 and in the right image, the convergence in the displacement and stress field mesh for $\mathcal{F} = 1.6$ are displayed. To obtain the convergence, the fields from a fine mesh of 5593 tetrahedrons are used for the comparison. It can be seen that the convergence in the field of displacements is adequate, and for the stress field, although it is not exact, it is clear that by further refining the meshes, convergence is obtained. Figure 3.43 shows the analogous results to the aforementioned but using the SM model.

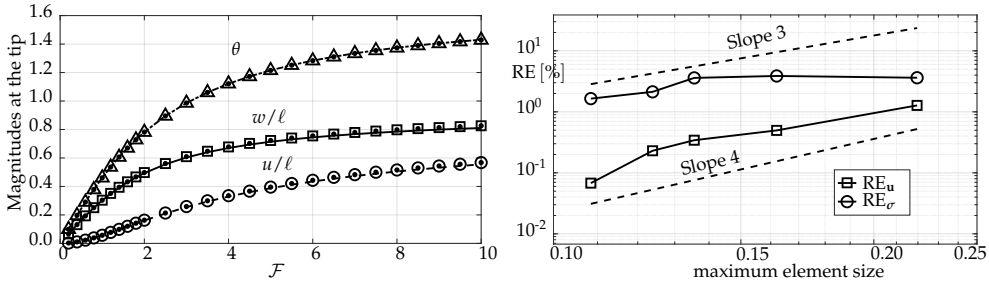

Figure 3.42: On the left image, the magnitudes at the tip for increasing magnitude of $\mathcal{F}$. Reference solution [15] (lines) and numerical results (points) of θ, u/ℓ, and w/ℓ using the SVK model. On the right image, the relative error of the displacement and stress fields for $\mathcal{F} = 1.6$ and SVK model.

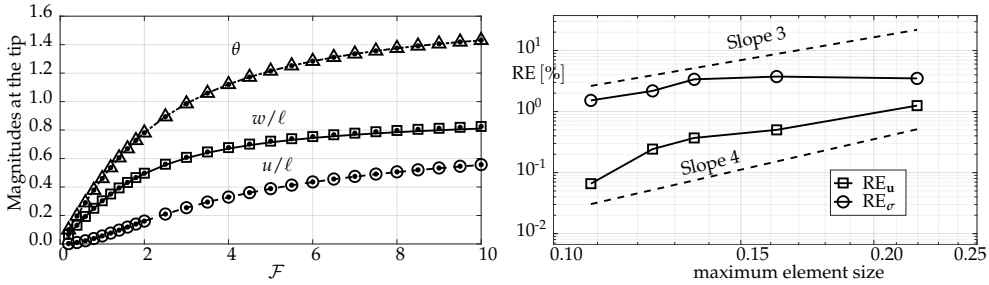

Figure 3.43: On the left image, the magnitudes at the tip for increasing magnitude of $\mathcal{F}$. Reference solution [15] (lines) and numerical results (points) of θ, u/ℓ, and w/ℓ using the SM model. On the right image, the relative error of the displacement and stress fields for $\mathcal{F} = 1.6$ and SM model.

In Figures 3.42 and 3.43, small deviations of the magnitudes for high loads can be seen with respect to what is obtained in [15]. This is because in [15], the axial and shear deformations are neglected, whereas, for thick beams, such as the one presented here, the shear strain plays a relevant role [8, 16]. As in [8], the case for $\mathcal{F} = 10$ is solved for slender beams with lengths $\ell = \{3, 4, 5, 6, 7, 8\}$ m, in order to verify that by increasing the length of the beam, the numerical result is more similar to the analytical one presented in [15]. The numerical results are presented in Table 3.12, compared with those obtained in [8]. Once again, it may be concluded that, with a much smaller number of elements, it is possible to obtain similar or even smaller errors using high-order interpolation.

Table 3.12: Analytical result comparison $w/\ell = 0.81061$ for slender beams.

ℓ[m]	[8] using SM			High order method using p_3				
					SVK		SM	
	# Elem	w/ℓ	RE[%]	# Elem	w/ℓ	RE[%]	w/ℓ	RE[%]
2	40960	0.82253	1.470	3803	0.82620	1.923	0.82533	1.816
3				1360	0.81686	0.771	0.81653	0.731
4	81920	0.81280	0.270	792	0.81379	0.393	0.81365	0.375
5				1046	0.81230	0.208	0.81209	0.183
6				1262	0.81163	0.126	0.81156	0.117
7				1412	0.81132	0.087	0.81125	0.078
8	163840	0.81050	0.014	1710	0.81072	0.013	0.81065	0.005

Figure 3.44 shows the deformation of the plane $Y = 0$ for different cases. The left image shows the deflection for a beam of length $\ell = 2$ m and different values of $\mathcal{F}$ while the right image shows the deflection for $\mathcal{F} = 10$ and different values of ℓ. Here, it is possible to observe how increasing the applied force (which is always in the $-Z$

direction), the beam begins to be aligned with it, which means that it can resist more force, that is, the deformation for $\mathcal{F} = 10$ is much less than 50 times that obtained for $\mathcal{F} = 0.2$ (a value that would correspond to small deformations).

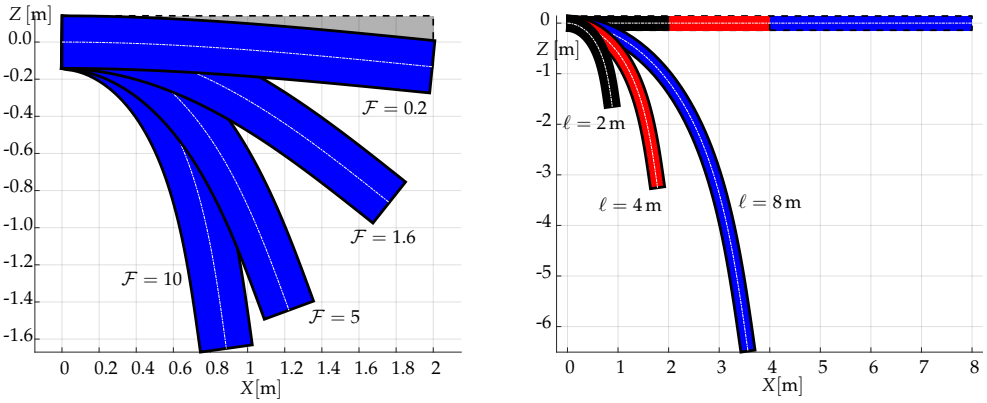

Figure 3.44: Deflection for a beam of length $\ell = 2\,\mathrm{m}$ and different values of $\mathcal{F}$ (left) and deflection for $\mathcal{F} = 10$ and different lengths ℓ (right).

3.3 Conclusions

In this chapter, an exhaustive analysis of the proposed method was performed by solving different classes of problems and providing comprehensive calibration and validation in two and three dimensions scenarios. All the parameters on which the presented method depends have been varied, and different types of meshes (structured and unstructured) have been analyzed. In addition, static and dynamic problems have been solved. Regarding the interpolation methods proposed, it may be concluded that the LRE is the most appropriate. For the case of two dimensions, it is recommended to use the stencil s_{eq}, see Section 2.3.3, due to its low computational cost. The recommended parameters for the two-dimensional case are $k = 6$, $N_g = 7$ and $N_n = N_{n,min} + 10$ where $N_{n\,,min}$ depends on the interpolation order used. In the case of three dimensions, it is recommended to use p_3 as interpolation, $k = 6$, and $N_n = 60$, with $N_g = 7$ or $N_g = 9$ for tetrahedrons or hexahedrons, respectively. Unlike the two-dimensional case, for three-dimensional problems, it is recommended to use the stencil s_{df}; see Section 2.3.3.

References

[1] F. Hecht. New development in freefem++. *J. of Numerical Math.*, 20(3-4):251–265, 2012.

[2] P. Cardiff, Ž. Tuković, H. Jasak, and A. Ivanković. A block-coupled Finite Volume methodology for linear elasticity and unstructured meshes. *Computers & Structures*, 175:100–122, oct 2016.

[3] Christophe Geuzaine and Jean François Remacle. Gmsh: A 3-D finite element mesh generator with built-in pre- and post-processing facilities. *International Journal for Numerical Methods in Engineering*, 79(11):1309–1331, 2009.

[4] Pablo Castrillo, Alfredo Canelas, Eugenio Schillaci, Joaquim Rigola, and Asensio Oliva. High-order finite volume method for linear elasticity on unstructured meshes. *Computers & Structures*, 268:106829, 2022.

[5] Pablo Castrillo, Eugenio Schillaci, and Joaquim Rigola. Analysis of high-order interpolationoschemes for solving linear problems in unstructured meshes using the finite volume method. In *8th European Congress on Computational Methods in Applied Sciences and Engineering*, Oslo, 2022.

[6] I. Demirdžić. A fourth-order finite volume method for structural analysis. *Applied Mathematical Modelling*, 40(4):3104–3114, feb 2016.

[7] Martin H. Sadd. *Elasticity: Theory, Applications, and Numerics*. Elsevier, 2009.

[8] Ignacio González Acedo. *Development of a finite volume method for elastic materials and fluid-solid coupled applications*. PhD thesis, Universitat Politècnica de Catalunya, 2019.

[9] A. K. Slone, C. Bailey, and M. Cross. Dynamic solid mechanics using finite volume methods. *Applied Mathematical Modelling*, 27(2):69–87, feb 2003.

[10] Sukomal Modak and Elisa D. Sotelino. The generalized method for structural dynamics applications. *Advances in Engineering Software*, 33(7-10):565–575, jul 2002.

[11] Francisco Armero and Eva Petocz. Formulation and analysis of conserving algorithms for frictionless dynamic contact/impact problems. *Computer Methods in Applied Mechanics and Engineering*, 158(3-4):269–300, 1998.

[12] Yuri Bazilevs, Kenji Takizawa, and Tayfun E. Tezduyar. *Computational Fluid-Structure Interaction: Methods and Applications*. John Wiley and Sons, dec 2012.

[13] Gerhard A. Holzapfel. *Nonlinear solid mechanics : a continuum approach for engineering*. Wiley, 2000.

[14] Željko Tuković and Hrvoje Jasak. Updated lagrangian finite volume solver for large deformation dynamic response of elastic body. *Transactions of FAMENA*, 31:1–18, 2007.

[15] Kjell Mattiasson. Numerical results from large deflection beam and frame problems analysed by means of elliptic integrals. *International Journal for Numerical Methods in Engineering*, 17(1):145–153, jan 1981.

[16] T. Kant and A. Gupta. A finite element model for a higher-order shear-deformable beam theory. *Journal of Sound and Vibration*, 125(2):193–202, sep 1988.

4

Analysis of a fluid-structure interaction phenomenon of turbulent flow through reed valves

Part of the work presented in this chapter has been published in:

[1] Pablo Castrillo, Eugenio Schillaci, and Joaquim Rigola. Simulation of Fluid-Structure Interaction and Impact Force on a Reed Valve. In *14th WCCM-ECCOMAS Congress 2020*, volume 1500, pages 1-12. Scipedia S.L., mar 2021. https://www.scipedia.com/public/Castrillo_et_al_2021a

[2] Muhammad Tofique, Alexander Löf, Eugenio Schillaci, Pablo Castrillo, and Joaquim Rigola. Experimental and Numerical Analysis of Reed Valve Movement In An Impact Fatigue Test System and Reciprocating Compressors. In *International Compressor Engineering Conference*. Purdue University, may 2021. https://docs.lib.purdue.edu/icec/2697/

[3] Alireza Naseri, Eugenio Schillaci, Ignacio González, Pablo Castrillo, and Joaquim Rigola. High-fidelity resolution of turbulent flow through reed valves with fluid-structure interaction. *Under review*. 2023.

4.1 Introduction

As introduced in Chapter 1, one of the engineering problems in which the numerical methods developed in this thesis can have a significant utility is the study of reed valves. As part of an industrial collaboration with the Voestalpine company, a compressor valve was studied through laboratory experiments [2] as a means of validation for numerical techniques capable of extracting detailed information regarding displacements, velocities, and internal stress by means of FEM simulations with quadratic interpolation of the displacement [1]. The objectives of those industrial collaborations were to characterize the behavior of a valve in its cyclic operation. Since the valve was very thin, the resolution of the same problem by means of FVM would have required to use a high-order method or employing a classical method using linear interpolation with a very fine mesh [4]. For this reason, the work carried out in [1] was one of the triggers for the development of the high-order interpolation method for FVM presented in this thesis since it was identified that there was no high-order method using the FVM for unstructured meshes in solids, as recently highlighted in [5]. A schematic sketch of the custom-built impact fatigue test rig can be found in [2]. Compressed air opens and closes a valve that repeatedly hits the seat, inducing impact fatigue stresses, see the left image of Figure 4.1. The geometry of the valve is shown in the right image of Figure 4.1, and valve dimensions can be found in [2]. In the experiment, the displacement and velocity of a point on the valve are measured using a laser at a sampling rate of 10000 values per second. The laser that detects the valve movement is located 2.5 mm from the top edge of the valve head along the centerline; see Figure 4.1.

The numerical characterization of the behavior of a valve requires the previous calculation of the valve's natural frequencies, maximum displacement, impact velocity, and valve impact stresses. To obtain the frequencies of the valves is possible to use commercial software, open source software such as FreeFEM [6], or the high-order method presented in the previous chapters. The methods used to obtain the maximum displacement and impact velocity are described in [1] and [2], where the TermoFluids software was used [7]. Those methods are detailed in Section 4.2 and submitted in [3], where a two-dimensional plate model with the mode superposition method was used to model the valve. In order to obtain a better representation of the impact forces and impact pressures, as well as a complete 3D map of internal stresses, it was decided to model the valve as a three-dimensional problem in FreeFEM [1]. For this simulation, the fluid pressure obtained from the simulation in TermoFluids was used as input data; see Section 4.3. Finally, Section 4.4 presents the results of all the magnitudes using the high-order method presented in this thesis.

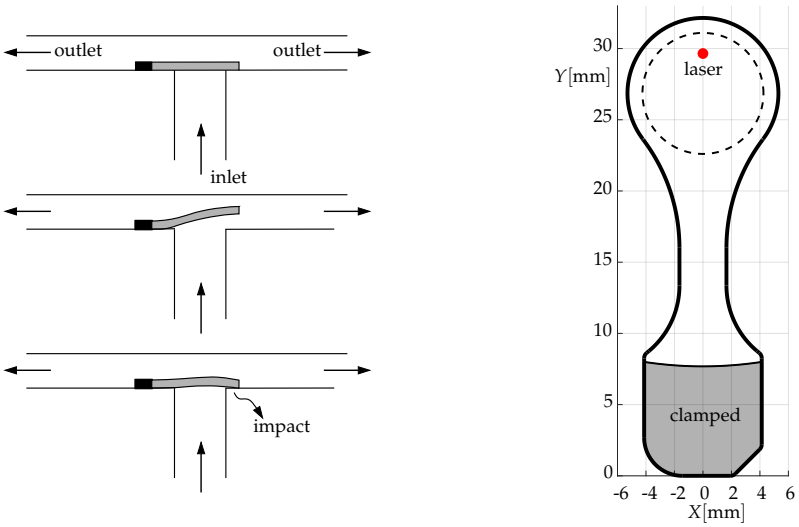

Figure 4.1: Opening and impact of the valve (left), and geometry of the valve (right).

4.2 Fluid-structure interaction simulation of turbulent flow through reed valves

The FSI simulation consists of a complex combination of different numerical techniques representing the interaction between a fluid (compressed air) and a solid (reed valve). In particular, the method is characterized by the following items: (1) gas resolution through a finite volume solver on a moving and unstructured mesh; (2) solving the movement of the solid using a plate model; (3) resolution of the fluid-structure interaction through a semi-implicit approach for strongly coupled problems [8].

The entire numerical method is implemented within the Termofluids code [7]. The fluid-structure coupled problem is solved numerically by a partitioned algorithm using independent solvers for fluid and structural sub-problems and adopting a coupling scheme to account for their interaction. This section describes the methods used for the FSI simulation, and the numerical results when using TermoFluids are compared with those obtained experimentally.

4.2.1 Fluid model

The fluid flow is solved using an Arbitrary Lagrangian-Eulerian (ALE) formulation with a conforming mesh that automatically adapts to the movement of the reed valve. An isothermal and incompressible fluid, governed by the unsteady Navier-Stokes

equations, is assumed. An ALE formulation of these equations in a moving domain is given by:

$$\frac{\partial \mathbf{v}_\mathrm{f}}{\partial t} + \mathbf{c} \cdot \nabla \mathbf{v}_\mathrm{f} = \frac{1}{\rho_\mathrm{f}} \nabla \cdot \sigma_\mathrm{f}\,, \tag{4.1}$$

$$\nabla \cdot \mathbf{v}_\mathrm{f} = 0\,, \tag{4.2}$$

where $\mathbf{v}_\mathrm{f}$ is the fluid velocity and ρ_f is the fluid density. $\mathbf{c}$ is the ALE convective velocity $\mathbf{c} = \mathbf{v}_\mathrm{f} - \mathbf{v}_\mathrm{m}$, which is the fluid velocity relative to a domain moving with a velocity $\mathbf{v}_\mathrm{m}$. σ_f is the fluid stress tensor, defined as the following for an incompressible Newtonian fluid:

$$\sigma_\mathrm{f} = -p\,\mathbf{I} + \mu_\mathrm{f} \left(\nabla \mathbf{v}_\mathrm{f} + \nabla \mathbf{v}_\mathrm{f}^\mathrm{T} \right)\,, \tag{4.3}$$

where p is the fluid pressure and μ_f is the dynamic viscosity of the fluid. A fractional-step projection method is used to solve the velocity-pressure coupling of the momentum equation, together with an explicit temporal discretization method [9]. This scheme leads to a three-step solution of the fluid governing equations from time step n to $n+1$, with a time increment of Δt:

$$\mathbf{v}_\mathrm{f}^\mathrm{p} = \mathbf{v}_\mathrm{f}^n - \frac{\Delta t}{2} \left[3 \left(\mathbf{c}^n \cdot \nabla \mathbf{v}_\mathrm{f}^n - \frac{\mu_\mathrm{f}}{\rho_\mathrm{f}} \Delta \mathbf{v}_\mathrm{f}^n \right) - \left(\mathbf{c}^{n-1} \cdot \nabla \mathbf{v}_\mathrm{f}^{n-1} - \frac{\mu_\mathrm{f}}{\rho_\mathrm{f}} \Delta \mathbf{v}_\mathrm{f}^{n-1} \right) \right]\,, \tag{4.4}$$

$$\frac{\Delta t}{\rho_\mathrm{f}} \Delta p^{n+1} = \nabla \cdot \mathbf{v}_\mathrm{f}^\mathrm{p}\,, \tag{4.5}$$

$$\mathbf{v}_\mathrm{f}^{n+1} = \mathbf{v}_\mathrm{f}^\mathrm{p} - \frac{\Delta t}{\rho_\mathrm{f}} \nabla p^{n+1}\,, \tag{4.6}$$

where $\mathbf{v}_\mathrm{f}^\mathrm{p}$ is a predicted velocity field that does not satisfy the incompressibility condition (Eq. (4.2)). The correction at Eq. (4.6) projects this intermediate velocity onto a divergence-free field.

A finite volume method is used for the spatial discretization of the governing equations. Second-order symmetry-preserving schemes discretize the equations on a collocated unstructured grid arrangement, guaranteeing the conservation of kinetic energy in the discrete representation, a crucial feature when dealing with turbulent flows [10–12]. Large Eddy Simulation (LES) models are used for turbulent flow. In LES, the largest scales of the flow are solved, while the small-scale motions are modeled by a SubGrid-Scale (SGS) model, reducing the computational cost of direct numerical simulations [13].

4.2.2 Moving meshes

A combination of the moving mesh technique and the Immersed Boundary Method (IBM) is used for modeling the moving structure in the fluid domain, as described in the rest of this section.

Due to the adoption of an ALE formulation on a deformable mesh framework, special attention should be paid to the evaluation of the domain velocity $\mathbf{v}_\mathrm{m}$ in order to satisfy the *Geometric Conservation Law* (GCL) [14, 15]. The movement of the reed valve is tracked by a moving mesh technique, adapting the fluid mesh to the new location of the moving structure. A significant advantage of the moving mesh technique is preserving high accuracy in the vicinity of the moving boundary. The employed moving mesh method, based on the work from Estruch et al. [16], provides the incremental displacement of the grid points, represented by $\mathbf{r}_\mathrm{m}(\mathbf{x})$, between two consecutive time steps n and $n+1$, at a spatial location $\boldsymbol{x}$ in the fluid, by solving a pure diffusive problem:

$$D_g \Delta \mathbf{r}_\mathrm{m}(\boldsymbol{x}) = \mathbf{0}\,, \tag{4.7}$$

where D_g is the diffusion coefficient. The system of equations is determined by defining boundary conditions of Dirichlet type (moving or fixed boundaries) or Neumann (sliding or free boundaries). The diffusion coefficient D_g inversely depends on the size of each element as:

$$D_g = 1/v^{\chi_\mathrm{m}}\,, \tag{4.8}$$

where v is the volume of the element and χ_m is a positive empirical coefficient. Consequently, the small cells, generally located in numerically or physically relevant areas, become stiffer and harder to deform. Therefore, the mesh quality in critical and sensitive areas is maintained. The softer large cells absorb the major distortion, which can readily tolerate the deformation without severely degrading their quality.

After the fluid mesh is moved, the domain velocity ($\mathbf{v}_\mathrm{m}$) needs to be evaluated at the faces of each control volume. The GCL guarantees that no volume is lost while moving the grid; therefore, the ALE scheme would preserve a constant field. For any control volume in the fluid domain, the GCL is stated as follows:

$$\frac{\partial v}{\partial t} - \int_s \mathbf{v}_\mathrm{m,face} \cdot \mathbf{n}\, \mathrm{d}A = 0\,, \tag{4.9}$$

where v and s stand for the volume and the boundary surface of the element, respectively, and $\mathbf{n}$ is the normal vector pointing outward. The time rate of change of volume of a element is equal to the sum of volumes swept by its faces. Then, the domain velocity is evaluated at each face $\mathbf{v}_\mathrm{m,face}$ based on the volume swept by that

face. With a second-order backward discretization, it reads:

$$\mathbf{v}_{\mathrm{m,face}}^{n+1} = \frac{3}{2}\left(\frac{\delta v}{A\,\Delta t}\mathbf{n}\right)^{n+1} - \frac{1}{2}\left(\frac{\delta v}{A\,\Delta t}\mathbf{n}\right)^{n}, \tag{4.10}$$

where A is the surface area, Δt is the time step, and δv is the volume swept by the face at one time step. A more detailed description of the evaluation of the domain velocity field and the satisfaction of the GCL can be found in [17].

On the other hand, the contact between the valve and the valve seat creates a change of topology in the mesh, which is challenging to tackle with the moving mesh method. This change in the mesh topology is handled using an immersed boundary method to avoid an expensive remeshing process.

The contact between the valve plate and the valve seat creates a change of topology in the fluid domain, i.e., when the valve is open, the pressure and discharge chambers are connected. However, as the valve closes, the flow passage is shut, and the chambers are disconnected. A possible contact between the valve and the outer wall or catcher also creates a similar change in the mesh topology. The moving mesh technique presented previously cannot adapt the mesh to the new topology. One approach to tackle this issue would be to remesh the fluid domain after the contact. However, this entails a tremendous computational effort. Moreover, retaining the quality of the mesh at every automatic remeshing remains a challenge. Alternatively, IBM places elements that behave as ordinary fluid cells at the flow passage when the valve is open and as *disregarded cells* when the valve closes and the flow passage is shut. These elements move with the valve plate and change state (from a fluid cell to a disregarded cell) when the valve plate meets the seat, and there is no fluid flow. The term *disregarded cells* is used because, at that state, no equation (neither fluid nor solid) is solved on these cells, and they are simply disregarded. This change in the nature of the elements is achieved using an immersed boundary method, as formulated and implemented by Favre et al. [18]. An example is represented in Figure 4.2. It shows the fluid mesh (in blue), as well as the disregarded mesh nodes (in pink) representing the valve seat and the outer wall, in two different situations: static valve position (left image) and during the opening process (right image).

4.2.3 Plate model

In this section, the governing equations describing the dynamic movement of the structure are presented. Moreover, the strategy employed to characterize the contact between the valve and the seat, i.e., the penalty method, is presented.

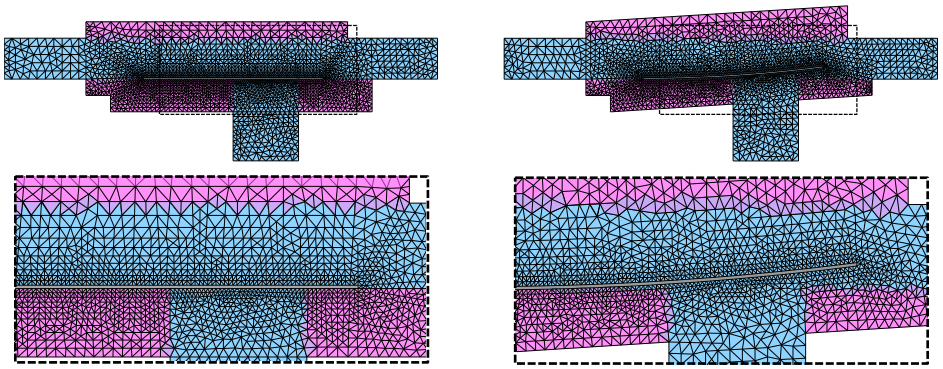

Figure 4.2: Fluid elements are shown in blue and immersed boundary elements (used as fluid cells or disregarded cells depending on the topology) are depicted in pink. A close view of the mesh near the valve and orifice when the valve is completely closed (bottom left) and a close view of the mesh near the valve and orifice when the valve is open (bottom right).

Kirchhoff-Love plate theory

The reed valve is considered as an arbitrarily shaped plate with uniform thickness in a Cartesian coordinate system $(X,\, Y,\, Z)$ where X and Y are the coordinates on its mid-surface, and Z is the coordinate in the thickness direction. Such structure is modeled by the isotropic Kirchhoff-Love plate theory [19], which is suitable for thin plates subjected to transverse loads $f_z\,(X,\, Y,\, t)$ and small strains and rotations. After applying the kinematics assumptions, the problem becomes two-dimensional in $(X,\, Y)$:

$$\frac{E\,h^3}{12\,(1-\nu^2)}\nabla^4\mathbf{u} + 2\,\rho_s\,h\,\frac{\partial^2\,\mathbf{u}}{\partial\,t^2} = f_z\,, \tag{4.11}$$

where $\mathbf{u} = [0, 0, u_z]^T$ and $u_z = u_z(X, Y, t)$ is the normal displacement of the middle surface of the plate, E is the Young modulus, h the plate thickness, ν the Poisson ratio, and ρ_s is the density of the solid. In order to reduce the computational cost of a direct time integration, the mode superposition method for linear analysis is followed. Thus, the motion of a vibration system can be approximated by a combination of a limited number N_q of its free vibration modes [20]:

$$u_z\,(X,\, Y,\, t) \approx \sum_{i=1}^{i=N_q} q_i(t)\,\phi_i\,(X,\, Y)\,, \tag{4.12}$$

where $\phi_i(X, Y, t)$ and q_i are the normal deformation pattern and the generalized coordinate corresponding to the vibration mode i, respectively. Mode shapes $\phi_i(X, Y)$ and natural frequencies ω_i have to be obtained beforehand by solving the eigenvalue problem of the free vibration equation of the system. Imposing the mode superposition to Equation (4.11) and considering their orthogonality ($\int_s \phi_i \phi_j \, \mathrm{d}s = 0$ if $i \neq j$, where s is the middle surface of the plate) transforms the original continuum equation into a set of N_q independent equations, one for each mode, written in terms of the generalized coordinates q_i [21]:

$$\frac{\partial^2 q_i(t)}{\partial t^2} + \omega_i^2 \, q_i(t) = \frac{\int_s \phi_i(X, Y) \, f_z(X, Y, t) \, \mathrm{d}s}{\rho_\mathrm{s} \, h \int_s \phi_i^2(X, Y) \, \mathrm{d}s} \,. \tag{4.13}$$

In order to use the plate model described above, a modal analysis needs to be carried out beforehand to determine the mode shapes $\phi_i(X, Y)$ and the natural frequencies ω_i of the free vibrating reed valve. Depending on the characteristics of the valve, and the required precision of the results, the number of normal modes employed for the discretization of the plate equation can be different. Three different sources of transverse load are considered in the reed system: fluid stress (pressure and shear) $\mathbf{t}_\mathrm{f} = \boldsymbol{\sigma}_\mathrm{f} \, \mathbf{n}$, gravitational acceleration $\mathbf{g}$ and the impact force due to the contact with the seat, $\mathbf{F}_\mathrm{imp}$. Any other force, such as reed pre-tension or stiction force, is neglected. The numerical resolution of the system of N_q equations (Eq. (4.13)) is conducted by integration over both the upper and lower surfaces of the valve plate. Once the load f_z on the face elements of the structure is known, the midpoint rule is used to approximate the right-hand side of Eq. (4.13), and a trapezoidal rule is used for time discretization.

Impact penalty method

The impact force $\mathbf{F}_\mathrm{imp}(X, Y, t)$ is generated by the contact between the valve plate and the rigid seat. The contact is considered to be frictionless and completely perpendicular (i.e., only producing impact force normal to the plate). Therefore, the impact force becomes $\mathbf{F}_\mathrm{imp}(X, Y, t) = [0, 0, f_\mathrm{imp}(X, Y, t)]^T$. A penalty method is used in this work to evaluate the impact force of the contact [22]. When an element on the valve (denoted by i) penetrates the seat, a local impact force proportional to this penetration δ_i is recalled:

$$(f_\mathrm{imp})_i = \begin{cases} \kappa_i \delta_i & \text{if } \delta_i > 0 \,, \\ 0 & \text{if } \delta_i \leqslant 0 \,, \end{cases} \tag{4.14}$$

where κ_i is the penalty stiffness. A higher stiffness increases the accuracy of the model by reducing the limit of allowed penetration (which should be zero in an exact

solution); however, it also creates more numerical instability. The penalty stiffness at every element is determined according to the recommendations at [23]:

$$\kappa_i = \beta \frac{K A_i}{h}\,, \tag{4.15}$$

where $K = E/(3\,(1-2\,\nu))$ is the plate bulk modulus, A_i is the area of the surface of the element, and β is a scale factor set to 1 due to the small time steps used. Similar to the fluid stress force, the impact force is evaluated implicitly in the equilibrium equation on the fluid-structure interface (strong coupling), as explained more thoroughly in the next section.

4.2.4 Fluid-solid coupling algorithm

The interaction of the fluid and structural domains on the common interface Γ is governed by the kinematic and dynamic equilibrium on the interface. For a no-slip type interface:

$$\mathbf{v}_{\mathrm{f},\Gamma} = \frac{\partial\, \mathbf{u}_{\mathrm{s},\Gamma}}{\partial\, t}\,, \tag{4.16}$$

$$\mathbf{t}_{\mathrm{f}} = \sigma_{\mathrm{s}}\, \mathbf{n}_{\Gamma} = \sigma_{\mathrm{f}}\, \mathbf{n}_{\Gamma}\,, \tag{4.17}$$

for any $\boldsymbol{x} \in \Gamma$, where $\mathbf{n}_{\Gamma}$ is the unit normal vector on the interface $\mathbf{n}_{\Gamma}$. σ_{s} and σ_{f} are the stresses tensors of the solid and the fluid, respectively, while $\mathbf{u}_{\mathrm{s},\Gamma}$ indicates the position of the solid boundary and $\mathbf{v}_{\mathrm{f},\Gamma}$ is the velocity of the fluid at the interface. Eq. (4.16) represents kinematic equilibrium, i.e., equal velocities for the fluid and the structure on the common interface, while Eq. (4.17) represents dynamic equilibrium, i.e., the equality of the traction on the interface.

A Dirichlet-Neumann (DN) domain decomposition method is used to solve the coupled FSI problem. In the DN decomposition, the kinematic equilibrium condition (Eq. (4.16)) is used as a Dirichlet boundary condition for fluid flow. Therefore, the fluid equations are solved for a known interface location. The structural equations, on the other hand, are subject to a Neumann boundary condition derived from the dynamic equilibrium condition (Eq. (4.17)). Therefore, the solid equations are solved for a known traction on the interface.

A semi-implicit FSI coupling method, similar to the ones proposed in [8,17] is used. The principal idea is segregating the fluid pressure term and coupling it strongly to the structure via coupling iterations. The remaining fluid terms are loosely coupled to the structure to reduce computational time. By using a projection method to solve the fluid equations, the fluid pressure term (Eq. (4.5)) is effectively segregated. Therefore, only the Poisson equation for pressure in the discretized fluid equations (Eq. (4.5)) is strongly coupled to the structure. The remaining fluid equations (Eq. (4.4) and (4.6)) are solved only once per time step. The impact force generated by the contact between

the valve plate and the seat is treated implicitly and included in the strong coupling iterations together with the fluid pressure term. A Newton-Krylov method with approximated Jacobian [8] is used to carry out the coupling iterations. A more detailed description of the numerical methods used for FSI coupling can be found in [8, 17, 24].

4.2.5 Numerical result validated with the experiment

In this section, the test case presented in [1, 2] for the validation of the numerical methods is illustrated. The problem is considered to its fullest extent, taking into account the strong coupling between the fluid flow and the structure, the flow turbulence, and the impact and rebound of the valve. Simulation results are validated by comparing against experimental data obtained on a test campaign and presented in detail by Tofique et al. [2]. In particular, the simulation of one entire cycle of a reed-valve subject to a pulsating inlet flow is reproduced, as described in the following.

Set-up and Boundary Conditions

In this test case, the evolution of the flow and the movement of the valve during an entire valve stress cycle is simulated, which lasts 10 ms (air flow pulse of 100 Hz). The reed valve analyzed in this test has a diameter $d = 10.6\,\text{mm}$ and thickness $h = 0.2\,\text{mm}$. The reed valve was manufactured from a high-strength stainless steel grade called Flap-X [2]. The valve shape is represented in Figure 4.1. The flow imposed at the entry of the domain mimics the air pulse of the experimental set-up. It grows rapidly, remains constant for a certain period, and then gradually decreases to 0 at $t = 4\,\text{ms}$ from the beginning. The inlet flow rate evolution along a working cycle, imposed as a boundary condition in the CFD simulation, is reported in Figure 4.3. In the resolution of incompressible Navier-Stokes equations, the compressed air is characterized by $\rho_a = 8.5\,\text{kg/m}^3$ and $\mu_a = 18.3 \times 10^{-6}\,\text{Pa}\cdot\text{s}$. The maximum Reynolds number resulting from the variable inlet flow is evaluated as $\text{Re} = \rho_a v_a D/\mu_a \simeq 170000$, where v_a is the maximum air velocity extracted from Figure 4.3[1]. The assembly consists of a feeding tube of diameter $D = 8.5\,\text{mm}$, with the reed valve placed on its top and the surrounding domain employed for the gas expansion. The physical properties of the flexible valve are set to be: $\rho_s = 7700\ \text{kg/m}^3$, $\nu = 0.28$ and $E = 2.20264 \times 10^{11}\,\text{Pa}$.

The domain is represented schematically in the top image of Figure 4.4, showing an inlet port where a variable inlet flow rate is imposed and lateral outlets where pressure-based conditions are set to mimic the flow discharge. The boundary in front of the valve in the discharge chamber (marked by SMB in the figure) is also a pressure-based outlet boundary, with the difference that it is allowed to move. The movement

[1] $v_a = \dfrac{Q}{\pi D^2/4}$, where $Q = 145\,\text{l/min}$, then $v_a = 42.6\,\text{m/s}$.

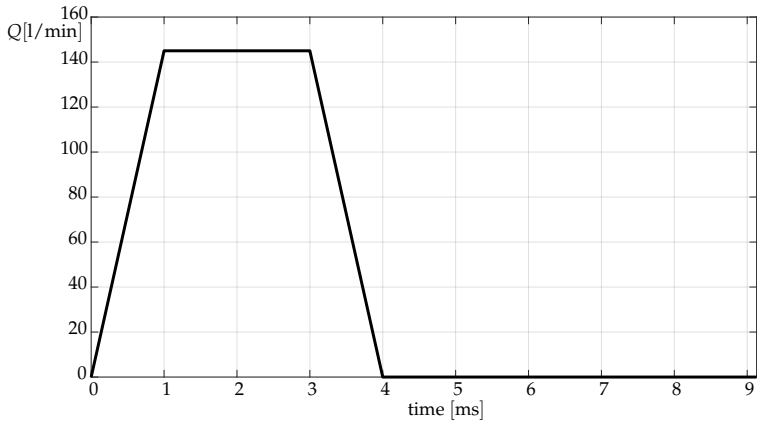

Figure 4.3: Profile of the inlet flow employed to represent the pulsating air flow inlet condition.

of this boundary helps to absorb morphological changes of the mesh during the valve opening and closing process, as mentioned in Section 4.2.2. The remaining walls are fixed solid wall boundaries. The indicated immersed boundary regions are employed to represent the solid region of the valve seat, as explained in Section 4.2.2. The base mesh is an unstructured tetrahedral mesh composed of around 300 thousand cells and represented in the bottom image of Figure 4.4. In order to use the plate model described in Section 4.2.3, a modal analysis needs to be carried out beforehand to determine the mode shapes $\phi_i(X, Y)$ and the natural radial frequencies ω_i of the free vibrating reed valve. The modal analysis has been carried out with a commercial structural software [25] using a clamped boundary condition at the valve root. Only the first four modes have been considered for this study, as the addition of further modes was not affecting the behaviour of the moving valve.

Large-eddy simulations are carried out: a subgrid-scale model is applied to represent the smallest scales, while only the larger eddies are explicitly solved. The chosen SGS scheme is the Wall-Adapting Local Eddy-viscosity (WALE) model. The time step is determined using a Courant-Friedrichs-Lewy condition.

Comparison to experimental results

In Figure 4.5, some instantaneous pictures of the valve cycle are depicted. The figure highlights the velocity field and the topology changes that the fluid domain undergoes to adapt to the opening/closing valve. Following the inlet flow profile reported in Figure 4.3, the inlet air flow increases to $t = 1$ ms and remains constant for approximately 2 ms. The valve opens progressively after the inlet air pulse,

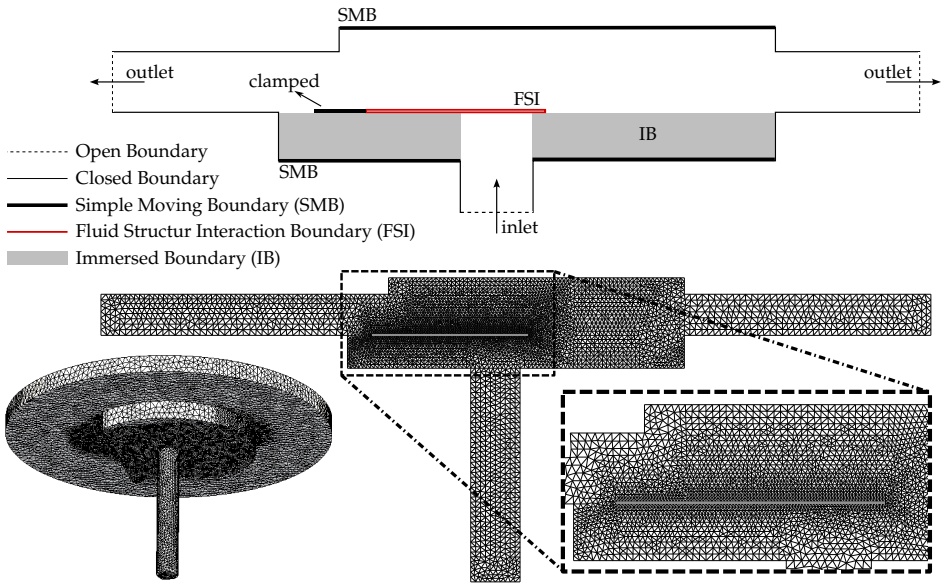

Figure 4.4: Geometry and mesh employed for the validation test of the reed valve movement and impact: Schematic domain (top) and detailed representation of the 3D unstructured mesh (bottom).

reaching its maximum displacement at $t \simeq 1.9\,\text{ms}$. Next, it employs the same time to close completely, with a slight delay compared to the end of the airflow pulse. The valve closes entirely and impacts the seat at $t = 4.5\,\text{ms}$. Hence, the valve opens and closes twice during the rest of the cycle, rebounding two times against the base. The maximum opening after the first impact occurs at $t = 5.4\,\text{ms}$.

As shown in the left image of Figure 4.6, valve displacement is slightly over-predicted in the ascent phase and down-predicted after the rebounds. However, the results show a good agreement between numerical and experimental data for valve displacement and velocity. This is especially true when considering that the experimental signal is a "typical" one, as inevitable variability is visible between successive cycles. In the same figure, tolerance bars highlight the variability in the maximum displacement between different cycles and the rebounds successive to the first opening. The experimental campaign can be found in more detail in [2].

Further differences between numerical and experimental results can be seen in the descent phase after the first opening. The numerical curve shows a deflection, probably because the incompressible gas in the inlet duct is an obstacle during the valve closure. Another difference can be noticed from the reed velocity curve,

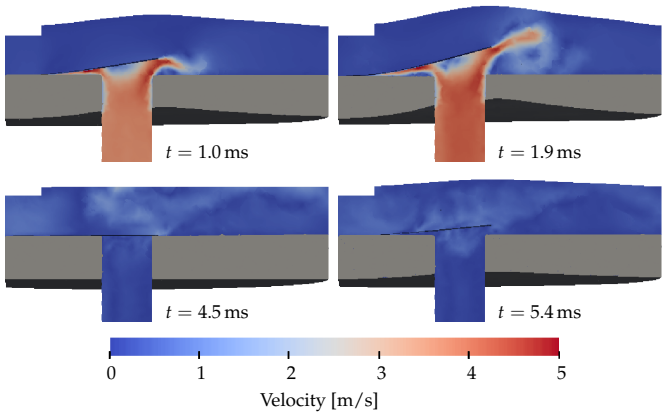

Figure 4.5: Velocity magnitude map in different phases of the reed valve cycle.

reported in the right image of Figure 4.6, at the point of the first impact: in the experimental signal, a certain plateau can be noticed, probably due to the flexion of the valve when it comes in contact with the base, while in the simulation the contact is practically "instantaneous" (sudden velocity increase), due to the formulation of the impact process using the penalty method. Velocity peaks are well predicted, both in ascending and descending phases.

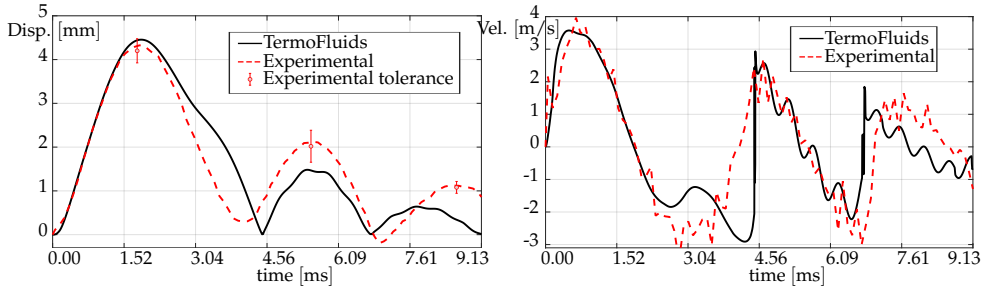

Figure 4.6: Reed valve movement and impact, comparison to experimental data reported in [2]: valve displacement (left) and valve velocity (right). The tolerance reported in the left image refers to variability within cycles in the experimental analysis.

4.3 Reed valve simulation using the FEM

This section shows some of the results already published in [1] and [2] using a three-dimensional model in FreeFEM for the valve. As explained in [1], the pressure applied by the fluid on the valve obtained with the simulation carried out in TermoFluids is used as an input parameter. Therefore, those external pressure are used to obtain the valve displacement again (for verification purposes) and to obtain additional insight regarding internal stresses. Additionally, a different impact model is introduced in the FreeFEM code to improve the evaluation of impact forces on the valve surface. For this scope, the work of Armero et al. [26] is implemented, which has slight differences with the impact method used in TermoFluids; see Section 4.2.3. For the time discretization, the HHT-α method is used, where the parameters of the generalized algorithm are displayed in Table 3.9.

Figure 4.7 describes the zone of the valve surface on which the contact pressure can be applied. In the formulation presented in [26] the function g called *gap* is defined as:

$$g = u_z - 0 = u_z \,, \tag{4.18}$$

where it is taken into account that the coordinate Z is equal to 0 at the base of the valve (Eq. (4.18) is particular for this case, the general equation can be found in [26]).

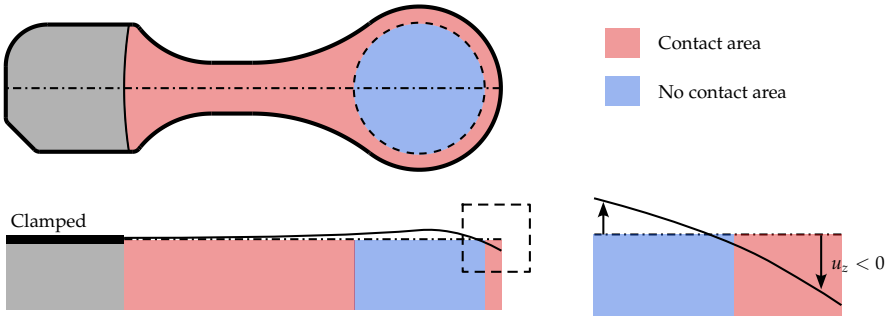

Figure 4.7: Contact zone used to obtain the impact pressure with the formulation presented in Armero et al. [26].

The formulation presented in [26] is applied on the surface $Z = 0$ of the valve and for the points that belong to the contact zone; see Figure 4.7. Then, the impact pressure p_{imp} on point $\boldsymbol{X}_\text{p} = (X_p, Y_p, 0)$ at time t_{n+1} is obtained with Algorithm 1.

The first condition in the Algorithm 1, $\left(\text{cont}^n(\boldsymbol{X}_\text{p}) == 1 \text{ or } g^{n+1}(\boldsymbol{X}_\text{p}) \leq 0\right)$, checks if there was contact at the last instant t_n or/and if there is contact at the current instant t_{n+1}, which means that the previous instant is taken into account to calculate

Algorithm 1 Impact pressure - ref Armero et al. [26]

Require: Displacements u_z^n and u_z^{n+1}, *dynamic gap* g_d^n, impact parameters k_imp and ϑ_imp, and contact function cont^n.

$g^{n+1} = u_z^{n+1}$

if $\left(\mathrm{cont}^n == 1 \text{ or } g^{n+1} \leq 0\right)$ **then**

$g_\mathrm{d}^{n+1} = g_\mathrm{d}^n + u_z^{n+1} - u_z^n$ ▷ Compute the *dynamic gap*

if $g_\mathrm{d}^{n+1} \leq 0$ **then**
$\mathrm{cont}^{n+1} = 1$
else
$\mathrm{cont}^{n+1} = 0$
end if

if $\left(g_\mathrm{d}^n \leq 0 \text{ and } g_\mathrm{d}^{n+1} \leq 0\right)$ **then** ▷ Persistent contact
$p_\mathrm{imp} = -k_\mathrm{imp}\left(\vartheta\, g_\mathrm{d}^{n+1} + (1-\vartheta)\, g_\mathrm{d}^n\right)$
else ▷ Initial contact and release
$U^n = \dfrac{k_\mathrm{imp}}{2}\dfrac{\left(g_\mathrm{d}^n - \left|g_\mathrm{d}^n\right|\right)^2}{4}$
$U^{n+1} = \dfrac{k_\mathrm{imp}}{2}\dfrac{\left(g_\mathrm{d}^{n+1} - \left|g_\mathrm{d}^{n+1}\right|\right)^2}{4}$
$p_\mathrm{imp} = -\left(\dfrac{U^{n+1} - U^n}{g_\mathrm{d}^{n+1} - g_\mathrm{d}^n}\right)$
end if

else

$\mathrm{cont}^{n+1} = 0$
$g_\mathrm{d}^{n+1} = g_\mathrm{d}^n$

end if

the current impact. This is the biggest difference with the penalty method used in TermoFluids, in which only the current instant is considered. It must be considered that before the first contact, the *dynamic gap* and the contact function are zero. The

contact parameter k_{imp} is determined for the problem, and, as in [1], different values of k_{imp} were considered. The parameter ϑ_{imp} is set equal to 1. The impact force $\mathbf{F}_{\text{imp}}$ is obtained as:

$$\mathbf{F}_{\text{imp}} = \int_{A_{\text{imp}}} p_{\text{imp}} \, \mathrm{d}A \, \mathbf{e}_z \, . \tag{4.19}$$

and is applied in FreeFEM with the corresponding variational formulation.

4.3.1 Spatial convergence test

To observe the spatial convergence, different meshes have been tested using FreeFEM with quadratic interpolation (p_2). The mesh refinement has been done in two ways: in the plane (left image of Figure 4.8) and in thickness (right image of Figure 4.8, where k_{tk} represents the number of refinement lines in that direction).

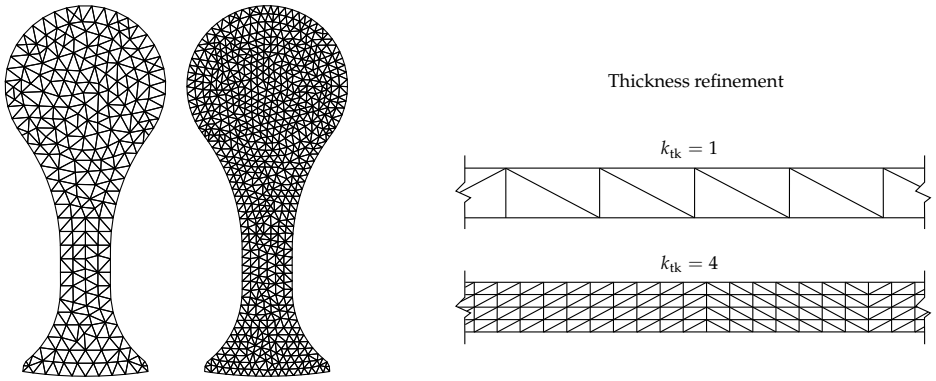

Figure 4.8: Mesh refinement has been done in two ways: in the plane (left image) and in thickness (right image, where k_{tk} represents the amount of refinement lines in that direction).

Figure 4.9 shows the displacement obtained at the point located on the laser. It is possible to observe that spatial convergence is achieved by refining the mesh in both directions. The relative error between the finest and coarse mesh using $k_{\text{kt}} = 1$, where the number of tetrahedrons is increased by 4872, is 0.52 %, while when comparing the finer meshes using $k_{\text{kt}} = 1$ and $k_{\text{kt}} = 4$, where the number of tetrahedrons is increased by 21015, the relative error is 0.08 %. Due to the above, and in order to reduce the computational cost, it is decided to use the finest mesh for $k_{\text{kt}} = 1$.

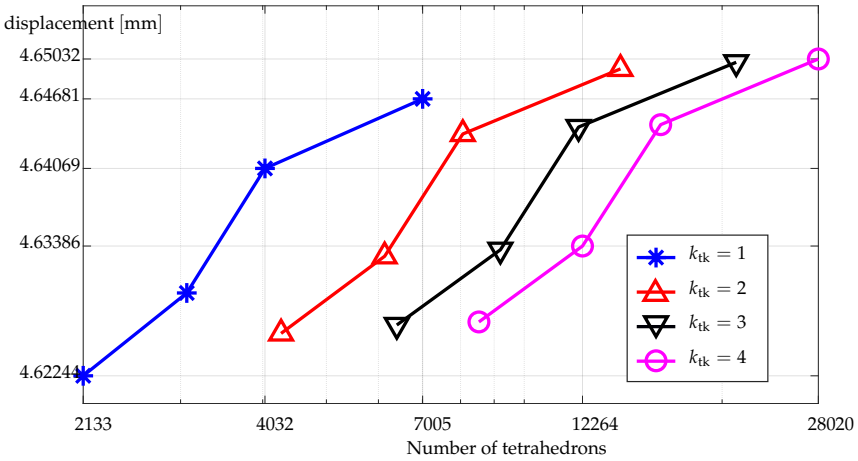

Figure 4.9: Convergence for different meshes of the displacement at the experimental measurement position.

4.3.2 Calibration of the contact parameter k_{imp}

In Figure 4.10, the displacement and velocity obtained for different values of k_{imp} are compared with those obtained with the TermoFluids software at the point where the laser makes the experimental measurements. It is observed that the best approximation, for the values of k_{imp} used, is for $k_{imp} = 5000\,\text{kPa/mm}$.

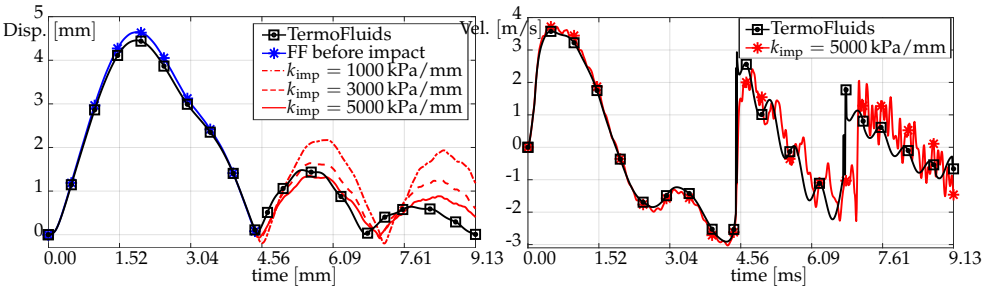

Figure 4.10: Reed valve movement using FreeFEM: valve displacement (left) and valve velocity (right). Comparison using different values of k_{imp} to the solution obtained with TermoFluids.

Once completed the calibration of the numerical parameter, the model was employed to obtain detailed insights regarding impact forces on valve surfaces and its internal stresses. The results are reported in the next section, where impact forces and pressure are analyzed and compared with that obtained with the high-order method

presented in this thesis.

4.4 Reed valve simulation using the 3D high order finite volume method

In this section, the FVM high-order method presented in this thesis is used to obtain comparable results to those presented in the previous section. The mesh and the time discretization used are the same as those presented in Section 4.3. In this case the contact force is approximated using $N_{\text{imp}} = 19$ Gauss points as:

$$\mathbf{F}_{\text{imp}}(\boldsymbol{X}_p) = \int_{A_{\text{imp}}} p_{\text{imp}}\, \mathbf{e}_z \, \mathrm{d}A \approx \sum_{p=1}^{p=N_{\text{imp}}} \alpha_p \, p_{\text{imp}}(\boldsymbol{X}_p)\, \mathbf{e}_z \,, \tag{4.20}$$

where α_p and $\boldsymbol{X}_p$ are the quadrature weights and the coordinates of the p-th Gauss point, respectively. The force $\mathbf{F}_{\text{imp}}$ is imposed as a Neumann condition. For the high-order method, a cubic interpolation with the LRE method is used.

4.4.1 Stiffness matrix derived from the impact force

As mentioned at the end of Section 2.5 to solve the nonlinear contact problem, the matrix $\mathbf{K}_{\text{c}}$ derived from the impact force may or may not be included. This matrix is obtained for each contact point as follows:

$$\mathbf{K}_{\text{c}} = \frac{\partial \mathbf{F}_{\text{c}}}{\partial\, \delta\Delta\, \ddot{\mathbf{u}}} \,, \tag{4.21}$$

therefore it is necessary to obtain the derivative of $p_{\text{imp}}(\boldsymbol{X}_p)\, \mathbf{e}_z$ respect to $\delta\Delta\, \ddot{\mathbf{u}}$[2]. From what has been mentioned above, it is clear that the matrix $\mathbf{K}_{\text{c}}$ is a diagonal matrix whose entries are all null except for the degrees of freedom associated with direction $\mathbf{e}_z$ in the nodes that are in contact. Those non-zero values are obtained as:

$$K_{\text{c}} = \frac{\beta_{\text{M},0}\, \Delta t^2}{6} \int_{A_{\text{imp}}} k_{\text{c}} \, \mathrm{d}A \approx \frac{\beta_{\text{M},0}\, \Delta t^2}{6} \sum_{p=1}^{p=N_{\text{imp}}} \alpha_p \, k_{\text{c}}(\boldsymbol{X}_p) \,, \tag{4.22}$$

where k_{c} is obtained by modifying Algorithm 1 with the statements indicated in Algorithm 2, which must be performed for each gauss point $\boldsymbol{X}_p$.

[2]The impact area A_{imp} does not change in time since the seat, where the valve hits, does not move.

Algorithm 2 Impact pressure and contact matrix - ref Armero et al. [26]

Require: Displacements $u_z^n(\boldsymbol{X}_\mathrm{p})$ and $u_z^{n+1}(\boldsymbol{X}_\mathrm{p})$, *dynamic gap* $g_\mathrm{d}^n(\boldsymbol{X}_\mathrm{p})$, impact parameters k_imp and ϑ_imp, and contact function $\mathrm{cont}^n(\boldsymbol{X}_\mathrm{p})$.

$g^{n+1}(\boldsymbol{X}_\mathrm{p}) = u_z^{n+1}(\boldsymbol{X}_\mathrm{p})$

if $\left(\,\mathrm{cont}^n(\boldsymbol{X}_\mathrm{p}) == 1 \text{ or } g^{n+1}(\boldsymbol{X}_\mathrm{p}) \leq 0\,\right)$ **then**

$g_\mathrm{d}^{n+1}(\boldsymbol{X}_\mathrm{p}) = g_\mathrm{d}^n(\boldsymbol{X}_\mathrm{p}) + u_z^{n+1}(\boldsymbol{X}_\mathrm{p}) - u_z^n(\boldsymbol{X}_\mathrm{p})$ ▷ Compute the *dynamic gap*

if $g_\mathrm{d}^{n+1}(\boldsymbol{X}_\mathrm{p}) \leq 0$ **then**, $\mathrm{cont}^{n+1}(\boldsymbol{X}_\mathrm{p}) = 1$, **else**, $\mathrm{cont}^{n+1}(\boldsymbol{X}_\mathrm{p}) = 0$, **end**

if $\left(\, g_\mathrm{d}^n(\boldsymbol{X}_\mathrm{p}) \leq 0 \text{ and } g_\mathrm{d}^{n+1}(\boldsymbol{X}_\mathrm{p}) \leq 0 \,\right)$ **then** ▷ Persistent contact

$p_\mathrm{imp}(\boldsymbol{X}_\mathrm{p}) = -k_\mathrm{imp}\left(\vartheta\, g_\mathrm{d}^{n+1}(\boldsymbol{X}_\mathrm{p}) + (1-\vartheta)\, g_\mathrm{d}^n(\boldsymbol{X}_\mathrm{p})\right)$

$k_\mathrm{c}(\boldsymbol{X}_\mathrm{p}) = k_\mathrm{imp}\,\vartheta$

else ▷ Initial contact and release

$$U^n(\boldsymbol{X}_\mathrm{p}) = \frac{k_\mathrm{imp}}{2}\,\frac{\left(g_\mathrm{d}^n(\boldsymbol{X}_\mathrm{p}) - \left|g_\mathrm{d}^n(\boldsymbol{X}_\mathrm{p})\right|\right)^2}{4}$$

$$U^{n+1}(\boldsymbol{X}_\mathrm{p}) = \frac{k_\mathrm{imp}}{2}\,\frac{\left(g_\mathrm{d}^{n+1}(\boldsymbol{X}_\mathrm{p}) - \left|g_\mathrm{d}^{n+1}(\boldsymbol{X}_\mathrm{p})\right|\right)^2}{4}$$

$$p_\mathrm{imp}(\boldsymbol{X}_\mathrm{p}) = -\left(\frac{U^{n+1}(\boldsymbol{X}_\mathrm{p}) - U^n(\boldsymbol{X}_\mathrm{p})}{g_\mathrm{d}^{n+1}(\boldsymbol{X}_\mathrm{p}) - g_\mathrm{d}^n(\boldsymbol{X}_\mathrm{p})}\right)$$

$$dU^{n+1}(\boldsymbol{X}_\mathrm{p}) = \frac{k_\mathrm{imp}}{2}\,\left(g_\mathrm{d}^{n+1}(\boldsymbol{X}_\mathrm{p}) - \left|g_\mathrm{d}^{n+1}(\boldsymbol{X}_\mathrm{p})\right|\right)$$

$$k_\mathrm{c}(\boldsymbol{X}_\mathrm{p}) = \frac{dU^{n+1}(\boldsymbol{X}_\mathrm{p}) + p_\mathrm{imp}(\boldsymbol{X}_\mathrm{p})}{g_\mathrm{d}^{n+1}(\boldsymbol{X}_\mathrm{p}) - g_\mathrm{d}^n(\boldsymbol{X}_\mathrm{p})}$$

end if

else

$\mathrm{cont}^{n+1}(\boldsymbol{X}_\mathrm{p}) = 0$

$g_\mathrm{d}^{n+1}(\boldsymbol{X}_\mathrm{p}) = g_\mathrm{d}^n(\boldsymbol{X}_\mathrm{p})$

end if

Figure 4.11 shows the number of iterations of the Newton-Raphson method used to solve the problem for $k_{\text{imp}} = 5000\,\text{kPa/mm}$. It is observed that including the contact matrix reduces the number of iterations and, therefore, the computational cost. Likewise, in Figure 4.11, it can be seen that at least two iterations of Newton-Raphson are always used, even at moments where there is theoretically no contact (initial opening of the valve). This is because the entire valve has been considered an impact surface, except the orifice through which the fluid comes (see Figure 4.7), and therefore near where the valve is clamped, whose displacements are very small, a possible contact is numerically detected. However, this contact is not relevant as has been studied in [1]. Although the inclusion of the matrix $\mathbf{K}_c$ reduces the iterations and, therefore, the computational cost, it is worth mentioning that obtaining it requires another computational effort, which in the case study in this thesis is minor. In a more complex case, where, for example, the two surfaces in contact are in motion, the cost of obtaining $\mathbf{K}_c$, theoretically and computationally, may be relevant.

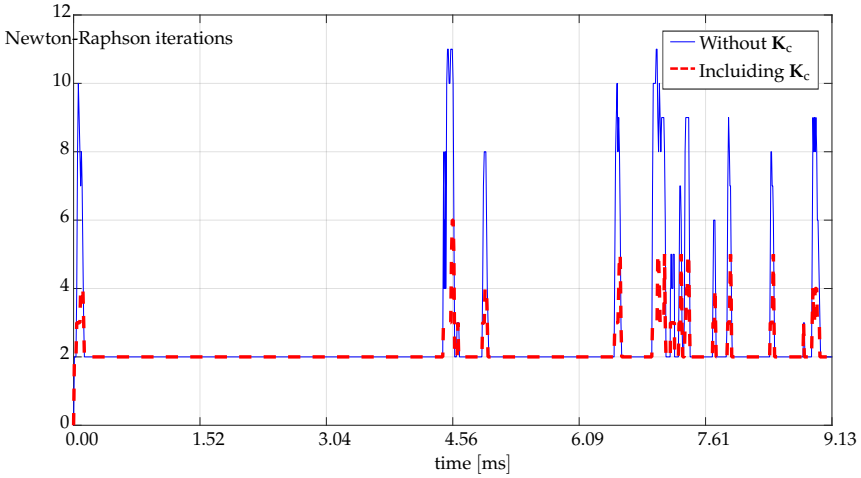

Figure 4.11: Number of iterations of the Newton-Raphson method.

Figure 4.12 illustrates the total impact force $F_{\text{imp}} = \left\|\mathbf{F}_{\text{imp}}\right\|$ and the instants where the two impacts occur. Those impacts are defined when contact is detected near the tip of the valve. It is observed that in the rest of the cycle, the contact force is negligible and occurs close to the clamped zone, which affects the movement of the valve in a lesser way.

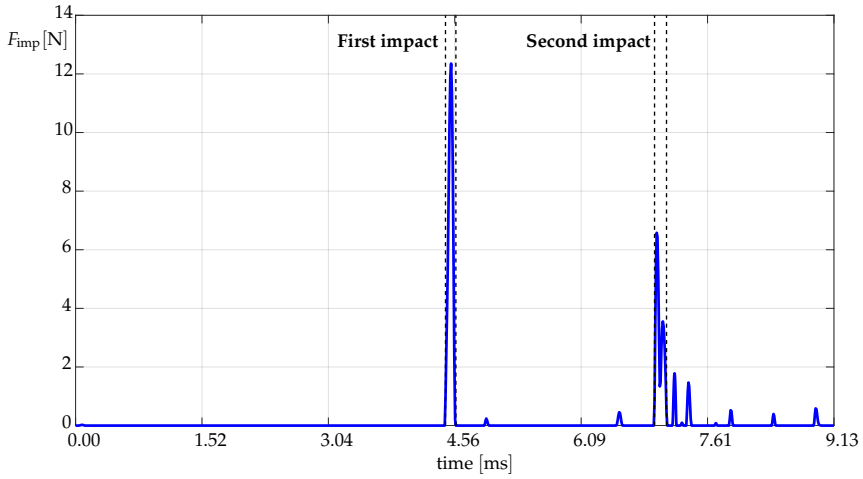

Figure 4.12: Total impact force $F_{\text{imp}} = \|\mathbf{F}_{\text{imp}}\|$.

4.4.2 Comparison between FEM and FVM for different k_{imp}

Figure 4.13 compares, for different values of k_{imp}, the results obtained using FEM with those obtained with the high-order FVM. It is observed that the differences are minimal throughout the valve work cycle. Figure 4.14 shows the comparison between the results obtained with the TermoFluids simulation, the high order method (for $k_{\text{imp}} = 5000\,\text{kPa/mm}$) and the values obtained experimentally. The left image shows the valve displacement, and the right image shows the velocity. It is possible to conclude that, as with TermoFluids, it is possible to capture the velocity peaks. A difference that can be seen with the three-dimensional models of the valve is that the opening of the valve after the second impact occurs a few moments later than in the TermoFluids model. This is explained because in TermoFluids the impacts are practically instantaneous (2-4 instants), while in three-dimensional models, these impacts take several instants, thus prolonging the opening of the valve.

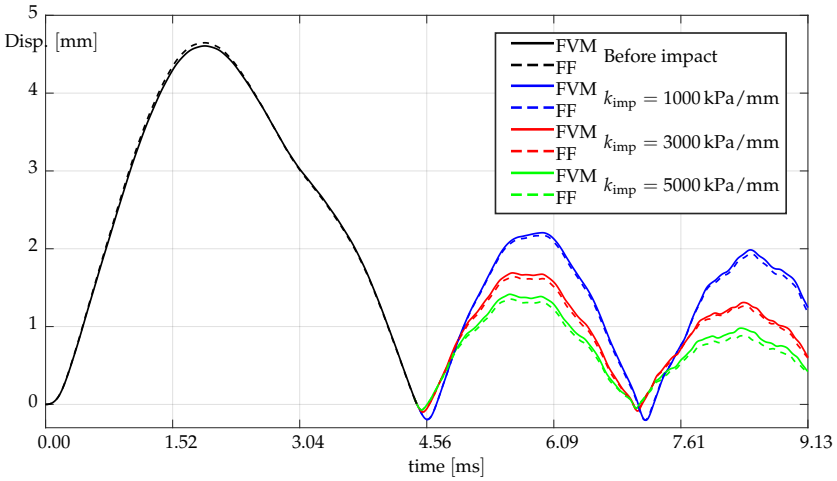

Figure 4.13: Comparison, for different values of k_{imp}, of the results obtained using FEM and the high-order FVM.

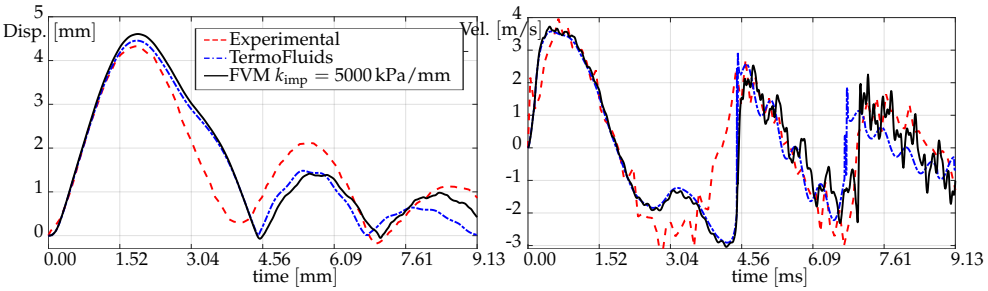

Figure 4.14: Comparison between the results obtained with the TermoFluids simulation, the high order method (for $k_{imp} = 5000\,kPa/mm$), and the values obtained experimentally: valve displacement (left) and valve velocity (right).

Each impact is analyzed in detail in the following section, similar to what was done in [1] and [2].

4.4.3 Detailed results of impact force and impact pressure: comparison to FEM

In this section, the results obtained with the FVM method regarding the impact force and pressure are reported in detail and compared with those obtained previously with FEM.

First impact

The first impact occurs during the time interval $T_{\mathrm{FI}} = [4.44, 4.58]$ ms. Figure 4.15 shows the total impact force and the maximum impact pressure obtained on the valve for the first impact. Both magnitudes grow to a maximum value in this impact and then fall and disappear. It is possible to observe that the solution obtained with both methods are very similar.

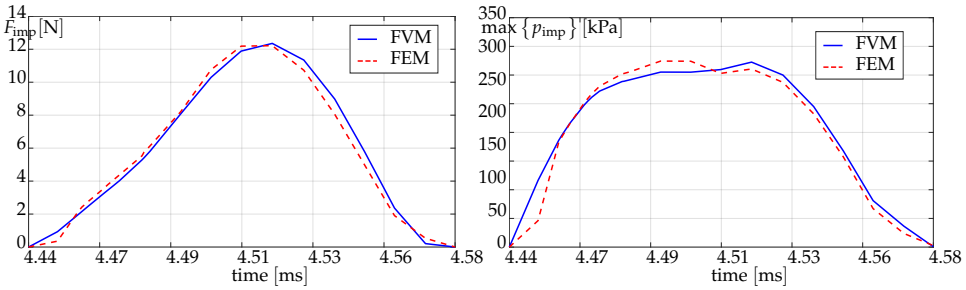

Figure 4.15: First impact: total impact force (left) and maximum impact pressure (right).

Figures 4.16 and 4.17 show the zone that is in contact in the first impact when using FVM or FEM, respectively. It can be seen that there are practically no differences between the methods. The differences that appear in the images in the second row of each figure are negligible pressure differences and, being close to the neck, have little effect on the behavior of the valve.

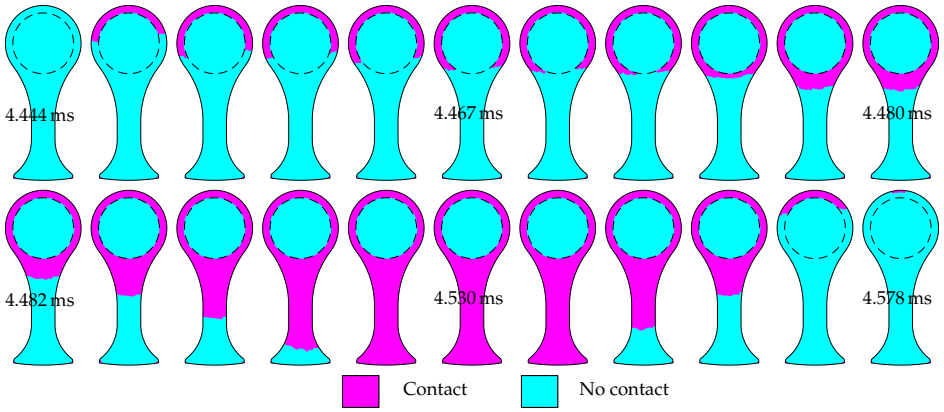

Figure 4.16: Area of the first impact using FVM.

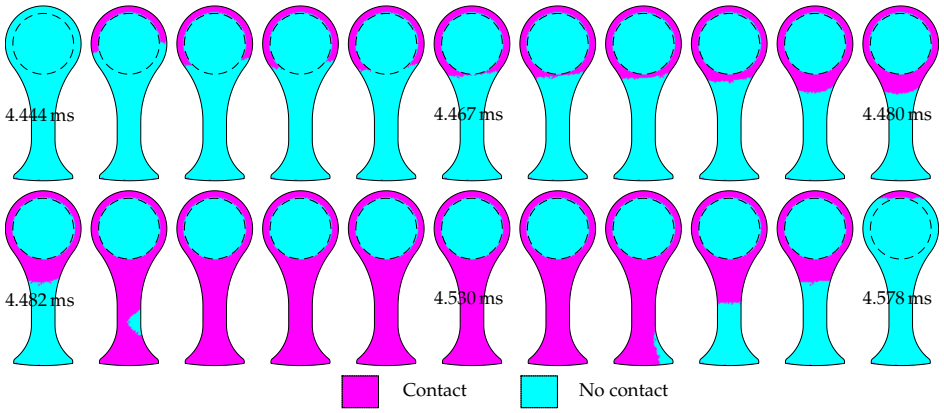

Figure 4.17: Area of the first impact using FEM.

Figures 4.18 and 4.19 show the distribution of the impact pressure on the surface $Z = 0$ for each of the instants of the interval T_{FI} using FVM or FEM, respectively. This impact can be sequenced as: (1) impact begins at the tip of the valve; (2) then the impact pressure is distributed over the valve surface; and (3) finally, the valve is released from the seat. As previously mentioned, the pressure differences near the valve neck in the images of the second row of each figure are negligible.

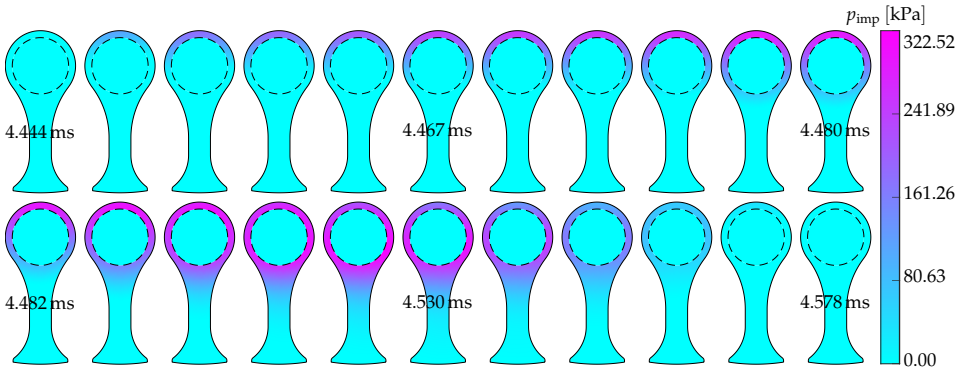

Figure 4.18: Distribution of the impact pressure in the first impact using FVM.

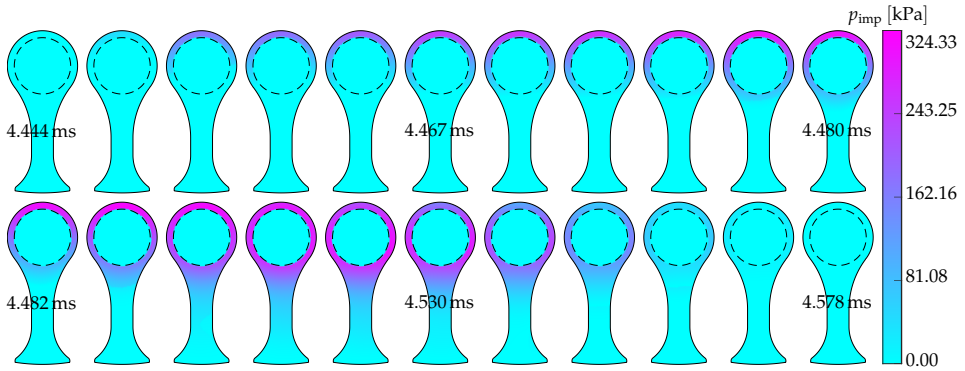

Figure 4.19: Distribution of the impact pressure in the first impact using FEM.

Second impact

For the second impact, some differences between the methods are appreciated. The first difference can be seen in Figure 4.20, where the time interval of the second impact is different for each method. The second impact, when using FEM, starts a few moments earlier with its time interval being $T_{\text{SI, FEM}} = [6.92, 7.13]$, whereas when using FVM, it is $T_{\text{SI, FVM}} = [6.96, 7.12]$. The most significant difference can be seen in the total impact force in the left image of Figure 4.20. It is observed that in the first part of the second impact (up to an instant $t_1 \approx 7.03$ ms), the force obtained with FVM is greater than with FEM, then both the force and the impact pressure are very similar between the two methods. For both methods, the two magnitudes grow to their maximum value and then fall, rise again, and fall until they disappear.

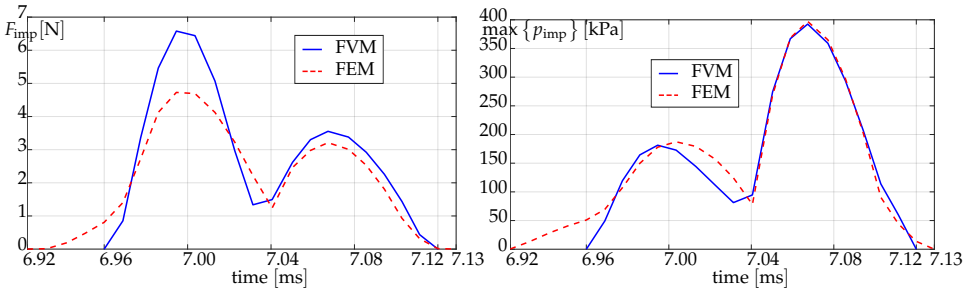

Figure 4.20: Second impact: total impact force (left) and maximum impact pressure (right).

Figure 4.21 shows the first part of the second impact. It is observed that in the case of FVM, the impact begins between the fluid inlet orifice and the neck of the valve,

while in the case of using FEM, the impact begins at the clamped edge and then goes toward the valve. The differences are close to the clamped edge; therefore, it does not create too much distortion between the two solutions in what remains of the process in terms of force and pressure amplitudes, as highlighted in the second part of the impact shown in Figure 4.20.

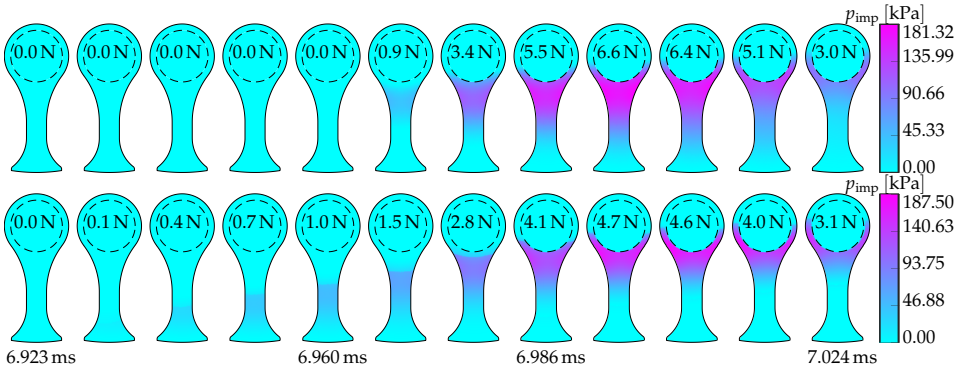

Figure 4.21: Impact pressure and impact force for the first instants of the second impact using FVM (top images) and FEM (bottom images).

These differences can be associated with the different interpolations used in each method (quadratic in FEM and cubic in FVM). One method may identify penetration at a different point than the other at the same instant. The important is that the general behavior of this first period of the second impact is similar because a stress concentration is generated near the fluid orifice for both methods (the growth, fall, and maximum values occur at the same instants for both methods). In general, this difference does not affect the behavior of the valve along its whole cycle, as previously seen in Figure 4.13.

Figures 4.22 and 4.23 show the areas where the second impact occurs when using FVM or FEM, respectively. In these images, the behavior mentioned above is observed. As previously mentioned in the first instants, there are differences in the contact between the methods; see images of the first row of each figure. However, in the second row, the behavior is practically the same, considering that the pressures near the clamped edge in Figure 4.23 do not affect the behavior of the valve.

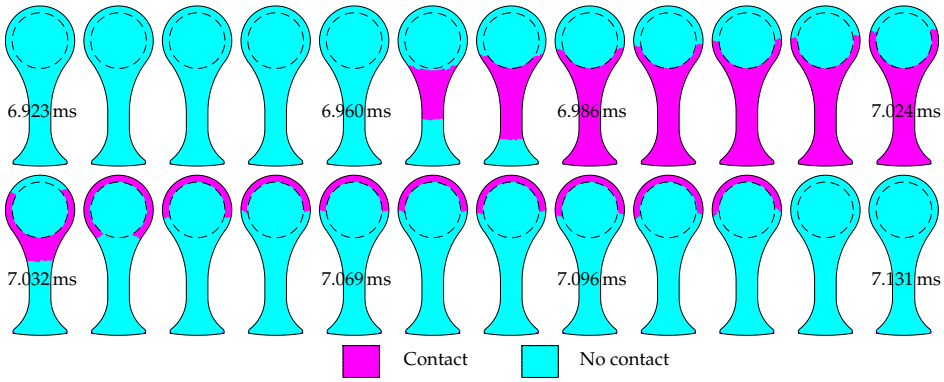

Figure 4.22: Area of the second impact using FVM.

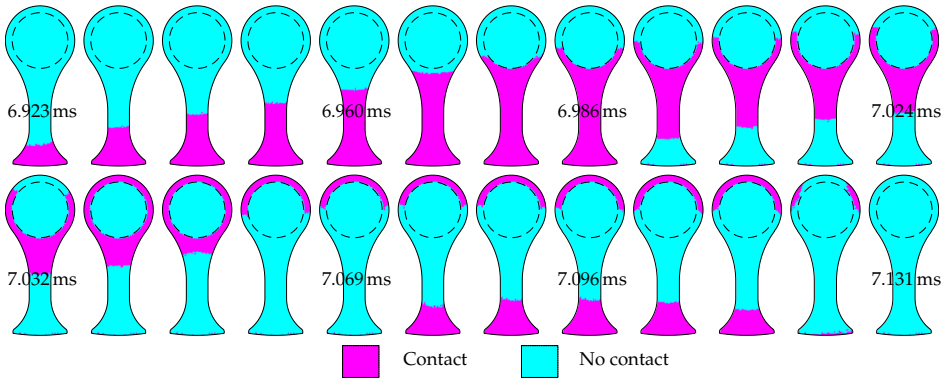

Figure 4.23: Area of the second impact using FEM.

Figures 4.24 and 4.25 show the distribution of the impact pressure on the surface $Z = 0$ for each of the instants of the interval T_{SI} when using FVM or FEM, respectively. This impact can be sequenced as: (1) impact begins between the clamped edge and the inlet fluid orifice spreading towards the tip of the valve; (2) the pressure drops and the impact is again at the tip but on a smaller surface; and (3) finally the valve is released from the seat.

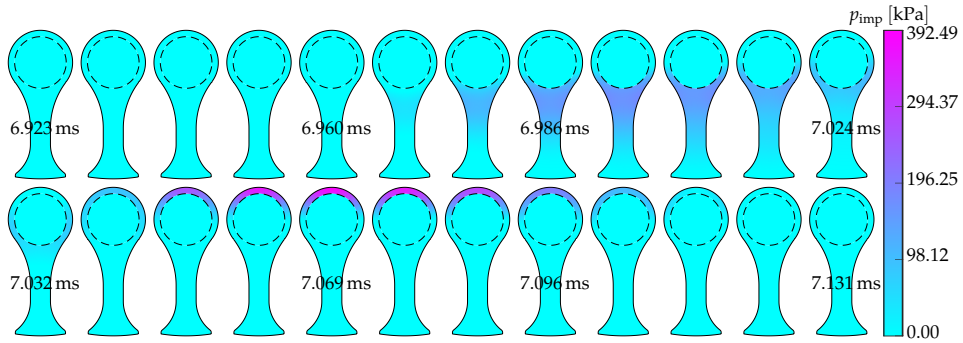

Figure 4.24: Distribution of the impact pressure in the second impact using FVM.

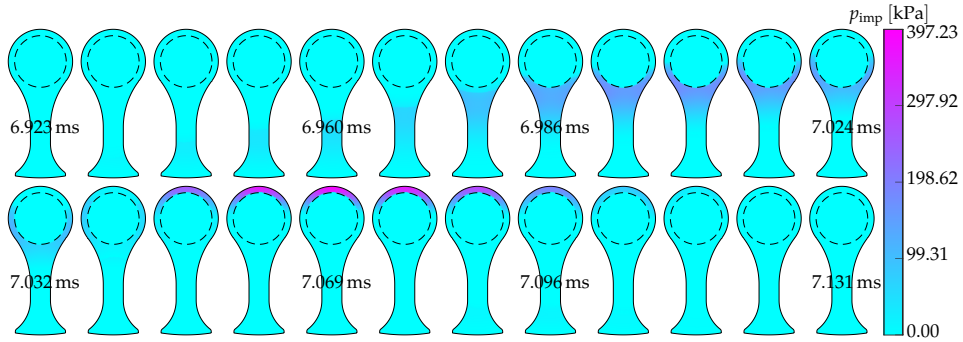

Figure 4.25: Distribution of the impact pressure in the second impact using FEM.

It is worth mentioning that a higher maximum pressure is obtained in the second impact compared to the first one. This is explained because, despite having lower impact forces, the impact area is smaller, leading to overall greater impact pressures.

4.4.4 Impact stresses at critical points

As previously discussed, the impact of the valve on the seat is often the cause of valve failure due to fatigue. Figure 4.26 shows failed reed valves in impact fatigue experiments [2].

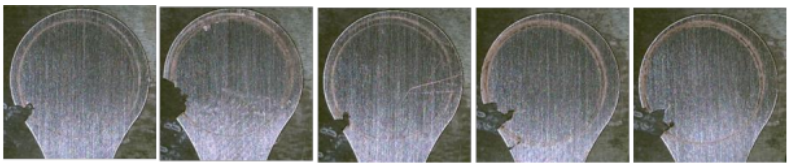

Figure 4.26: Reed valves in impact fatigue experiments.

Some points of the tip of the valve are analyzed to observe the evolution of some stresses. The points to be studied are illustrated in the left image of Figure 4.27. The stresses analyzed are the maximum and minimum principal stress, σ_I and σ_{III}, respectively, and the von Mises stress, commonly used to limit the elastic behavior of ductile materials (especially steels).

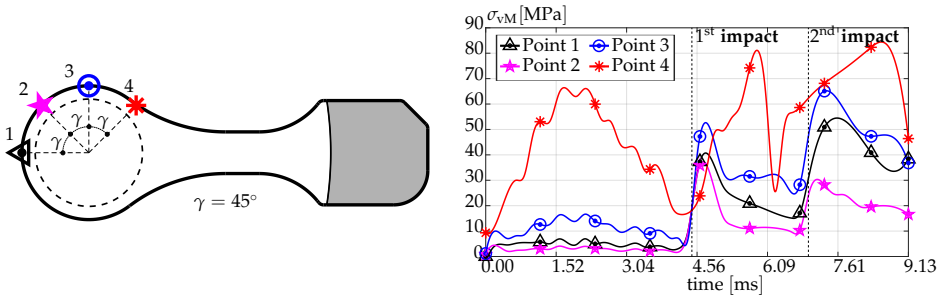

Figure 4.27: Points to observe the evolution of stresses (left) and von Mises stresses (right).

In the right image of Figure 4.27 it is observed that the von Mises stress increases for all points in each impact. In those points that are practically not affected by bending (1,2, and 3), a high increase in tensions is noted. Likewise, point 4, which suffers a little from bending, increases stresses due to the impact. Similar results are obtained in Figure 4.28 for the maximum and minimum principal stresses. Therefore, it is possible to conclude that the numerical simulation shows that the impact generates an important change in the stresses at the points where failures are experimentally observed.

4.4.5 Computational time comparison

A fully exhaustive comparison between the two numerical methods employed in the current chapter for structural analysis (in-house FVM and FreeFEM) would require an analysis of the computational cost required by each of them to perform the proposed simulations. However, a quantitative comparison between them was impossible

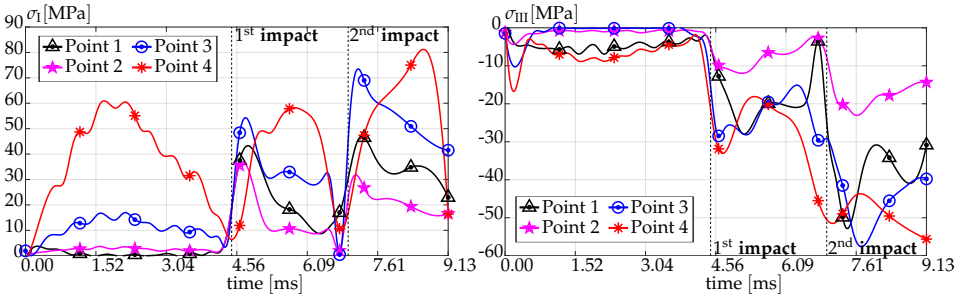

Figure 4.28: Principal stresses: maximum σ_{I} (left) and minimum σ_{III} (right).

due to the inherent differences between the structure of the two codes, which would have made such a comparison unfair. Generally, pre-process calculations, which have significant importance over the global computational cost, especially for static calculations, are much faster with the FreeFEM code, developed in C++ and employed in pre-compiled form. On the other side, the FVM method was developed in MATLAB R2021a to verify and validate the method easier, but needing to be more efficient from a computational point-of-view. The intention of the author is to leave the code optimization for future work by translating it into a high-performance compiled language, thus, allowing the comparison of FVM and FEM not only from the point-of-view of accuracy but also from that of computational efficiency.

4.5 Conclusions

This chapter analyzes the problem of a reed valve subjected to real working conditions using different computational methods. The results highlighted that the high-order FVM method presented in this thesis can be used to analyze in detail real engineering problems, such as the reed valve of a compressor subjected to highly pressurized flow. The validation of the results was possible thanks to experimental data obtained from an industrial collaboration with the Voestalpine company, describing the cycle of a reed valve subjected to a pulsating inlet flow in terms of valve lift and velocity. First, the results obtained using the FSI model developed in the TermoFluids software, already submitted in [3], have been compared with experimental results in terms of lift and velocity. Hence, valve pressures obtained with the FSI model were employed as an input of structural codes (in-house FVM and FreeFEM) to verify their capability of computing the valve dynamics. Again, experimental results were compared with FreeFEM and the method presented in this thesis regarding valve lift and velocity, providing a very good agreement. Next, structural codes have been employed to obtain detailed insights regarding internal stresses. A detailed quantitative analysis

of the time evolution along a valve cycle of forces and pressure distribution associated with the impacts suffered by the valve against its seat has been proposed. The presented FVM method provides close results to the universally accepted FEM strategy regarding forces and pressure distribution. Finally, it has been shown that the points indicated as critical and particularly susceptible to rupture from experimental observations suffer a considerable increase in stress due to the impact of the valve.

References

[1] P. Castrillo, E. Schillaci, and J. Rigola. Simulation of Fluid-Structure Interaction and Impact Force on a Reed Valve. In *14th WCCM-ECCOMAS Congress 2020*, volume 1500, pages 1–12. Scipedia S.L., mar 2021.

[2] Muhammad Tofique, Alexander Löf, Eugenio Schillaci, Pablo Castrillo, and Joaquim Rigola. Experimental and Numerical Analysis Of Reed Valve Movement In An Impact Fatigue Test System and Reciprocating Compressors. In *International Compressor Engineering Conference*, may 2021.

[3] Alireza Naseri, Eugenio Schillaci, Ignacio González, Pablo Castrillo, and Joaquim Rigola. High-fidelity resolution of turbulent flow through reed valves with fluid-structure interaction. *Under review*, 2023.

[4] P. Cardiff, Ž. Tuković, H. Jasak, and A. Ivanković. A block-coupled Finite Volume methodology for linear elasticity and unstructured meshes. *Computers & Structures*, 175:100–122, oct 2016.

[5] P. Cardiff and I. Demirdžić. Thirty Years of the Finite Volume Method for Solid Mechanics. *Archives of Computational Methods in Engineering*, 28:3721–3780, 2021.

[6] F. Hecht. New development in freefem++. *J. of Numerical Math.*, 20(3-4):251–265, 2012.

[7] Termo fluids s.l., www.termofluids.com, 2020.

[8] Alireza Naseri, Oriol Lehmkuhl, Ignacio Gonzalez, Eduard Bartrons, Carlos David Pérez-Segarra, and Assensi Oliva. A semi-implicit coupling technique for fluid-structure interaction problems with strong added-mass effect. *Journal of Fluids and Structures*, 80:94–112, jul 2018.

[9] N. N. Yanenko. *The Method of Fractional Steps*. Springer Berlin Heidelberg, 1971.

[10] R. W.C.P. Verstappen and A. E.P. Veldman. Symmetry-preserving discretization of turbulent flow. *Journal of Computational Physics*, 187(1):343–368, may 2003.

[11] Lluís Jofre, Oriol Lehmkuhl, Jordi Ventosa, F. Xavier Trias, and Assensi Oliva. Conservation Properties of Unstructured Finite-Volume Mesh Schemes for the Navier-Stokes Equations. *http://dx.doi.org/10.1080/10407790.2013.836335*, 65(1):53–79, jan 2013.

[12] F. X. Trias, O. Lehmkuhl, A. Oliva, C. D. Pérez-Segarra, and R. W.C.P. Verstappen. Symmetry-preserving discretization of Navier-Stokes equations on collocated unstructured grids. *Journal of Computational Physics*, 258:246–267, feb 2014.

[13] F. Nicoud and F. Ducros. Subgrid-Scale Stress Modelling Based on the Square of the Velocity Gradient Tensor. *Flow, Turbulence and Combustion 1999 62:3*, 62(3):183–200, 1999.

[14] P. D. Thomas and C. K. Lombard. Geometric Conservation Law and Its Application to Flow Computations on Moving Grids. *https://doi.org/10.2514/3.61273*, 17(10):1030–1037, may 1979.

[15] Michel Lesoinne and Charbel Farhat. Geometric conservation laws for flow problems with moving boundaries and deformable meshes, and their impact on aeroelastic computations. *Computer Methods in Applied Mechanics and Engineering*, 134(1-2):71–90, jul 1996.

[16] O. Estruch, O. Lehmkuhl, R. Borrell, C. D.Pérez Segarra, and A. Oliva. A parallel radial basis function interpolation method for unstructured dynamic meshes. *Computers & Fluids*, 80(1):44–54, jul 2013.

[17] Alireza Naseri, Ignacio Gonzalez, Ahmad Amani, Carlos David Pérez-Segarra, and Assensi Oliva. A second-order time accurate semi-implicit method for fluid-structure interaction problems. *Journal of Fluids and Structures*, 86:135–155, apr 2019.

[18] F. Favre, O. Antepara, C. Oliet, O. Lehmkuhl, and C. D. Perez-Segarra. An immersed boundary method to conjugate heat transfer problems in complex geometries. Application to an automotive antenna. *Applied Thermal Engineering*, 148:907–928, feb 2019.

[19] O. A. Bauchau and J. I. Craig, editors. *Structural analysis : with applications to aerospace structures*, volume 163 of *Solid Mechanics and Its Applications*. Springer Netherlands, Dordrecht, 2009.

[20] William Tyrrell. Thomson and Marie Dillon. Dahleh. *Theory of vibration with applications*. Prentice Hall, 1998.

[21] Werner Soedel. *Mechanics, Simulation and Design of Compressor Valves, Gas Passages and Pulsation Mufflers*. Purdue University, 1992.

[22] P. Cardiff, A. Karač, and A. Ivanković. Development of a finite volume contact solver based on the penalty method. *Computational Materials Science*, 64:283–284, nov 2012.

[23] J. O. Hallquist, G. L. Goudreau, and D. J. Benson. Sliding interfaces with contact-impact in large-scale Lagrangian computations. *Computer Methods in Applied Mechanics and Engineering*, 51(1-3):107–137, sep 1985.

[24] Alireza Naseri, Amin Totounferoush, Ignacio González, Miriam Mehl, and Carlos David Pérez-Segarra. A scalable framework for the partitioned solution of fluid-structure interaction problems. *Computational Mechanics*, 66(2):471–489, aug 2020.

[25] SolidWorks. Solid Works https://www.solidworks.com/es, 2022.

[26] Francisco Armero and Eva Petocz. Formulation and analysis of conserving algorithms for frictionless dynamic contact/impact problems. *Computer Methods in Applied Mechanics and Engineering*, 158(3-4):269–300, 1998.

5

Conclusions

In this thesis, a high-order finite volume method for hyperelastic materials using unstructured meshes has been proposed. As thoroughly described in the introduction, until now, there was a clear gap in the resolution of solid problems when using the method of finite volumes since there was no possibility of using high-order interpolation for the displacement in unstructured meshes [1]. In the case of using methods with linear interpolation of the displacement, it is necessary to carry out a refinement that, in many cases, generates an inadmissible computational effort. The main contribution of the presented thesis is the formulation of a FVM that allows solving problems where the shear locking effect appears, employing a reasonable amount of computational resources.

The accuracy and order of convergence of the method have been evaluated considering several examples and many different settings of the following parameters: type of stencil (s), type of mesh, interpolation order (p_i), stencil size (N_n), shape parameter of the weight function (k), and the number of Gaussian points (N_g). Besides, two high-order interpolations have been used and analyzed: the moving least squares and the local regression estimators. In addition, problems of two and three dimensions have been solved, concluding in each case which is the appropriate set of parameters. The method has been used to solve various types of examples: static and dynamic, including non-linear forces (impact force), with linear elastic or hyperelastic materials, and has been validated and verified in each case with analytical solutions. In several cases, the solutions were compared with those obtained with other software, both open-source or in-house. Finally, the method was used to solve a three-dimensional unstructured example for which experimental data are available, obtaining acceptable results and accuracy.

Two-dimensional problems In Section 3.1.1, considering a two-dimensional analytical example, the order of convergence of the method has been analyzed, concluding that when using LRE, the appropriate orders of convergence for the stresses are

obtained. However, when using the interpolation p_2 and p_4 for the displacement, the numerically estimated order of convergence was one unit less than expected, but the errors are smaller than those obtained using p_1 and p_3, respectively. After performing a results breakdown, the range $5 \leq k \leq 10$ is recommended for the shape parameter. Regarding the type of stencil, for the two stencils presented, good results are obtained, so it is recommended to use s_{eq}, see Section 2.3.3, since it is the least expensive from a computational point of view. Concerning the different meshes analyzed, it is observed that the method usually has better behavior for structured meshes. The number of Gaussian points recommended is $N_g \geq 2$. For the rest of the two-dimensional examples, it has been decided to use $k = 6$, $N_n = N_{n,min} + 10$[1] and $N_g = 7$.

Next, this thesis presents two original examples. In Section 3.1.2, a beam with a uniformly varying load is introduced, showing that the method can solve problems where the shear locking effect appears. In Section 3.1.3, an example where stress concentrations appear in complex geometry is shown. In both cases, the obtained results are close to the analytical solution, presenting the same or better behavior than using the finite element method. In [3,4] more examples of two-dimensional problems are presented, showing that the method can deal with problems with stress concentrations and complex geometries where unstructured meshes are required.

As a general remark, it is possible to conclude that within the two adopted high-order interpolation schemes (MLS and LRE), the MLS presents a poor performance in some examples. At the same time, LRE always provides accurate results. It is possible to state that it is much simpler to get the parameters to achieve the TOC for the different interpolation orders when using the LRE rather than the MLS. Moreover, the LRE is more straightforward and less expensive from a computational point of view. Therefore, the LRE scheme is strongly recommended.

Three-dimensional problems A whole set of three-dimensional problems were studied in Section 3.2 to analyze the sensibility of the high-order method when applied to unstructured meshes. First, in Section 3.2.1, a problem with an analytical solution was exhaustively analyzed by employing different kinds of interpolation order, schemes, and stencils to obtain a suitable set of parameters which allows the generalization of the method. In three-dimensional cases, the interpolation p_4 has not been used due to the computational expense this would entail. Considering the two-dimensional conclusions regarding the LRE overall better performance compared to MLS, the exhaustive analysis was carried out using only the first scheme mentioned. Nevertheless, some results were obtained for the MLS, reaffirming that its use is not recommended. Regarding the parameters used for the three-dimensional case, one

[1] See Section 2.3.3 where is defined the minimum number of nodes N_n [2].

of the most significant differences from those obtained in the two-dimensional case lies in the types of stencils. It was concluded that for three-dimensional problems, it is preferable to use the stencil s_{df}. Another point to highlight when comparing to the two dimensions case is that when using p_2, no difficulties were observed in obtaining the theoretical order of convergence of the displacement field. On the other hand, similar behavior was observed for the shape parameter k, recommending that $4 \geq k \geq 7$. Finally, in the case of using structured meshes of hexahedrons, it is recommended to use $N_g \geq 9$, while $N_g \geq 7$ for meshes of tetrahedrons.

For the rest of the three-dimensional problems, unstructured meshes were used, and the parameters $k = 6$, $N_g = 7$, and $N_n = N_{n,\min} + 40$ were selected. In Section 3.2.2, a beam with a uniformly distributed load is solved, showing that the method can deal with the shear locking effect in three-dimensional problems. Later, Section 3.2.3 presents the example of a cantilever beam that vibrates after a load is applied. This problem reveals how the method can also be used for dynamics problems, obtaining the beam's natural frequencies and the displacement of the free end, and comparing results with the work presented in [5]. The section ends with two examples using hyperelastic materials. In Section 3.2.4, an example with an analytical solution is solved, obtaining accurate results, which is helpful to validate the method presented in this thesis and to show its convergence for hyperelastic materials. However, when using p_2, the order of convergence is lower than expected, so, as in the case of two dimensions, it is recommended to use p_3 for the high-order interpolation. In Section 3.2.5, the benchmark example of the large deformation of a clamped beam presented in [6] and [7] is solved by the proposed high-order method. It is worth noting that, in the case of the hyperelastic clamped beam, better or similar results were obtained using fewer elements than in other works.

Example with experimental data The last case, presented in Chapter 4, consists in employing the formulation presented in this thesis to analyze and characterize the behavior of a reed valve in an air compressor. This test case, validated by comparison to experimental data, represents a possible application of the models developed in the current thesis to the real engineering world. First, the model used to obtain valve pressures using a FVM fluid-structure interaction solver developed in TermoFluids [8] is presented. The results obtained with TermoFluids, submitted in [9], are presented in detail. Subsequently, the pressures, forces, and stresses generated by the impact were analyzed with three-dimensional finite element models (results presented in [3]) and with the high-order model presented in this thesis. A correct approximation of the experimental results is observed in all cases, while differences between results provided by the two methods are highlighted. Once validated, the method obtains valuable physical insights into the case under analysis. Similar results were obtained in this sense by employing both FVM and FEM. The impact pressure and force

evolution for each of the two impacts observed in a valve work cycle were studied. Finally, stresses at points near the tip of the valve were identified, showing their vicinity with the zone where failures have been experimentally observed. It can be deduced that the stresses increase significantly at these points due to impacts, which explains why these points are still failure sites despite suffering low stresses due to bending.

Future work Several lines of research can be continued from this thesis:

1. Use the high order model presented for other physics, for example, plastic behavior or material damage [10].
2. Use another way of building the stencils, like the ones presented in [11].
3. Use the method presented in a vertex-centered formulation of the method of finite volumes.
4. Add to the analysis of the reed valve the effects of fatigue, plastification, and damage [12].

References

[1] I. Demirdžić. A fourth-order finite volume method for structural analysis. *Applied Mathematical Modelling*, 40(4):3104–3114, feb 2016.

[2] Sofiane Khelladi, Xesús Nogueira, Farid Bakir, and Ignasi Colominas. Toward a higher order unsteady finite volume solver based on reproducing kernel methods. *Computer Methods in Applied Mechanics and Engineering*, 200(29-32):2348–2362, jul 2011.

[3] Pablo Castrillo, Alfredo Canelas, Eugenio Schillaci, Joaquim Rigola, and Asensio Oliva. High-order finite volume method for linear elasticity on unstructured meshes. *Computers & Structures*, 268:106829, 2022.

[4] Pablo Castrillo, Eugenio Schillaci, and Joaquim Rigola. Analysis of high-order interpolationoschemes for solving linear problems in unstructured meshes using the finite volume method. In *8th European Congress on Computational Methods in Applied Sciences and Engineering*, Oslo, 2022.

[5] A. K. Slone, C. Bailey, and M. Cross. Dynamic solid mechanics using finite volume methods. *Applied Mathematical Modelling*, 27(2):69–87, feb 2003.

[6] Željko Tuković and Hrvoje Jasak. Updated lagrangian finite volume solver for large deformation dynamic response of elastic body. *Transactions of FAMENA*, 31:1–18, 2007.

[7] Kjell Mattiasson. Numerical results from large deflection beam and frame problems analysed by means of elliptic integrals. *International Journal for Numerical Methods in Engineering*, 17(1):145–153, jan 1981.

[8] Termo fluids s.l., www.termofluids.com, 2020.

[9] Alireza Naseri, Eugenio Schillaci, Ignacio González, Pablo Castrillo, and Joaquim Rigola. High-fidelity resolution of turbulent flow through reed valves with fluid-structure interaction. *Under review*, 2023.

[10] Bibiana Luccioni, Sergio Oller, and Rodolfo Danesi. Coupled plastic-damaged model. *Computer Methods in Applied Mechanics and Engineering*, 129(1-2):81–89, jan 1996.

[11] Luis Ramírez, Xesús Nogueira, Sofiane Khelladi, Jean-Camille Chassaing, and Ignasi Colominas. A new higher-order finite volume method based on Moving Least Squares for the resolution of the incompressible Navier-Stokes equations on unstructured grids. *Computer Methods in Applied Mechanics and Engineering*, 278:883–901, aug 2014.

[12] L. G. Barbu, S. Oller, X. Martinez, and A. Barbat. High cycle fatigue simulation: A new stepwise load-advancing strategy. *Engineering Structures*, 97:118–129, aug 2015.

Appendix A

Newton-Raphson method for large deformations

Applying the Netwon-Raphson method to Eq. (2.40)

$$\mathbf{r}(\chi_{k+1}) = \mathbf{r}(\chi_k) + \frac{\mathrm{d}}{\mathrm{d}\,\epsilon}\left[\mathbf{r}(\chi_k + \epsilon\,\delta\mathbf{u})\right]\Big|_{\epsilon=0} = \mathbf{0}\ , \tag{A.1}$$

where $\chi_{k+1} = \chi_k + \delta\mathbf{u}$ and $\mathbf{u}_{k+1} = \mathbf{u}_k + \delta\mathbf{u}$. Assuming that $\mathbf{b}_0$ do not depend on χ

$$\frac{\mathrm{d}}{\mathrm{d}\,\epsilon}\left[\mathbf{r}(\chi_k + \epsilon\,\delta\mathbf{u})\right]\Big|_{\epsilon=0} = \int_{\partial\mathcal{P}_0} \frac{\mathrm{d}}{\mathrm{d}\,\epsilon}\left[\mathbf{P}(\chi_k + \epsilon\,\delta\mathbf{u})\right]\Big|_{\epsilon=0} \mathbf{n}_0\,\mathrm{d}A_0 - \int_{\mathcal{P}_0} \rho_0\,\delta\ddot{\mathbf{u}}\,\mathrm{d}V_0\,, \tag{A.2}$$

using that $\mathbf{P} = \mathbf{F}\,\mathbf{S}$ then

$$\frac{\mathrm{d}}{\mathrm{d}\,\epsilon}\left[\mathbf{P}(\chi_k + \epsilon\,\delta\mathbf{u})\right] = \frac{\mathrm{d}}{\mathrm{d}\,\epsilon}\left[\mathbf{F}(\chi_k + \epsilon\,\delta\mathbf{u})\right]\,\mathbf{S}(\chi_k) + \mathbf{F}(\chi_k)\,\frac{\mathrm{d}}{\mathrm{d}\,\epsilon}\left[\mathbf{S}(\chi_k + \epsilon\,\delta\mathbf{u})\right]\,. \tag{A.3}$$

Remembering that $\mathbf{F}(\chi) = \nabla_0\,\chi$ then

$$\frac{\mathrm{d}}{\mathrm{d}\,\epsilon}\left[\mathbf{F}(\chi_k + \epsilon\,\delta\mathbf{u})\right]\Big|_{\epsilon=0} = \frac{\mathrm{d}}{\mathrm{d}\,\epsilon}\left[\nabla_0\,\chi + \epsilon\,\nabla_0\,\delta\mathbf{u}\right]\Big|_{\epsilon=0} = \nabla_0\,\delta\mathbf{u}\,. \tag{A.4}$$

Using the chain rule and Eq. (2.28)

$$\frac{\mathrm{d}}{\mathrm{d}\,\epsilon}\left[\mathbf{S}(\chi_k + \epsilon\,\delta\mathbf{u})\right]\Big|_{\epsilon=0} = \frac{\partial\,\mathbf{S}}{\partial\,\mathbf{C}}(\chi_k) : \frac{\mathrm{d}}{\mathrm{d}\,\epsilon}\left[\mathbf{C}(\chi_k + \epsilon\,\delta\mathbf{u})\right]\Big|_{\epsilon=0}\,, \tag{A.5}$$

where

$$\mathbb{C} = 2\,\frac{\partial\,\mathbf{S}}{\partial\,\mathbf{C}} = 4\,\frac{\partial^2\,\psi}{\partial\,\mathbf{C}\,\partial\,\mathbf{C}}\,, \tag{A.6}$$

is a fourth order tensor and it is called *elastic moduli* or *elasticity tensor*. The derivative of $\mathbf{C}$ is found using that $\mathbf{C} = \mathbf{F}^{\mathrm{T}}\,\mathbf{F}$:

$$\frac{\mathrm{d}}{\mathrm{d}\,\epsilon}\left[\mathbf{C}(\chi_k + \epsilon\,\delta\mathbf{u})\right] = \frac{\mathrm{d}}{\mathrm{d}\,\epsilon}\left[\mathbf{F}^{\mathrm{T}}(\chi_k + \epsilon\,\delta\mathbf{u})\right]\,\mathbf{F} + \mathbf{F}^{\mathrm{T}}\,\frac{\mathrm{d}}{\mathrm{d}\,\epsilon}\left[\mathbf{F}(\chi_k + \epsilon\,\delta\mathbf{u})\right]\,, \tag{A.7}$$

therefore

$$\frac{\mathrm{d}}{\mathrm{d}\,\epsilon}\left[\mathbf{C}(\chi_k + \epsilon\,\delta\mathbf{u})\right]\Big|_{\epsilon=0} = \left[\nabla_0\,\delta\mathbf{u}\right]^{\mathrm{T}}\,\mathbf{F} + \mathbf{F}^{\mathrm{T}}\,\left[\nabla_0\,\delta\mathbf{u}\right]\,. \tag{A.8}$$

Finally the solution is $\mathbf{u}_{k+1}(t) = \mathbf{u}_k(t) + \delta\,\mathbf{u}$ such as:

$$\begin{aligned}\mathbf{r}(\chi_{k+1}) &= \mathbf{r}(\chi_k) + \int_{\partial\mathcal{P}_0}\mathbf{f}_{\mathbf{S}}(\chi_k,\delta\mathbf{u})\,\mathrm{d}A_0 + \int_{\partial\mathcal{P}_0}\mathbf{f}_{\mathbf{C}}(\chi_k,\delta\mathbf{u})\,\mathrm{d}A_0 \\ &\quad - \int_{\mathcal{P}_0}\rho_0\,\delta\ddot{\mathbf{u}}\,\mathrm{d}V_0\,, \\ &= \mathbf{0}\,,\end{aligned} \tag{A.9}$$

where

$$\mathbf{f}_{\mathbf{S}}(\chi_k,\delta\mathbf{u}) = \left[\nabla_0\,\delta\mathbf{u}\right]\,\mathbf{S}(\chi_k)\,\mathbf{n}_0\,, \tag{A.10}$$

$$\mathbf{f}_{\mathbf{C}}(\chi_k,\delta\mathbf{u}) = \mathbf{F}(\chi_k)\,\mathbb{C}(\chi_k) : \left[\frac{\left(\nabla_0\,\delta\mathbf{u}\right)^{\mathrm{T}}\,\mathbf{F}(\chi_k) + \mathbf{F}^{\mathrm{T}}(\chi_k)\,\left(\nabla_0\,\delta\mathbf{u}\right)}{2}\right]\,\mathbf{n}_0\,. \tag{A.11}$$

Appendix B

Numerical quadrature

This appendix presents the Gauss points necessary for the presented formulation.

B.1 Gauss points for one dimension

In two-dimensional problems, the surface integrals are line integrals; therefore, finding Gauss points on line segments is necessary. Furthermore, the method presented in this section can be extrapolated for quadrilateral and hexahedral problems, as shown in the following sections.

Figure B.1 shows the line segment AB between points A and B whose coordinates are $\boldsymbol{X}_\mathrm{A} = (X_\mathrm{A}, Y_\mathrm{A}, Z_\mathrm{A})$ and $\boldsymbol{X}_\mathrm{B} = (X_\mathrm{B}, Y_\mathrm{B}, Z_\mathrm{B})$, respectively. The coordinates of the g-th Gauss point are:

$$\boldsymbol{X}_g = \left(\frac{\boldsymbol{X}_\mathrm{B} - \boldsymbol{X}_\mathrm{A}}{2}\right) \xi_g + \frac{\boldsymbol{X}_\mathrm{B} + \boldsymbol{X}_\mathrm{A}}{2}\,, \tag{B.1}$$

where ξ_g is defined for each point in Tables B.1 and B.2.

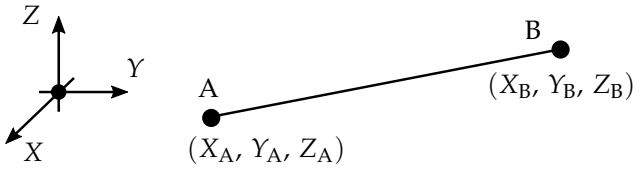

Figure B.1: Gauss points for one dimension.

Tables B.1 and B.2 shows the weights

$$\alpha_g = J_g\, w_g\,, \tag{B.2}$$

where the numerical values of the tables can be found in https://www.unioviedo.es/compnum/laboratorios_web/Laborat10_inte/Laborat07b_integracion.html. The coefficients ξ_g and w_g are obtained by making a change of variables in the integral on AB to a reference segment on $[-1, 1]$, where $J_g = \ell/2$ is the determinant of the Jacobian matrix of that change of variable, being $\ell = \|\boldsymbol{X}_\mathrm{B} - \boldsymbol{X}_\mathrm{A}\|$ the length of the segment. Then the integration of a function $f(\boldsymbol{X})$ in the segment AB is approximated as:

$$\int_{\mathrm{AB}} f(\boldsymbol{X})\,\mathrm{ds} \approx \sum_{g=1}^{g=N_g} \alpha_g\, f(\boldsymbol{X}_g)\,, \tag{B.3}$$

where N_g is the amount of Gauss points used. With N_g points, a polynomial of order $p = 2\,N_\mathrm{g} - 1$ is integrated exactly.

Table B.1: 1D Gauss points using $N_\mathrm{g} = \{1, 2, 3, 4, 5\}$.

p	N_g	g	ξ_g	w_g
1	1	1	0	2
3	2	$\{1, 2\}$	$\pm\frac{1}{\sqrt{3}}$	1
5	3	1	0	$\frac{8}{9}$
		$\{2, 3\}$	$\pm\sqrt{\frac{3}{5}}$	$\frac{5}{9}$
7	4	$\{1, 2\}$	$\pm\sqrt{\frac{3}{7}-\frac{2}{7}\sqrt{\frac{6}{5}}}$	$\frac{18+\sqrt{30}}{36}$
		$\{3, 4\}$	$\pm\sqrt{\frac{3}{7}+\frac{2}{7}\sqrt{\frac{6}{5}}}$	$\frac{18-\sqrt{30}}{36}$
9	5	1	0	$\frac{128}{225}$
		$\{2, 3\}$	$\pm\frac{1}{3}\sqrt{5-2\sqrt{\frac{10}{7}}}$	$\frac{322+13\sqrt{70}}{900}$
		$\{4, 5\}$	$\pm\frac{1}{3}\sqrt{5+2\sqrt{\frac{10}{7}}}$	$\frac{322-13\sqrt{70}}{900}$

Table B.2: 1D Gauss points using $N_g = \{6, 7, 8, 9, 10\}$.

p	N_g	g	ξ_g	w_g
11	6	$\{1, 2\}$	± 0.2386191861	0.4679139346
		$\{3, 4\}$	± 0.6612093865	0.3607615730
		$\{5, 6\}$	± 0.9324695142	0.1713244924
13	7	1	0	0.4179591837
		$\{2, 3\}$	± 0.4058451514	0.3818300505
		$\{4, 5\}$	± 0.7415311856	0.2797053915
		$\{6, 7\}$	± 0.9491079123	0.1294849662
15	8	$\{1, 2\}$	± 0.1834346425	0.3626837834
		$\{3, 4\}$	± 0.5255324099	0.3137066459
		$\{5, 6\}$	± 0.7966664774	0.2223810345
		$\{7, 8\}$	± 0.9602898565	0.1012285363
17	9	1	0	0.3302393550
		$\{2, 3\}$	± 0.3242534234	0.3123470770
		$\{4, 5\}$	± 0.6133714327	0.2606106964
		$\{6, 7\}$	± 0.8360311073	0.1806481607
		$\{8, 9\}$	± 0.9681602395	0.0812743883
19	10	$\{1, 2\}$	± 0.1488743390	0.2955242247
		$\{3, 4\}$	± 0.4333953941	0.2692667193
		$\{5, 6\}$	± 0.6794095683	0.2190863625
		$\{7, 8\}$	± 0.8650633667	0.1494513492
		$\{9, 10\}$	± 0.9739065285	0.0666713443

B.2 Gauss points for two dimensions

In two dimensions, it is necessary to make surface integrals to obtain the volume force or the mass matrix. On the other hand, surface integrals are employed for three-dimensional cases to obtain the stiffness matrix. In this thesis, quadrilaterals and triangles are used as surface elements. For this reason, the following shows how to obtain the integration points for these geometries.

The integral over a surface S is approximated as:

$$\int_S f(\boldsymbol{X})\,\mathrm{d}A \approx \sum_{g=1}^{g=N_g} \alpha_g\, f(\boldsymbol{X}_g)\,, \tag{B.4}$$

where

$$\alpha_g = J_g\, w_g\,, \tag{B.5}$$

being J_p, w_g, and $\boldsymbol{X}_g$ defined in what follows for quadrilaterals and triangles.

B.2.1 Quadrilateral element

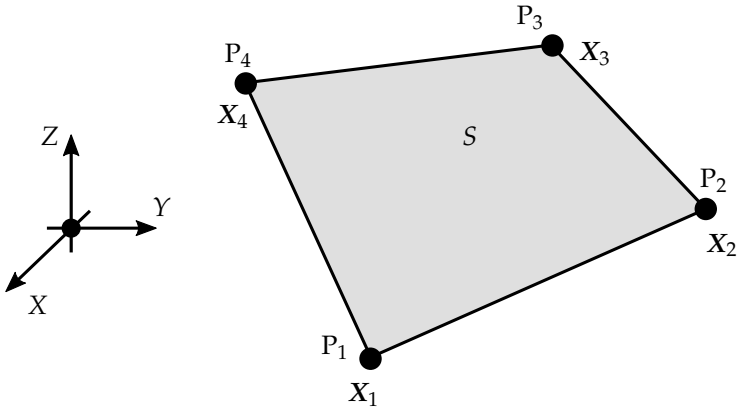

Figure B.2: Gauss points for a two dimensions quadrilateral element.

Let be the quadrilateral of Figure B.2, where the points P_1, P_2, P_3 and P_4 define the surface S. In this case w_g is obtained from the weights $w_{g,1\mathrm{D}}$, illustrated in Section B.1, as:

$$w_g = w_{r,1\mathrm{D}}\, w_{m,1\mathrm{D}} \text{ where } \{r,\, m\} = 1, \cdots, \sqrt{N_\mathrm{g}}\,. \tag{B.6}$$

The coordinates of the g-th point are obtained similarly:

$$\mathbf{X}_g = \boldsymbol{Q} + \mathbf{v}_1\, \xi_{g,x} + \mathbf{v}_2\, \xi_{g,y} + \mathbf{v}_3\, \xi_{g,x}\, \xi_{g,y}\,, \tag{B.7}$$

where

$$\xi_{g,x} = \xi_r \text{ and } \xi_{g,y} = \xi_m\,, \tag{B.8}$$

being ξ_i presented in Tables B.1 and B.2. $\boldsymbol{Q}$ and vectors $\mathbf{v}_i$ are defined from the coordinates $\boldsymbol{X}_i$ of points P_i as:

$$\begin{array}{rcl} \boldsymbol{Q} & = & \left(\boldsymbol{X}_1 + \boldsymbol{X}_2 + \boldsymbol{X}_3 + \boldsymbol{X}_4\right)/4\,, \\ \mathbf{v}_1 & = & \left(-\boldsymbol{X}_1 + \boldsymbol{X}_2 + \boldsymbol{X}_3 - \boldsymbol{X}_4\right)/4\,, \\ \mathbf{v}_2 & = & \left(-\boldsymbol{X}_1 - \boldsymbol{X}_2 + \boldsymbol{X}_3 + \boldsymbol{X}_4\right)/4\,, \\ \mathbf{v}_3 & = & \left(\boldsymbol{X}_1 - \boldsymbol{X}_2 + \boldsymbol{X}_3 - \boldsymbol{X}_4\right)/4\,. \end{array} \tag{B.9}$$

The coefficient J_g is obtained as:

$$J_g = \|\mathbf{w}_1 \times \mathbf{w}_2\|\,, \tag{B.10}$$

where $\times$ is the cross product and the $\mathbf{w}_i$ vectors are defined as:

$$\mathbf{w}_1 = \mathbf{v}_1 + \mathbf{v}_3\,\xi_{g,y} \text{ and } \mathbf{w}_2 = \mathbf{v}_2 + \mathbf{v}_3\,\xi_{g,x}\,. \tag{B.11}$$

An example using $N_\mathrm{g} = 9$ is presented in Table B.3, analogous results can be obtained for $N_\mathrm{g} = \{1, 4, 16, 25, 36, 49, 64, 91, 100\}$.

Table B.3: 2D Gauss points using $N_\mathrm{g} = 9$ for quadrilaterals elements.

p	N_g	g	$\xi_{g,x}$	$\xi_{g,y}$	w_g
5	9	1	0	0	$\frac{64}{81}$
		$\{2, 3\}$	0	$\pm\sqrt{\frac{3}{5}}$	$\frac{40}{81}$
		$\{4, 5\}$	$\pm\sqrt{\frac{3}{5}}$	0	$\frac{40}{81}$
		$\{6, 7\}$	$\pm\sqrt{\frac{3}{5}}$	$\pm\sqrt{\frac{3}{5}}$	$\frac{25}{81}$
		$\{8, 9\}$	$\pm\sqrt{\frac{3}{5}}$	$\mp\sqrt{\frac{3}{5}}$	$\frac{25}{81}$

B.2.2 Triangular element

In this case the surface S is generated by three points: P_1, P_2 and P_3 as can be seen in Figure B.3. The coordinates of the g-th point are:

$$\mathbf{X}_g = \boldsymbol{X}_1 + \mathbf{v}_1\,\xi_{g,x} + \mathbf{v}_2\,\xi_{g,y}\,, \tag{B.12}$$

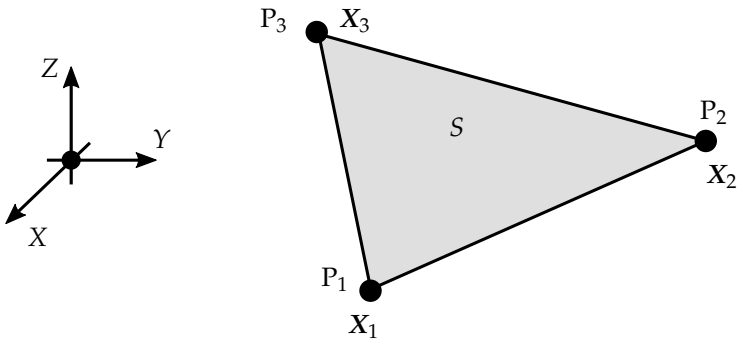

Figure B.3: Gauss points for a two dimensions triangular element.

where $\xi_{g,x}$ and $\xi_{g,y}$ are defined in Table B.4, and the vectors $\mathbf{v}_i$ are obtained as:

$$\begin{aligned} \mathbf{v}_1 &= \boldsymbol{X}_2 - \boldsymbol{X}_1 \,, \\ \mathbf{v}_2 &= \boldsymbol{X}_3 - \boldsymbol{X}_1 \,. \end{aligned} \tag{B.13}$$

In this case, J_g is equal to all the Gauss points and is obtained as:

$$J_g = \frac{1}{2} \| \mathbf{v}_1 \times \mathbf{v}_2 \| \,, \tag{B.14}$$

and the weights w_g are shown in Table B.4. More cases are available in [1] to exactly integrate polynomials up to order 20 with 79 Gauss points.

B.3 Gauss points for three dimensions

In the case of three dimensions, it is necessary to make volume integrals to obtain the volume force and the mass matrix. In this thesis, hexahedrons and tetrahedrons are used as volume elements. For this reason, the following shows how to obtain the integration points for these geometries.

The integral over a volume V is approximated as:

$$\int_V f(\boldsymbol{X}) \, \mathrm{d}V \approx \sum_{g=1}^{g=N_g} \alpha_g \, f(\boldsymbol{X}_g) \,, \tag{B.15}$$

where

$$\alpha_g = J_g \, w_g \,, \tag{B.16}$$

being J_p, w_g, and $\boldsymbol{X}_g$ defined in what follows for hexahedral and tetrahedral elements.

Table B.4: 2D Gauss points using $N_g = \{1, 3, 7\}$ for triangular elements.

p	N_g	g	$\xi_{g,x}$	$\xi_{g,y}$	w_g
1	1	1	1/3	1/3	1
		1	2/3	1/6	1/3
2	3	2	1/6	2/3	1/3
		3	1/6	1/6	1/3
		1	0.333333333333333	0.333333333333333	0.225000000000000
		2	0.059715871789770	0.470142064105115	0.132394152788506
		3	0.470142064105115	0.059715871789770	0.132394152788506
5	7	4	0.470142064105115	0.470142064105115	0.132394152788506
		5	0.797426985353087	0.101286507323456	0.125939180544827
		6	0.101286507323456	0.797426985353087	0.125939180544827
		7	0.101286507323456	0.101286507323456	0.125939180544827

B.3.1 Hexahedral element

Let be the hexahedral of Figure B.4, where the points P_1, P_2, P_3, P_4, P_5, P_6, P_7 and P_8 define the volume V.

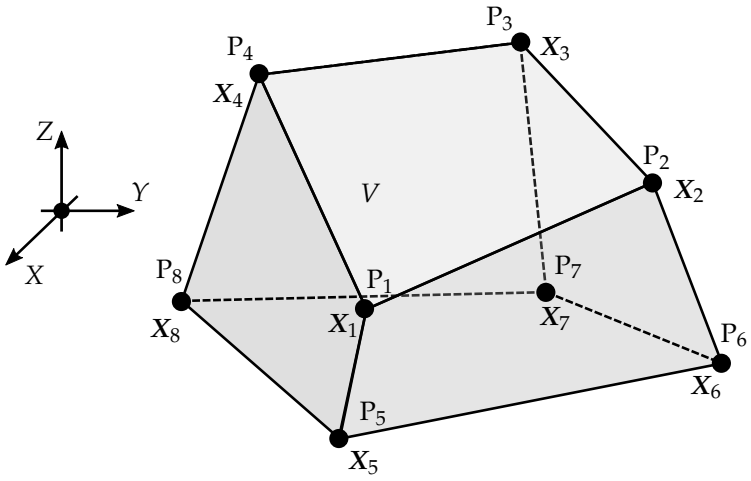

Figure B.4: Gauss points for a three dimensions hexahedral element.

As for the two-dimensional quadrilateral element, in this case, what is obtained in Section B.1 is used for each of the three directions. From the above:

$$w_g = w_{r,1D}\, w_{m,1D}\, w_{k,1D} \text{ where } \{r,\, m,\, k\} = 1, \cdots, \sqrt[3]{N_g}\,, \tag{B.17}$$

with $N_g = \{1, 8, 27, 64, 125, 216, 343, 512, 729, 1000\}$.

The coordinates of the g-th point are obtained similarly:

$$\begin{aligned}\mathbf{X}_g = \boldsymbol{Q} + \mathbf{v}_1\, \xi_{g,x} + \mathbf{v}_2\, \xi_{g,y} + \mathbf{v}_3\, \xi_{g,z} \\ + \mathbf{v}_4\, \xi_{g,x}\, \xi_{g,y} + \mathbf{v}_5\, \xi_{g,x}\, \xi_{g,z} + \mathbf{v}_6\, \xi_{g,y}\, \xi_{g,z} + \mathbf{v}_7\, \xi_{g,x}\, \xi_{g,y}\, \xi_{g,z}\,,\end{aligned} \tag{B.18}$$

where

$$\xi_{g,x} = \xi_r,\ \xi_{g,y} = \xi_m \text{ and } \xi_{g,z} = \xi_k\,, \tag{B.19}$$

being ξ_i presented in Tables B.1 and B.2. $\boldsymbol{Q}$ and vectors $\mathbf{v}_i$ are defined from the coordinates $\boldsymbol{X}_i$ of points P_i as:

$$\begin{aligned}
\boldsymbol{Q} &= \left(\boldsymbol{X}_1 + \boldsymbol{X}_2 + \boldsymbol{X}_3 + \boldsymbol{X}_4 + \boldsymbol{X}_5 + \boldsymbol{X}_6 + \boldsymbol{X}_7 + \boldsymbol{X}_8\right)/8\,, \\
\mathbf{v}_1 &= \left(-\boldsymbol{X}_1 + \boldsymbol{X}_2 + \boldsymbol{X}_3 - \boldsymbol{X}_4 - \boldsymbol{X}_5 + \boldsymbol{X}_6 + \boldsymbol{X}_7 - \boldsymbol{X}_8\right)/8\,, \\
\mathbf{v}_2 &= \left(-\boldsymbol{X}_1 - \boldsymbol{X}_2 + \boldsymbol{X}_3 + \boldsymbol{X}_4 - \boldsymbol{X}_5 - \boldsymbol{X}_6 + \boldsymbol{X}_7 + \boldsymbol{X}_8\right)/8\,, \\
\mathbf{v}_3 &= \left(-\boldsymbol{X}_1 - \boldsymbol{X}_2 - \boldsymbol{X}_3 - \boldsymbol{X}_4 + \boldsymbol{X}_5 + \boldsymbol{X}_6 + \boldsymbol{X}_7 + \boldsymbol{X}_8\right)/8\,, \\
\mathbf{v}_4 &= \left(\boldsymbol{X}_1 - \boldsymbol{X}_2 + \boldsymbol{X}_3 - \boldsymbol{X}_4 + \boldsymbol{X}_5 - \boldsymbol{X}_6 + \boldsymbol{X}_7 - \boldsymbol{X}_8\right)/8\,, \\
\mathbf{v}_5 &= \left(\boldsymbol{X}_1 - \boldsymbol{X}_2 - \boldsymbol{X}_3 + \boldsymbol{X}_4 - \boldsymbol{X}_5 + \boldsymbol{X}_6 + \boldsymbol{X}_7 - \boldsymbol{X}_8\right)/8\,, \\
\mathbf{v}_6 &= \left(\boldsymbol{X}_1 + \boldsymbol{X}_2 - \boldsymbol{X}_3 - \boldsymbol{X}_4 - \boldsymbol{X}_5 - \boldsymbol{X}_6 + \boldsymbol{X}_7 + \boldsymbol{X}_8\right)/8\,, \\
\mathbf{v}_7 &= \left(-\boldsymbol{X}_1 + \boldsymbol{X}_2 - \boldsymbol{X}_3 + \boldsymbol{X}_4 + \boldsymbol{X}_5 - \boldsymbol{X}_6 + \boldsymbol{X}_7 - \boldsymbol{X}_8\right)/8\,.
\end{aligned} \tag{B.20}$$

The coefficient J_g is obtained as:

$$J_g = \left|\mathbf{w}_1 \cdot (\mathbf{w}_2 \times \mathbf{w}_3)\right| \tag{B.21}$$

where $\times$ is the cross product, $\cdot$ the dot product and the $\mathbf{w}_i$ vectors are defined as:

$$\begin{aligned}
\mathbf{w}_1 &= \mathbf{v}_1 + \mathbf{v}_4\, \xi_{g,y} + \mathbf{v}_5\, \xi_{g,z} + \mathbf{v}_7\, \xi_{g,y}\, \xi_{g,z}\,, \\
\mathbf{w}_2 &= \mathbf{v}_2 + \mathbf{v}_4\, \xi_{g,x} + \mathbf{v}_6\, \xi_{g,z} + \mathbf{v}_7\, \xi_{g,x}\, \xi_{g,z}\,, \\
\mathbf{w}_3 &= \mathbf{v}_3 + \mathbf{v}_5\, \xi_{g,x} + \mathbf{v}_6\, \xi_{g,y} + \mathbf{v}_7\, \xi_{g,x}\, \xi_{g,y}\,.
\end{aligned} \tag{B.22}$$

An example using $N_g = 8$ is presented in Table B.5

B.3.2 Tetrahedral element

For volume integrals in tetrahedrons, what is presented in [2] is used. In this case the volume V is generated by four points: P_1, P_2, P_3 and P_4 as can be seen in Figure B.5.

Table B.5: 3D Gauss points using $N_g = 8$ for hexahedrals elements.

p	N_g	g	$\xi_{g,x}$	$\xi_{g,x}$	$\xi_{g,z}$	w_g
3	8	$\{1, 2\}$	$\pm \frac{1}{\sqrt{3}}$	$\pm \frac{1}{\sqrt{3}}$	$\pm \frac{1}{\sqrt{3}}$	1
		$\{3, 4\}$	$\pm \frac{1}{\sqrt{3}}$	$\pm \frac{1}{\sqrt{3}}$	$\mp \frac{1}{\sqrt{3}}$	1
		$\{5, 6\}$	$\pm \frac{1}{\sqrt{3}}$	$\mp \frac{1}{\sqrt{3}}$	$\mp \frac{1}{\sqrt{3}}$	1
		$\{7, 8\}$	$\pm \frac{1}{\sqrt{3}}$	$\mp \frac{1}{\sqrt{3}}$	$\pm \frac{1}{\sqrt{3}}$	1

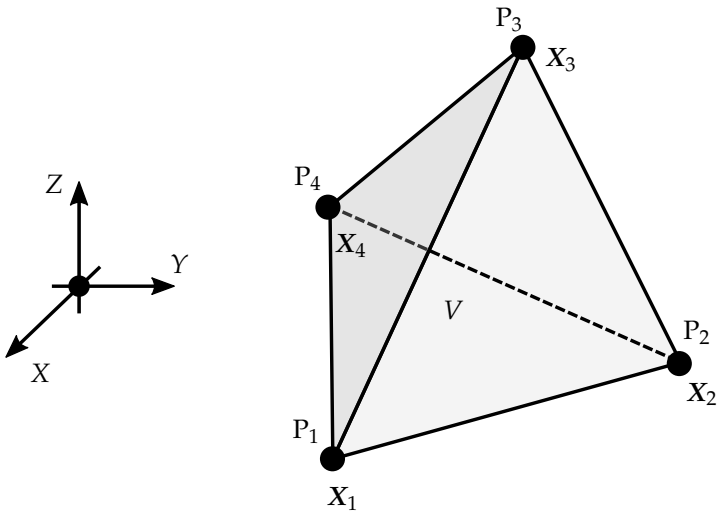

Figure B.5: Gauss points for a three dimensions tetrahedral element.

The coordinates of the g-th point are:

$$\mathbf{X}_g = \boldsymbol{X}_1\, a_{g,1} + \boldsymbol{X}_2\, a_{g,2} + \boldsymbol{X}_3\, a_{g,3} + \boldsymbol{X}_4\, a_{g,4}\,, \tag{B.23}$$

where $a_{g,i}$ are defined in Table B.6. In this case, J_g is equal to all the Gauss points and is obtained as:

$$J_g = \frac{1}{6}\,|(\mathbf{w}_1 \times \mathbf{w}_2) \cdot \mathbf{w}_3|\,, \tag{B.24}$$

being

$$\mathbf{w}_1 = \boldsymbol{X}_2 - \boldsymbol{X}_1,\ \mathbf{w}_2 = \boldsymbol{X}_3 - \boldsymbol{X}_1 \text{ and } \mathbf{w}_3 = \boldsymbol{X}_4 - \boldsymbol{X}_1\,, \tag{B.25}$$

and the weights w_g for $N_g = 10$ are shown in Table B.6. More cases are available in [2] to exactly integrate polynomials up to order 6 with 56 Gauss points.

Table B.6: 3D Gauss points using $N_g = 10$ for tetrahedral elements.

p	N_g	g	$a_{g,1}$	$a_{g,2}$	$a_{g,3}$
3	10	1	0.7784952948213300	0.0738349017262234	0.0738349017262234
		2	0.0738349017262234	0.7784952948213300	0.0738349017262234
		3	0.0738349017262234	0.0738349017262234	0.7784952948213300
		4	0.0738349017262234	0.0738349017262234	0.0738349017262234
		5	0.4062443438840510	0.4062443438840510	0.0937556561159491
		6	0.4062443438840510	0.0937556561159491	0.4062443438840510
		7	0.4062443438840510	0.0937556561159491	0.0937556561159491
		8	0.0937556561159491	0.4062443438840510	0.4062443438840510
		9	0.0937556561159491	0.4062443438840510	0.0937556561159491
		10	0.0937556561159491	0.0937556561159491	0.4062443438840510

p	N_g	g	$a_{g,4}$	w_g
3	10	1	0.0738349017262234	0.0476331348432089
		2	0.0738349017262234	0.0476331348432089
		3	0.0738349017262234	0.0476331348432089
		4	0.7784952948213300	0.0476331348432089
		5	0.0937556561159491	0.1349112434378610
		6	0.0937556561159491	0.1349112434378610
		7	0.4062443438840510	0.1349112434378610
		8	0.0937556561159491	0.1349112434378610
		9	0.4062443438840510	0.1349112434378610
		10	0.4062443438840510	0.1349112434378610

References

[1] D. A. Dunavant. High degree efficient symmetrical Gaussian quadrature rules for the triangle. *International Journal for Numerical Methods in Engineering*, 21(6):1129–1148, jun 1985.

[2] Lee Shunn and Frank Ham. Symmetric quadrature rules for tetrahedra based on a cubic close-packed lattice arrangement. *Journal of Computational and Applied Mathematics*, 236(17):4348–4364, nov 2012.

Appendix C

Evaluation of equations using the high order finite volume method presented

This appendix describes how to evaluate the governing equations using the finite volume method presented in Section 2.2 with the high-order method presented in Section 2.3. Section C.1 illustrates the notation that is used in this chapter. Then in Section C.2, the equations assuming the small deformations hypothesis are discretized. Finally, in Section C.3, the evaluation of equations for large deformations is shown.

C.1 Notation

The high-order interpolation method for the displacement field $\mathbf{u}$ and its derivatives is described in Section (2.3):

$$\begin{aligned} \mathbf{u}(\boldsymbol{X}) &= \sum_{n=1}^{n=N_\mathrm{n}} c_n(\boldsymbol{X})\,\mathbf{u}_n, & \frac{\partial \mathbf{u}}{\partial X}(\boldsymbol{X}) &= \sum_{n=1}^{n=N_\mathrm{n}} c_{X,n}(\boldsymbol{X})\,\mathbf{u}_n, \\ \frac{\partial \mathbf{u}}{\partial Y}(\boldsymbol{X}) &= \sum_{n=1}^{n=N_\mathrm{n}} c_{Y,n}(\boldsymbol{X})\,\mathbf{u}_n, & \frac{\partial \mathbf{u}}{\partial Z}(\boldsymbol{X}) &= \sum_{n=1}^{n=N_\mathrm{n}} c_{Z,n}(\boldsymbol{X})\,\mathbf{u}_n\,, \end{aligned} \tag{C.1}$$

where c_n, $c_{X,n}$, $c_{Y,n}$ and $c_{Z,n}$ are the interpolation coefficients that depend on the MLS and LRE methods which were described in Section (2.3.1) and Section (2.3.2), respectively. It is helpful to define the vector of coefficients for a point n of a certain point $\boldsymbol{X}$:

$$\mathbf{c}^{\mathrm{T}}_{\mathbf{x},n}(\boldsymbol{X}) = (c_{X,n}(\boldsymbol{X}),\, c_{Y,n}(\boldsymbol{X}),\, c_{Z,n}(\boldsymbol{X}))\,, \tag{C.2}$$

and the displacement vector of a node n as:

$$\mathbf{u}_n^{\mathrm{T}}(\boldsymbol{X}) = \left(u_{x,n},\, u_{y,n},\, u_{z,n}\right) . \tag{C.3}$$

In what follows, the dependency on $\boldsymbol{X}$ is omitted for clarity. The material gradient of the displacement field is:

$$\nabla_0 \mathbf{u} = \begin{pmatrix} \dfrac{\partial u_x}{\partial X} & \dfrac{\partial u_x}{\partial Y} & \dfrac{\partial u_x}{\partial Z} \\ \dfrac{\partial u_y}{\partial X} & \dfrac{\partial u_y}{\partial Y} & \dfrac{\partial u_y}{\partial Z} \\ \dfrac{\partial u_z}{\partial X} & \dfrac{\partial u_z}{\partial Y} & \dfrac{\partial u_z}{\partial Z} \end{pmatrix} = \sum_{n=1}^{n=N_{\mathrm{n}}} \begin{pmatrix} c_{X,n}u_{x,n} & c_{Y,n}u_{x,n} & c_{Z,n}u_{x,n} \\ c_{X,n}u_{y,n} & c_{Y,n}u_{y,n} & c_{Z,n}u_{y,n} \\ c_{X,n}u_{z,n} & c_{Y,n}u_{z,n} & c_{Z,n}u_{z,n} \end{pmatrix} , \tag{C.4}$$

and the outward-pointing normal in material description of a face Σ_f is:

$$\mathbf{n}_{0,f}^{\mathrm{T}} = \left(N_{x,f},\, N_{y,f},\, N_{z,f}\right) . \tag{C.5}$$

C.2 Evaluation of equations for small deformations

In this section it is evaluated the first term of Eq. (2.36) that were firstly discretized with the finite volume method in Eq. (2.45):

$$\mathbf{d}_1 = \sum_{f=1}^{f=N_{\mathrm{f}}} \left[\sum_{g=1}^{g=N_{\mathrm{g}}} \alpha_g \left(\lambda\, \mathrm{tr}\left(\nabla_0 \mathbf{u}\right)\, \mathbf{I} + \mu\, \nabla_0 \mathbf{u} + \mu\, \left(\nabla_0 \mathbf{u}\right)^{\mathrm{T}} \right) \right] \mathbf{n}_{0,f} , \tag{C.6}$$

therefore it is necessary to obtain expressions for:

$$\mathbf{d}_2 = \mathrm{tr}\left(\nabla_0 \mathbf{u}\right) \mathbf{I}\, \mathbf{n}_{0,f}, \quad \mathbf{d}_3 = \left(\nabla_0 \mathbf{u}\right)\, \mathbf{n}_{0,f} \quad \text{and} \quad \mathbf{d}_4 = \left(\nabla_0 \mathbf{u}\right)^{\mathrm{T}}\, \mathbf{n}_{0,f} . \tag{C.7}$$

Note that $\mathbf{d}_2 = \mathrm{tr}\left(\nabla_0 \mathbf{u}\right) \mathbf{I}\, \mathbf{n}_{0,f} = \mathrm{tr}\left(\nabla_0 \mathbf{u}\right) \mathbf{n}_{0,f} = \mathbf{n}_{0,f}\, \mathrm{tr}\left(\nabla_0 \mathbf{u}\right)$, then using Eqs. (C.1):

$$\begin{aligned} \mathrm{tr}\left(\nabla_0 \mathbf{u}\right) &= \frac{\partial u_x}{\partial X} + \frac{\partial u_y}{\partial Y} + \frac{\partial u_z}{\partial Z} , \\ &= \sum_{n=1}^{n=N_{\mathrm{n}}} c_{X,n}\, u_{x,n} + c_{Y,n}\, u_{y,n} + c_{Z,n}\, u_{z,n} = \sum_{n=1}^{n=N_{\mathrm{n}}} \mathbf{c}_{\mathbf{x},n}^{\mathrm{T}}\, \mathbf{u}_n , \\ \Rightarrow \quad \mathbf{d}_2 &= \sum_{n=1}^{n=N_{\mathrm{n}}} \left[\mathbf{n}_{0,f}\, \mathbf{c}_{\mathbf{x},n}^{\mathrm{T}} \right] \mathbf{u}_n . \end{aligned} \tag{C.8}$$

Using Eqs. (C.1), (C.4) and (C.5):

$$\begin{aligned}
\nabla_0 \mathbf{u}\, \mathbf{n}_{0,f} &= \sum_{n=1}^{n=N_\mathrm{n}} \begin{pmatrix} c_{X,n}u_{x,n}N_{x,f} + c_{Y,n}u_{x,n}N_{y,f} + c_{Z,n}u_{x,n}N_{z,f} \\ c_{X,n}u_{y,n}N_{x,f} + c_{Y,n}u_{y,n}N_{y,f} + c_{Z,n}u_{y,n}N_{z,f} \\ c_{X,n}u_{z,n}N_{x,f} + c_{Y,n}u_{z,n}N_{y,f} + c_{Z,n}u_{z,n}N_{z,f} \end{pmatrix}, \\
&= \sum_{n=1}^{n=N_\mathrm{n}} \begin{pmatrix} \mathbf{c}_{\mathbf{x},n}^\mathrm{T}\, \mathbf{n}_{0,f}\, u_{x,n} \\ \mathbf{c}_{\mathbf{x},n}^\mathrm{T}\, \mathbf{n}_{0,f}\, u_{y,n} \\ \mathbf{c}_{\mathbf{x},n}^\mathrm{T}\, \mathbf{n}_{0,f}\, u_{z,n} \end{pmatrix}, \\
\Rightarrow \quad \mathbf{d}_3 &= \sum_{n=1}^{n=N_\mathrm{n}} \left[\mathbf{c}_{\mathbf{x},n}^\mathrm{T}\, \mathbf{n}_{0,f}\, \mathbf{I} \right] \mathbf{u}_n \,.
\end{aligned} \tag{C.9}$$

For the last expression, it is possible to obtain that:

$$\begin{aligned}
(\nabla_0 \mathbf{u})^\mathrm{T}\, \mathbf{n}_{0,f} &= \sum_{n=1}^{n=N_\mathrm{n}} \begin{pmatrix} c_{X,n}u_{x,n}N_{x,f} + c_{X,n}u_{y,n}N_{y,f} + c_{X,n}u_{z,n}N_{z,f} \\ c_{Y,n}u_{x,n}N_{x,f} + c_{Y,n}u_{y,n}N_{y,f} + c_{Y,n}u_{z,n}N_{z,f} \\ c_{Z,n}u_{x,n}N_{x,f} + c_{Z,n}u_{y,n}N_{y,f} + c_{Z,n}u_{z,n}N_{z,f} \end{pmatrix}, \\
&= \sum_{n=1}^{n=N_\mathrm{n}} \begin{pmatrix} c_{X,n}N_{x,f} & c_{X,n}N_{y,f} & c_{X,n}N_{z,f} \\ c_{Y,n}N_{x,f} & c_{Y,n}N_{y,f} & c_{Y,n}N_{z,f} \\ c_{Z,n}N_{x,f} & c_{Z,n}N_{y,f} & c_{Z,n}N_{z,f} \end{pmatrix} \begin{pmatrix} u_{x,n} \\ u_{y,n} \\ u_{z,n} \end{pmatrix}, \\
\Rightarrow \quad \mathbf{d}_4 &= \sum_{n=1}^{n=N_\mathrm{n}} \left[\mathbf{c}_{\mathbf{x},n}\, \mathbf{n}_{0,f}^\mathrm{T} \right] \mathbf{u}_n \,.
\end{aligned} \tag{C.10}$$

C.3 Evaluation of equations for large deformations

In this section Eqs. (2.42) and (2.43) are discretized and evaluated using the proposed high-order method. First, for Eq. (2.42) it is convenient to define:

$$\mathbf{f}_{\mathbf{S},f,k} = \mathbf{S}(\chi_k)\, \mathbf{n}_{0,f} \,, \tag{C.11}$$

therefore using Eq. (C.9)

$$\mathbf{f}_\mathbf{S}(\chi_k, \delta\mathbf{u}) = [\nabla_0\, \delta\mathbf{u}]\; \mathbf{S}(\chi_k)\, \mathbf{n}_0 = [\nabla_0\, \delta\mathbf{u}]\; \mathbf{f}_{\mathbf{S},f,k} = \sum_{n=1}^{n=N_\mathrm{n}} \left[\mathbf{c}_{\mathbf{x},n}^\mathrm{T}\, \mathbf{f}_{\mathbf{S},f,k}\, \mathbf{I} \right] \delta\mathbf{u}_n \,. \tag{C.12}$$

In order to evaluate the Eq. (2.43) it is convenient to define:

$$\mathbf{f}_\mathrm{C} = \mathbf{F}\, \mathbf{H}\, \mathbf{n}_{0,f} \,, \tag{C.13}$$

where

$$\mathbf{H} = \mathbb{C} : \mathbf{G} \quad \text{with} \quad \mathbf{G} = \frac{(\nabla_0 \delta\mathbf{u})^{\mathrm{T}} \mathbf{F} + \mathbf{F}^{\mathrm{T}} (\nabla_0 \delta\mathbf{u})}{2}, \tag{C.14}$$

where $\mathbf{H}$ is a symmetric second order tensor and $(:)$ is a double contraction of the fourth order tensor $\mathbb{C}$, see [1]. Using Voigt notation and assuming that $\mathbb{C}$ is symmetric[1]:

$$\begin{pmatrix} H_{11} \\ H_{22} \\ H_{33} \\ H_{23} \\ H_{13} \\ H_{12} \end{pmatrix} = \begin{pmatrix} C_{1111} & C_{1122} & C_{1133} & C_{1123} & C_{1113} & C_{1112} \\ & C_{2222} & C_{2233} & C_{2223} & C_{2213} & C_{2212} \\ & & C_{3333} & C_{3323} & C_{3313} & C_{3312} \\ & & & C_{2323} & C_{2313} & C_{2312} \\ & \text{sym} & & & C_{1313} & C_{1312} \\ & & & & & C_{1212} \end{pmatrix} \begin{pmatrix} G_{11} \\ G_{22} \\ G_{33} \\ 2\,G_{23} \\ 2\,G_{13} \\ 2\,G_{12} \end{pmatrix}, \tag{C.15}$$

where H_{ij} and G_{ij} are the entries of the symmetric second order tensors $\mathbf{H}$ and $\mathbf{G}$ respectively. Because $\mathbf{G}$ is symmetric, it is only necessary to obtain the expression of $\mathbf{G}_1 = \mathbf{F}^{\mathrm{T}} (\nabla_0 \delta\mathbf{u})$ to obtain $\mathbf{G} = (\mathbf{G}_1 + \mathbf{G}_1^{\mathrm{T}})/2$:

$$\mathbf{G}_1 = \mathbf{F}^{\mathrm{T}} [\nabla_0 \mathbf{u}] = \sum_{n=1}^{n=N_n} \begin{pmatrix} c_{X,n}\, \mathbf{F}_{\mathrm{c}_1}^{\mathrm{T}}\, \delta\mathbf{u}_n & c_{Y,n}\, \mathbf{F}_{\mathrm{c}_1}^{\mathrm{T}}\, \delta\mathbf{u}_n & c_{Z,n}\, \mathbf{F}_{\mathrm{c}_1}^{\mathrm{T}}\, \delta\mathbf{u}_n \\ c_{X,n}\, \mathbf{F}_{\mathrm{c}_2}^{\mathrm{T}}\, \delta\mathbf{u}_n & c_{Y,n}\, \mathbf{F}_{\mathrm{c}_2}^{\mathrm{T}}\, \delta\mathbf{u}_n & c_{Z,n}\, \mathbf{F}_{\mathrm{c}_2}^{\mathrm{T}}\, \delta\mathbf{u}_n \\ c_{X,n}\, \mathbf{F}_{\mathrm{c}_3}^{\mathrm{T}}\, \delta\mathbf{u}_n & c_{Y,n}\, \mathbf{F}_{\mathrm{c}_3}^{\mathrm{T}}\, \delta\mathbf{u}_n & c_{Z,n}\, \mathbf{F}_{\mathrm{c}_3}^{\mathrm{T}}\, \delta\mathbf{u}_n \end{pmatrix}, \tag{C.16}$$

where $\mathbf{F}_{\mathrm{c}_i}$ is the i-th column of tensor $\mathbf{F}$. Therefore in Voigt notation:

$$\mathbf{G} = \begin{pmatrix} G_{11} \\ G_{22} \\ G_{33} \\ 2\,G_{23} \\ 2\,G_{13} \\ 2\,G_{12} \end{pmatrix} = \begin{pmatrix} c_{X,n}\, \mathbf{F}_{\mathrm{c}_1}^{\mathrm{T}}\, \delta\mathbf{u}_n \\ c_{Y,n}\, \mathbf{F}_{\mathrm{c}_2}^{\mathrm{T}}\, \delta\mathbf{u}_n \\ c_{Z,n}\, \mathbf{F}_{\mathrm{c}_3}^{\mathrm{T}}\, \delta\mathbf{u}_n \\ \left[c_{Y,n}\, \mathbf{F}_{\mathrm{c}_3}^{\mathrm{T}} + c_{Z,n}\, \mathbf{F}_{\mathrm{c}_2}^{\mathrm{T}}\right] \delta\mathbf{u}_n \\ \left[c_{X,n}\, \mathbf{F}_{\mathrm{c}_3}^{\mathrm{T}} + c_{Z,n}\, \mathbf{F}_{\mathrm{c}_1}^{\mathrm{T}}\right] \delta\mathbf{u}_n \\ \left[c_{X,n}\, \mathbf{F}_{\mathrm{c}_2}^{\mathrm{T}} + c_{Y,n}\, \mathbf{F}_{\mathrm{c}_1}^{\mathrm{T}}\right] \delta\mathbf{u}_n \end{pmatrix}. \tag{C.17}$$

From the above it is possible to prove that:

$$\begin{aligned} \mathbf{f}_{\mathbb{C}}(\chi_k, \delta\mathbf{u}) = \mathbf{C}_{\mathbf{x}}(\chi_k) \sum_{n=1}^{n=N_n} c_{X,n}\, \delta\mathbf{u}_n \\ + \mathbf{C}_{\mathbf{y}}(\chi_k) \sum_{n=1}^{n=N_n} c_{Y,n}\, \delta\mathbf{u}_n + \mathbf{C}_{\mathbf{z}}(\chi_k) \sum_{n=1}^{n=N_n} c_{Z,n}\, \delta\mathbf{u}_n, \end{aligned} \tag{C.18}$$

[1] This is true for the materials that are considered in this work.

where

$$\mathbf{C_x} = \mathbf{F}\left(\mathbf{C}_{\mathbb{C},c_1}\,\mathbf{n}_0\,\mathbf{F}_{c_1}^{\mathrm{T}} + \mathbf{C}_{\mathbb{C},c_6}\,\mathbf{n}_{0,f}\,\mathbf{F}_{c_2}^{\mathrm{T}} + \mathbf{C}_{\mathbb{C},c_5}\,\mathbf{n}_0\,\mathbf{F}_{c_3}^{\mathrm{T}}\right), \tag{C.19}$$

$$\mathbf{C_y} = \mathbf{F}\left(\mathbf{C}_{\mathbb{C},c_6}\,\mathbf{n}_0\,\mathbf{F}_{c_1}^{\mathrm{T}} + \mathbf{C}_{\mathbb{C},c_2}\,\mathbf{n}_{0,f}\,\mathbf{F}_{c_2}^{\mathrm{T}} + \mathbf{C}_{\mathbb{C},c_4}\,\mathbf{n}_0\,\mathbf{F}_{c_3}^{\mathrm{T}}\right), \tag{C.20}$$

$$\mathbf{C_z} = \mathbf{F}\left(\mathbf{C}_{\mathbb{C},c_5}\,\mathbf{n}_0\,\mathbf{F}_{c_1}^{\mathrm{T}} + \mathbf{C}_{\mathbb{C},c_4}\,\mathbf{n}_{0,f}\,\mathbf{F}_{c_2}^{\mathrm{T}} + \mathbf{C}_{\mathbb{C},c_3}\,\mathbf{n}_0\,\mathbf{F}_{c_3}^{\mathrm{T}}\right), \tag{C.21}$$

being $\mathbf{C}_{\mathbb{C},c_i}$ the second order tensor formed by the i-th column of $\mathbb{C}$, for example:

$$\mathbf{C}_{\mathbb{C},c_1} = \begin{pmatrix} C_{1111} & C_{1112} & C_{1113} \\ & C_{1122} & C_{1123} \\ \text{sym} & & C_{1133} \end{pmatrix}. \tag{C.22}$$

Saint Venant-Kirchhoff material model For this material the elastic moduli is [2]:

$$\mathbb{C} = \begin{pmatrix} \lambda+2\,\mu & \lambda & \lambda & 0 & 0 & 0 \\ & \lambda+2\,\mu & \lambda & 0 & 0 & 0 \\ & & \lambda+2\,\mu & 0 & 0 & 0 \\ & & & \mu & 0 & 0 \\ & \text{sym} & & & \mu & 0 \\ & & & & & \mu \end{pmatrix}, \tag{C.23}$$

where λ and μ are the Lamé parameters.

Simo-Miehe material model For this material the elastic moduli is [2]:

$$\begin{aligned} \mathbb{C} = & \left(\frac{2}{9}\,\mu\,J^{-2/3}\,\mathrm{tr}(\mathbf{C}) + \kappa\,J^2\right)\mathbf{C}^{-1}\otimes\mathbf{C}^{-1} \\ & + \left(\frac{2}{3}\,\mu\,J^{-2/3}\,\mathrm{tr}(\mathbf{C}) - \kappa\,\left(J^2-1\right)\right)\mathbf{C}^{-1}\odot\mathbf{C}^{-1} \\ & - \frac{2}{3}\,\mu\,J^{-2/3}\left(\mathbf{I}\otimes\mathbf{C}^{-1} + \mathbf{C}^{-1}\otimes\mathbf{I}\right). \end{aligned} \tag{C.24}$$

where $\kappa = \lambda + 2\,\mu/3$ and

$$\mathbf{I} \otimes \mathbf{C}^{-1} + \mathbf{C}^{-1} \otimes \mathbf{I} = \begin{pmatrix} 2\,D_{11} & D_{11}+D_{22} & D_{11}+D_{33} & D_{23} & D_{13} & D_{12} \\ & 2\,D_{22} & D_{22}+D_{33} & D_{23} & D_{13} & D_{12} \\ & & 2\,D_{33} & D_{23} & D_{13} & D_{12} \\ & & & 0 & 0 & 0 \\ & \text{sym} & & & 0 & 0 \\ & & & & & 0 \end{pmatrix}, \tag{C.25}$$

$$\mathbf{C}^{-1} \otimes \mathbf{C}^{-1} = \begin{pmatrix} D_{11}\,D_{11} & D_{11}\,D_{22} & D_{11}\,D_{33} & D_{11}\,D_{23} & D_{11}\,D_{13} & D_{11}\,D_{12} \\ & D_{22}\,D_{22} & D_{22}\,D_{33} & D_{22}\,D_{23} & D_{22}\,D_{13} & D_{22}\,D_{12} \\ & & D_{33}\,D_{33} & D_{33}\,D_{23} & D_{33}\,D_{13} & D_{33}\,D_{12} \\ & & & D_{23}\,D_{23} & D_{23}\,D_{13} & D_{23}\,D_{12} \\ & \text{sym} & & & D_{13}\,D_{13} & D_{13}\,D_{12} \\ & & & & & D_{12}\,D_{12} \end{pmatrix}, \tag{C.26}$$

$$\mathbf{C}^{-1} \odot \mathbf{C}^{-1} = \begin{pmatrix} D_{11}^2 & D_{12}^2 & D_{13}^2 & D_{13}D_{12} & D_{11}D_{13} & D_{11}D_{12} \\ & D_{22}^2 & D_{23}^2 & D_{22}D_{23} & D_{12}D_{23} & D_{22}D_{12} \\ & & D_{33}^2 & D_{33}D_{23} & D_{13}D_{33} & D_{13}D_{23} \\ & & & \dfrac{D_{33}\,D_{22}+D_{23}^2}{2} & \dfrac{D_{12}\,D_{33}+D_{23}\,D_{13}}{2} & \dfrac{D_{12}\,D_{23}+D_{22}\,D_{13}}{2} \\ & \text{sym} & & & \dfrac{D_{11}\,D_{33}+D_{13}^2}{2} & \dfrac{D_{11}\,D_{23}+D_{12}\,D_{13}}{2} \\ & & & & & \dfrac{D_{11}\,D_{22}+D_{12}^2}{2} \end{pmatrix}, \tag{C.27}$$

being D_{ij} the entries of $\mathbf{C}^{-1}$ (the inverse of $\mathbf{C}$):

$$\mathbf{C}^{-1} = \begin{pmatrix} D_{11} & D_{12} & D_{13} \\ & D_{22} & D_{23} \\ \text{sym} & & D_{33} \end{pmatrix}. \tag{C.28}$$

References

[1] David C. Kellermann, Mario M. Attard, and Daniel J. O'Shea. Fourth-order tensor algebraic operations and matrix representation in continuum mechanics. *Archive of Applied Mechanics*, 91(12):4631–4668, dec 2021.

[2] Yuri Bazilevs, Kenji Takizawa, and Tayfun E. Tezduyar. *Computational Fluid-Structure Interaction: Methods and Applications*. John Wiley and Sons, dec 2012.

Appendix D

Additional results of analytical examples

This appendix shows additional results that complement the results presented in the body of the thesis.

D.1 Two-dimensional analytical example

Figures D.1, D.2, D.3 and D.4 show the evolution[1] thought the first 18 meshes of Table E.1 using p_1, p_2, p_3 and p_4, respectively. The gray color indicates that the number of cells of the mesh is smaller than N_{n} or a NaN solution due to bad system conditioning. Figure D.5 illustrates the OC for the displacement and stress field. It is observed that the convergence for all cases is adequate, obtaining a more accurate result for p_{i+1} than for p_1, as it was expected.

[1] Using UTM, LRE, $N_{\mathrm{g}} = 7$ and s_{eq}.

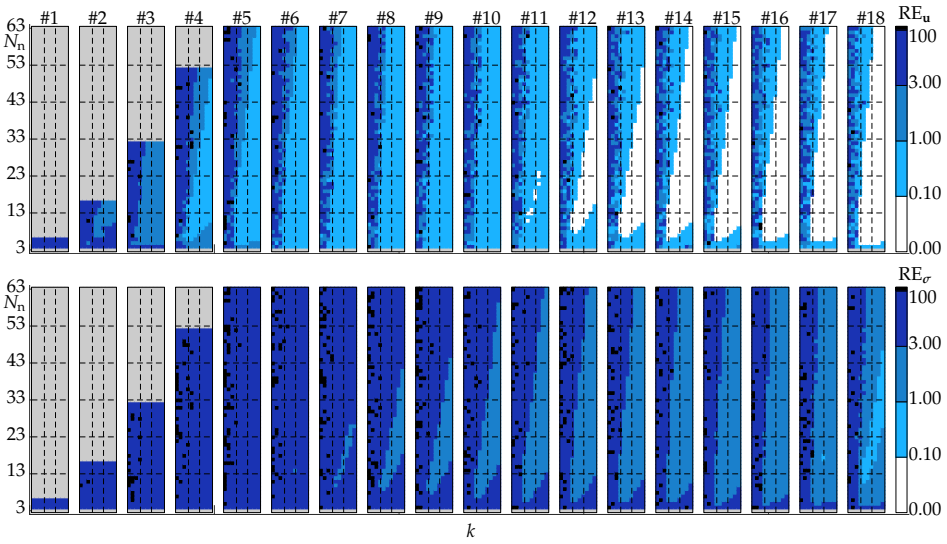

Figure D.1: $RE_{\mathbf{u}}$ (top) and RE_σ (bottom) using UTM with LRE and p_1.

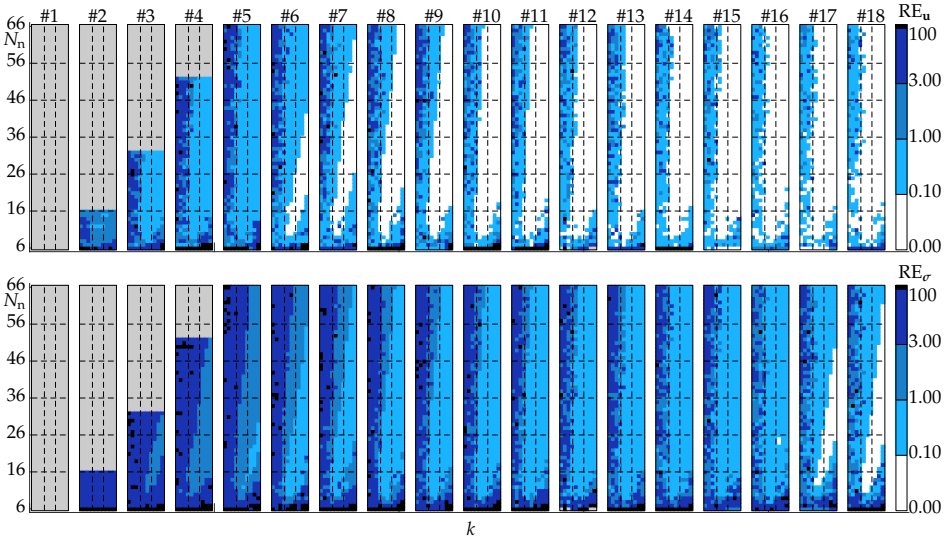

Figure D.2: $RE_{\mathbf{u}}$ (top) and RE_σ (bottom) using UTM with LRE and p_2.

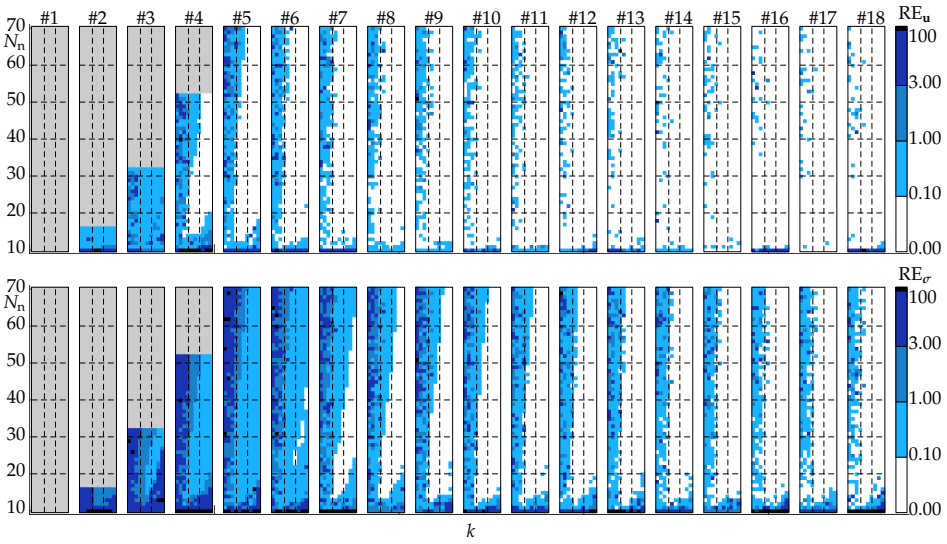

Figure D.3: $RE_{\mathbf{u}}$ (top) and RE_{σ} (bottom) using UTM with LRE and p_3.

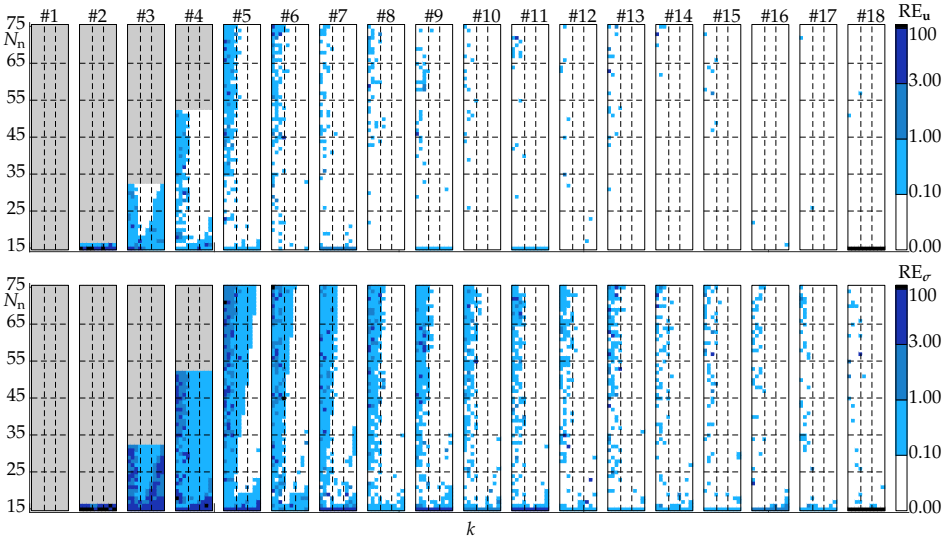

Figure D.4: $RE_{\mathbf{u}}$ (top) and RE_{σ} (bottom) using UTM with LRE and p_4.

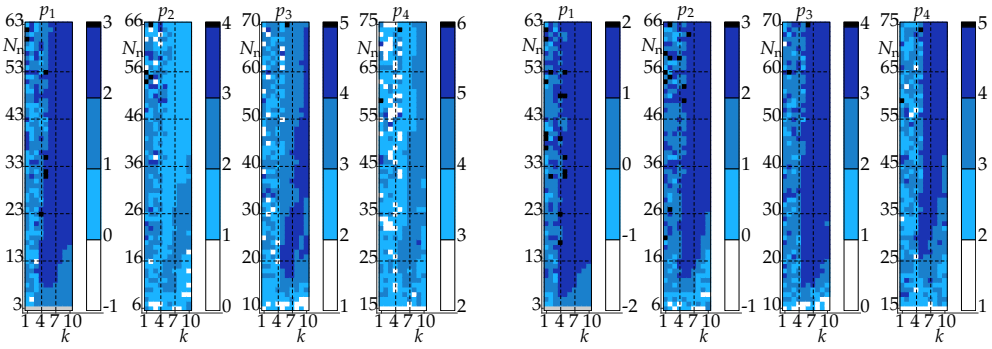

Figure D.5: $\mathrm{OC}_{\mathbf{u}}$ (left) and OC_{σ} (right) using UTM with LRE.

Figures D.6 and D.7 show the convergence of $\mathrm{AE}_{\mathbf{u}}$ and AE_{σ} for LRE and MLS, respectively, using the parameters of Table 3.1 for SQM; while Figures D.8 and D.9 show the convergence of $\mathrm{AE}_{\mathbf{u}}$ and AE_{σ} for LRE and MLS, respectively, using the parameters of Table 3.1 for STM.

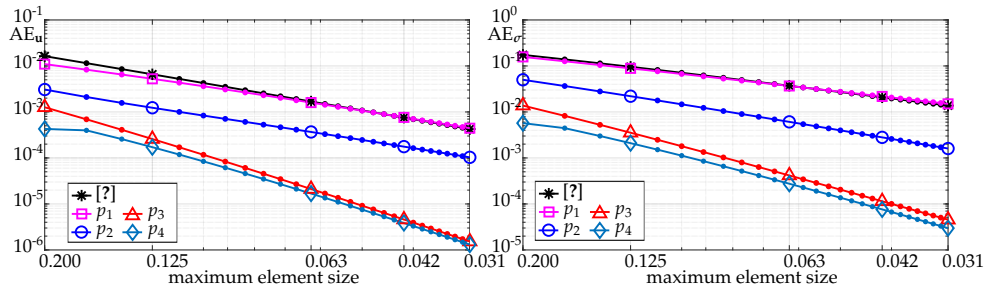

Figure D.6: Convergence of $\mathrm{AE}_{\mathbf{u}}$ (left) and AE_{σ} (right) using LRE with the parameters of Table 3.1 for SQM.

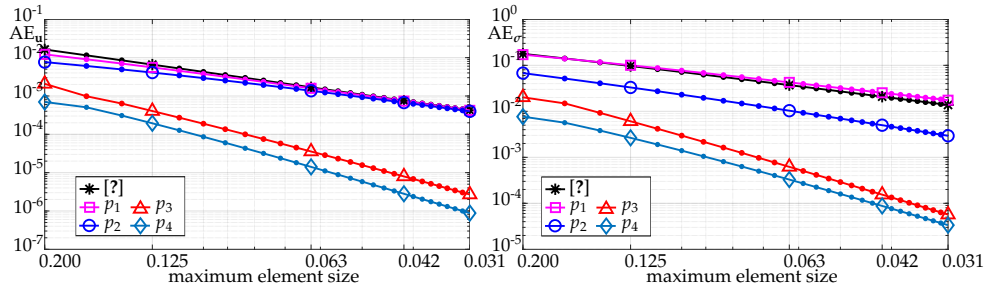

Figure D.7: Convergence of $\mathrm{AE}_{\mathbf{u}}$ (left) and AE_{σ} (right) using MLS with the parameters of Table 3.1 for SQM.

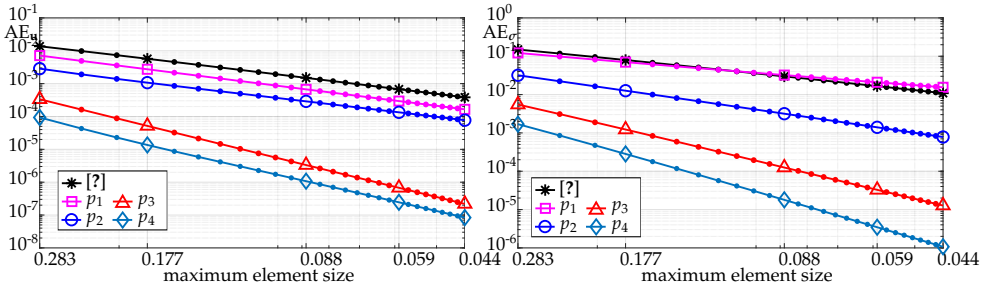

Figure D.8: Convergence of $\mathrm{AE}_{\mathbf{u}}$ (left) and AE_{σ} (right) using LRE with the parameters of Table 3.1 for STM.

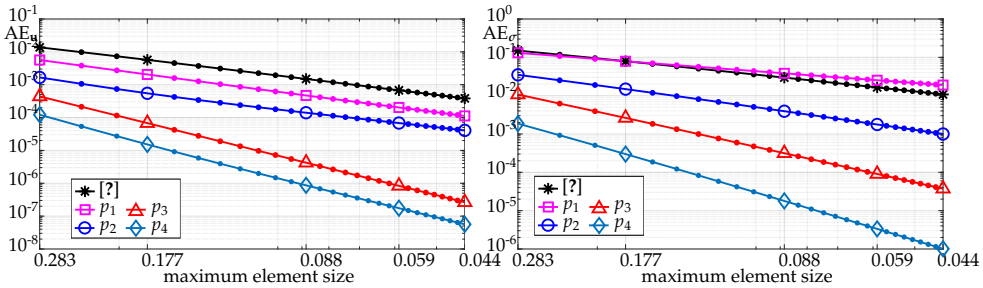

Figure D.9: Convergence of $\mathrm{AE}_{\mathbf{u}}$ (left) and AE_{σ} (right) using MLS with the parameters of Table 3.1 for STM.

Tables D.1, D.2 and D.3 show the order of convergences of the displacement and stress field for the SQM, STM and UTM, respectively. These OC where obtained using the 32 meshes of Table E.1.

Table D.1: Order of convergence using mesh #18 for the displacement and stress fields using SQM and LRE or MLS.

Order	N_n	**Disp. field (u)**			**Stress field (σ)**		
		TOC	LRE	MLS	TOC	LRE	MLS
p_1	13	2	1.71	1.78	1	1.26	1.21
	18	2	1.97	1.89	1	1.49	1.37
	26	2	1.95	1.92	1	1.38	1.36
p_2	16	3	1.86	1.58	2	1.84	1.67
	21	3	1.61	1.79	2	1.88	1.74
	29	3	1.56	2.63	2	1.99	2.38
p_3	20	4	3.61	3.65	3	3.06	3.04
	25	4	3.79	3.60	3	3.24	3.10
	33	4	3.74	3.58	3	3.33	3.29
p_4	25	5	3.29	3.70	4	2.93	3.00
	30	5	3.69	3.91	4	3.71	3.71
	38	5	3.45	4.71	4	3.67	3.96

Table D.2: Order of convergence using mesh #18 for the displacement and stress fields using STM and LRE or MLS.

Order	N_n	**Disp. field (u)**			**Stress field (σ)**		
		TOC	LRE	MLS	TOC	LRE	MLS
p_1	13	2	2.03	2.10	1	1.11	1.05
	18	2	2.02	2.15	1	1.31	1.25
	26	2	2.08	1.96	1	1.44	1.37
p_2	16	3	2.04	2.11	2	1.97	1.88
	21	3	1.79	2.21	2	1.96	1.92
	29	3	1.76	2.22	2	2.04	2.04
p_3	20	4	3.93	3.74	3	3.25	3.11
	25	4	3.92	4.04	3	3.26	3.05
	33	4	3.80	3.99	3	3.22	3.05
p_4	25	5	3.81	4.14	4	3.93	4.02
	30	5	3.80	4.22	4	3.86	3.86
	38	5	3.81	4.07	4	3.98	3.89

Table D.3: Order of convergence using mesh #18 for the displacement and stress fields using UTM and LRE or MLS.

Order	N_n	**Disp. field (u)**			**Stress field (σ)**		
		TOC	LRE	MLS	TOC	LRE	MLS
p_1	13	2	2.08	1.64	1	1.21	0.84
	18	2	2.09	2.13	1	1.43	1.34
	26	2	2.13	2.15	1	1.53	1.49
p_2	16	3	2.03	2.00	2	2.09	1.95
	21	3	1.91	1.99	2	2.09	2.00
	29	3	1.88	2.31	2	2.20	2.20
p_3	20	4	4.02	2.19	3	3.19	1.31
	25	4	4.08	2.94	3	3.34	2.37
	33	4	3.94	3.94	3	3.43	3.27
p_4	25	5	4.11	4.50	4	4.06	4.03
	30	5	3.96	4.35	4	4.08	4.02
	38	5	3.79	4.42	4	4.10	4.08

D.2 Three-dimensional analytical example

Figures D.10, D.11 and D.12 show the evolution[2] thought the seven meshes of Table E.4 using p_1, p_2 and p_3, respectively. The gray color indicates that the number of cells of the mesh is smaller than N_n or a NaN solution due to bad system conditioning. It is observed that the convergence for all cases is adequate, obtaining a more accurate result for p_{i+1} than for p_1, as it was expected.

[2]Using UTM, LRE, $N_g = 37$ and s_{df}.

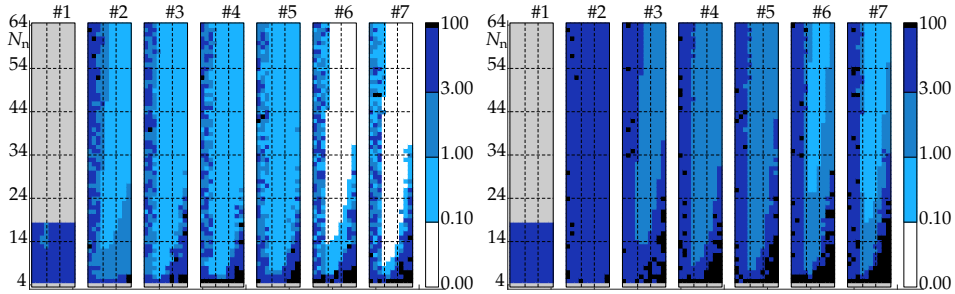

Figure D.10: $RE_{\mathbf{u}}$ (left) and RE_{σ} (right) using UTM with LRE and p_1.

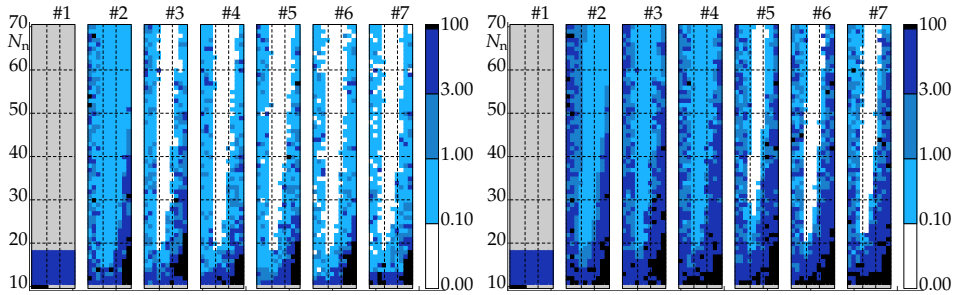

Figure D.11: $RE_{\mathbf{u}}$ (left) and RE_{σ} (right) using UTM with LRE and p_2.

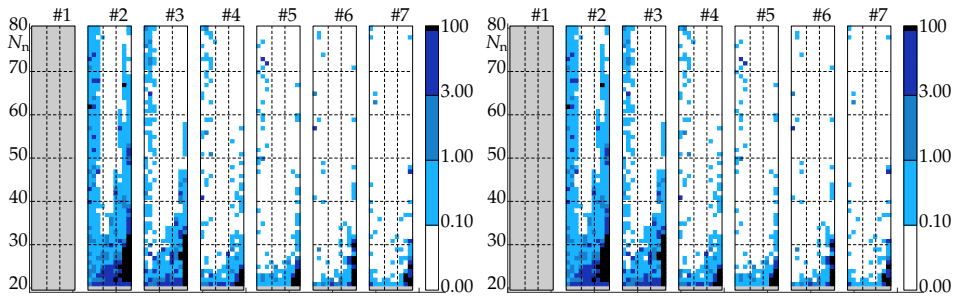

Figure D.12: $RE_{\mathbf{u}}$ (left) and RE_{σ} (right) using UTM with LRE and p_3.

Figures D.13, D.14 and D.15 show the convergence of the absolute error of the displacement field using LRE in SHM, STM and UpTM meshes, respectively, for the values in Table 3.4. It is possible to observe how for the structured meshes (SHM and

STM) the difference between using s_{df} and s_{eq} is negligible. However, in the case of UpTM, the differences, especially with p_3, are appreciable, as in the case of UTM developed in the body of this thesis, see Section 3.2.1. The above indicates that it is recommended to use s_{df}.

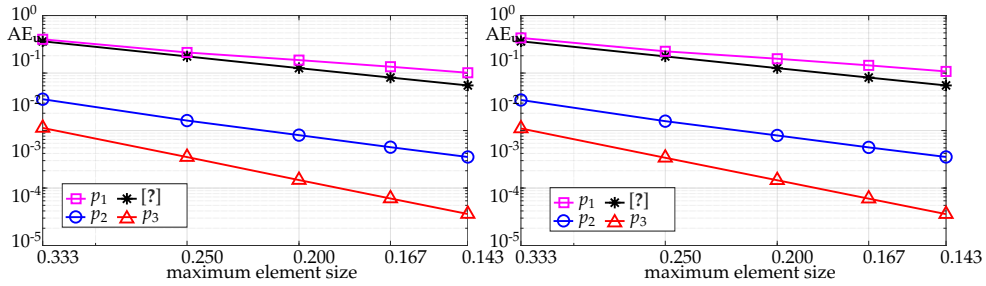

Figure D.13: Convergence of $AE_{\mathbf{u}}$ using LRE and s_{df} (left) or s_{eq} (right) with the parameters of Table 3.4 for SHM.

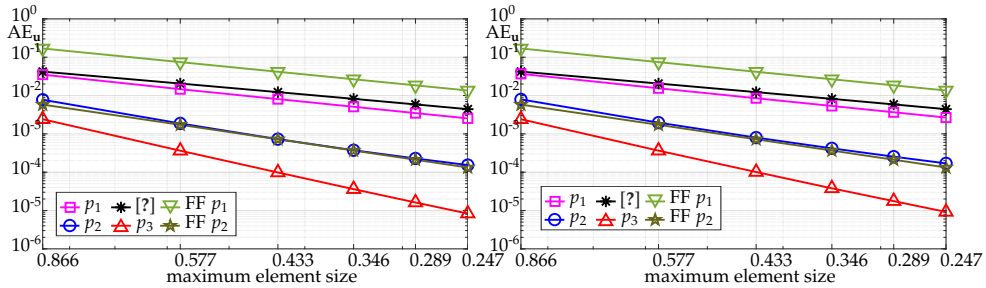

Figure D.14: Convergence of $AE_{\mathbf{u}}$ using LRE and s_{df} (left) or s_{eq} (right) with the parameters of Table 3.4 for STM.

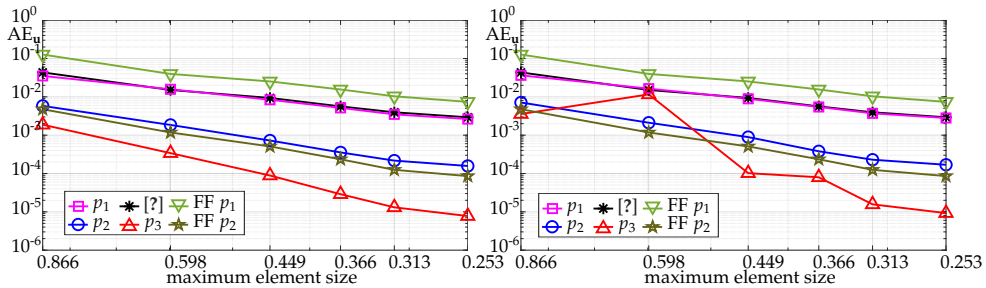

Figure D.15: Convergence of $AE_{\mathbf{u}}$ using LRE and s_{df} (left) or s_{eq} (right) with the parameters of Table 3.4 for UpTM.

Tables D.4, D.5, D.6 and D.7 show the OC, using either MLS or LRE, with s_{df} or s_{eq}, for the SHM, STM, UpTM and UTM meshes, respectively, for the interpolations p_1, p_2 and p_3 considering different values of N_n.

Table D.4: Order of convergence using mesh #7 for the displacement and stress fields using SHM and LRE or MLS. For all the cases $N_g = 49$.

Order	N_n	**Disp. field (u)**					**Stress field (σ)**				
		TOC	LRE		MLS		TOC	LRE		MLS	
			s_{df}	s_{eq}	s_{df}	s_{eq}		s_{df}	s_{eq}	s_{df}	s_{eq}
p_1	14	2	2.03	2.01	2.05	1.99	1	0.84	0.82	0.99	0.96
	24	2	1.99	2.14	2.06	2.14	1	1.00	1.06	0.89	0.91
	34	2	1.64	1.65	1.81	1.85	1	1.57	1.58	1.36	1.38
	44	2	1.55	1.55	1.75	1.78	1	1.71	1.70	1.58	1.59
	54	2	1.81	1.77	1.95	1.96	1	1.81	1.79	1.71	1.71
p_2	20	3	2.85	2.87	1.72	1.59	2	1.97	1.98	1.45	1.38
	30	3	2.86	2.83	1.83	1.91	2	2.01	2.00	1.56	1.57
	40	3	2.93	2.93	1.82	1.88	2	2.02	2.01	1.80	1.80
	50	3	2.72	2.68	2.13	2.19	2	1.94	1.95	1.91	1.92
	60	3	2.67	2.71	2.48	2.44	2	1.90	1.95	2.02	2.04
p_3	30	4	2.72	2.71	2.71	2.68	3	1.93	1.95	1.93	1.94
	40	4	2.59	2.43	2.56	2.39	3	2.33	2.24	2.33	2.25
	50	4	2.40	2.40	2.39	2.40	3	2.35	2.38	2.34	2.37
	60	4	4.07	4.05	4.01	4.03	3	3.32	3.32	3.14	3.15
	70	4	4.09	4.08	4.05	4.08	3	3.41	3.41	3.27	3.28

Table D.5: Order of convergence using mesh #7 for the displacement and stress fields using STM and LRE or MLS. For all the cases $N_g = 37$.

Order	N_n	**Disp. field** ($\mathbf{u}$)					**Stress field** (σ)				
		TOC	LRE		MLS		TOC	LRE		MLS	
			s_{df}	s_{eq}	s_{df}	s_{eq}		s_{df}	s_{eq}	s_{df}	s_{eq}
p_1	14	2	2.18	2.05	-1.17	NaN	1	1.05	1.01	NaN	NaN
	24	2	2.02	2.01	1.93	-1.64	1	1.00	1.04	0.88	-2.65
	34	2	2.12	2.12	2.16	2.02	1	1.16	1.18	1.06	1.01
	44	2	2.09	2.09	2.15	2.05	1	1.42	1.47	1.26	1.29
	54	2	2.16	2.14	2.21	2.14	1	1.53	1.59	1.33	1.40
p_2	20	3	3.18	-0.23	2.83	NaN	2	2.16	-1.11	1.83	NaN
	30	3	3.11	0.60	3.04	-1.08	2	2.14	-0.19	2.05	-2.09
	40	3	3.15	3.07	3.24	3.19	2	2.30	2.26	2.09	2.07
	50	3	3.14	3.06	3.31	3.27	2	2.28	2.28	2.09	2.09
	60	3	3.12	3.10	3.37	3.32	2	2.27	2.28	2.13	2.14
p_3	30	4	-2.40	-2.61	-2.93	-2.68	3	-3.34	-4.07	-3.94	-3.84
	40	4	3.43	3.05	1.47	1.65	3	2.40	2.39	0.96	0.98
	50	4	4.51	3.36	3.19	-0.19	3	3.49	2.45	1.70	-1.02
	60	4	4.52	4.44	4.06	0.31	3	3.53	3.52	2.57	-0.94
	70	4	4.51	4.46	4.57	1.96	3	3.55	3.56	3.42	0.79

Table D.6: Order of convergence using mesh #7 for the displacement and stress fields using UpTM and LRE or MLS. For all the cases $N_g = 37$.

Order	N_n	**Disp. field (u)**					**Stress field (σ)**				
		TOC	LRE		MLS		TOC	LRE		MLS	
			s_{df}	s_{eq}	s_{df}	s_{eq}		s_{df}	s_{eq}	s_{df}	s_{eq}
p_1	14	2	2.11	1.65	-0.62	NaN	1	0.99	0.57	NaN	NaN
	24	2	2.09	2.07	-1.45	NaN	1	1.22	1.23	NaN	NaN
	34	2	2.13	2.10	1.31	0.00	1	1.45	1.48	NaN	NaN
	44	2	2.17	2.15	2.18	2.11	1	1.62	1.66	1.30	1.34
	54	2	2.18	2.16	2.19	2.15	1	1.70	1.74	1.36	1.41
p_2	20	3	1.37	1.79	0.86	NaN	2	0.26	0.71	NaN	NaN
	30	3	3.10	2.18	2.85	2.51	2	2.21	1.08	NaN	NaN
	40	3	3.06	0.29	2.88	2.92	2	2.32	-0.58	NaN	NaN
	50	3	3.06	3.18	2.95	2.92	2	2.38	2.46	2.25	2.25
	60	3	3.04	3.16	3.03	2.96	2	2.41	2.47	2.30	2.32
p_3	30	4	3.95	2.59	1.89	2.10	3	3.01	1.47	NaN	NaN
	40	4	4.43	3.49	1.85	1.29	3	3.49	2.52	NaN	NaN
	50	4	4.56	4.35	1.42	2.17	3	3.59	3.38	0.35	1.24
	60	4	4.64	5.87	2.57	2.21	3	3.69	4.90	1.55	1.41
	70	4	4.71	4.34	4.47	1.55	3	3.78	3.41	3.50	0.71

Table D.7: Order of convergence using mesh #7 for the displacement and stress fields using UTM and LRE or MLS. For all the cases $N_g = 37$.

Order	N_n	**Disp. field (u)** TOC	LRE		MLS		**Stress field (σ)** TOC	LRE		MLS	
			s_{df}	s_{eq}	s_{df}	s_{eq}		s_{df}	s_{eq}	s_{df}	s_{eq}
p_1	14	2	2.15	1.83	0.01	NaN	1	1.11	0.87	NaN	NaN
	24	2	2.04	2.05	-1.31	2.45	1	1.16	1.21	NaN	NaN
	34	2	2.07	2.10	-1.38	-1.11	1	1.39	1.44	NaN	NaN
	44	2	2.16	2.21	0.58	-0.50	1	1.53	1.60	-0.32	-1.51
	54	2	2.22	2.28	1.97	1.11	1	1.64	1.72	1.05	0.35
p_2	20	3	1.02	1.07	3.11	NaN	2	-0.11	-0.01	NaN	NaN
	30	3	2.30	0.91	3.25	3.81	2	1.36	-0.24	NaN	NaN
	40	3	3.28	-0.08	3.40	3.58	2	2.39	-0.47	2.24	2.51
	50	3	3.34	2.45	3.51	3.42	2	2.49	1.72	2.34	2.26
	60	3	3.35	3.39	3.56	3.64	2	2.51	2.51	2.40	2.49
p_3	30	4	6.54	2.04	3.16	3.29	3	5.59	1.04	NaN	NaN
	40	4	4.43	1.24	1.27	0.86	3	3.59	0.38	0.28	-0.09
	50	4	4.34	3.31	1.50	1.34	3	3.41	2.53	0.22	0.39
	60	4	4.54	3.96	0.13	0.95	3	3.60	3.20	-1.09	-0.16
	70	4	4.61	4.52	1.90	1.85	3	3.67	3.64	0.68	0.93

Appendix E

Information of meshes

Table E.1: Mesh information for the 2D analytic example, see Section 3.1.1.

#m	**Structured**						**Untructured (UTM)**		
	squares (SSM)			**triangles (STM)**					
	N_{ic}	N_{bc}	$\ell_{\max}$	N_{ic}	N_{bc}	$\ell_{\max}$	N_{ic}	N_{bc}	$\ell_{\max}$
1	1	4	1.00000	2	4	1.41421	2	4	1.41421
2	4	8	0.50000	8	8	0.70711	8	8	0.70711
3	9	12	0.33333	18	12	0.47140	20	12	0.49691
4	16	16	0.25000	32	16	0.35355	36	16	0.37268
5	25	20	0.20000	50	20	0.28284	58	20	0.30642
6	36	24	0.16667	72	24	0.23570	88	24	0.26517
7	49	28	0.14286	98	28	0.20203	116	28	0.20910
8	64	32	0.12500	128	32	0.17678	152	32	0.19642
9	81	36	0.11111	162	36	0.15713	192	36	0.17806
10	100	40	0.10000	200	40	0.14142	240	40	0.16977
11	121	44	0.09091	242	44	0.12856	280	44	0.15080
12	144	48	0.08333	288	48	0.11785	346	48	0.12672
13	169	52	0.07692	338	52	0.10879	404	52	0.11697
14	196	56	0.07143	392	56	0.10102	466	56	0.11526
15	225	60	0.06667	450	60	0.09428	536	60	0.10341
16	256	64	0.06250	512	64	0.08839	604	64	0.09775
17	289	68	0.05882	578	68	0.08319	676	68	0.09586
18	324	72	0.05556	648	72	0.07857	778	72	0.08879
19	361	76	0.05263	722	76	0.07443	854	76	0.08233
20	400	80	0.05000	800	80	0.07071	952	80	0.07756
21	441	84	0.04762	882	84	0.06734	1026	84	0.07641
22	484	88	0.04545	968	88	0.06428	1142	88	0.06922
23	576	96	0.04167	1152	96	0.05893	1366	96	0.06473
24	625	100	0.04000	1250	100	0.05657	1456	100	0.06373
25	676	104	0.03846	1352	104	0.05439	1588	104	0.06266
26	729	108	0.03704	1458	108	0.05238	1726	108	0.06016
27	784	112	0.03571	1568	112	0.05051	1860	112	0.05946
28	841	116	0.03448	1682	116	0.04877	1992	116	0.05336
29	900	120	0.03333	1800	120	0.04714	2096	120	0.05121
30	1024	128	0.03125	2048	128	0.04419	2416	128	0.04812

Table E.2: Mesh information for the 2D example of clamped beam with uniformly varying loading, see Section 3.1.2.

$\#m$	N_{ic}	N_{bc}	ℓ_{max}
1	206	104	1.500
2	460	156	0.994
3	854	208	0.800
4	1278	260	0.625
5	1996	312	0.512
6	2844	364	0.434
7	3358	416	0.395
8	4146	468	0.351
9	5142	520	0.329
10	6296	572	0.296
11	7616	624	0.267

Table E.3: Mesh information for the 2D example of an infinite plane with an elliptical hole, see Section 3.1.3.

b	F_{σ_∞}	N_{ic}	N_{bc}	ℓ_{max}
0.3	1.5	2765	207	107.00
0.5	2.0	2983	217	107.16
0.8	2.5	2885	217	107.05
1.0	3.0	3058	226	107.13
1.3	3.5	3158	232	107.14
1.5	4.0	3262	238	107.14
1.8	4.5	3352	244	107.12
2.0	5.0	3449	251	107.17
2.3	5.5	3543	255	152.05
2.5	6.0	3676	264	107.16
2.8	6.5	3771	269	107.13
3.0	7.0	3834	276	107.15
3.3	7.5	4006	284	107.15
3.5	8.0	4129	291	107.16
3.8	8.5	4230	298	107.18
4.0	9.0	4299	303	107.13
4.3	9.5	4394	310	107.14
4.5	10.0	4537	317	107.15
4.8	10.5	4650	324	107.15
5.0	11.0	4777	331	107.15

Table E.4: Mesh information for the 3D analytic example, see Section 3.2.1.

#m	**SCM**			**STM**		
	N_{ic}	N_{bc}	$\ell_{\max}$	N_{ic}	N_{bc}	$\ell_{\max}$
1	1	6	1.00000	6	12	1.73205
2	8	24	0.50000	48	48	0.86603
3	27	54	0.33333	162	108	0.57736
4	64	96	0.25000	384	192	0.43301
5	125	150	0.20000	750	300	0.34641
6	216	216	0.16667	1296	432	0.28868
7	343	294	0.14286	2058	588	0.24744
#m	**UpTM**			**UTM**		
	N_{ic}	N_{bc}	$\ell_{\max}$	N_{ic}	N_{bc}	$\ell_{\max}$
1	6	12	1.73205	6	12	1.73205
2	48	48	0.86603	48	48	0.86603
3	180	112	0.59836	241	108	0.50776
4	432	200	0.44876	551	192	0.43301
5	870	316	0.36591	1142	300	0.34641
6	1584	464	0.31320	2035	432	0.28868
7	2436	624	0.25325	3296	588	0.24744

Table E.5: Mesh information for the 3D cantilever beam with a uniformly distributed load, see Section 3.2.2.

#m	**UTM**		
	N_{ic}	N_{bc}	$\ell_{\max}$
1	980	768	2.22764
2	1097	832	2.19688
3	2229	1528	2.23427
4	2124	1512	1.72200
5	2192	1608	1.63100
6	2386	1720	1.50100
7	4075	1832	1.36861

Table E.6: Mesh information for the 3D vibrating cantilever beam, see Section 3.2.3.

$\#m$	UTM		
	N_{ic}	N_{bc}	ℓ_{max}
1	446	336	2.2150178329
2	436	336	2.1961356607
3	882	632	2.1859733660
4	971	648	1.6593758355
5	988	672	1.6453817186
6	876	632	1.6327449280
7	875	648	1.6207957652
8	863	640	1.6102484280
9	940	672	1.6001349644
10	1715	784	1.4142135624
11	1638	800	1.4011434196
12	1842	856	1.3474061940
13	2618	1392	1.3266591763
14	2768	1456	1.3033588149
15	2254	1176	1.2906602961
16	2372	1224	1.1614745233
17	3753	1424	1.0531736507

Table E.7: Mesh information for the hyperelastic cantilever beam, see Section 3.2.5.

$\#m$	UTM		
	N_{ic}	N_{bc}	ℓ_{max}
1	448	328	0.21960943536
2	889	648	0.16207957652
3	1674	808	0.13560497524
4	2318	1192	0.12392242035
5	3803	1416	0.10842918795
$\ell[\text{m}]$	UTM		
	N_{ic}	N_{bc}	ℓ_{max}
2	3803	1416	0.10842918795
3	1360	976	0.16179604445
4	792	656	0.22150178329
5	1046	832	0.22039682393
6	1262	1000	0.21968798329
7	1412	1128	0.22124457055
8	1710	1352	0.21927610449